Development of a multi-scale projection method with immersed boundaries for chemically reactive flows and its application to examine flame stabilization and blow-off mechanisms

by

Kushal Sharad Kedia

S. M., Computation for Design and Optimization,
Massachusetts Institute of Technology (2010)

M.Tech., B.Tech., Aerospace Engineering,
Indian Institute of Technology Madras (2008)

Submitted to the Department of Mechanical Engineering
in partial fulfillment of the requirements for the degree of

Doctor of Philosophy

at the

MASSACHUSETTS INSTITUTE OF TECHNOLOGY

September 2013

Author .....
Department of Mechanical Engineering
August 15, 2013

Certified by .....
Ahmed F. Ghoniem
Ronald C. Crane (1972) Professor
Thesis Supervisor

Accepted by .....
David E. Hardt
Chairman, Department Committee on Graduate Studies

Development of a multi-scale projection method with immersed boundaries for chemically reactive flows and its application to examine flame stabilization and blow-off mechanisms

by

Kushal Sharad Kedia

Submitted to the Department of Mechanical Engineering
on August 15, 2013, in partial fulfillment of the
requirements for the degree of
Doctor of Philosophy

Abstract

High-fidelity multi-scale simulation tools are critically important for examining energy conversion processes in which the coupling of complex chemical kinetics, molecular transport, continuum mixing and acoustics play important roles. The objectives of this thesis are: (i) to develop a state-of-the-art numerical approach to capture the wide spectra of spatio-temporal scales associated with reacting flows around immersed boundaries, and (ii) to use this tool to investigate the underlying mechanisms of flame stabilization and blow-off in canonical configurations.

A second-order immersed boundary method for reacting flow simulations near heat conducting, grid conforming, solid object has been developed. The method is coupled with a block-structured adaptive mesh refinement (SAMR) framework and a semi-implicit operator-split projection algorithm. The immersed boundary approach captures the flame-wall interactions. The SAMR framework and the operator-split algorithm resolve several decades of length and time efficiently. A novel "buffer zone" methodology is introduced to impose the solid-fluid boundary conditions such that symmetric derivatives and interpolation stencils can be used throughout the interior of the domain, thereby maintaining the order of accuracy of the method. Near an immersed solid boundary, single-sided buffer zones are used to resolve the species discontinuities, and dual buffer zones are used to capture the temperature gradient discontinuities. This eliminates the need to utilize artificial flame anchoring boundary conditions used in existing state-of-the-art numerical methods. As such, using this approach, it is possible for the first time to analyze the complex and subtle processes near walls that govern flame stabilization. The approach can resolve the flow around multiple immersed solids using coordinate conforming representation, making it valuable for future research investigating a variety of multi-physics reacting flows while incorporating flame-wall interactions, such as catalytic and plasma interactions.

Using the numerical method, limits on flame stabilization in two canonical configurations: bluff-body and perforated-plate, were investigated and the underlying physical mechanisms were elucidated. A significant departure from the conventional two-zone premixed flame-structure was observed in the anchoring region for both configurations. In the bluff-body wake, the location where the flame is initiated, preferential diffusion and conjugate heat exchange furnish conditions for ignition and enable streamwise flame continuation. In the perforated-plate, on the other hand, a combination of conjugate heat exchange and flame curvature is responsible for local anchoring. For both configurations, it was found that a flame was stable when (1) the local flame displacement speed was equal to the flow speed (static stability), and (2) the gradient of the flame displacement speed normal to its surface was higher than the gradient of the flow speed along the same direction (dynamic stability). As the blow-off conditions were approached, the difference between the former and the latter decreased until the dynamic stability condition (2) was violated. The blow-off of flames stabilized in a bluff-body wake start downstream, near the end of the combustion-products dominated recirculation zone, by flame pinching into an upstream and a downstream propagating sections. The blow-off of flames stabilized in a perforated-plate wake start in the anchoring region, near the end of the preheated reactants-filled recirculation zone, with the entire flame front convecting downstream. These simulations elucidated the thus far unknown physics of the underlying flame stabilization and blow-off mechanisms, understanding which is crucial for designing flame-holders for combustors that support continuous burning. Such an investigation is not possible without the advanced numerical tool developed in this work.

Based on the insight gained from the simulations, analytical models were developed to describe the dynamic response of flames to flow perturbations in an acoustically coupled environment. These models are instrumental in optimizing combustor designs and applying active control to guarantee dynamic stability if necessary.

Thesis Supervisor: Ahmed F. Ghoniem
Title: Ronald C. Crane (1972) Professor

Acknowledgments

First and foremost, I would like to thank my advisor, Prof. Ahmed Ghoniem. No words can completely describe my gratitude towards him. This thesis would not have been possible without his impeccable technical guidance. He has always motivated me to think out of the box and gave me ample room to explore research independently. I have greatly benefited from his unique curiosity for the detailed understanding of any problem while never losing sight of the bigger-picture. Prof. Ghoniem will always be a great role model for me.

I would like to acknowledge my thesis committee: Prof. Green, Prof. Marzouk, Prof. Hadjiconstantinou and Dr. Najm for their invaluable inputs. I would like to specially thank Dr. Habib Najm and his colleagues at the Combustion Research Facility in Sandia National Laboratories[1]: Dr. Cosmin Safta and Dr. Jaideep Ray, for their support in the numerical tool development. Cosmin has been exceptionally patient and helpful. My sincere thanks to King Abdullah University of Science and Technology for sponsoring my research via KAUST Award No. KUS-11-010-01. A part of the numerical tool development was also supported by the US Department of Energy (DOE), Office of Basic Energy Sciences (BES) Division of Chemical Sciences, Geosciences, and Biosciences.

I am thankful to Santosh, Anup, Murat, Ray, Fabrice, James, Cristina, Addison, Nwike and all the other past and current RGD lab members. Santosh and Ray made my work a lot easier by efficiently managing the cluster and frequently brain-storming with me. I feel privileged to be part of this dynamic research group. Many thanks to Lorraine and Leslie for handling all the administrative aspect of my work.

I am grateful to all my friends outside the laboratory, especially Vikrant, Vivek and Abishek. Crazy discussions with them on any and every topic under the sun were great stress-busters, especially during the daily coffee sessions in DuDo and weekly hangouts at the Muddy. The stint with Vikrant and Abishek as room-mates will be etched in

[1]Sandia National Laboratories is a multi-program laboratory managed and operated by Sandia Corporation, a wholly owned subsidiary of Lockheed Martin Corporation, for the U.S. Department of Energy's National Nuclear Security Administration under contract DE-AC04-94-AL85000.

my memory forever. I would also like to acknowledge Sriram, Sahil, Chaitanya, Kasture, Sumeet, Hosur, Kshitij, Ashwin, Mukul, Harish, Ahmedali, Rathi, Pari, Sarvee, Vibhu, Sudhish and all other MIT desi junta for being incredible friends.

I am indebted to my truly awesome wife - Vainatha, for sharing this incredible journey with me, providing unconditional love, understanding, laughter and motivation along the way. I would not have completed this work without her moral support.

I owe every bit of this thesis to the two most wonderful people on earth: my mom Smt. Meena Kedia and my dad Shri. Sharad Kedia. I am blessed to have their constant support and encouragement for every step in my life. I want to share this special occasion with my amazing sister Ashita, who stood-by me during all ups and downs and supported me in my every endeavor. I would also like to thank Sahil, Pratik and Gauthami for being great friends and family members. None of this would have been possible without the love and support of my family.

Finally, I would like to thank God for giving me this opportunity.

Contents

List of Figures

THIS PAGE INTENTIONALLY LEFT BLANK

List of Tables

THIS PAGE INTENTIONALLY LEFT BLANK

Chapter 1

Introduction

1.1 Motivation

In practical combustors, the inlet velocity of the premixed reactants is typically much higher than the laminar flame speed of the mixture. Bluff-bodies and perforated-plate are often used to furnish the necessary mechanism for flame stabilization and continuous burning in such combustors. Two typical burner configurations and schematic illustrations of their canonical configurations are shown in Fig 1-1. These combustors are common in a variety of propulsion devices (air-breathing and non-air-breathing engines), industrial combustors (furnaces, heat exchangers) and domestic gas stoves. The length scales vary from the meter-scale combustor geometric details to the thin sub-millimeter-scale flame fronts. The time scales span the slow conjugate heat exchange processes between the burner wall and the flow, and the rapid diffusion and reaction phenomena. There is a significant flame-wall interaction near the anchoring region. Understanding the steady and dynamic flame characteristics near these burners has been an active research area because of its immense practical importance. High-order efficient numerical methods are critically important to carry out such investigations. A numerical approach to accurately capture the flame-wall interactions is still missing from the current state-of-the-art tools. Such a high-fidelity tool, when developed, can provide deep insight into the complex underlying physical mechanisms of fundamental processes like flame stabilization, extinction and blow-off, which still

remain elusive because of their complex multi-physics nature. Increasing modern computing power and massively parallel architecture has further made this within reach. Development of an advanced immersed boundary method for reacting flows and its application to the mechanistic understanding of fundamental processes of combustion form the basis of my PhD thesis. This tool can also play a vital role in complementing experimental investigations near the combustor walls; which is challenging due to the harsh environment, limited optical access and often inadequate field data. It has a wide range of applicability to other multi-scale combustion problems.

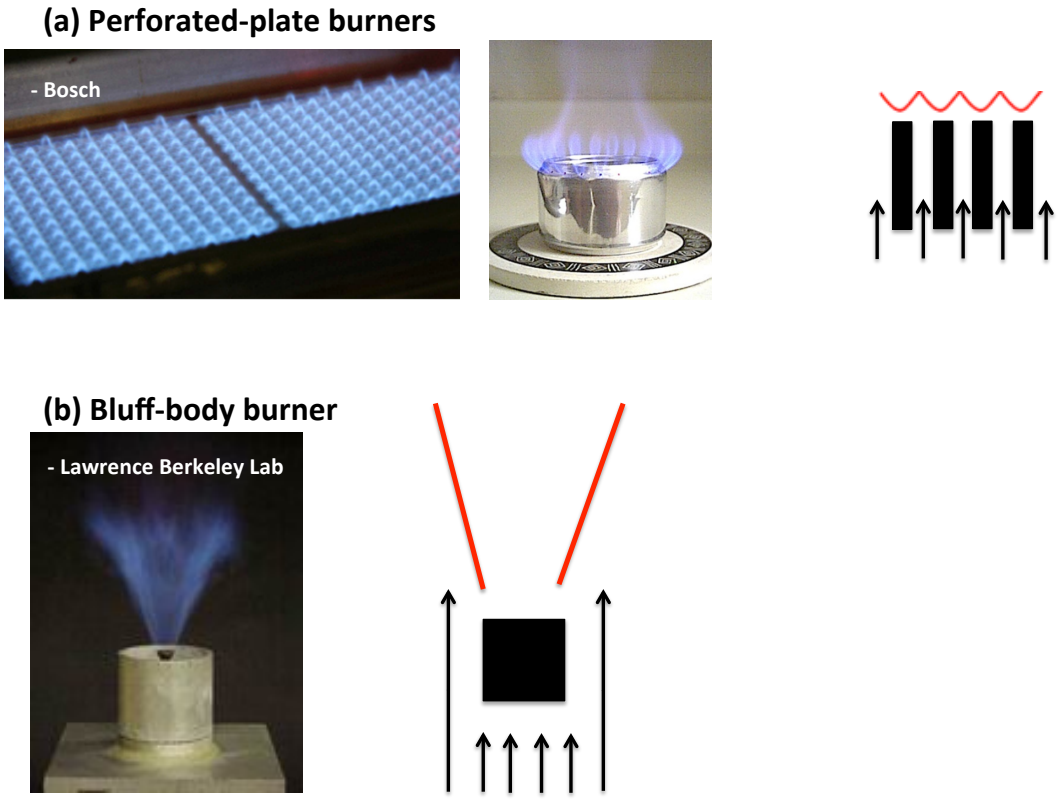

Figure 1-1: Some typical burner configurations and their schematic illustrations.

1.2 Literature

1.2.1 Numerical method development

Accurate and efficient simulation tools to capture flame-wall interactions, allowing the flame to find a stable location naturally, are still unexplored and essential for understanding the localized phenomenon of flame anchoring. In fact, artificial flame anchoring conditions are often employed: a high temperature hot-spot in [1], isothermal flame-holders in [2] and hot combustion products co-flowing with reactants at the inlet in [3]. As a result, current Direct Numerical Simulations (DNS) investigations are limited to the flow-field far away from the anchoring region. These artificial anchoring conditions are however advantageous because the slow time-scale of the conjugate heat exchange between the flame and burner wall is decoupled from the rapid combustion and flow time-scales. Gruber et al. [1] showed that incorporating heat exchange between isothermal (highly simplified model) channel walls and the interior reacting flow in a combustor was critical for accurate prediction of the high convective heat fluxes associated with the rapid radical quenching; however flame-wall interactions near the anchoring region were ignored.

DNS involve solving the governing reacting flow equations on a computational grid that resolves all the relevant scales. Most DNS codes use fully explicit schemes on a uniformly spaced or a stretched regular grid allowing simpler numerical implementation [1, 4]. This enables the use of high-order finite difference schemes to minimize numerical diffusion: fourth-order temporally accurate and eight-order spatially accurate simulations were performed in [1, 4]. The stable time-step used in such codes is typically close to few nanoseconds for hydrocarbon combustion (4×10^{-9}s in [1]), primarily restricted by the stiffness of the chemical kinetics. A compressible flow construction, used in [1], imposes additional restriction on the stable time-step based on the sonic CFL condition. This extremely small time-stepping was significantly increased by constructing a low-Mach, semi-implicit, operator-split projection method, performing the transport and reactive time-advancement via specialized integrators [5, 6].

For typical burners employing a premixed mixture of the inflowing reactants, thin reaction fronts exist only in a small fraction of the total domain. These regions have very sharp gradients in the scalar fields of species mass-fractions, temperature and density. For such problems, one may employ structured adaptive mesh refinement (SAMR) for higher efficiency. SAMR was first suggested by Berger and Oliger [7] and implemented for simulation of shock waves in [8]. Thereafter, it has been used in the simulation of flames with complex chemistry in a variety of laboratory configurations [3, 9]. Hybrid Lagrangian/Eulerian 3D methods for high Reynolds number reactive flows were developed by Schlegel [10]. Safta et al. [11] developed a spatially fourth-order and temporally second-order operator-split projection scheme for the study of chemically reacting flows at the low-Mach number limit using the SAMR framework, which forms the basis of this thesis. This modular code was developed using a Common Component Architecture (CCA) framework [12].

The numerical method for multi-physics reacting flows must also account for detailed chemical kinetics model. Westbrook and Dryer [13] proposed various single-step mechanisms using curve fitting techniques for methane-air flames. They concluded that the single-step mechanisms could not accurately describe the chemical structure of the flame, although they could reproduce experimentally observed flammability limits and flame speeds within a certain range of conditions. A simplification of the complex multi-step chemical kinetics processes in numerical modeling may capture some physics qualitatively (McIntosh [14], Rook et al. [15] and Rook [16]), but may not agree quantitatively with detailed kinetic mechanism simulations, especially with regards to the flame structure. Accurately capturing the chemical structure of the flame, especially near the burner walls where the flame anchors, is critical for investigating stabilization mechanisms.

The SAMR framework development for chemically reacting flows has hitherto been limited to fluid-only domains. Originally developed by Peskin [17] to simulate blood flow in the heart, the Immersed Boundary Method(IBM) has now found widespread use in a variety of engineering applications, although primarily limited to non-reacting flows. The primary advantage of the IBM is that the non-grid conforming complex

immersed bodies can be tackled on a regular Cartesian grid. Mittal and Iaccarino [18] presented a comprehensive review of the IBM. The presence of the solid body becomes known to the fluid through a forcing function, which is consistently constructed using the transport equations and the solid body constraint. Based on the method of forcing used, IBM can be categorized into a continuous forcing approach (forcing imposed in the governing equations before discretization) or a discrete forcing approach (forcing imposed in the governing equations after discretization). In the direct forcing method [19], the solution is first obtained in the combined solid-fluid domain, and then corrected inside the solid to the desired value by imposing the boundary conditions.

Breugem and Boersma [20] presented a method for non-reacting cold flow simulation in porous media using Cartesian mesh-aligned solid cubes in a three-dimensional fluid domain. An IBM variant has been proposed for conjugate heat transfer problems with moving and stationary particles, as well as constant and variable temperature particles; using RANS models in [21] and using LES/DNS models in [22]. For low-Mach number flows, Paravento et al. [23] proposed an IBM to include heat exchange between a Cartesian grid-aligned rectangular object and the non-reacting single-species fluid surrounding it. This heat-exchange method was not generalized for flows with varying (temperature and composition dependent in reacting flows) thermal conductivity. These challenges are further compounded by the presence of chemical reactions and multi-species transport equations. IBM for reacting flows with fully coupled momentum-species-energy transport and conjugate heat exchange with complex immersed walls are not yet developed to the best of my knowledge.

In an effort toward bridging this gap, in this thesis I present a second-order "buffer zone" IBM to incorporate flame-wall interactions and couple it with the numerical development presented in [11]. The development is currently limited to a Cartesian grid conforming immersed solid object. The developed numerical method allows the detailed mechanistic investigation of flame-stabilization and blow-off for the first time. This is performed in this thesis using two canonical configurations. The literature survey on the existing investigations and their limitations are discussed below.

1.2.2 Bluff-body stabilized flames

Bluff-body flames stabilize in the shear layer separating from the burner (Fig.1-1). Blow-off of bluff-body stabilized premixed flames has been widely investigated in the literature, primarily using experiments. However, there does not exist any literature (experimental or numerical) describing the mechanism of bluff-body flame anchoring or the simultaneous dynamic and heat transfer interactions between the reacting flow and the bluff-body, to the best of my knowledge. Experimental investigations face severe limitations such as optical diagnostics issues, harsh combustion environment and lack of detailed species-field data. Numerical simulations have not yet been performed in the literature incorporating detailed chemical kinetics and flame-wall interactions for bluff-body flames due to the large computational expense. Barlow et al. [24], Dunn and Barlow [25] recently investigated the effects of preferential diffusion in bluff-body stabilized turbulent premixed flames using high resolution experimental diagnostics. They demonstrated a local increase in the local equivalence ratio in the recirculation zone downstream of the bluff-body, a unique observation not reported in the literature before.

Soteriou and co-workers [26, 27] studied the physics of the bluff-body stabilized premixed flame at high Reynolds number using an unsteady two-dimensional vortex element method. They analyzed the role of baroclinic vorticity generation, wall-generated vorticity and the dilatation due to the combustion heat release in shifting the asymmetric non-reacting flow in the von-Karman regime to a symmetric shedding field. An adiabatic boundary condition at the bluff-body was imposed in these simulations thereby forcing an artificial flame anchoring condition. Furthermore, the influence of the multi-species transport on flame anchoring cannot be investigated with their tool due to the kinematic flame-sheet modeling of the reacting flow.

The impact of global parameters on bluff-body blow-off such as chemical and aerodynamic parameters has been studied experimentally in classical investigations [28–31]. In these studies, the role of the bluff-body geometry, inflow velocity of the premixed reactants, and various other operating conditions on blow-off were ana-

lyzed. Typical blow-off curves were reported in the form of a plot of the maximum inlet reactant velocity for which the flame is stable at different equivalence ratios. Many phenomenological explanations for blow-off were proposed based on the observed data. It was hypothesized that the flame blows off when the heat demand by the combustible stream in the shear layer for ignition exceeds the heat received by the recirculation zone [30, 32]. Longwell et al. [29] proposed that blow-off occurs when the mass transfer of fresh reactants into the recirculation zone (which is viewed as a perfectly well-stirred reactor) and the rate of its consumption (equivalently the rate of burning) is not balanced. A similar idea was proposed in [28, 33], suggesting that blow-off is caused by the imbalance between the heat supplied to the fresh reactants from the recirculation zone and the heat released by the reaction. Shanbhogue et al. [34] comprehensively reviewed the blow-off dynamics of the bluff-body stabilized flames at various Reynolds numbers. They demonstrated that the Damköhler number, based on various definitions discussed in Section 4.2.6, correlated very well with the experimentally observed data; essentially encapsulating the physics governing bluff-body flame blow-off. Recent high-speed laser diagnostics based experimental investigations of turbulent bluff-body flames showed that extreme stretch rate in the shear layer results in local flame sheet extinction, which is a precursor to blow-off [35, 36]. However, laminar flame blow-off mechanism cannot be explained from these investigations. The simulations, discussed in this thesis, did not show any local extinction in the shear layer during blow-off.

Williams et al. [28] and Russi et al. [37] studied the impact of the flame-holder temperature on flame stabilization. They concluded that the conjugate heat exchange impacts the blowout limits in turbulent flames; heating/cooling the flame-holder decreases/increases the blowout tendency thus widening/shrinking the stability limit. However, Russi et al. [37] also demonstrated that the flame-holder temperature plays a weak role in the blow-off for low Reynolds number flow. The recent experimental investigation of reacting flow in a backward-facing step combustor in [38] revealed that the conjugate heat exchange with a backward-facing step in a combustor can significantly modify or sometimes even suppress the onset of the combustion instability

depending on the operating conditions. A more thermally conductive steel step was reported to be more susceptible to the self-sustained oscillations than a less thermally conductive ceramic step.

Although a large literature exists on the bluff-body flame blow-off, its underlying physical mechanism is still unclear. In almost all of the experimental investigations discussed above, a flow-based timescale (such as heat transfer rate, mass transfer rate, residence time in the recirculation zone) was compared to a chemical timescale (such as burning rate, ignition, extinction) to globally explain the blow-off phenomenon. These phenomenological hypotheses are based on the observed data correlation and thus lack a physical portrait of the local blow-off mechanism.

1.2.3 Perforated-plate stabilized flames

A perforated-plate burner flame is composed of a periodic array of bell-shaped flames connected with U-shaped flames downstream of the hole and the heat-conducting plate, respectively (Fig.1-1). Previous studies have focused on the mechanisms of stabilization and blow-off of inverted flame downstream of a single thin rod or a twin-slot burner. The results of these studies are not directly applicable to perforated-plate stabilized flames because of significant flame-wall interaction in the latter, although some similarities are expected. Aerodynamic stretching, preferential diffusion effects due to non-unity Lewis number, conductive heat losses to the burner plate, as well as volumetric heat loss via radiation have been suggested as physical mechanisms that impact stabilization and blow-off. However, there still exists strong disagreement and contradictory hypothesis in the literature on these mechanisms even for flames downstream of a single thin rod or a twin-slot burner.

One of the earliest theories on flame blow-off was proposed by Lewis and von Elbe [40, 41]. These pioneering studies extended the flame stretch theory of Karlovitz et al. [42] and postulated that blow-off occurs when a critical velocity gradient in the nozzle near the burner plate is reached in the unburnt mixture. A schematic diagram showing the velocity gradient is shown in Fig. 1-2(a). The criterion was formulated in terms of a critical value of the Karlovitz number, $K_b = \eta_0 g_b / S_{u0}$, where η_0 is the

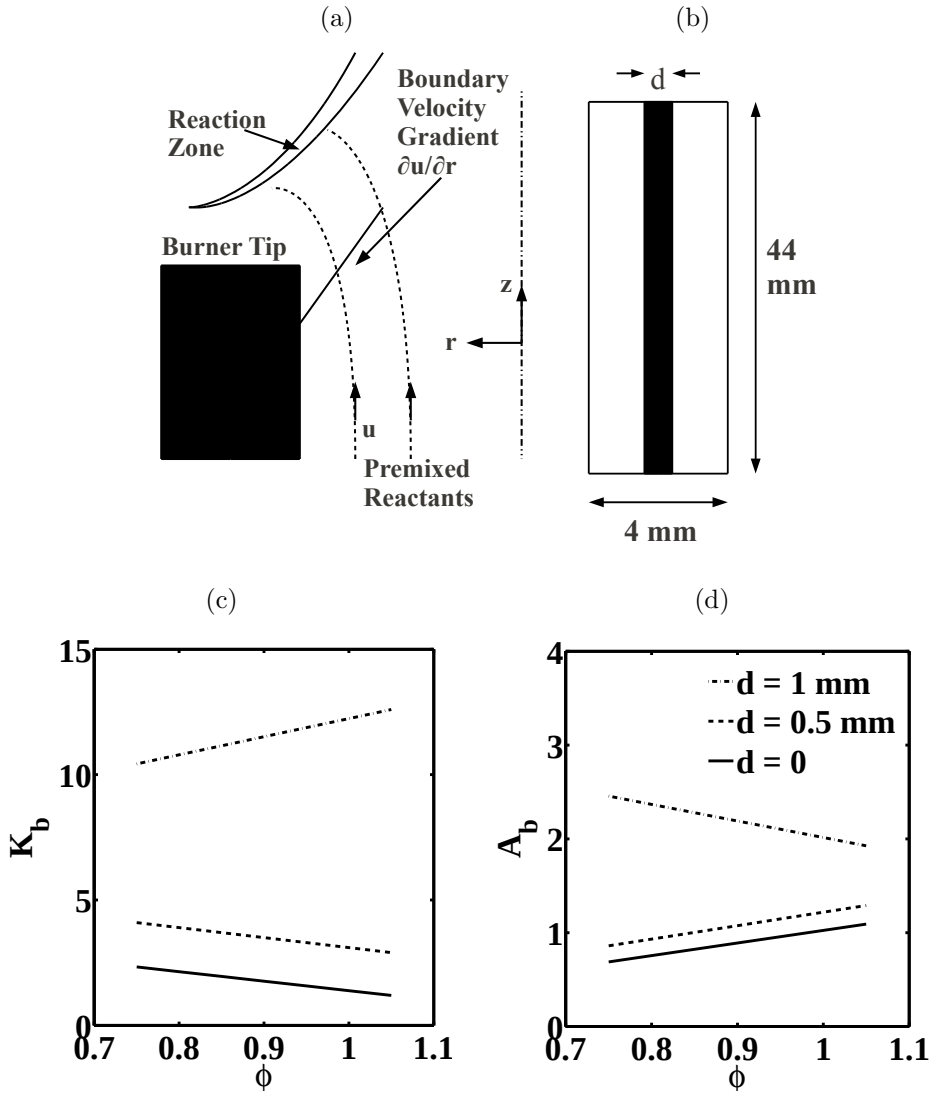

Figure 1-2: (a) Schematic diagram of boundary velocity gradient at the burner exit; (b) Cross-section of the rectangular twin-slot burner exit used by Kawamura et al. [39]; (c) Experimentally determined critical Karlovitz number, $K_b = \eta_0 \frac{\partial u}{\partial r}/S_{u0}$; (d) Experimentally determined critical area increase factor $A_b = \eta_0/R_b$ for methane-air inverted flames stabilized on the rectangular twin-slot burner shown in (b). Data taken from Ref. [39]. $d = 0$ corresponds to a very sharp edge. Results show that $1 < K_b < 10$ and $1 < A_b < 2$.

characteristic length of the preheat zone, g_b is the velocity gradient near the burner plate and S_{u0} is the adiabatic burning velocity. This critical value depends on the configuration used to stabilize the flame, and its value ranges between 1.3 to 2.0 for wire stabilized flames, 0.7 to 3.0 for pilot stabilized flames, and 1.5 to 11 for bluff-body stabilized flames [43]. I will refer to this theory as the 'critical velocity gradient theory'. Lewis and von Elbe assumed that the velocity gradient at the flame base is almost the same as the velocity gradient near the exit of the burner plate. Edmondson and Heap [44] provided additional support for the theory of Lewis and von Elbe by performing experimental analysis of blow-off of inverted methane-air flames stabilized on thin plates. Reed [43] extended Karlovitz's flame stretch concept to flame blow-off on burners with no secondary air dilution.

Melvin and Moss [45] analyzed the 'critical velocity gradient theory' and concluded that it is largely unsatisfactory. The 'critical velocity gradient theory' was also challenged by Kawamura et al. [39, 46]. They proposed that the flame area increase factor (in the Lagrangian sense) due to the strong positive curvature at the flame base (which is concave towards the products) is responsible for blow-off. They demonstrated that a critical value of area-increase factor, which they define as $A_b = \eta_0/R_b$, where R_b is the radius of curvature of the flame base, correlates better with flame blow-off than the Karlovitz number, K_b, used by Lewis and von Elbe. I refer to this area-increase theory as the 'curvature theory'. Kawamura et al. ([39]) performed experiments on a twin-slot rectangular burner. Figure 1-2(b) shows a cross-sectional area of the burner. Figure 1-2(c) shows the measured critical values of K_b and Fig. 1-2(d) shows the critical values of A_b for different equivalence ratios and stabilization plate thicknesses, d. Note that $1 < K_b < 10$ whereas $1 < A_b < 2$. For a given equivalence ratio, the variation of the critical value of K_b is larger for different plate thicknesses as compared to the variation of the critical value of A_b. Moreover, the order of magnitude of the critical value of A_b is unity across the range of ϕ and d investigated in the experiment. Kawamura et al. concluded that the blow-off of inverted flames can be predicted better by the area-increase factor (corresponding to the 'curvature theory') than by the Karlovitz number (corresponding to

the 'critical velocity gradient theory'). However, the figures also show that K_b and A_b have significant variation with thicker plates, demonstrating that both theories fail as the plate thickness increases. The distance between the neighboring holes in a typical perforated plate is comparable to the size of the holes, and it is equivalent to the plate thickness in the twin-slot rectangular burner configuration. Thus, the stabilization plate thickness is large in such perforated-plate burners.

A recent numerical investigation of an inverted methane-air flame stabilized on a slot burner was carried out by Mallens et al. [47]. They concluded that the hydrodynamic straining of the flame base plays a significant role in flame stabilization and not the flame stretch associated with curvature. They challenged the observations of Kawamura et al. [39, 46], once again opening up the debate on the leading mechanisms of flame stabilization and blow-off. The numerical study of Mallens et al. modeled the effect of heat loss by adjusting the parameters of the single-step kinetics mechanism, which were determined using their experimental results. The experimentally determined velocity profiles near and within the flame were matched to the numerical results obtained using the single-step chemistry. The temperature profiles in these simulations did not show significant gradients near the burner wall (thus no heat loss to the burner) and it was concluded that heat losses played no role in flame stabilization or blow-off.

A more fundamental understanding of flame stabilization and blow-off is needed, sidestepping the aim to formulate a global blow-off criterion. For instance, the role of heat transfer to the burner plate in flame stabilization and blow-off remains unclear. Trevino et al. [48] argued that heat transfer to the plate is necessary for the stabilization of inverted flames. On the other hand, Sung et al. [49] demonstrated the existence of solutions where inverted flame can stabilize without heat loss to the thin stabilizing rod. However, they emphasize that the conclusions of Trevino et al. may still be valid when the flame stabilizes close to the rod. Kawamura et al. [39, 46] concluded that the heat loss plays an insignificant role in the flame blow-off mechanism.

The dynamic response of the perforated-plate flame to velocity perturbations de-

termines the nature of the self-excited oscillations in closed combustion system, which may result in fatal structural damage. Durox et al. [50] experimentally investigated the dynamic flame response using flame transfer functions (FTF) under different configurations and determined that at certain low frequencies, the normalized heat release amplitude is greater than the non-dimensional velocity oscillations. For V-shaped and M-shaped flames, resonance (overshoot in the FTF gain) was attributed to flame-area oscillations. In recent investigations, it was shown that for perforated-plate burners, this behavior arises because of a significant thermal interaction between the gases and the plate [51–53]. An analytical model for the prediction of perforated-plate stabilized FTFs was proposed by Altay et al. [52]. The model relied on specifying the steady-state flame standoff distance which was obtained from the perforated-plate's surface temperature using Rook's model [15, 16]. This plate temperature was kept as a free parameter. The model further assumed that the mean burning velocity of the flame base is the adiabatic laminar flame speed. These assumptions encompass the flame-wall thermal interaction information. In this thesis, I analytically model this flame-wall interaction using the understanding of the perforated-plate flame stabilization mechanism.

1.3 Thesis outline

My objective is to develop a second-order state-of-the-art numerical method to capture the wide spectra of spatio-temporal scales associated with combustion using an operator-split projection algorithm and a block-structured adaptive mesh refinement (SAMR) framework coupled with an immersed boundary formalism. No artificial boundary conditions are used for flame anchoring. Using this new method, one can simultaneously tackle (a) Cartesian mesh-aligned immersed wall undergoing conjugate heat exchange with the surrounding reacting flow allowing the flame to naturally anchor, (b) multiscale processes using the operator-split projection scheme, (c) detailed chemical kinetics for multi-species transport, and (d) dynamic tracking of the flame with SAMR. I describe this novel numerical method in Chapter 2.

Using the numerical method, limits on flame stabilization in two different configurations: bluff-body and perforated-plate, are investigated and the underlying anchoring and blow-off mechanisms are elucidated in Chapters 3-5. The sequence of events during the blow-off process is discussed. The role of conjugate heat exchange with the flame-holder was also investigated. I focus on laminar flames only, thereby decoupling the additional complexities of flow unsteadiness and vortex shedding associated with turbulent flames. Based on the insight gained from the simulations, an analytical model is developed in Chapter 6 to describe the dynamic response of flames to flow perturbations in an acoustically coupled environment. Advanced numerical developments showing the three-dimensional extension and the immersed stair-stepped solid treatment are discussed in Chapter 7. The thesis summary and suggested future work are presented in Chapter 8.

THIS PAGE INTENTIONALLY LEFT BLANK

Chapter 2

A second order buffer zone method to incorporate flame-wall interactions

2.1 Overview

State-of-the-art reacting flow simulations need to account for a wide spectrum of spatio-temporal length and time scales. This mulstiscale problem is tackled by coupling my novel immersed boundary method (IBM) with a low Mach semi-implicit operator-split projection method and a block-structured adaptive mesh refinement (SAMR) framework presented in [11] . A "buffer zone" methodology is introduced to impose the solid-fluid boundary conditions such that the solver uses symmetric derivatives and interpolation stencils throughout the interior of the numerical domain; irrespective of whether it describes fluid or solid cells. The development discussed in this chapter is limited to a two-dimensional Cartesian grid-conforming solid. I present validation of the code using benchmark simulations documented in the literature. I also demonstrate the overall second-order convergence of my numerical method.

2.2 Governing equations

At the low-Mach number limit, the continuity, momentum and scalar equations are written in compact form as

$$\nabla \cdot \mathbf{v} = -\frac{1}{\rho}\frac{D\rho}{Dt} \tag{2.1a}$$

$$\frac{\partial \mathbf{v}}{\partial t} = -\frac{1}{\rho}\nabla p + C_U + D_U \tag{2.1b}$$

$$\frac{\partial T}{\partial t} = C_T + D_T + S_T \tag{2.1c}$$

$$\frac{\partial Y_k}{\partial t} = C_{Y_k} + D_{Y_k} + S_{Y_k} \quad k = 1, 2, \ldots, N_s \tag{2.1d}$$

where $\mathbf{v}$ is the velocity vector, ρ the density, T the temperature, Y_k the mass-fraction of species k, p is the hydrodynamic pressure, and N_s is the number of chemical species. The $\frac{D}{Dt}$ operator represents the material derivative, $\frac{D}{Dt} = \frac{\partial}{\partial t} + \mathbf{v} \cdot \nabla$. The system of governing equations is closed with the equation of state for an ideal gas

$$P_0 = \frac{\rho \Re T}{\overline{W}} = \rho \Re T \sum_{k=1}^{N_s} \frac{Y_k}{W_k} = \text{const} \tag{2.2}$$

where P_0 is the thermodynamic pressure, $\Re$ is the universal gas constant, W_k is the molecular weight of species k, and $\overline{W}$ is the molecular weight of the mixture. The thermodynamic pressure is spatially uniform in the low-Mach number limit. Further, restricting the focus to flow in an open domain, P_0 is assumed constant.

The convection and diffusion terms in (2.1) are given by

$$C_U = -\left(\mathbf{v} \cdot \nabla\right)\mathbf{v}, \qquad D_U = \frac{1}{\rho}\nabla \cdot \tau, \tag{2.3a}$$

$$C_T = -\left(\mathbf{v} \cdot \nabla\right)T, \qquad D_T = \frac{1}{\rho c_p}\nabla \cdot (\lambda \nabla T) - \left(\sum_{k=1}^{N_s} c_{p,k} Y_k \mathbf{V}_k\right) \cdot \nabla T \tag{2.3b}$$

$$C_{Y_k} = -\left(\mathbf{v} \cdot \nabla\right)Y_k, \qquad D_{Y_k} = -\frac{1}{\rho}\nabla\left(\rho Y_k \mathbf{V}_k\right) \tag{2.3c}$$

and the source terms by

$$S_T = -\frac{1}{\rho c_p}\sum_{k=1}^{N_s} h_k \dot{\omega}_k, \qquad S_{Y_k} = \frac{\dot{\omega}_k}{\rho} \tag{2.4}$$

where τ is the stress tensor given by $\tau_{ij} = \mu\left(\frac{\partial u_i}{\partial x_j} + \frac{\partial u_j}{\partial x_i} - \frac{2}{3}\delta_{ij}\nabla\cdot\mathbf{v}\right)$, μ is the dynamic viscosity, and λ is the mixture thermal conductivity. Further,

$$\mathbf{V}_k = -\frac{D_{k,m}}{Y_k}\left(\nabla Y_k + \frac{Y_k}{\overline{W}}\nabla\overline{W}\right), \tag{2.5}$$

is the diffusion velocity of species k, where $D_{k,m}$ is the mixture-averaged diffusivity of species k. Finally, c_p and $c_{p,k}$ are the specific heats at constant pressure for the mixture and species k, respectively, and h_k and $\dot{\omega}_k$ are the specific enthalpy and molar production rate, respectively, of species k. The equation of state Eq. (2.2) is used to derive an expression for the right hand side of the continuity equation (2.1a)

$$\frac{DP_0}{Dt} = 0 \rightarrow \frac{1}{\rho}\frac{D\rho}{Dt} = -\frac{1}{T}\frac{DT}{Dt} - \sum_{k=1}^{N_s}\frac{\overline{W}}{W_k}\frac{DY_k}{Dt} \tag{2.6}$$

$$= -\frac{1}{T}\left(D_T + S_T\right) - \sum_{k=1}^{N_s}\frac{\overline{W}}{W_k}\left(D_{Y_k} + S_{Y_k}\right) \tag{2.7}$$

The Soret and Dufour effects are negligible for hydrocarbon combustion and are not included in the transport model. Radiation is ignored. A mixture-averaged formulation is used to compute the transport properties of the gas mixture.

There is thermal contact between the immersed solid body and the surrounding fluid. This conjugate heat exchange between the solid and the surrounding reacting fluid is incorporated by simultaneously integrating the equations governing the reacting flow with the transient heat conduction equation inside the solid:

$$\frac{\partial T}{\partial t} = \frac{1}{\rho_s c_s}\nabla\cdot\left(\lambda_s \nabla T\right) \tag{2.8}$$

where ρ_s is the density, λ_s is the thermal conductivity and c_s is the heat capacity of

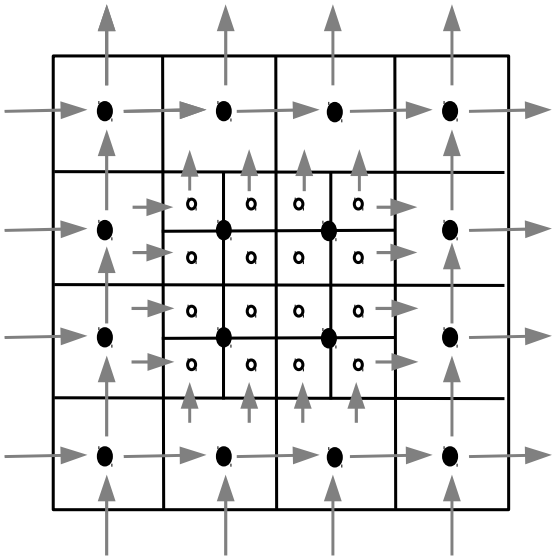

Figure 2-1: Schematic cell topology of a SAMR grid at two consecutive levels; filled circles are cell centers of a coarse grid level $L = 0$ and open circles are cell centers of a fine grid level $L = 1$. Velocity components are computed at the coarse grid face centers marked by large arrows and interpolated to the fine grid face centers marked by small arrows.

the solid.

2.3 Numerical Methodology

The semi-implicit operator-split projection method using the SAMR framework, developed for chemically reacting flows in [11] for fluid-only domains, forms the basis of my numerical method. In this section I briefly summarize it and then couple it with the new buffer zone method to accurately incorporate flame-wall interactions.

2.3.1 SAMR framework

SAMR is used to adaptively refine the computational grid in regions where the internal flame structure needs to be resolved accurately. Figures 2-1 and 2-2 show a schematic illustration of the SAMR grid topology. A relatively coarse Cartesian mesh is laid over the entire domain and the field variables are initialized on it. The grid

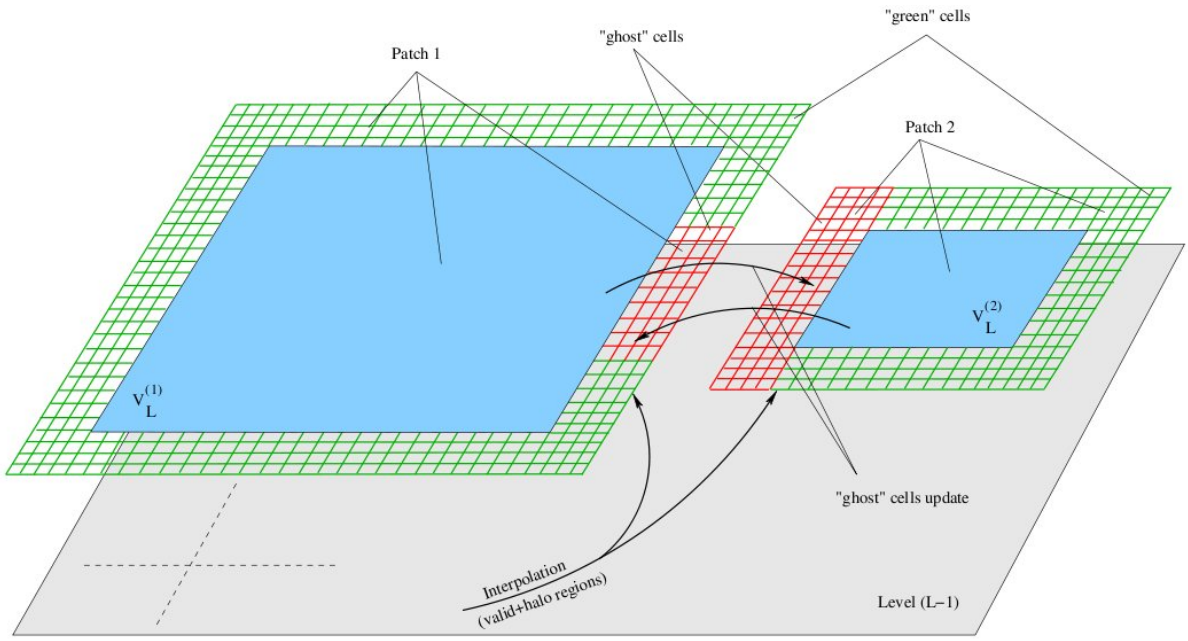

Figure 2-2: Schematic cell topology of a SAMR grid at two consecutive levels; Patches 1 and 2 reside on fine grid level L and have adjacent valid regions, V_L^1 and V_L^2

cells are collated into rectangular patches and finer grids, known as *children* patches (obtained by splitting each cell in half in each dimension) are formed in regions of sharp gradients (based on temperature or the species of choice). This refinement is performed recursively, until a hierarchy of patches is formed. A layer of ghost cells are added to each patch at all levels to allow the use of symmetric stencils for derivatives and interpolations. The adaptive nature of SAMR arises from the periodic process of identifying cells requiring refinement (followed by the addition of finer patches) and the simultaneous coarsening of regions which no longer require refinement. In the current implementation, the momentum equations are discretized and solved on a uniform mesh only, and are coupled to the solution of the species and energy conservation equations on the adaptive mesh hierarchy. For a typical premixed flame, scalar gradients are much sharper than velocity gradients. The characteristic thickness of the reaction zone of the flame (typical of the scalar length-scales) is approximately 5$\sim$10 times smaller than the characteristic thickness of the convection-diffusion zone

(typical of the velocity length-scales) for a conventional hydrocarbon flame[1]. Moreover, the integration of the momentum equations is typically a small fraction ($\sim$ 10%) of the total iteration time [11]. Thus it is efficient to choose a uniform base grid capable of fully resolving the velocity field and using the SAMR hierarchy only for the scalars. This is additionally advantageous because one avoids the complex pressure Poisson solver on the SAMR grid in the projection step, which is currently much slower than its uniform grid counterpart.

A binary marker function (value 1 in the solid and value 0 in the fluid) is used as indicator for the solid cells at all the levels of refinement. The entire domain is treated as a single-material (fluid-only) domain with physical properties (heat conductivity, specific heat and density) appropriately changed in the solid region using the marker function. Layers of fictitious cells, called a buffer zone in this chapter (discussed in Section 2.3.3), are created within the numerical domain near the solid-fluid boundary and their values are filled such that the boundary conditions get imposed automatically when the derivative and interpolation routines are implemented. This allows the usage of the symmetric stencils throughout the interior of the domain. The marker function approach allows for disjoint multiple solid objects (rectangular or block-rectangular) in the computational domain; useful for practical applications such as flow simulation around an array of heat-conducting flame-holders or T-shaped burners in a combustor.

2.3.2 Semi-implicit operator-split projection algorithm

On each rectangular patch in the domain, a staggered mesh is used: variables are defined at the cell-centers (scalars) and the edge-centers (vectors). The numerical integration of the system of equations is performed in three stages. First, a projection approach is adopted for the momentum equations on a fixed uniform mesh. In the second stage, a symmetric Strang splitting scheme is recursively implemented at

[1] $\frac{\delta_R}{\delta_T} \approx \frac{n}{Z}$ for a premixed flame where δ_R is the reaction-diffusion zone thickness, δ_T is the convection-diffusion zone thickness, n is the overall reaction order ($\approx$ 1-3 for methane-air combustion) and Z is the Zeldovich number ($\approx$ 11 for methane-air combustion)

all the SAMR levels beginning with the chemical source term contribution for half the time step (implicit integration), followed by the contributions from the convection and diffusion terms for a full time step (explicit integration), and concluded by the remaining contribution from the reaction term for half the time step (implicit integration). The time stepping is concluded with the third stage, which repeats the projection algorithm for the momentum equations using the updated scalar fields. The sequential stages of the modified numerical algorithm to efficiently integrate the multiscale governing equations, based on [11], are described below. My new buffer zone IBM to incorporate the flame-wall interactions is then presented in detail in Section 2.3.3.

Stage 1_a

The second-order Adams-Bashforth scheme is used to advance the velocity field using convection and diffusion terms only

$$\frac{\hat{\mathbf{v}}^{n+1} - \mathbf{v}^n}{\Delta t} = \left(1 + \frac{1}{2}\frac{\Delta t}{\Delta t_o}\right)\left(C_U^n + D_U^n\right) - \frac{1}{2}\frac{\Delta t}{\Delta t_o}\left(C_U^{n-1} + D_U^{n-1}\right) \tag{2.9}$$

where $\Delta t = t^{n+1} - t^n$ and $\Delta t_o = t^n - t^{n-1}$. Superscripts n and $n-1$ refer to values at the current t^n and previous t^{n-1} times, respectively. The rigid rectangular immersed body is stationary and the solid marker function is used to impose the no-slip condition on the provisional velocity field $\hat{\mathbf{v}}_s^{n+1} = 0$; subscript s denotes a solid cell.

Stage 1_b

The provisional velocity field, $\hat{\mathbf{v}}$, does not satisfy the continuity Eq. (2.1a). This equation is used in conjunction with Eq. (2.1b) to derive an equation for the hydrodynamic pressure field which is then used to correct $\hat{\mathbf{v}}$.

$$\nabla \cdot \left(\frac{1}{\rho^{n+1}}\nabla p\right) = \frac{1}{\Delta t}\left(\nabla \cdot \hat{\mathbf{v}}^{n+1} + \frac{1}{\rho}\frac{D\rho}{Dt}\bigg|^{n+1}\right), \tag{2.10}$$

Since the scalar fields at t^{n+1} are not yet known, $\frac{1}{\rho}\frac{D\rho}{Dt}\Big|^{n+1}$ is estimated by extrapolation:

$$\frac{1}{\rho}\frac{D\rho}{Dt}\Big|^{n+1} = \left(1+\frac{\Delta t}{\Delta t_o}\right)\frac{1}{\rho}\frac{D\rho}{Dt}\Big|^{n} - \frac{\Delta t}{\Delta t_o}\,\frac{1}{\rho}\frac{D\rho}{Dt}\Big|^{n-1} \tag{2.11}$$

$\frac{1}{\rho}\frac{D\rho}{Dt}$ is evaluated using Eq. (2.7), where the scalar values at time steps n and $n-1$ are appropriately used. The density, ρ^{n+1}, is also extrapolated from values at t^n and t^{n-1} similar to Eq. (2.11).

A second-order discretization of the pressure Eq. (2.10) is described in Section (2.3.2).

Stage 1_c

The gradient of the hydrodynamic pressure is used to correct the provisional velocity field $\hat{\mathbf{v}}^{n+1}$ to obtain the predicted velocity at $n+1$

$$\mathbf{v}^{n+1,p} = \hat{\mathbf{v}}^{n+1} - \frac{\Delta t}{\rho^{n+1}}\nabla p, \tag{2.12}$$

Superscript p refers to the predicted velocity values.

Stage 2_a

The scalars (temperature and species mass fractions) are advanced over half the time step based on contributions from the source terms, S_T and S_{Y_k}.

$$\begin{aligned} T^* - T^n &= \int_{\Delta t/2} S_T dt \\ Y_k^* - Y_k^n &= \int_{\Delta t/2} S_{Y_k} dt \quad k = 1, 2, \ldots, N_s \end{aligned} \tag{2.13}$$

The CVODE stiff integrator package [54] is used to integrate Eqs. (2.13). The source terms for species and energy equations are set to zero for the solid body using the binary marker function.

Stage 2_b

A second-order, multi-stage, Runge-Kutta-Chebyshev (RKC) scheme is used to advance scalars based on the contributions from convection and diffusion terms:

$$\begin{aligned} T^{**} - T^{*} &= \int_{t^n}^{t^{n+1}} \underbrace{C_T + D_T}_{F_T} dt \\ Y_k^{**} - Y_k^{*} &= \int_{t^n}^{t^{n+1}} \underbrace{C_{Y_k} + D_{Y_k}}_{F_{Y_k}} dt \quad k = 1, 2, \ldots, N_s \end{aligned} \tag{2.14}$$

As scalars are advanced from t^n to t^{n+1}, velocity values needed to construct convection fluxes for the intermediate RKC times are computed by interpolation based on the values at t^n and $\mathbf{v}^{n+1,p}$ at $t^{n+1} = t^n + \Delta t$:

$$\mathbf{v}^{(s)} = (1 - c_s)\,\mathbf{v}^n + c_s \mathbf{v}^{n+1,p}.$$

where $c_s = (t_s - t_n)/\Delta t$ is the time fraction corresponding to RKC stage s, $1 \leq s \leq M$. The convection terms for species and energy equations are zero for the solid cells since the velocity field is zero. The no penetration boundary condition for species mass-fractions and the conjugate heat exchange matching conditions for temperature, as discussed in Section 2.3.3 are imposed at each RKC stage.

Stage 2_c

Stage 2_c is a repeat of Stage 2_a, using the "**" scalar values as initial conditions

$$\begin{aligned} T^{n+1} - T^{**} &= \int_{\Delta t/2} S_T dt \\ Y_k^{n+1} - Y_k^{**} &= \int_{\Delta t/2} S_{Y_k} dt \quad k = 1, 2, \ldots, N_s \end{aligned} \tag{2.15}$$

At the end of this stage all scalars correspond to t^{n+1}.The species mass-fraction of the diluent (N_2 for air combustion) is computed by imposing the consistency condition $\sum_k Y_k = 1$.

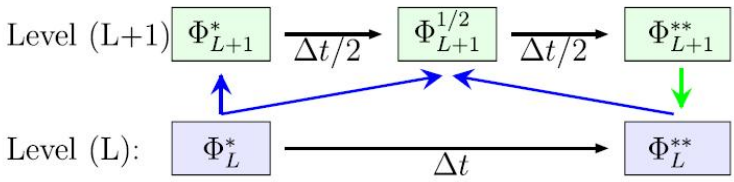

Figure 2-3: Schematic illustration of the time integration on the SAMR mesh hierarchy, ϕ denotes a scalar field

Time integration on the mesh hierarchy

Temperature and species mass-fractions have to be integrated on the successively refined mesh in the SAMR framework. On adjacent mesh levels, L and $L+1$ in the grid (see Fig. 2-1 and 2-2), the scalars are first advanced on the coarse level L using the RKC algorithm described above. After the advancement is completed on L, the solution on this level is used to provide boundary conditions (via coarse-to-fine prolongation) for the solution advancement on $L+1$. The values at various intermediate times between t^n and $t^n + \Delta t$ are computed by interpolation on level L and the results are interpolated to level $L+1$. The grid size on the finer mesh level $L+1$ is half compared to L. The time step is also halved for stability purposes. At the end of the two sub-steps on $L+1$ the fine-grid solution is interpolated to the coarse grid L via fine-to-coarse restriction. This is schematically illustrated in Figure 2-3

Stage 3_a

The provisional velocity field values at t^{n+1} are re-evaluated based on the scalar values obtained at the end of Stage 2 and on the predicted velocity values at the end of Stage 1

$$\frac{\hat{\mathbf{v}}^{n+1} - \mathbf{v}^n}{\Delta t} = \frac{1}{2}\left((C_U^n + D_U^n) + \left(C_U^{n+1} + D_U^{n+1}\right)\right) \tag{2.16}$$

Similar to the Stage 1_a, the no-slip boundary condition at the immersed boundaries is imposed using the binary marker function.

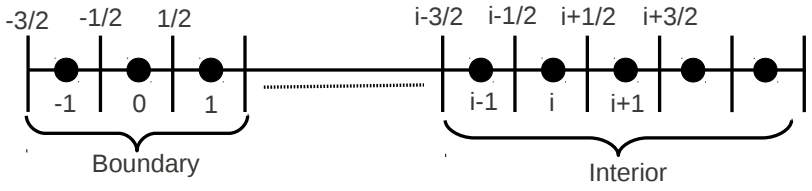

Figure 2-4: Indices of the cell centers and face centers in the interior and at the boundary of the computational domain.

Stage 3_b

The hydrodynamic pressure field is re-computed using Eq. (2.10). The divergence term that enters the rhs for this equation is constructed using the provisional velocity field obtained in Stage 3_a, while Eq. (2.7) is used to compute $\frac{1}{\rho}\frac{D\rho}{Dt}\Big|^{n+1}$ based on scalar values at t^{n+1}, obtained in Stage 2.

Stage 3_c

This final stage in the iteration is similar to Stage 1_c. The gradient of the hydrodynamic pressure obtained at Stage 3_b is used to correct the velocity obtained at the end of Stage 3_a.

The interpolation and derivative stencils are chosen such that an overall second-order accuracy is achieved. A fourth-order derivative stencil is used for all the terms in the governing equations where second-derivatives need to be computed (e.g. the diffusion terms). A second-order derivative stencil is used for all the terms in the governing equations where only a first-derivative needs to be computed (e.g. the convection terms). Second-order stencils are used for the interpolations required during the multigrid prolongation and restriction in the SAMR framework. The interpolation and derivative stencils for various orders of accuracy are presented in [55].

Discretization of the pressure equation

A second-order finite difference discretization for the variable coefficient pressure Poisson Eq. (2.10) is presented here. A one-dimensional configuration, with the indices for the cell and edge centers is shown in Fig. 2-4. The pressure gradient, $\frac{\partial p}{\partial x}$, is first computed at face centers using a 2^{nd} order approximation

$$\left.\frac{\partial p}{\partial x}\right|_{i+\frac{1}{2}} = \frac{1}{2h_x}\left(p_{i+1} - p_i\right) \tag{2.17}$$

Density is interpolated from cell centers to edge centers using a 2^{nd} order stencil [55]. The 2^{nd} order derivative stencil is applied again to the product $\frac{1}{\rho}\frac{\partial p}{\partial x}$ resulting in

$$\left.\frac{\partial}{\partial x}\left(\frac{1}{\rho}\frac{\partial p}{\partial x}\right)\right|_i = \frac{1}{\left(2h_x\right)^2}\left(ap_{i-1} + bp_i + cp_{i+1}\right) \tag{2.18}$$

where

$$a = \frac{1}{\rho_{i-\frac{1}{2}}}; \quad b = -\left(\frac{1}{\rho_{i-\frac{1}{2}}} + \frac{1}{\rho_{i+\frac{1}{2}}}\right); \quad c = \frac{1}{\rho_{i+\frac{1}{2}}} \tag{2.19}$$

The pressure stencil is appropriately adjusted near the computational domain boundaries and the immersed solid boundaries. No-slip boundary conditions are used at the walls using the binary marker function. A staggered grid avoids the usage of an explicit pressure boundary condition at the computational domain boundaries and the immersed wall. The pressure value in the cell-center of one of the corner cells in the outflow boundary of the domain is fixed to unity. The face-centered densities at $(-1/2)$ and $(-3/2)$ are extrapolated using

$$\begin{aligned} \rho_{-1/2} &= \frac{1}{2}\left(3\rho_0 - \rho_1\right) \\ \rho_{-3/2} &= \frac{1}{2}\left(5\rho_0 - 3\rho_1\right) \end{aligned} \tag{2.20}$$

The *hypre* package is used to solved the linear system resulting from the above second-order discretization. The solution is based on the iterative conjugate gradient

method. The tolerance threshold for the residual is typically set to 10^{-14}–10^{-17} to limit the propagation of convergence errors.

Boundary conditions

Standard Dirichlet boundary conditions are imposed for the velocity components normal to inflow and symmetric boundaries. For components tangential to these types of boundaries, slip boundary conditions are applied through appropriate stencils used to compute the corresponding convective and diffusion fluxes.

A "convective" boundary condition is used for the velocity components normal to the outflow boundaries.

$$\frac{\partial \left(\mathbf{v}\cdot\mathbf{n}\right)_b}{\partial t} + U_0 \frac{\partial \left(\mathbf{v}\cdot\mathbf{n}\right)_b}{\partial n} = 0 \tag{2.21}$$

Here, subscript b refers to the boundary values, $\mathbf{n}$ is the unit vector normal to the boundary pointing outside the computational domain and $\partial/\partial n$ is the partial derivative normal to the boundary. Outflow boundary conditions are commonly used in incompressible or low-Mach number flow computations to ensure that numerical errors near outflow boundaries are convected out of the computational domain.

The "convective" velocity U_0 is computed using a global mass conservation constraint obtained by integrating the continuity eq. (2.1a) over the computational domain.

$$\int_V \left(\nabla\cdot\mathbf{v} + \frac{1}{\rho}\frac{D\rho}{Dt}\right) dv = 0 \rightarrow U_0 = \pm\frac{1}{A_{out}}\left(\int_{A_{in}} (\mathbf{v}\cdot\mathbf{n}) d\sigma + \int_V \frac{1}{\rho}\frac{D\rho}{Dt} dv\right) \tag{2.22}$$

Here A_{in} and A_{out} are the areas of the inflow and outflow boundaries and the sign of the velocity depends on the direction of the unit normal $\mathbf{n}$. For Stage 1_a, U_0 is computed using $\frac{1}{\rho}\frac{D\rho}{Dt}\Big|^{n+1}$ extrapolated with eq. (2.11), while for Stage 3_a this term is computed using scalar values obtained in Stage 2.

The pressure solver requires global mass conservation to be satisfied to machine precision. In order to ensure this, eq. (2.1a) is again integrated over the computational

domain after the boundary conditions are applied at the end of Stages 1_a and 3_a

$$\int_V \left(\nabla \cdot \mathbf{v} + \frac{1}{\rho} \frac{D\rho}{Dt} \right) dv = \pm \epsilon A_{out} \tag{2.23}$$

An average velocity correction ϵ is then added to the velocity components normal to the outflow boundaries in order to ensure global mass conservation.

For Stage 2_b, Dirichlet conditions are used for the scalar fields at the inflow boundaries. The Neumann conditions corresponding to symmetry boundary conditions are imposed through appropriate stencils in the calculation of convective and diffusion fluxes in eq. (2.1c-2.1d). A "convective" transport equation is used for scalars at outflow boundaries, similar to eq. (2.21) for the velocity field.

In addition to the above, the no-slip boundary condition and the following scalar matching conditions at each cell edge at the solid-fluid boundary of the immersed object are enforced.

- Temperature matching $T|_{fluid} = T|_{solid}$
- Heat flux matching $\lambda \frac{\partial T}{\partial n}|_{fluid} = \lambda \frac{\partial T}{\partial n}|_{solid}$
- No penetration of species $\frac{\partial Y_i}{\partial n}|_{fluid} = 0$

These matching conditions are imposed using the novel buffer zone approach described in the next section.

2.3.3 Buffer zone method

The buffer zone approach is introduced here: the solution is first obtained in the combined solid-fluid domain, and then corrected inside the solid to the desired value by imposing the boundary conditions. Similar techniques are well developed in the literature for non-reacting flows, even for complex non-grid conforming immersed solid bodies. However a methodology similar to the one described in the following section, that solves multi-species reacting flows in the SAMR framework incorporating solid-fluid conjugate heat exchange, is still missing to the best of my knowledge.

Buffer zones, comprised of a very thin layer of fictitious valued-cells, are employed near the solid-fluid boundary inside the numerical domain. These cells are created at each sub-step of the scalar RKC integration in Stage 2 such that the boundary matching conditions are automatically imposed when the symmetric stencils are used within the solvers for computing derivatives and interpolations. This makes the numerical implementation simpler as the entire domain can then be regarded as a fluid-only domain. The no-penetration of the species is imposed by using single-sided buffer zones and the temperature and heat flux matching conditions are imposed by using dual buffer zones.

Single-sided buffer zones for species mass-fractions

The highest order of interpolation and derivatives needed for an overall second-order accurate scheme is four [11]. Due to the presence of second derivatives in the diffusion terms, the right-hand-side term in Eq. (2.1d) at each cell center then depends on a 3×3 grid cells around it (for a two dimensional stencil). Thus, to impose the no-penetration of species condition at the fluid-solid boundary, a 3-cell deep layer of buffer zone is created inside the rectangular solid body, refer to Fig. 2-5a for a schematic illustration. The species mass-fractions do not physically exist inside the immersed solid object allowing us to re-use the solid cells' data structures originally defined assuming they were fluid cells. This construction does not add significantly to the iteration cost because the number of cells in the buffer zones are a very small fraction of the total number of cells in the full numerical domain.

Consider, for simplicity, a one-dimensional configuration, with the indices for the cell and edge centers as shown in Fig. 2-5b. The zero-gradient scalar no penetration condition, $\frac{\partial f}{\partial x} = 0$, at the face center of the solid-fluid boundary using a 4^{th} order

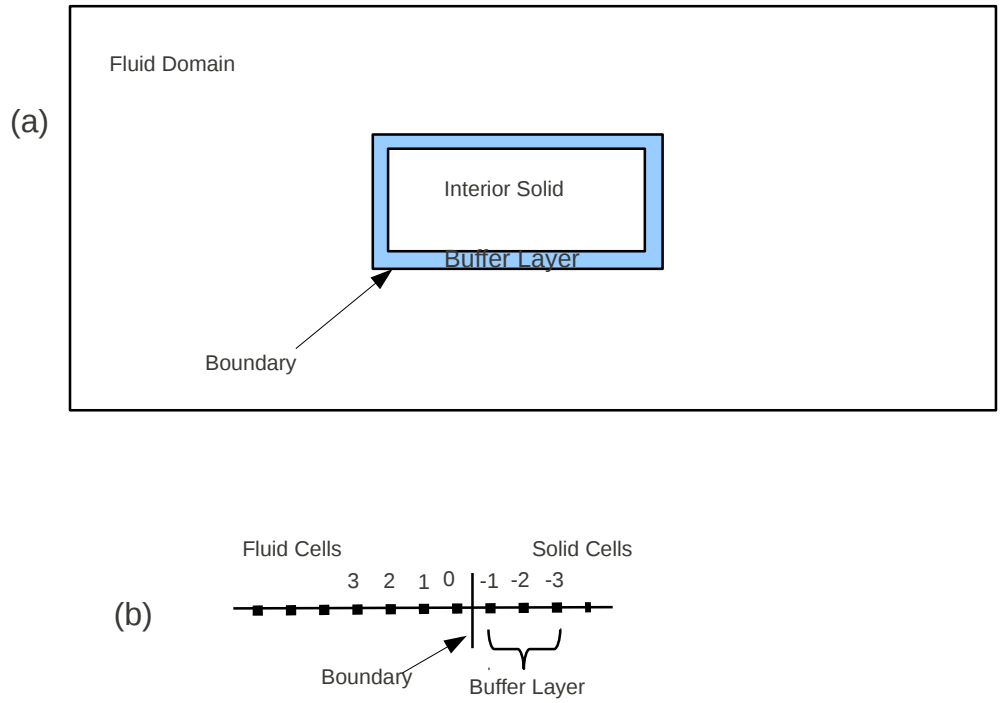

Figure 2-5: (a) Schematic of a Cartesian solid body inside a fluid domain; the shaded region is a 3-cell wide single-sided buffer zone (b) Cell-center indices for a one-dimensional grid marking the single-sided buffer zone.

derivative stencil and 4^{th}order extrapolations for cells (-2) and (-3) gives

$$\begin{aligned} \frac{1}{24h_x}\left(f_{-2} - 27f_{-1} + 27f_0 - f_1\right) &= 0 \\ f_{-2} - 4f_{-1} + 6f_0 - 4f_1 + f_2 &= 0 \\ f_{-3} - 4f_{-2} + 6f_{-1} - 4f_0 + f_1 &= 0 \end{aligned} \tag{2.24}$$

leading to

$$\begin{aligned} f_{-1} &= \frac{1}{23}\left(21f_0 + 3f_1 - f_2\right) \\ f_{-2} &= \frac{1}{23}\left(-54f_0 + 104f_1 - 27f_2\right) \\ f_{-3} &= \frac{1}{23}\left(-250f_0 + 375f_1 - 102f_2\right) \end{aligned} \tag{2.25}$$

These expressions are used to construct the buffer zone for the species mass-fractions

inside the solid. The fluid cells adjacent in the y-direction are used as 0, 1 and 2 for the y-normal edge of the solid body. Similarly the fluid cells adjacent in the x-direction are used as 0, 1 and 2 for x-normal edge.

Corner treatment

Special corner treatment is required for the 4 corners of the immersed solid because of the ambiguity in the direction to choose. The buffer zone is modified in the 3×3 cells in each corner, see Fig. 2-6 for a schematic illustration. A set of 9 consistent equations with these 9 unknowns are formulated and the corner cells (marked as 1, 2, 3 ..., 9 in Fig. 2-6) are appropriately filled. A zero-gradient condition is imposed at the solid-fluid faces adjacent to cells 2, 3, 4 and 7. Corner point (cell 1) is a numerical singularity and does not exist in reality. Hence I approximate a zero-gradient along the diagonal of cell 1. This results in

$$\begin{aligned}
\frac{1}{h_y}\left(f_5 - 27f_2 + 27f_{b0} - f_{b1}\right) &= 0 \\
\frac{1}{h_y}\left(f_6 - 27f_3 + 27f_{c0} - f_{c1}\right) &= 0 \\
\frac{1}{h_x}\left(f_5 - 27f_4 + 27f_{f0} - f_{f1}\right) &= 0 \\
\frac{1}{h_x}\left(f_8 - 27f_7 + 27f_{g0} - f_{g1}\right) &= 0 \\
\frac{1}{\sqrt{h_x^2 + h_y^2}}\left(f_5 - 27f_1 + 27f_{d0} - f_{d1}\right) &= 0
\end{aligned} \tag{2.26}$$

where h_x and h_y are the grid spacings in the x and y directions respectively. 4^{th}order extrapolations along the diagonal direction are chosen for cells 5 and 9, along the x-direction for cell 8 and along the y-direction for cell 6 on the basis of proximity.

This results in

$$\begin{aligned}
(f_5 - 4f_1 + 6f_{d0} - 4f_{d1} + f_{d2}) &= 0 \\
(f_9 - 4f_5 + 6f_1 - 4f_{d0} + f_{d1}) &= 0 \\
(f_8 - 4f_7 + 6f_{g0} - 4f_{g1} + f_{g2}) &= 0 \\
(f_6 - 4f_3 + 6f_{c0} - 4f_{c1} + f_{c2}) &= 0
\end{aligned} \tag{2.27}$$

Above is a set of 9 equations and 9 unknowns (Scalar values f_1, f_2, ..., f_9) based on 21 knowns (f_{a0}, f_{a1}, f_{a2}, f_{b0}, f_{b1}, f_{b2}, ... , f_{g0}, f_{g1}, f_{g2}). The explicit solution is

$$\begin{aligned}
f_1 &= \frac{1}{23}\left(21f_{d0} + 3f_{d1} - f_{d2}\right) \\
f_2 &= f_{b0} - \frac{1}{27}f_{b1} - \frac{2}{23}f_{d0} + \frac{104}{621}f_{d1} - \frac{1}{23}f_{d2} \\
f_3 &= \frac{1}{23}\left(21f_{a0} + 3f_{a1} - f_{a2}\right) \\
f_4 &= f_{f0} - \frac{1}{27}f_{f1} - \frac{2}{23}f_{d0} + \frac{104}{621}f_{d1} - \frac{1}{23}f_{d2} \\
f_5 &= \frac{1}{23}\left(-54f_{d0} + 104f_{d1} - 27f_{d2}\right) \\
f_6 &= \frac{1}{23}\left(-54f_{a0} + 104f_{a1} - 27f_{a2}\right) \\
f_7 &= \frac{1}{23}\left(21f_{g0} + 3f_{g1} - f_{g2}\right) \\
f_8 &= \frac{1}{23}\left(-54f_{g0} + 104f_{g1} - 27f_{g2}\right) \\
f_9 &= \frac{1}{23}\left(-250f_{d0} + 375f_{d1} - 102f_{d2}\right)
\end{aligned} \tag{2.28}$$

Eqs. (2.25) and (2.28) together form the stencils for the single-sided buffer zones for the species mass-fraction fields. They are constructed for each species at all the levels of the SAMR grid and at every sub-step of the multistage RKC integration of the scalar field.

I performed a simple test to check the second-order accuracy of the constructed stencils. These stencils incorporated a zero-gradient (no penetration) condition of the species mass-fractions at the solid-fluid boundary. To test for its accuracy, I first analytically manufactured a test-field with circular contours around a reference point.

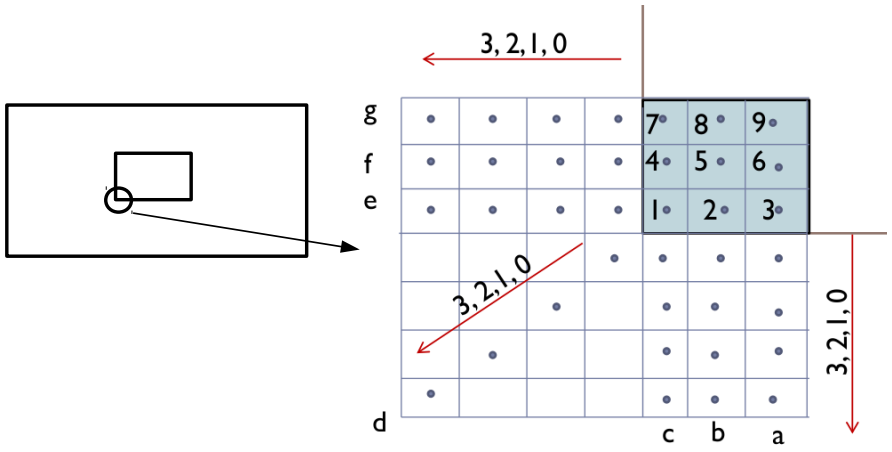

Figure 2-6: (left) Schematic of a Cartesian corner region inside the domain (right) Indices for the special corner treatment for the buffer zones; shaded region is the zoomed-in meshed corner inside the solid body.

I then constructed the 3-cell wide single-sided buffer zone near two perpendicular lines originating from that reference point (normal to the circular contours). The manufactured test-field and the reconstructed field were then compared for order of accuracy estimation. Figure 2-7 shows a uniformly discretized 256×256 square domain. I chose the point corresponding to index (176+1/2,176+1/2) as the reference origin (x_0, y_0) and computed the analytical distance ($d = \sqrt{(x-x_0)^2 + (y-y_0)^2}$) of all the points in the numerical domain from it. The left plot in Fig. 2-7 shows the distance contours of the manufactured test field; which are circular around the reference point by mathematical construction. Two perpendicular line segments with the indices; (1) $i = (176+1/2)$ and $(176+1/2) \leq j \leq 256$ and (2) $(176+1/2) \leq i \leq 256$ and $j = (176 + 1/2)$ were chosen as left and bottom edges of a 80×80 square in the top right corner of the domain. The contours of the test field are normal to these lines. I reconstructed the test field in the 3-cell wide buffer zone marked by the region $177 \leq i, j \leq 179$ using the single-sided buffer zone stencils. The manufactured test-field and the reconstructed field were compared for the error using the ℓ_1 norm ($\ell_1 = \frac{\sum_{ij} |d_{ij} - d_{ij,a}|}{N_p}$). I repeated this by decreasing the resolution: 128×128 discretization of the domain with reference point as (88+1/2,88+1/2). The order of accuracy was computed [56] to be $\log_2 \frac{L_{1,256}}{L_{1,128}} = 2.03$. This manufactured solution test

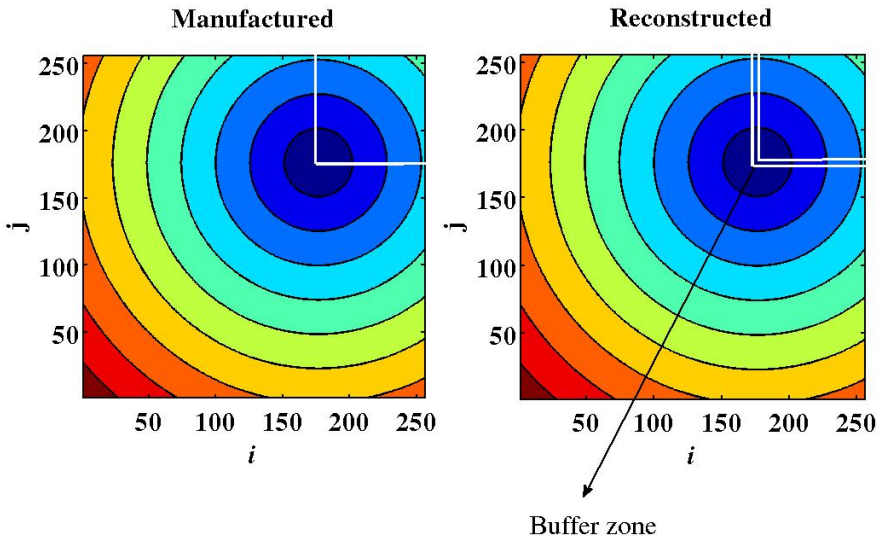

Figure 2-7: Contours of distance from the lower bottom corner of the white square is plotted using $d = \sqrt{(x - x_0)^2 + (y - y_0)^2}$ (left) everywhere in the domain without any special treatment to any cells (right) everywhere in the domain except the 3-cell wide single-sided buffer zone inside the white square using Eqs. (2.25) and (2.28). Grid indices are labeled on the horizontal and vertical axes.

confirmed the second-order accuracy of the single-sided buffer zone stencil. Detailed overall convergence order tests using various reacting and non-reacting flows will be discussed in Section 2.5.

Note

3^{rd} order extrapolations for cells (-2) and (-3) may be used instead of 4^{th}-order extrapolations to reduce numerical oscillations during a rapid transient such as an artificial initial condition of ignition during the start of a combustion simulation. I observed that this reduces the overall order of accuracy to 1. I describe the stencil for such a construction below. Similar to what was done before:

$$\begin{aligned} \frac{1}{24h_x}\left(f_{-2} - 27f_{-1} + 27f_0 - f_1\right) &= 0 \\ f_{-2} - 3f_{-1} + 3f_0 - 1f_1 &= 0 \\ f_{-3} - 3f_{-2} + 3f_{-1} - 1f_0 &= 0 \end{aligned} \tag{2.29}$$

leading to

$$\begin{aligned} f_{-1} &= f_0 \\ f_{-2} &= f_{-1} \\ f_{-3} &= 3f_1 - 2f_0 \end{aligned} \tag{2.30}$$

The corresponding lower order corner point stencil is

$$\begin{aligned} f_1 &= f_{d0} \\ f_2 &= f_{b0} - \frac{1}{27} f_{b1} + \frac{1}{27} f_{d1} \\ f_3 &= f_{a0} \\ f_4 &= f_{f0} - \frac{1}{27} f_{f1} + \frac{1}{27} f_{d1} \\ f_5 &= f_{d1} \\ f_6 &= f_{a1} \\ f_7 &= f_{g0} \\ f_8 &= f_{g1} \\ f_9 &= 3f_{d1} - 2f_{d0} \end{aligned} \tag{2.31}$$

Extension to third dimension

Although the buffer zone construction is shown for a two-dimensional immersed object, it can be easily extended to three-dimensions. The corner will then correspond to a $3 \times 3 \times 3$ cube instead of a 3×3 square and an equivalent 27-point stencil can be analogously derived. The 9-point stencils derived above can be directly used for the sharp edges of the 3D immersed object.

Dual buffer zones for temperature

The numerical approach for buffer zones described in the previous section is valid for the species mass-fractions as they cease to exist inside the solid body. The buffer zones

were constructed based on the values in the fluid. Thus, for computing derivatives and interpolations near the solid-fluid boundary, in the fluid domain, these variables are continuous and smooth. This is not the case for the non-smooth temperature field. The temperature field has a discontinuity in its derivative (a kink) at the fluid-solid boundary in non-isothermal flows because of a large jump in the thermal conductivity: two orders of magnitude jump at an air-ceramic boundary and even higher for an air-metal boundary. Most conventional high-order derivatives and interpolations stencils failed near such a boundary and reduced the overall accuracy because their derivation assumes a smooth field variable.

In this section, I formulate a dual buffer zone approach to address this issue. I construct two temperature fields in the numerical domain. One corresponds to the fluid domain solution (T^f) with a 2-cell wide buffer layer penetrating inside the solid domain, similar in concept to the single-sided buffer zone discussed above. The other complementary field corresponds to the solid domain solution (T^s) with a 2-cell wide buffer layer penetrating inside the fluid domain. Figure 2-8a shows a schematic of the dual buffer zone. Both temperature fields are the same at all the grid points in the numerical domain, except in the 4-cell wide layer of cells around the solid-fluid boundary. This construction, like the single-sided buffer zones, does not add significantly to the cost of each iteration because the number of cells in the buffer zones are again a small fraction of the total number of cells in the full numerical domain. The increase in the memory requirement is also minor because only one additional field needs to be stored in the computational memory along with all the primary variables (temperature, pressure, velocity-field, species mass-fractions) and other auxiliary variables during each iteration. The two temperature fields are independently smooth in their valid domain and their corresponding buffer zones. This allows the conventional derivative and interpolation stencils operating on T_s and T_f to each be of high-order accuracy.

The dual buffer cells are constructed sequentially such that the matching conditions at the fluid-solid boundary ($T^s = T^f$ and $\lambda_f \frac{\partial T^f}{\partial n} = \lambda_s \frac{\partial T^s}{\partial n}$) discussed in Section 2.3.2 are imposed. The buffer cells (-1) are first constructed by matching the 4^{th}order

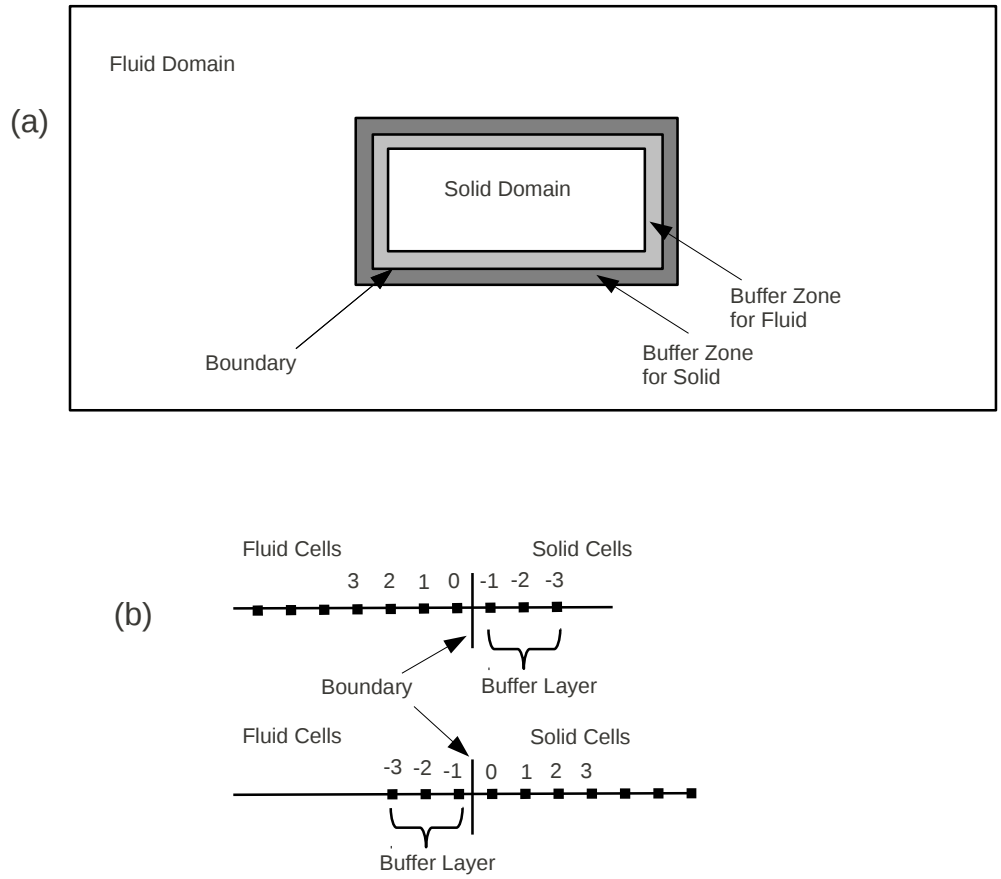

Figure 2-8: (a) Schematic of a Cartesian solid body inside a fluid domain; the shaded regions are 2-cell wide dual buffer zones for the solid and fluid domains (b) Cell-center indices for a one-dimensional grid marking the dual buffer zones.

interpolations for temperature and and 4^{th}order derivatives for flux matching on the boundary from both the solid and the fluid sides. This gives

$$\begin{aligned} \frac{1}{8}(3T^s_{-1} + 6T^s_0 - T^s_1) &= \frac{1}{8}(3T^f_{-1} + 6T^f_0 - T^f_1) \\ \frac{\lambda_s}{24}(-23T^s_{-1} + 21T^s_0 + 3T^s_1 - T^s_2) &= -\frac{\lambda_f}{24}(-23T^f_{-1} + 21T^f_0 + 3T^f_1 - T^f_2) \end{aligned} \tag{2.32}$$

where λ_s and λ_f are the thermal conductivities of the solid and the fluid cells respectively. The same matching conditions are then satisfied using a symmetric 4^{th}order

stencil as

$$\frac{1}{16}(-T^s_{-2} + 9T^s_{-1} + 9T^s_0 - T^s_1) = \frac{1}{16}(-9T^f_{-2} + 9T^f_{-1} + 9T^f_0 - T^f_1)$$
$$\frac{\lambda_s}{24}(T^s_{-2} - 27T^s_{-1} + 27T^s_0 - T^s_1) = -\frac{\lambda_f}{24}(T^f_{-2} - 27T^f_{-1} + 27T^f_0 - T^f_1) \tag{2.33}$$

Equations (2.32) and (2.33) are sequentially solved to fill (-1) and (-2) cells. A third set of conditions is required because the second derivative of the temperature (computed for the thermal diffusion) needs a 3$^{\text{rd}}$buffer cell for computation. I choose a 4$^{\text{th}}$-order extrapolation condition on the heat flux $F_i = \lambda_i \frac{\partial T_i}{\partial n}$. The heat fluxes are computed on the face centers of the staggered grid. The imposed extrapolation is

$$F^f_{-3/2} = 4F^f_{-1/2} - 6F^f_{1/2} + 4F^f_{3/2} - F^f_{5/2}$$
$$F^s_{-3/2} = 4F^s_{-1/2} - 6F^s_{1/2} + 4F^s_{3/2} - F^s_{5/2} \tag{2.34}$$

If the thermal conductivity is constant in both the fluid and the solid domains, Eqs. (2.34) gets simplified in terms of a temperature value at the third buffer cell (-3) using 4$^{\text{th}}$order derivative stencils as

$$T^f_{-3} = 31T^f_{-2} - 141T^f_{-1} + 275T^f_0 - 275T^f_1 + 141T^f_2 - 31T^f_3 + T^f_4$$
$$T^s_{-3} = 31T^s_{-2} - 141T^s_{-1} + 275T^s_0 - 275T^s_1 + 141T^s_2 - 31T^s_3 + T^s_4 \tag{2.35}$$

However, the thermal conductivity varies for a reacting flow and using Eq. (2.35) exhibited numerical instabilities. I used Eqs. (2.34) in the implementation.

Like the single-sided counterpart, the dual buffer zones are constructed at all the levels of the SAMR grid and before the beginning of each stage in the multistage RKC scheme (Stage 2_b in the algorithm). Thereby, the conjugate heat exchange condition is enforced at the beginning of each sub-stage. In a multi-species transport simulation, the iteration time-step size is already small enough to ensure that errors are small in between two stages of the multistage RKC, when the conjugate heat exchange condition is not explicitly enforced. The dual buffer zones are required only for the

construction of the thermal diffusion term in the energy equation. I thus compute this term sequentially by sweeping first in the x-direction and then in the y-direction. More specifically, the thermal diffusion due to the y-gradients in temperature is first ignored and the dual buffer zones are formed in the x-direction and the diffusion term is computed. The thermal diffusion due to the x-gradients in temperature is then ignored and the dual buffer zones are formed in the y-direction and the diffusion term is computed. These two terms are then added to get the total thermal diffusion in each cell for the two-dimensional domain. This allows us to avoid the sharp corner treatment as was necessary for the species mass-fraction fields[2].

A conceptually similar Matched Interface and Boundary method was presented by Zhou et al. [57]. They outlined a generalized method to obtain high-order accurate solution of elliptic equations with discontinuous coefficients and singular sources on Cartesian grids. They successfully demonstrated it using non-reacting test cases with non-grid conforming immersed boundaries. However, a method for a more complex problem such as multi-species reacting flows was not formulated. A second-order buffer zone IBM coupled with an operator-split projection algorithm and SAMR framework for multi-species reacting flows is unique in my method. Complex immersed boundaries-SAMR coupling (irregular geometries with boundary cutting through the grid cells) is a far more challenging task.

2.4 Performance gain

It has been previously shown that the semi-implicit operator-splitting algorithm can boost performance by 20 times when compared to conventional fully-explicit numerical methods [58]. Figure 2-9 shows that this can be further improved by employing an SAMR framework. I simulated a stoichiometric planar flame propagating in two-dimensions using a uniform grid of 20 microns resolution. I repeated this with a 40 micron uniform grid and one level of refinement and with a 80 micron uniform grid

[2] 2^{nd} derivatives of the species mass-fractions need to be computed multiple times per iteration making the alternate direction sweeping technique used for the dual buffer zone cumbersome for implementation in the numerical method

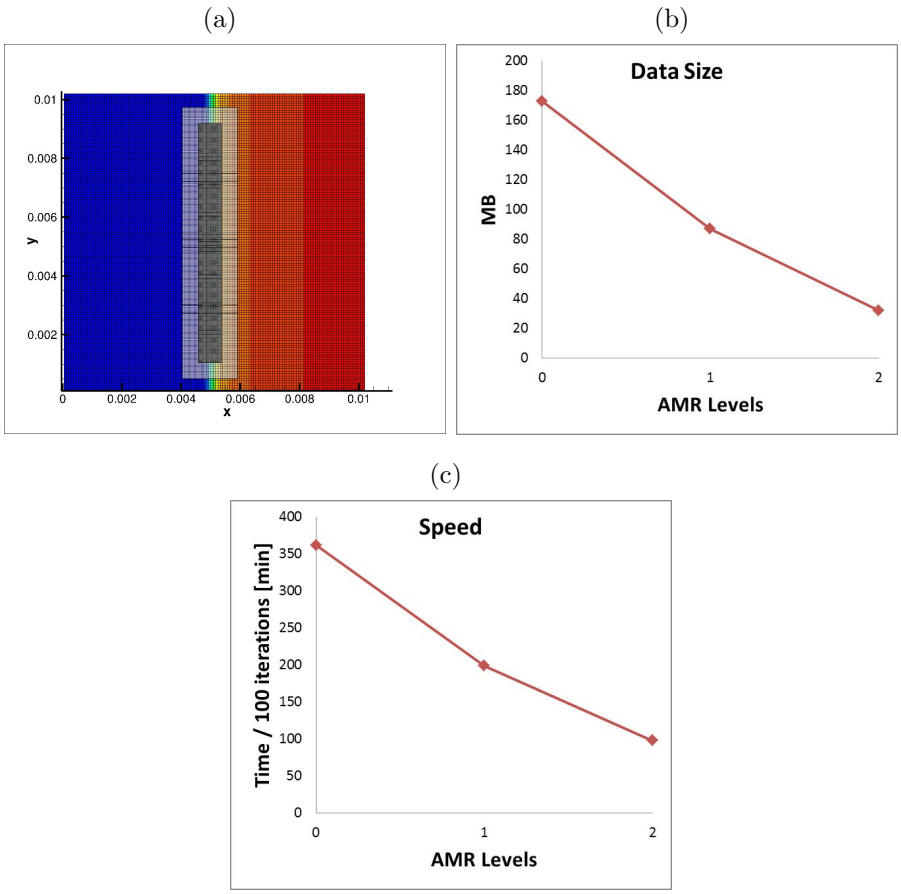

Figure 2-9: (a) Planar stoichiometric premixed flame simulation with 2 levels of refinement (b) Iteration time improvement (c) Data size advantage

and two levels of refinement. In this way, the effective flame resolution of 20 microns was maintained constant in all the cases. The data size and wall clock time per iteration were compared and show in Fig. 2-9. A significant performance boost of about 3.5 times is observed for the 2-level simulation when compared to the uniform grid simulation. The data size also decreases because of the lesser number of total grid cells in the domain when SAMR framework was used. This gain will however saturate as more levels are used because of the increasing overhead in multigrid interpolations. I verified that the performance gain was not reduced by my buffer zone method for incorporating solid-fluid coupling because majority of the iteration time is spent in integrating the reaction source terms and the diffusion terms [11].

2.5 Code validation and convergence studies

In this section, I validate the overall construction and demonstrate its second-order temporal and spatial convergence using various test cases.

2.5.1 Impulsively started thin vertical plate in a non-reacting isothermal cross-flow: validation and temporal convergence

The flow past a thin flat plate normal to the free stream is a classic example of bluff-body flows. I use this test case to validate the no-slip implementation and the pressure solver in the presence of the immersed solid in the momentum integration stages, which is solved only on a uniform grid as noted before. I consider a fixed vertical plate of height d in a cross-flow where the undisturbed velocity far away from the plate is U. This configuration has been extensively used for benchmarking in the literature; experiments of Taneda and Honji [59] and Dennis et al. [60], finite element simulations of Yoshida and Nomura [61], Laval and Quartapelle [62] and Tamaddon-Jahromi et al. [63], vortex method simulation of Koumoutsakos and Shiels [64]. As the plate is impulsively started, a recirculation zone starts to form on the downstream face of the thin vertical plate and it starts to grow with time. Figure 2-10 shows a comparison of the location of this growing symmetric recirculation during its early development. The recirculation zone size is defined as the distance of the downstream stagnation point from the downstream edge of the plate. An inflow $\mathrm{Re_d} = 126$ based on d was chosen in the simulation. The thickness of the plate was used as $0.15d$, where $d = 5$mm. 320×128 grid points were used with the domain size of $20d \times 12.5d$. Symmetry conditions were used at the boundaries parallel to the flow direction. Figure 2-10 shows an excellent agreement with the transient data documented in the literature; here the lengths and velocities are nondimensionalized by d and U respectively. For a better visualization, a representative streamline pattern and vorticity at an intermediate time instant is shown in the insert of Fig. 2-10. The scatter in the literature data increases with the non-dimensional t^* due to the increasing influence of the boundaries

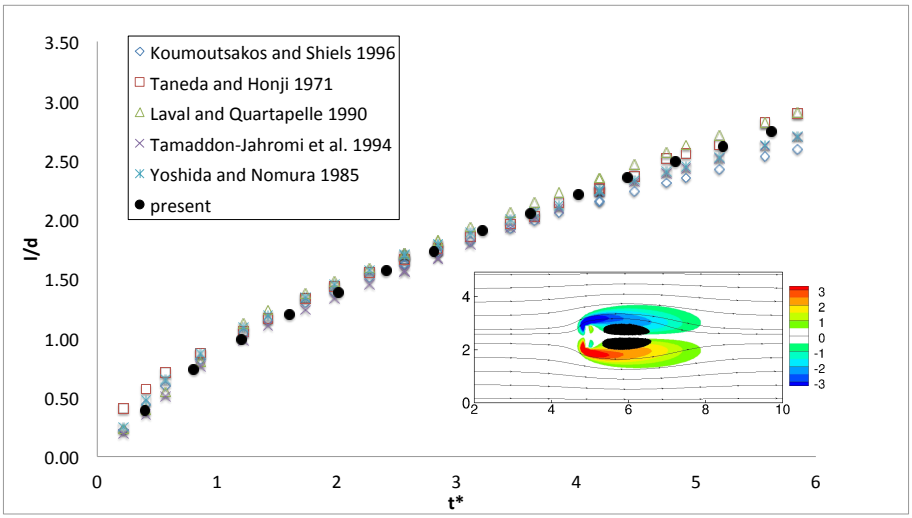

Figure 2-10: Experimental and numerical comparison of the recirculation zone growth for a case with an impulsively started thin vertical plate in a cross flow. References in the legend: [59, 61–64]. Literature data is reproduced using Fig. 19 in [64]. A representative streamline pattern and colored non-dimensional vorticity contours at an intermediate time instant $t^* = 3.5$ is shown in the insert.

parallel to the flow depending on the experimental conditions and the numerical approximation.

I further used the above uniform grid isothermal case to verify that an overall second-order temporal accuracy is achieved. Projection methods for incompressible flows have been reported to be potentially first-order accurate in time in the presence of a no-slip wall due to the ambiguity in the boundary conditions to be used for the intermediate velocity field before the pressure Poisson correction [65, 66]. Weinan and Liu [66] reviewed the different boundary conditions proposed for the intermediate velocity field to achieve an overall second-order temporal accuracy. I did not use any such corrections but still observed that the second-order temporal accuracy was maintained. As discussed in the numerical method, I impose a no-slip wall boundary condition for the intermediate velocity field. The unsteady test case discussed above was simulated for $t^* = 1$ (corresponding to time when the recirculation zone length is almost equal to the plate height d) using three different time-steps: coarse $dt^* = \frac{t^*}{1000}$, medium $dt^* = \frac{t^*}{2000}$ and fine $dt^* = \frac{t^*}{4000}$. The spatial grid resolution was the same in all the three simulations. The ℓ_1 norms were used to compute the errors in the velocity

Ã	u	v	p
O_{ℓ_1}	2.001	2.001	1.998

Table 2.1: Temporal convergence orders for the uniform grid simulation of an impulsively started thin vertical plate in a cross flow.

and the pressure field.

$$\ell_1 = \frac{\sum_{i,j} | (\phi_{i,j} - \phi_{i,j,ref}) |}{N_p} \tag{2.36}$$

where N_p is the number of grid points. The grid convergence order was then estimated as [56]

$$O_{\ell_1} = \log_2 \frac{err_{1,c-m}}{err_{1,m-f}} \tag{2.37}$$

where err denotes the ℓ_1 error and subscripts $c-m$ and $m-f$ denote the coarse and medium temporal errors when compared to the medium and fine time-step simulations respectively. The temporal convergence orders are shown in Table 2.1. The overall second-order temporal accuracy for the velocity and the pressure field is verified.

2.5.2 Unsteady non-reacting isothermal flow: validation

I present another unsteady cold flow validation of the momentum transport using a uniform 320×128 grid simulation. A fully developed parabolic inlet profile for the streamwise velocity was assumed. Figure 2-11 shows the instantaneous vorticity contours of an unsteady channel-confined cold flow around a square cylinder at $\mathrm{Re_d} = 100$ for a blockage ratio $d/H = 0.2$, where H is the y-direction width of the computational domain. The vorticity was non-dimensionalized by the global maximum value. The cold flow was observed to be unsteady at these conditions. For this flow, the value of the Strouhal number $\mathrm{S_d} = \frac{fd}{U}$ reported by Suzuki et al. [67] was 0.222 (on a stretched 207×54 grid points two-dimensional simulation); f is the frequency of vortex shedding. I calculated this to be $\mathrm{S_d} = 0.232$. Figure 2-11 also shows that the strong vorticity near the upper and lower channel walls, associated with localized moving recirculation zones, is captured similar to observations in [68].

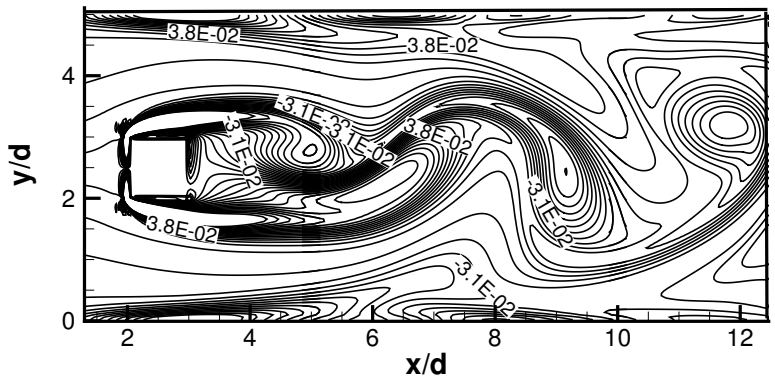

Figure 2-11: Instantaneous non-dimensional vorticity contours of an unsteady channel-confined cold flow around a square cylinder at $\mathrm{Re_d} = 100$ for a blockage ratio $d/H = 0.2$.

2.5.3 Steady-state conjugate heat exchange between air and a ceramic solid object: validation and spatial convergence

I present here a simple test case to validate the dual buffer zone method. I tested the accuracy of the conjugate heat exchange between stationary air having a temperature dependent thermal conductivity and a ceramic solid object of a constant thermal conductivity of $\lambda_s = 1.5$W/mK (approximately 50 times larger than air). Only the energy equation was integrated; the momentum projection and chemical source terms were decoupled from the governing equations. The number of RKC steps for Stage 2b of the numerical algorithm was fixed to $M = 8$. Symmetry conditions were imposed at y_{min} and y_{max} boundaries. Dirichlet boundary conditions for temperature were used: 300K at x_{min} and 600K at x_{max} boundaries. The steady-state solution on a 64×64 uniform grid was obtained, shown in the contour plot in Fig. 2-12. x and y were non-dimensionalized by the height of the heat-conducting solid object, d (white square in Fig. 2-12). In the absence of any immersed solid, the temperature would increase "almost" linearly from x_{min} to x_{max}; a small nonlinearity resulting from the temperature dependence of the thermal conductivity of air. This is seen near the y_{min} and y_{max} boundaries in Fig. 2-12(top), where the influence of the immersed solid is

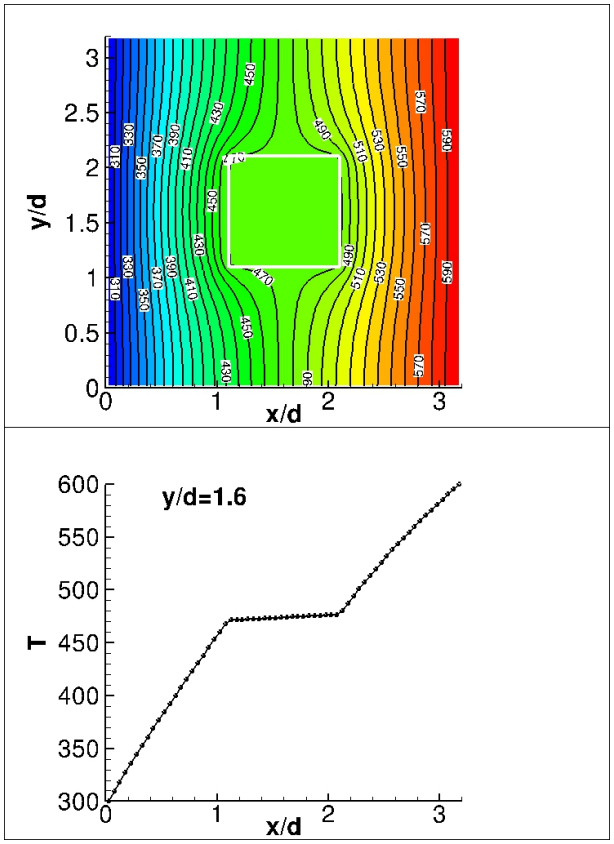

Figure 2-12: (top) Temperature contours at steady-state, white square marks the immersed ceramic solid object in stationary air (bottom) Temperature profile at $y/d = 1.6$.

small. The temperature field is non-smooth at the edges of the solid body due to the large change in the thermal conductivity. For a dual buffer zone implementation, that accurately resolves the kink in T during the conjugate heat exchange, the change in the slope of T must be equal to the thermal conductivity ratio. Fig. 2-12(bottom) shows the temperature kink at the left and the right edge of the immersed solid. I verified this jump at each edge to be equal to the thermal conductivity ratio of the solid and the air at the corresponding temperature; thereby validating the dual buffer zone construction.

I further verified the spatially second-order convergence of the numerical method using the above test-case using three simulations. The steady-state simulations were obtained on fine (64×64 base grid + 2 levels of refinement equivalent to a grid size of 256×256), medium (64×64 base grid + 1 level of refinement equivalent to a grid

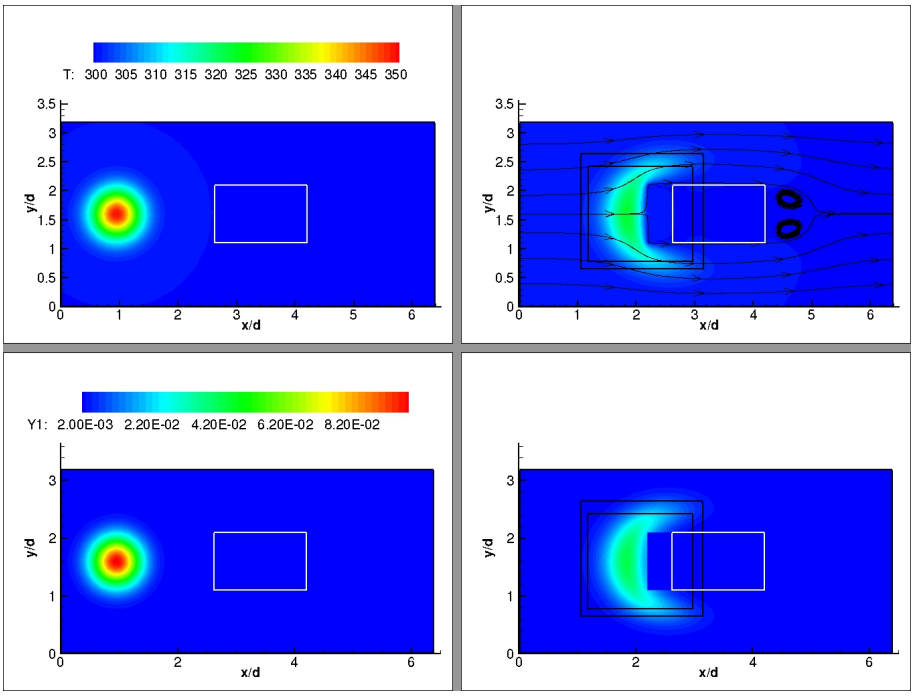

Figure 2-13: Contours of (top) T and (bottom) Y_{CH_4} at $t = 0$ (left column: initial condition for the SAMR convection-diffusion convergence test) and $t = 10$ms (right column). Rectangular solid is shown by white rectangle; level 1 and level 2 fine grid patches are marked by the black rectangles in the right column. Streamlines are overlaid on the T contours at $t = 10$ms.

size of 128×128) and coarse (a unilevel 64×64) grids. The temperature solution fields for the three grids at the coarsest (base) grid level were compared. The ℓ_1 norm (Eq. 2.36) was used to compute errors. The grid convergence order was estimated as [56]

$$O_{\ell_1} = \log_2 \frac{err_{1,c-m}}{err_{1,m-f}} \tag{2.38}$$

where err denotes the ℓ_1 error and subscripts $c-m$ and $m-f$ denote the coarse and medium grid errors when compared to the medium and fine grid respectively. The convergence order of 2.19 was obtained showing that the non-smooth temperature profile was resolved with a second-order accuracy using the dual buffer zone method.

2.5.4 Convection-diffusion test: spatial convergence

The momentum and scalar transport equations were coupled with the SAMR framework in the simulations discussed in the remaining sections. Both single-sided and

dual buffer zones were thus constructed simultaneously.

Figure 2-13 shows a 2-level flow simulation of a Gaussian field of temperature and species mass-fraction around an immersed rectangular solid. The black rectangles mark the refined patches in the domain. The outer rectangle is the level 1 patch refined by factor of 2 from the base grid and the inner rectangle is the level 2 patch refined further by a factor of 2 from the level 1 grid. The flow direction is from left to right. The flow was composed of a non-reacting mixture of 2 species (CH_4 and N_2). The chemical source terms were switched off during this test case, thereby considering a non-isothermal but non-reacting multi-species simulation. An initial condition of an upstream Gaussian scalar field of T, Y_{CH_4} and Y_{N_2} was specified (note that $\sum_k Y_k = 1$ and thus $Y_{N_2} = 1 - Y_{CH_4}$) such as

$$\phi(x/d, y/d) = \phi_0 \exp(-\frac{(x/d - x_0)^2 (y/d - y_0)^2}{\delta^2}) \tag{2.39}$$

where $d = 2.4$ mm is the height of the solid body in the y-direction and non-dimensional $\delta = 0.4$, $x_0 = 1.0$ and $y_0 = 1.6$. The mean inlet flow velocity was fixed at $U = 0.3$ m/s which was equivalent to an inflow $\mathrm{Re}_d = 45$ based on d. A small time step $dt = 1 \times 10^{-5}$sec was chosen. This corresponds to convective and diffusive CFL numbers of $udt/dx = 0.05$ and $\nu dt/dx^2 = 0.05$ respectively; on the base coarse grid. The number of RKC steps for Stage 2b of the numerical algorithm was fixed to $M = 8$. Symmetry conditions were imposed at y_{min} and y_{max} boundaries. The thermal properties of the solid body (corresponding to steel) were $\lambda_s = 12$W/mK, $\rho_s = 8000$kg/m^3 and $c_s = 503$J/kgK. The simulation was performed for 10 ms on fine (256×128 base grid + 2 levels of refinement equivalent to a grid size of 1024×512), medium (256×128 base grid + 1 level of refinement equivalent to a grid size of 512×256) and coarse (a unilevel 256×128) grids. The flow is from left to right. The scalar solution field for the three grids at the coarsest (base) grid level were compared. The ℓ_1 norm (Eq. 2.36) was used to compute errors. The grid convergence order was estimated similar to the previous section; its values are shown in Table 2.2. The errors were computed only in the refined region in the SAMR simulations. A Gaussian field

$\tilde{\text{A}}$	T	Y_{CH_4}	Y_{N_2}
O_{ℓ_1}	1.96	1.82	1.82

Table 2.2: Spatial convergence orders for the convection-diffusion SAMR simulations.

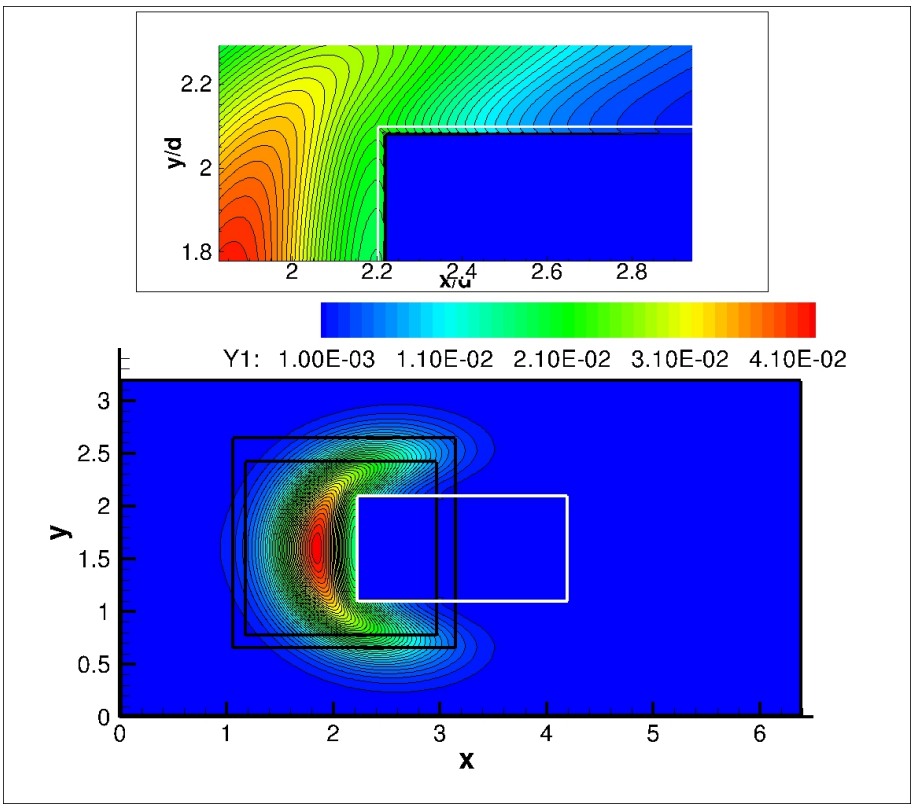

Figure 2-14: (top) Zoomed-in single-sided buffer zone for Y_{CH_4} (bottom) Fine grid patches overlaid on the Y_{CH_4} contours with the buffer-zone hidden.

of only Y_{CH_4} and Y_{N_2} for an isothermal flow; and a Gaussian field of only T were also independently tested for convergence using the same flow conditions and convergence orders of 1.85 and 1.96 were respectively obtained.

Figure 2-14 shows a visualization of the single-sided buffer zone for the species mass-fraction of Y_{CH_4} corresponding to the lower right contour plot shown in Fig. 2-13. The contours inside the zoomed top figure visually show the fictitious values inside the single-sided species buffer zone and the zero-gradient condition at the fluid-solid boundary. It must be noted that for a refined patch, the penetration of buffer zone inside the solid is smaller since the 3-cell zone covers less area on a finer patch when compared to a coarser patch.

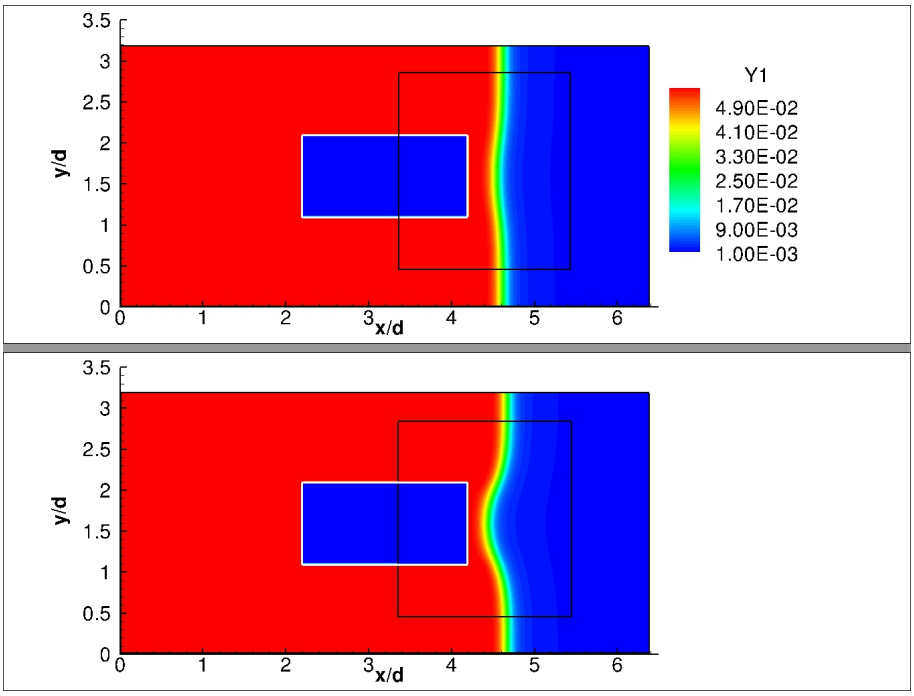

Figure 2-15: Fuel (Y_{CH_4}) contours for a premixed flame corresponding to a stoichiometric mixture interacting with a bluff body (white rectangle) (top) initial condition corresponding to $t = 0$ (bottom) after $t = 1$ms. A level 1 fine grid patch is marked by the black rectangle.

2.5.5 Reacting flow: spatial convergence

I now demonstrate the overall second-order convergence of the buffer zone method using fully-coupled reacting flow simulations.

Premixed flame using a single-step chemical kinetics model

Figure 2-15 shows the fuel (methane) contours of a premixed flame interacting with a bluff-body at the downstream end. A time-step of $dt = 1 \times 10^{-6}$sec, corresponding to convective and diffusive CFL numbers of 0.005, was chosen. The reactants are flowing from left to right. A global single-step chemical mechanism for methane-air combustion was chosen as

$$CH_4 + O_2 + 3.76N_2 \rightarrow CO_2 + 2H_2O + 3.76N_2 \tag{2.40}$$

$\tilde{\text{A}}$	T	Y_{CH_4}	Y_{O_2}	Y_{CO_2}	Y_{H_2O}	Y_{N_2}
O_{ℓ_1}	2.01	2.03	2.06	2.05	1.99	1.98

Table 2.3: Spatial convergence orders for the premixed flame SAMR simulations using a global single-step chemical kinetics model.

The overall reaction rate expression for the single-step chemistry is given by

$$k_f = AT^n \exp(\frac{-E_a}{RT})[CH_4]^a[O_2]^b \tag{2.41}$$

where the Arrhenius constant $A = 9.0 \times 10^{23}$ cm^3/mol/sec, activation energy $E_a =$ 55000 cal/moles, $a = b = 1$ were used. These values are representative of hydrocarbon combustion for methane-air [13].

The same thermal properties for the solid material, inflow $\text{Re}_d = 45$ and the domain boundary conditions as used in the previous section were used for this investigation. The laminar flame speed for a stoichiometric premixed methane air flame is approximately 40 cm/s. The average streamwise velocity of 30 cm/s was chosen at the inflow, thereby resulting in an overall flame motion towards the incoming reactants in the Eulerian frame. A planar premixed flame solution using Chemkin was initialized with the flame downstream of the solid block. The solution was evolved on a coarse grid with no adaptive meshes (256×128) to a time when there was a reasonable interaction with the flame and the wall (Fig. 2-15 top). This solution was then used as an initial condition for 3 simulations: fine (256×128 base grid + 2 levels of refinement equivalent to a grid size of 1024×512), medium (256×128 base grid + 1 level of refinement equivalent to a grid size of 512×256) and coarse (a unilevel 256×128) grids. The simulations were performed for 1ms allowing the flame to travel by approximately four reaction zone thickness length in the domain. The ℓ_1 norms for the scalars were used to estimate convergence order shown in Table 2.3. An overall second-order convergence was computed for all the scalar fields demonstrating the accuracy of the single-sided and dual buffer zone method in a fully coupled reacting flow simulation.

$\tilde{A}$	T	Y_{CH_4}	Y_{O_2}	Y_{CO_2}	Y_{H_2O}	Y_{CO}	Y_H	Y_{OH}	Y_{CH3}	Y_{HCO}
O_{ℓ_1}	2.03	2.07	2.07	2.05	2.03	2.03	1.97	1.95	2.07	1.93

Table 2.4: Spatial convergence orders for the premixed flame SAMR simulations using a detailed chemical kinetics model: C1 model described by Smooke et al. [69].

Premixed Flame using a detailed chemical kinetics model

I repeated the above discussed convergence test using a detailed chemical kinetics model. A 16 species 46 reactions C1 chemical kinetics described by Smooke et al. [69] was used for the simulations using similar flow conditions and domain configuration as described in the previous section. Again a simulation for a total of 1ms was performed for this test, corresponding to flame motion equivalent to approximately four reaction zone thickness. The iteration time-step was however reduced to $dt = 5 \times 10^{-7}$sec unlike the $dt = 1 \times 10^{-6}$sec used in the single-step test. The methane contours of the premixed flame interacting with the solid at its downstream end were visually similar to the contours shown in Fig. 2-15. The convergence orders using the ℓ_1 norms of the major and minor species and temperature field are shown in Table 2.4. The overall second-order accuracy of the buffer zone method using a fully coupled reacting flow simulation, in the presence of rapidly reacting radicals, is also confirmed[3].

The SAMR simulation with 2 levels of refinement on a 256×128 base grid was observed to be $3.5\times$ faster than the equivalent setup (same finest mesh resolution) of a unilevel 1024×512 grid. The data size of the simulation in terms of disk-space for the former was $4\times$ smaller compared to the latter. This is indicative of the large performance gain that can be achieved for reacting flow simulations using a coupled immersed boundary-SAMR approach.

2.6 Conclusions

In this chapter, I introduced a spatio-temporal second-order accurate numerical method for a low-Mach number chemically reacting flow simulation near Cartesian grid-

[3]Additional convergence studies using the same detailed chemical kinetics model for fluid-only domains are shown in [11]

conforming immersed walls. I presented a novel buffer zone method to impose the solid-fluid boundary matching conditions eliminating the need to use one-directional stencils near the heat-conducting walls. These buffer zones coupled with a block-structured adaptively refined mesh and an operator-split projection algorithm provide a fast and efficient tool to investigate flame-wall interactions by resolving all the scales of the problem. The numerical method treats the entire domain as if it were completely fluid, allowing us to efficiently use the modular code developed using the CCA framework for fluid-only domains [11, 12]. The solid cells are tracked using a binary marker function allowing prescribing multiple solid bodies in the simulation.

I described a single-sided buffer zone construction to capture the species mass-fractions discontinuity and presented the associated stencils. The buffer zones are formed inside the solid using the zero-gradient conditions and high order extrapolations. The stencils were tested for the second-order of accuracy using a manufactured solution test. A dual buffer zone construction to capture the temperature gradient discontinuity was also introduced. A sequential construction of the buffer cells in the solid and fluid is done by imposing the boundary matching conditions maintaining an overall second-order accuracy. The buffer zones are constructed at all the levels of the SAMR grid and before each stage of the multistage RKC integration of the scalar transport. The overall second-order convergence of the buffer zone method was demonstrated using various non-reacting and reacting SAMR simulations. Validation of the code using benchmark cases from the literature was also shown.

The accurate treatment of the flame-wall interactions through the conjugate heat exchange between the reacting flow and the nearby wall allows the flame to naturally anchor; thereby not requiring any artificial anchoring conditions often used in existing numerical investigations. Flame stabilization, extinction and blow-off are classical multiphysics problems that can be mechanistically investigated using this method. I will present detailed flame stabilization and blowoff investigations in the next three chapters. I will also present advanced developmental efforts undertaken to incorporate stair-stepped solid geometries and three-dimensionalizing the SAMR code in Chapter 7.

Chapter 3

Mechanism of laminar premixed flame anchoring on a bluff-body

3.1 Overview

The objective of this chapter is to investigate the mechanism of the laminar premixed flame anchoring near a heat-conducting bluff-body using the numerical method described in Chapter 2. Simulations show a shear-layer stabilized flame just downstream of the bluff-body, with a recirculation zone formed by the products of combustion. A significant departure from the conventional two-zone flame-structure is shown in the anchoring region. In this region, the reaction zone is associated with a large negative energy convection (directed from products to reactants) resulting in a negative flame-displacement speed. It is shown that the premixed flame anchors at an immediate downstream location near the bluff-body where favorable ignition conditions are established; a region associated with (1) a sufficiently high temperature impacted by the conjugate heat exchange between the heat-conducting bluff-body and the hot reacting flow and (2) a locally maximum stoichiometry characterized by the preferential diffusion effects. I also discuss the unsteady behavior of the reacting flow-field during the ignition process to start a simulation and in response to a sinusoidal inflow velocity perturbation towards the end of this chapter.

3.2 Results and discussions

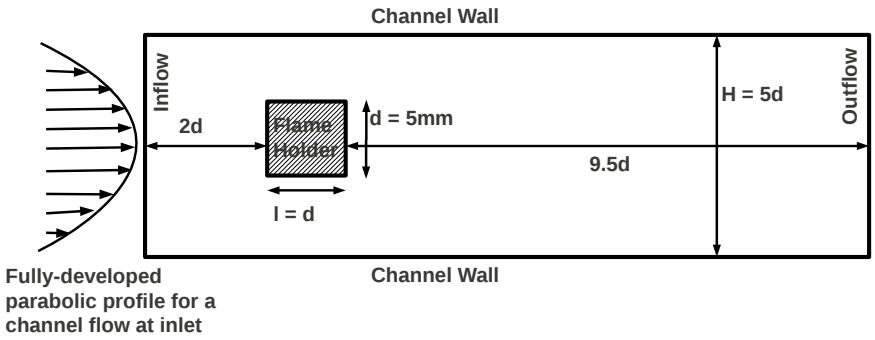

Figure 3-1: Schematic illustration of the numerical domain for the two-dimensional simulation.

The multistep C1 skeletal mechanism (16 species and 46 reversible reactions) was used for defining the chemical kinetics of methane-air combustion [69]. The following parameters were kept constant throughout the numerical simulations: the dimensions of the bluff-body (see Fig. 3-1), $l \times d = 5\text{mm} \times 5\text{mm}$; the channel width, $H = 25$ mm; the corresponding blockage ratio, $d/H = 0.2$; the inlet temperature, T_u= 300 K; the average inlet velocity $U_{in} = 1.6$ m/s. The corresponding inflow Reynolds number based on the inlet fluid properties and the bluff-body width is $\mathbf{Re}_d = 500$. The cell size on the coarsest grid level is $\Delta x = \Delta y = 196$ μm and one additional fine grid level in the SAMR grid is used. This is equivalent to a flame resolution of 98 μm. A grid independence study using 25, 50 and 100 μm was conducted to ensure that flame structure is accurately captured by this finest grid resolution for lean premixed flames with mixture equivalence ratio $\phi \leq 0.8$. A constant time step of $\Delta t = 2$ μs was chosen for the simulations; such a large value is attainable because of the semi-implicit operator-split stiff projection algorithm (Chapter 2) used. A fully-developed parabolic channel profile was imposed at the inlet, at a distance $2d$ from the upstream face of the bluff-body. The domain length was chosen to be $9.5d$ from the downstream face of the bluff-body for all the cases, except for $\phi \leq 0.45$, for which $17d$ was used because of the associated large recirculation zone sizes. To investigate

flame anchoring, cases with ϕ =0.5, 0.55, 0.6 and 0.7 were simulated keeping all the other operating conditions the same. $\mathbf{Re}_d$ was fixed at 500. Two bluff-body flame-holders with thermal properties (1) Ceramic : the density ρ_{fh} = 673 kg/m^3, the specific heat c_{fh} = 840 J/kgK, the thermal conductivity , λ_{fh} = 1.5 W/mK and (2) Steel: ρ_{fh} = 8000 kg/m^3, c_{fh} = 503 J/kgK, and λ_{fh} = 12 W/mK were used in the simulations. No artificial flame anchoring boundary conditions were imposed. The flame was allowed to naturally choose an anchoring location by accurately solving for the flame-wall conjugate heat exchange as discussed in Chapter 2. This is essential to mechanistically study the flame anchoring region.

3.2.1 Non-reacting flow simulation

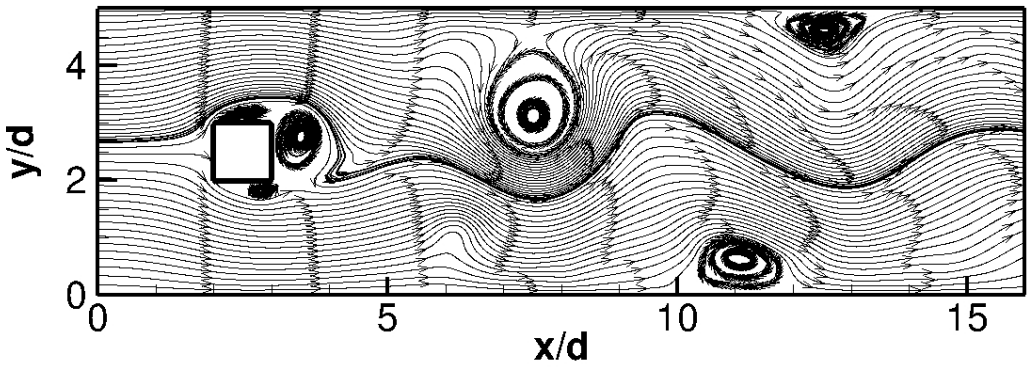

Figure 3-2: The streamlines around the confined bluff-body (marked by black square) for a non-reacting case at $\mathbf{Re}_d = 500$ for a blockage ratio $d/H = 0.2$.

The reacting flow was observed to be steady for all the simulated cases; even though its cold-flow counterpart at $\mathbf{Re}_d$ = 500 was observed to shed vortices in the Von-Karman vortex sheet regime as shown in Fig. 3-2. For this non-reacting case, I computed the vortex shedding Strouhal number (fd/U_{in} where f is the vortex shedding frequency) of 0.23. Vortex shedding is visible from the streamline patterns. Secondary recirculation zones were formed near the outer channel walls due to the confinement, similar to the observations in [68]. Using two-dimensional Lagrangian

simulations, Mehta and Soteriou [26] investigated reacting and non-reacting turbulent bluff-body flows at $\mathbf{Re}_d = 20000$ in a channel with blockage $d/H = 0.16$. The reacting flow was shown to be more symmetric and very less coherent in shedding than its non-reacting asymmetric flow counterpart, which shed coherent Von-Karman vortices. They concluded that the symmetry in the reacting flow in the near-field of the bluff-body is primarily caused by the dilatation associated with the combustion heat release and is sustained in the far-field by the baroclinic vorticity generation. The large increase in the kinematic viscosity was shown to have a secondary impact on the near-field symmetry.

3.2.2 Reacting flow simulations

Figure 3-3 shows a laminar flame simulation at $\phi = 0.7$. The flow is from left to right. The flow separated at the leading edge of the bluff-body, similar to the corresponding non-reacting flow behavior shown in Fig. 3-2, consistent with the observations reported in [68]. Temperature contours show the conjugate heat exchange between the heat-conducting bluff-body and the reacting flow around it. The fine grid level rectangular patches are overlaid on the contours showing the adaptive flame tracking by the SAMR framework. The mass-fraction contours of Y_{CH_4} (middle) and Y_{HCO} (bottom) with a few representative streamlines are also shown in Fig. 3-3. A recirculation zone is formed by the products of combustion behind the bluff-body. As shown below, Y_{HCO} contours visualize the reaction zone of the flame. The premixed flame anchored at a downstream location near the bluff-body wall and stabilized in the shear layer separating from it. The flame region is a very small fraction of the overall computational domain in such flows. SAMR framework thus makes such a computationally expensive study of bluff-body stabilized flames possible while maintaining the flame resolution.

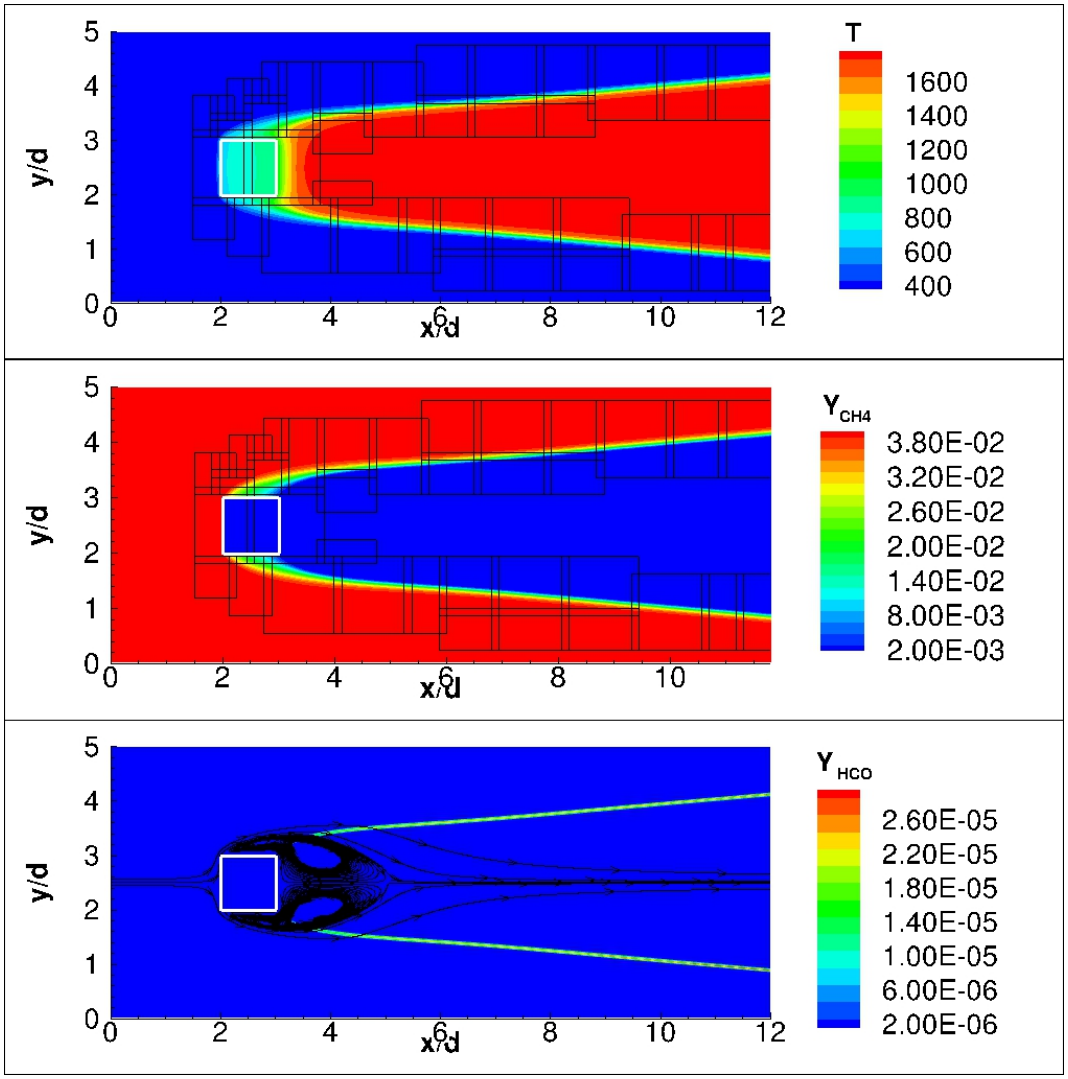

Figure 3-3: (top) Temperature contours with overlaid fine grid patches (middle) Fuel Y_{CH_4} contours with overlaid fine grid patches (bottom) intermediate species Y_{HCO} contours with overlaid streamlines of a reacting flow at equivalence ratio $\phi = 0.7$ around a confined ceramic bluff-body (marked by the white square) at a flow $\mathbf{Re}_d = 500$ for a blockage ratio $d/H = 0.2$.

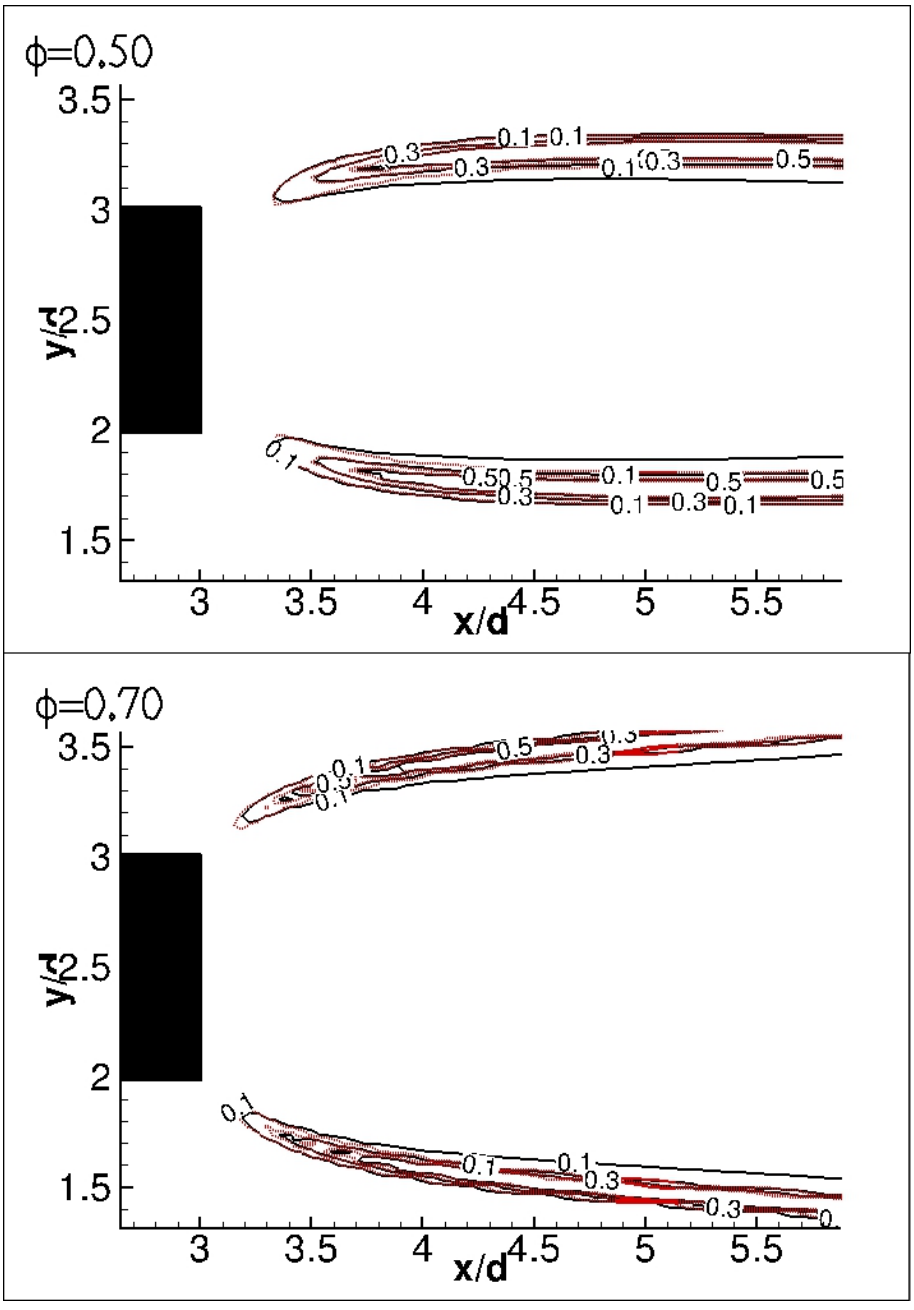

Figure 3-4: Normalized contour lines of Y_{HCO} species (red dotted lines) and reaction-rate (solid black lines) for the cases with $\phi = 0.5$ and $\phi = 0.7$ using the ceramic bluff-body. The filled black region marks the bluff-body.

3.2.3 Y_{HCO} and the definition of the flame anchoring location

Najm et al. [70] showed that the HCO species strongly correlated with the heat-release rate for premixed flames over a wide range of unsteady flame stretch. I verified this using the simulations at different ϕ. The flame stretch[1] for these cases is shown to be weak in Chapter 4. Results for the cases with $\phi = 0.50$ and $\phi = 0.70$ using the ceramic bluff-body are shown in Fig. 3-4. Only a part of the computational domain, focusing on the flame anchoring region, is shown. The red-dotted lines mark the normalized Y_{HCO} mass-fraction contours and the black-solid lines represent the normalized reaction-rate. Both are normalized by their respective maximum values far downstream of the bluff-body. Figure 3-4 confirms the strong correlation between the heat-release rate zone of the flame and the Y_{HCO} species mass-fractions. It was also observed to be very strong in the downstream region (beyond the field shown in the figure). The same result was also observed for all other equivalence ratios and bluff-body materials investigated in this paper and is not shown here. I will thus use the normalized Y_{HCO} contours as a surrogate for visualizing the heat-release zone or equivalently the reaction zone in this paper.

Due to the continuous nature of all the scalar fields, I define the anchoring location as the most upstream position where the value of the normalized Y_{HCO} is 0.1 (equivalently the most upstream location where 10% of its far downstream maximum value is reached). Figure 3-4 shows that the flame anchored at a location closer to the bluff-body for the case with $\phi = 0.7$ than the $\phi = 0.5$ flame. This, as will be shown in Section 3.2.5, is because of the higher temperature values associated with the former. The flame angle relative to the streamwise direction for $\phi = 0.7$ is larger than $\phi = 0.5$ because of higher flame speed associated with the former. On the contrary, the flame thickness for the latter case is visibly larger.

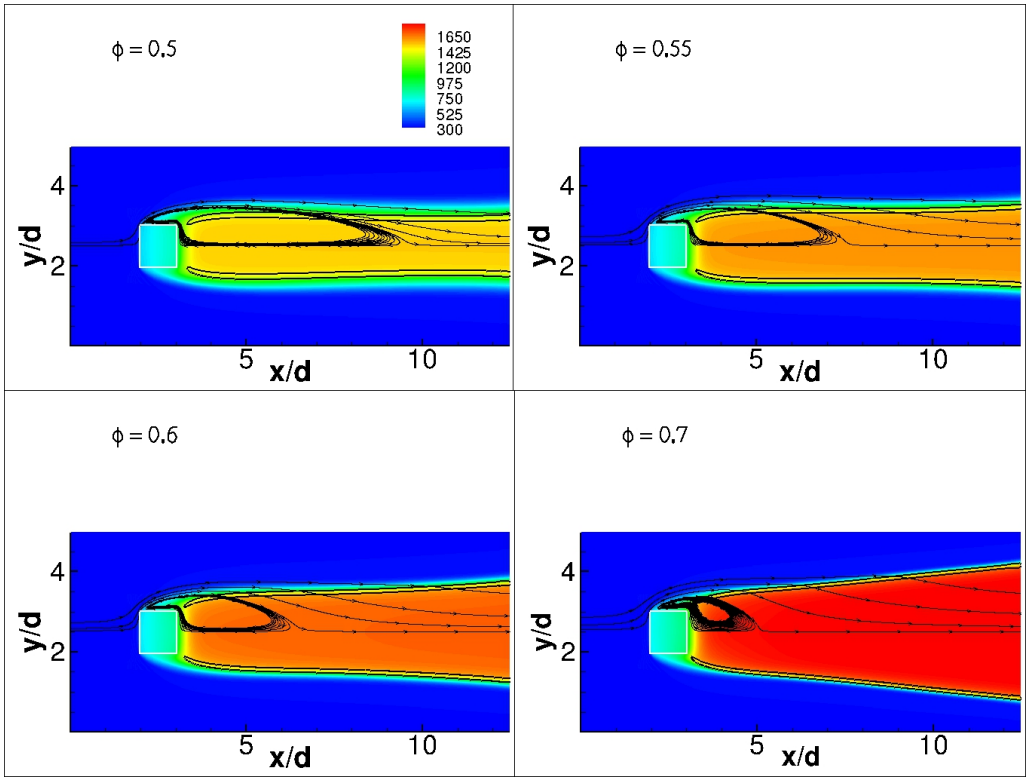

Figure 3-5: Temperature contours with overlaid streamlines and 10% Y_{HCO} black contour line for various ϕ using a ceramic bluff-body marked by the white square.

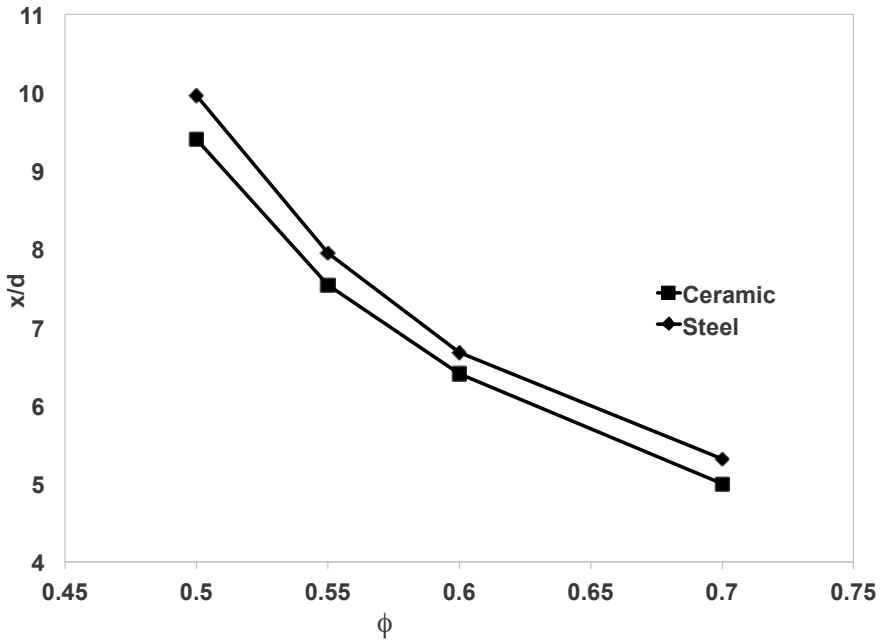

Figure 3-6: The non-dimensional x-position of the end of the recirculation zone at the centerline $y/d = 2.5$ for different ϕ using the steel and ceramic bluff-bodies. The downstream face of the bluff-body was at $x/d = 3$.

3.2.4 Flame structure near the flame anchoring location

Figure 3-5 shows the flame simulations at various ϕ using the ceramic bluff-body. A steady anchored flame was observed for all the cases. The colored contours show the temperature distribution. The black contour line shows the 10% Y_{HCO} location, visualizing the flame as discussed above. Few representative streamlines are overlaid on each plot. The recirculation zone was observed to grow in size as ϕ was reduced. The flame angle with respect to the streamwise direction was greater and the flame was thinner for larger ϕ, as expected. Figure 3-6 shows the non-dimensional location of the downstream stagnation point of the recirculation zone for various ϕ using both the steel and the ceramic bluff-bodies. The downstream face of the bluff-body corresponds to $x/d = 3$. The recirculation zone rapidly grew in size as ϕ was reduced[2]. For each ϕ, the recirculation zone length for the steel case was slightly larger (order of a flame thickness) than its ceramic case counterpart. This is because the flame anchored at a slightly downstream distance from the bluff-body (also of the order of a flame thickness as shown in Section 3.2.5) for the former.

Figure 3-7 shows the flame structure for the cases $\phi = 0.5$ (top row) and $\phi = 0.7$ (bottom row) using the ceramic bluff-body. The convection, diffusion and reaction terms of the energy equation are plotted along the flame normal at four different locations for each case; (1) anchoring location marked by the "start" column, (2) the middle and (3) the end of the recirculation zone and (4) far downstream. These terms correspond to C_T, D_T and S_T terms respectively in Eqs. 2.3 and 2.4. Each term was non-dimensionalized by the maximum reaction-rate value far downstream. The x-axis corresponds to the flame normal co-ordinate in [mm]; with 0 value corresponding to the maximum reaction-rate location in each plot. For both the flames, the flame structure far downstream ("far" column in Fig. 3-7)[3] was observed to be similar to a one-dimensional unstrained flame structure: a two-zone structure with a convection-

[1]It is shown to be strain-dominated. The curvature contribution is shown to be finite but small near the anchoring location and almost zero further downstream.

[2]For all the other operating conditions fixed, the recirculation zone length was shown to vary inversely as the square root of the blockage ratio in [31]

[3]The y-axis scale was changed in for the "far" column of Fig. 3-7 compared to the three left columns to show the overall flame structure.

diffusion preheat zone and a reaction-diffusion zone. The two zones of the $\phi = 0.7$ flame are thinner than the $\phi = 0.5$ flame, as expected. However, the flame structure was observed to be significantly different near the anchoring location for both the cases. The flames here were visibly weaker as observed from the small values of the S_T terms in the "start" column. This is because of the large conjugate heat exchange with the nearby bluff-body wall. Furthermore, the flame at the anchoring location lacked the conventional sharp reaction-diffusion zone. Instead all the three terms were comparable in the reaction-zone; demonstrating that the conventional premixed flame correlations for stretch, flame-speed, flame-thickness must be used with extreme caution in this flame-anchoring region. Similar departure from the conventional flame structure near the flame anchoring region for the perforated-plate stabilized premixed flames will be reported in Chapter 5.

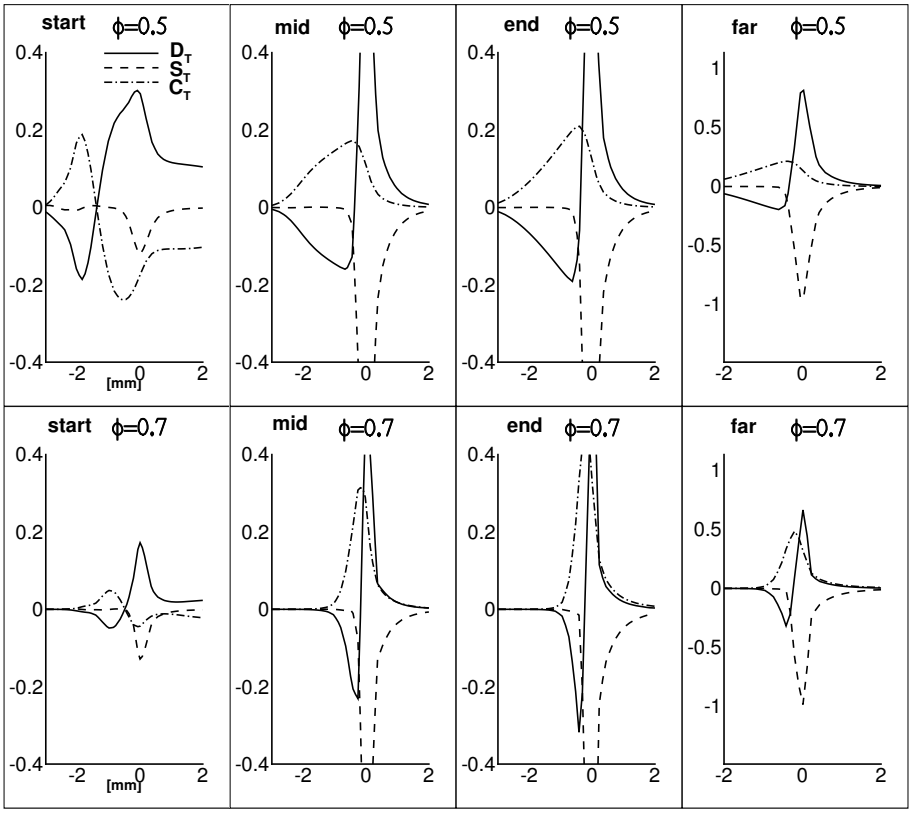

Figure 3-7: The flame structure: the convection (C_T), diffusion (D_T) and reaction (S_T) terms of the energy equation normal to the flame-front at four different locations relative to the recirculation zone; for the cases with $\phi = 0.5$ and $\phi = 0.7$.

Figure 3-7 "start" column also shows that the reaction-zone at the anchoring location had a strong negative convection of energy (bulk flow is directed from the products to the reactants). Thus a significant heat-release associated with combustion takes place within the recirculation zone. This is clearly visualized in Figs. 3-8 and 3-9. The 10% Y_{HCO} contour lines in the flame anchoring region start well inside the recirculation zone. This is similar to the "negative flame displacement speed" phenomenon reported in literature for premixed flame in a strongly turbulent flow [71]. Due to the presence of heat-release, the consumption rate of the flame (and thus its consumption speed) is positive even though there is a "negative flame displacement speed". I thus conclude that the fresh reactants must reach the reaction zone inside the recirculation zone primarily by the mass diffusion across the streamlines. The reaction-zone was also observed to be embedded inside the recirculation zone for the $\phi = 0.55$ and $\phi = 0.6$ cases (see Fig.3-5); the embedded length of the flame rapidly shrunk as ϕ was increased. The steel bluff-body also showed similar results. To the best of my knowledge, this observation for laminar flames near the flame anchoring zone has not been reported anywhere in the literature. High resolution experimental measurements will be very useful to investigate this region in more detail.

Figure 3-7 also shows that the flame structure changed downstream from the anchoring region and the conventional two-zone structure was observed to recover near the center of the recirculation zone; although the magnitudes of the C_T, S_T and D_T terms were observed to be relatively smaller than the "far" column. Towards the end of the recirculation zone, the conventional two-zone structure was almost entirely recovered.

3.2.5 Influence of conjugate heat exchange on flame anchoring

Figures 3-8 and 3-9 show the temperature contours with overlaid streamlines in the near-field downstream of the bluff-body for three different thermal conductivities of the bluff-body (corresponding to an almost adiabatic, ceramic and steel material) for

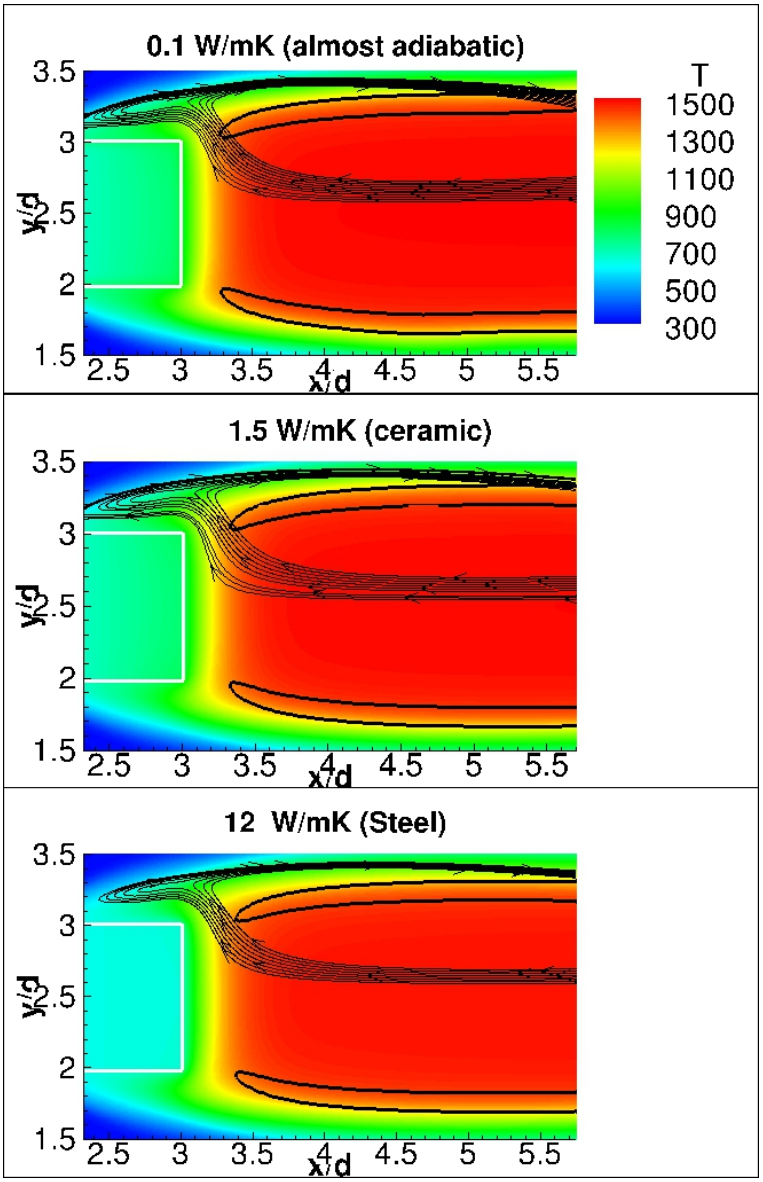

Figure 3-8: Temperature contours with overlaid streamlines and 10% Y_{HCO} black contour line for the case with $\phi = 0.5$ for three different thermal conductivities of the bluff-body (marked by the white square).

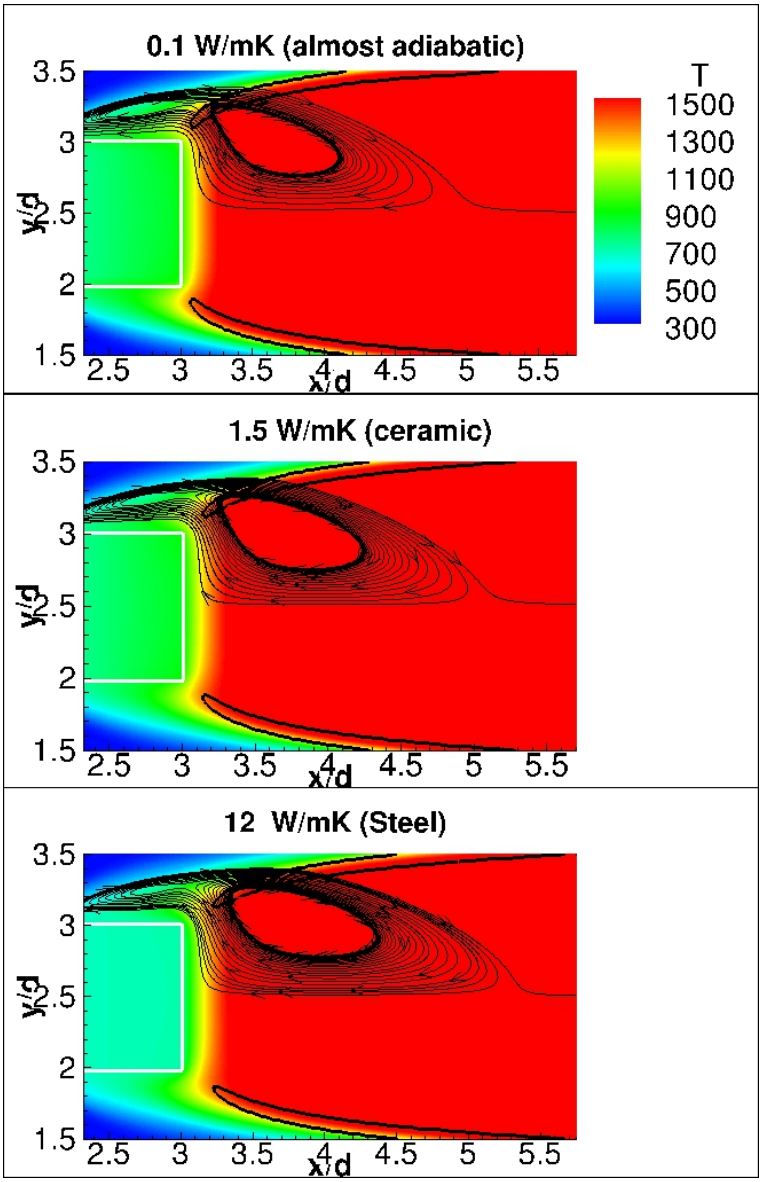

Figure 3-9: Temperature contours with overlaid streamlines and 10% Y_{HCO} black contour line for the case with $\phi = 0.7$ for three different thermal conductivities of the bluff-body (marked by the white square).

the cases with $\phi = 0.5$ and $\phi = 0.7$. The 10 % Y_{HCO} black contour line visualizes the reaction zone. The almost adiabatic bluff-body showed that the flame anchoring location was very close to the buff-body compared to the other materials. Figure 3-9 confirms the above reported result (in Fig. 3-6) that a lower thermal conductivity material results in a smaller recirculation zone. The temperature contours visually show that the bluff-body is hotter for the low thermal-conductivity cases, consistent with the laminar flame computations of perforated-plate stabilized premixed flames shown in Chapter 5 and the experimental investigation of a backward-facing step combustor in [38]. The bluff-body tends to be almost isothermal for the high conductivity case with its temperature depending on operating conditions and the thermal conductivity. However apriori estimation of this temperature for isothermal modeling of the bluff-body in numerical simulations (one of the many artificial flame anchoring conditions used in literature) is not-trivial. For both the ϕ case, the flame anchoring location followed the upstream movement of the temperature contours as the thermal conductivity was reduced.

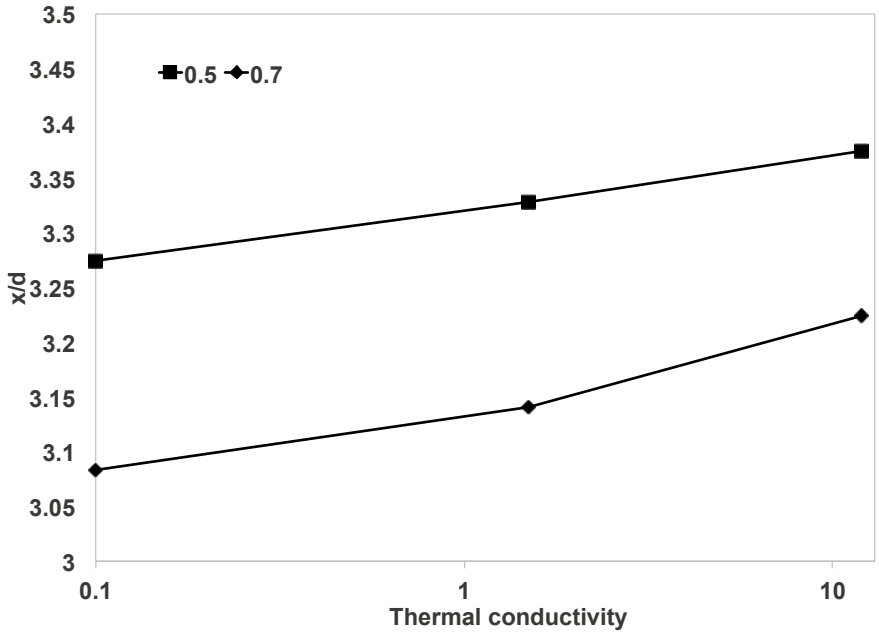

Figure 3-10: The non-dimensional x-position of the flame anchoring location for three different bluff-body materials for the cases with $\phi = 0.5$ and $\phi = 0.7$.

Fig. 3-10 shows that the anchoring location depended nonlinearly on the thermal-

conductivity[4]. This will also be analytically shown in Chapter 6; the flame standoff distance and the flame-holder surface temperature for a perforated-plate stabilized flame depends non-linearly on the plate thermal conductivity for very low values, and it saturates for larger values (beyond 20-30 W/mK). Similar observation was also made by McIntosh and Clarke [72] in the context of one-dimensional plane flame on porous-plug burners.

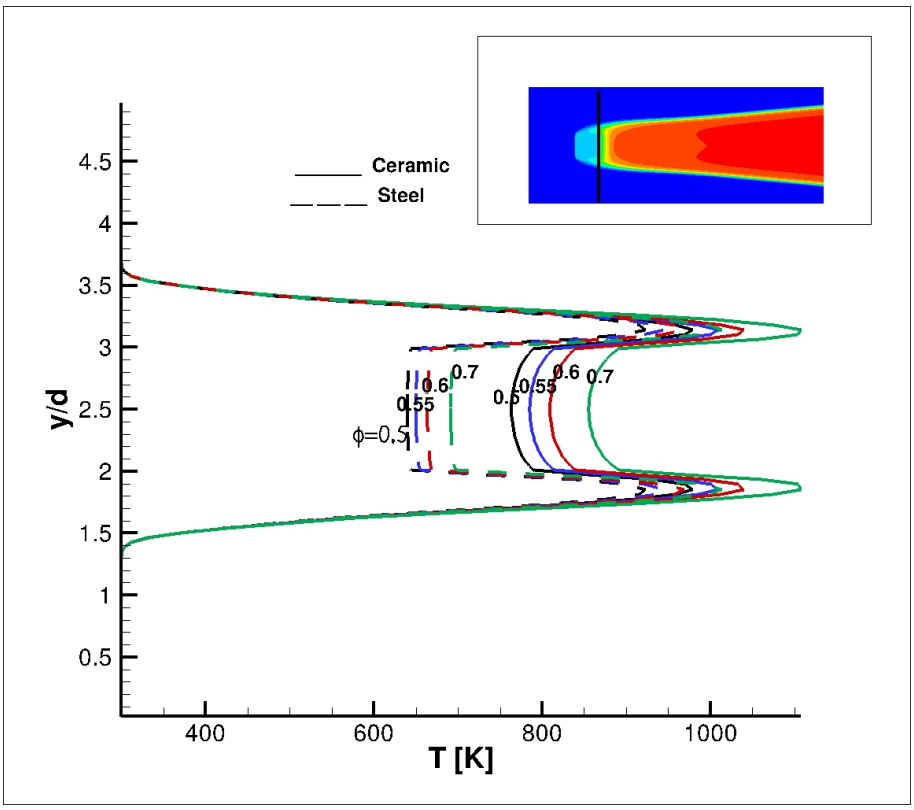

Figure 3-11: The y-profile of the temperature field at $x/d = 3$ for various ϕ using the steel and the ceramic bluff-bodies. The insert shows a visualization of the x/d slice.

The anchoring location was shown to depend on the thermal properties of the bluff-body above. This depends on the conjugate heat exchange between the bluff-body and the reacting flow. The bluff-body provides a pathway for the heat transfer from the downstream hot products to the upstream cold reactants. Figure 3-11 shows the y-profile of temperature at the downstream face of the bluff-body (at $2 \leq y/d \leq 3$ and $x/d = 3$) for the cases with different ϕ for both the steel and the ceramic bluff-

[4]Same trends were also observed using other flame anchoring definitions such as most upstream location of the normalized 5%, 15% and 20% Y_{HCO} contour

bodies. The temperature of the reactants towards the channel wall was 300K, it peaked near the region where the shear layer separated from the bluff-body and dropped at the face due to high thermal conductivity relative to the reacting flow. For each ϕ, the ceramic bluff-body was hotter than the steel counterpart by 20-25%. Figure 3-12 shows the heat-flux entering the downstream face of the bluff-body (marked by the thick black line in the inserted contour plot) for all the above cases. For each ϕ, the steel bluff-body allowed 8-10% higher heat flux to enter (thereby allowing a higher heat-flux out of the sides of the bluff-body at steady-state) relative to the corresponding ceramic case because of its higher thermal conductivity. The temperature and the flux both expectedly grew as ϕ was increased because of the associated increase in the combustion heat-release. The above discussed results that flame anchoring location moves upstream when the thermal conductivity was reduced or when the equivalence ratio was increased is thus justified.

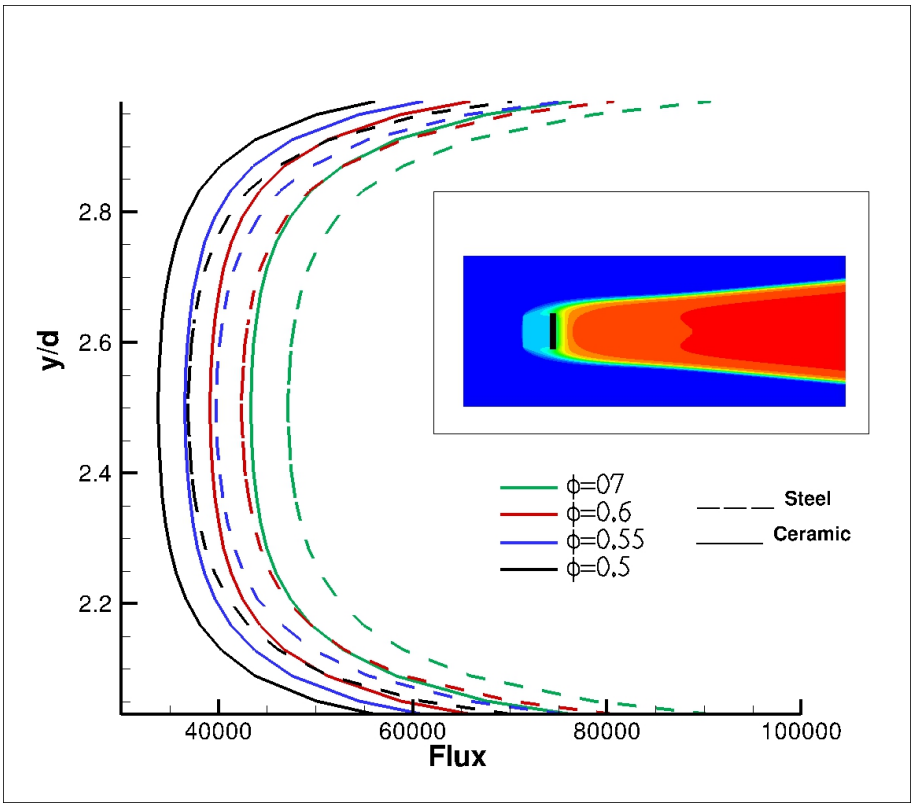

Figure 3-12: The y-profile of the heat flux entering the downstream face of the bluff-body ($x/d = 3$ and $2 \leq y/d \leq 3$) for the steel and the ceramic bluff-bodies for various ϕ. The insert shows a visualization of the x/d slice.

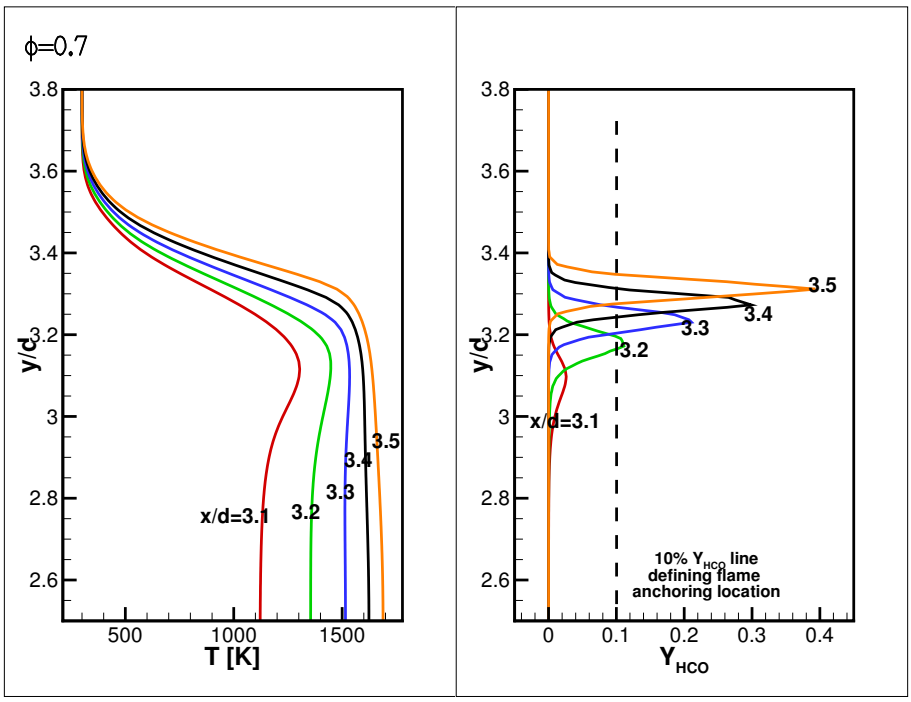

Figure 3-13: The y-profiles of temperature and normalized Y_{HCO} species at various x/d slices in the downstream vicinity of the ceramic bluff-body for the case with $\phi = 0.7$. Only $y/d > 2.5$ is shown because of symmetry.

The temperature and normalized Y_{HCO} profiles at different x/d, in the immediate vicinity downstream of the ceramic bluff-body, are plotted in Fig. 3-13 for the case with $\phi = 0.7$. Only $y/d > 2.5$ is shown because of the observed symmetry in the flow-field. The flame anchoring definition used in this paper is plotted using the dashed line in Fig. 3-13(right). The temperature at this anchoring point was observed to be approximately 1400 K. This region was also associated with a peak in the temperature profile, as seen in the green curve marked by $x/d = 3.2$ in Fig.3-13. The maximum value of Y_{HCO} and T both increased downstream. Figure 3-14 shows the anchoring location (defined in Section 3.2.3) relative to the temperature contours for all the ϕ cases investigated in this paper using a ceramic bluff-body. The anchoring location was observed to be associated with a temperature in the range of 1330K (for $\phi = 0.5$) - 1400K (for $\phi = 0.7$). Similar temperature range was also obtained for the steel bluff-body. All these results indicate that the peak the Y_{HCO} mass-fractions (equivalently the reaction-zone) depends very strongly on the temperature field in the reacting flow.

In summary, it was shown in this section that the flame anchoring location depends strongly on the conjugate heat exchange between the bluff-body and the reacting flow.

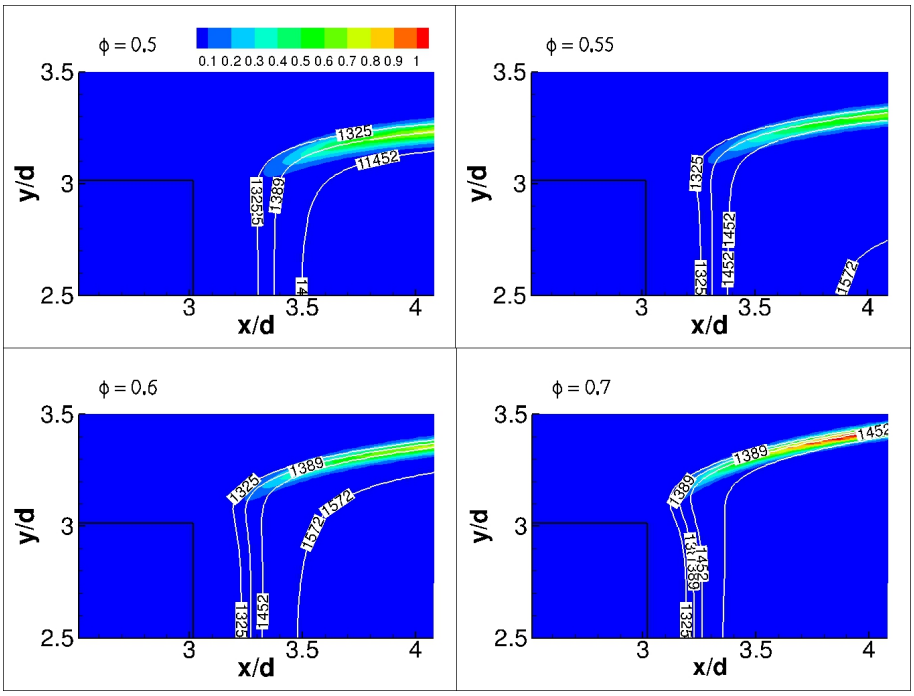

Figure 3-14: Normalized Y_{HCO} contours with overlaid temperature contour lines for various ϕ using a ceramic bluff-body marked by the black square.

3.2.6 Influence of preferential diffusion on flame anchoring

Preferential diffusion, when present, changes the local stoichiometry of the premixed mixture due to a mismatch in the mass-diffusivities of the different species. It cannot be captured using a single-step chemical kinetics because of the nature of its origin in multi-species transport. Furthermore, it is different from the thermo-diffusive effects which results from a mismatch in the thermal and the mass diffusivities of each species (commonly termed as the non-unity Lewis number effect). Barlow and co-workers recently reported strong preferential diffusion in the recirculation zone of bluff-body stabilized turbulent premixed flames using high resolution experimental diagnostics in [24, 25]. They showed an increase in the local equivalence ratio and the carbon-to-hydrogen atom (C/H) ratio across the turbulent flame brush (increase from reactants to products). They conjectured the existence of preferential diffusion

in anchored laminar flames oriented at a high angle to the direction of the incoming reactants; similar to the flames investigated in this paper. I use the simulations discussed above to study this and investigate its role in flame anchoring.

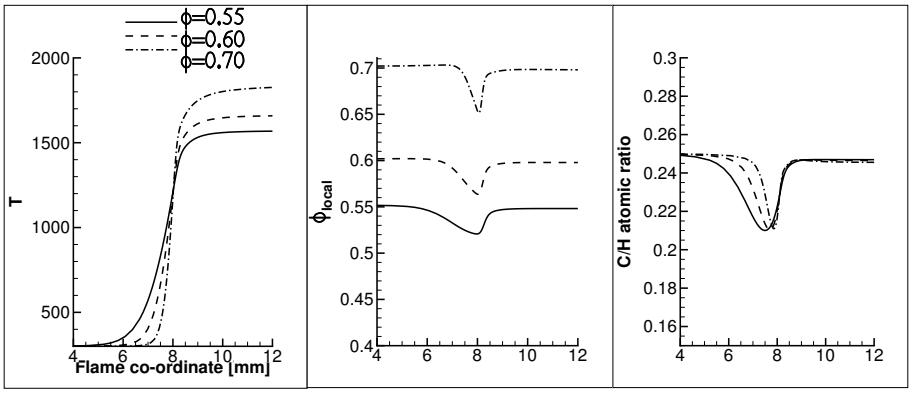

Figure 3-15: Profiles of various quantities along the flame-normal co-ordinate using the unstrained adiabatic laminar flame calculations from Chemkin for the cases with $\phi = 0.55$, $\phi = 0.6$ and $\phi = 0.7$.

Barlow et al. [24] defined a local equivalence ratio on the basis of the local fuel/oxygen atom balance using major species to investigate preferential diffusion.

$$\phi_{local} = \frac{0.5(X_{H_2} + X_{H_2O}) + X_{CO_2} + X_{CO} + 2X_{CH_4}}{0.5(X_{CO} + X_{H_2O}) + X_{O_2} + X_{CO_2}} \tag{3.1}$$

where X_k is the mole-fraction of species k. I used the same definition for consistency in this paper. I first show results for an unstrained adiabatic one-dimensional flame simulation using the multistep C1 skeletal mechanism using Chemkin for three different ϕ in Fig. 3-15. The temperature, ϕ_{local} and the C/H atomic ratio are shown along the flame-normal co-ordinate (units [mm]). Due to the different diffusion coefficients of each species, ϕ_{local} and C/H atomic ratios decrease just ahead of the flame for all the three cases. However, upstream and downstream away from the flame, these quantities were equal to their corresponding incoming flow values. Similar results were also reported in [24] using temperature as the x-axis.

Figures 3-16-3-20 show these quantities in the two-dimensional simulations, using only the ceramic bluff-body for various ϕ. All the results reported here were also observed using the steel bluff-body. Figure 3-16 shows the colored contours of $\phi_{local} - \phi$

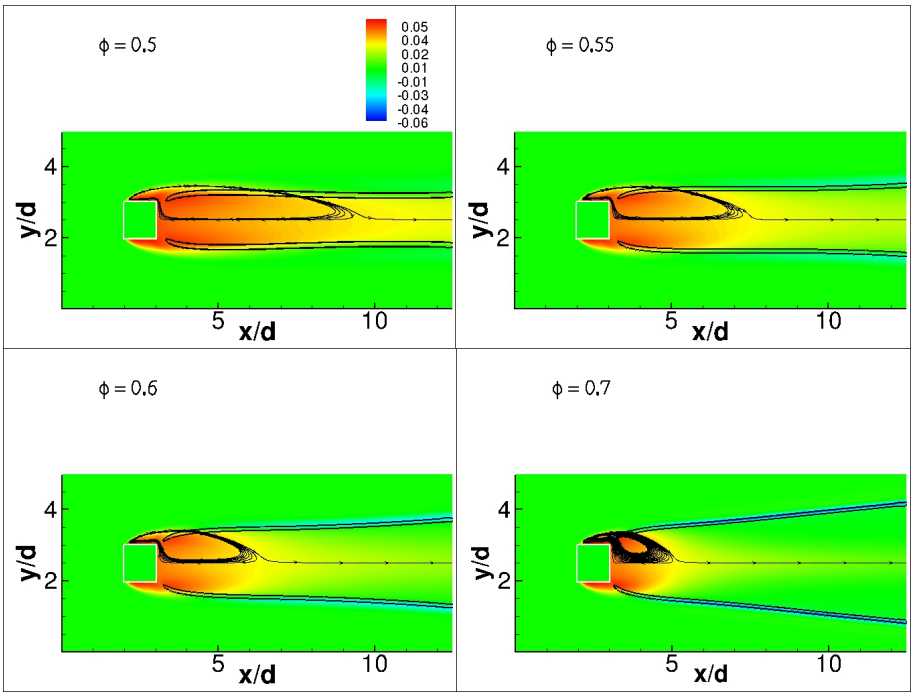

Figure 3-16: Colored contours of $\phi_{local} - \phi$ (departure from the incoming reactants equivalence ratio) with overlaid streamlines and 10% Y_{HCO} black contour line for various ϕ using a ceramic bluff-body marked by the white square.

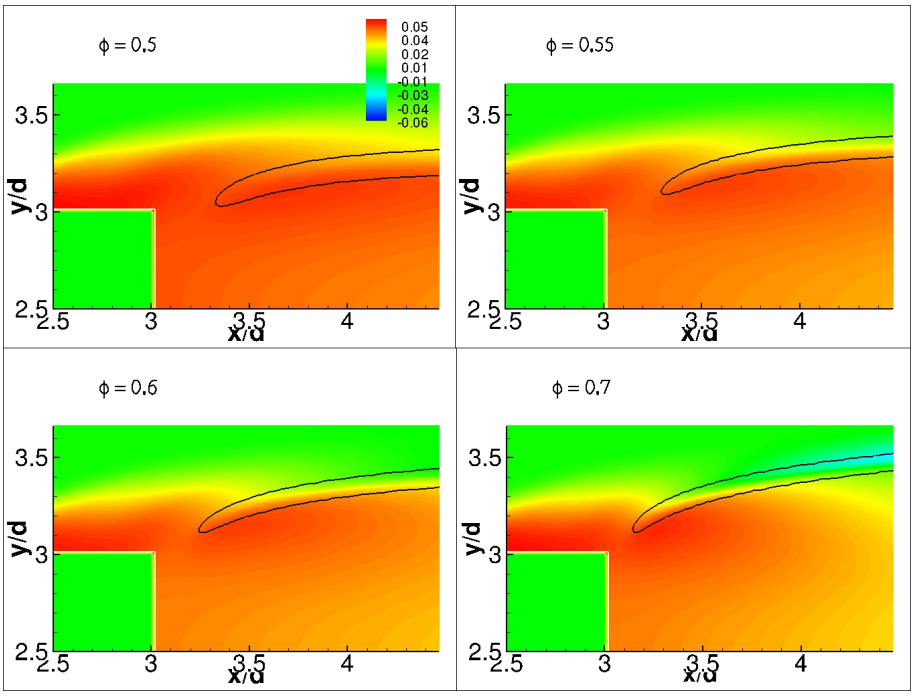

Figure 3-17: Close-up of the $\phi_{local} - \phi$ contours shown in Fig. 3-16 near the anchoring location.

(the departure of ϕ_{local} from ϕ of the incoming reactants) with overlaid streamlines and the 10% Y_{HCO} black contour line. An increase in ϕ_{local} (approximately 7-10%) was observed in the anchoring zone. Figure 3-17 shows that for all the cases, the flame anchored at a location downstream of the bluff-body where ϕ_{local} was the maximum; equivalently where the departure from the ϕ of the incoming reactants was the maximum.

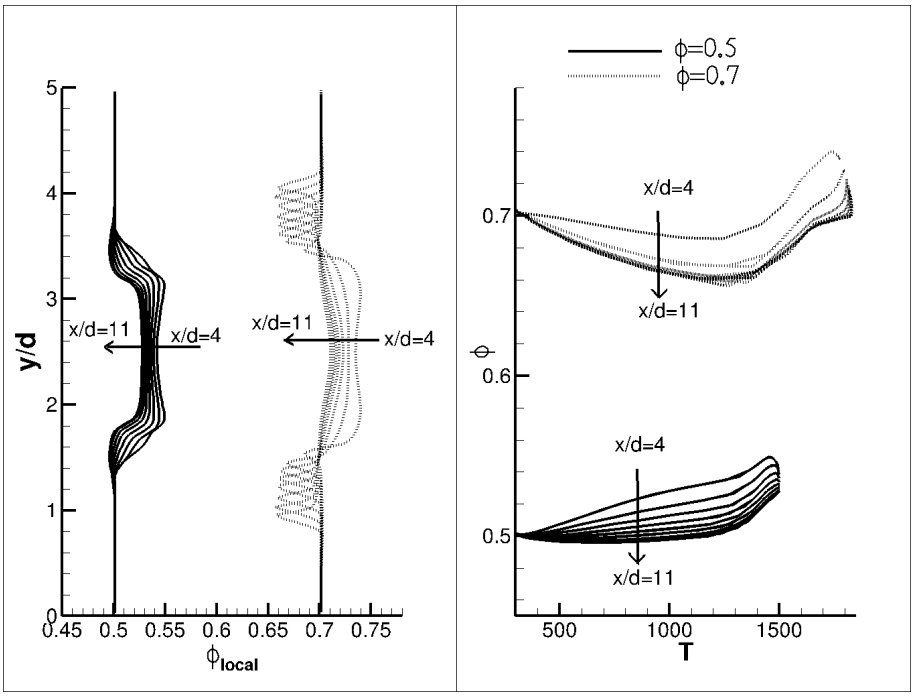

Figure 3-18: ϕ_{local} profiles (left) at various x/d slices (right) as a function of the temperature; for the cases with $\phi = 0.5$ and $\phi = 0.7$.

The increase in the local stoichiometry in the recirculation zone was observed to depend on the relative location in the zone. Far downstream of the recirculation zone, the one-dimensional observation of a ϕ_{local} drop just ahead of the flame (see Fig. 3-15) is recovered for all the cases; except for the weakest $\phi = 0.5$ case discussed below. ϕ_{local} profiles at different x/d slices are plotted for the case with $\phi = 0.5$ and $\phi = 0.7$ in Fig. 3-18. An alternate plot of ϕ_{local} v/s T is also shown for comparison with the results reported by Barlow et al. [24]. In their experimental investigations, the measurements were taken at a fixed location downstream for different $\mathbf{Re}_d$ (presumably changing the size of the recirculation zone in the process) and the increase in the stoichiometry

was compared. However, Fig. 3-18 shows that a better location to compare these cases would be a "fluid-dynamically equivalent" location such as half length of the recirculation zone because of the significant change in the values within the zone itself. I will show in Chapter 4 that the flame-stretch was weak in the laminar bluff-body flames. I thus conclude that the preferential diffusion is not enhanced by the possible presence of a strong stretch in the laminar flame configuration; as speculated in [25].

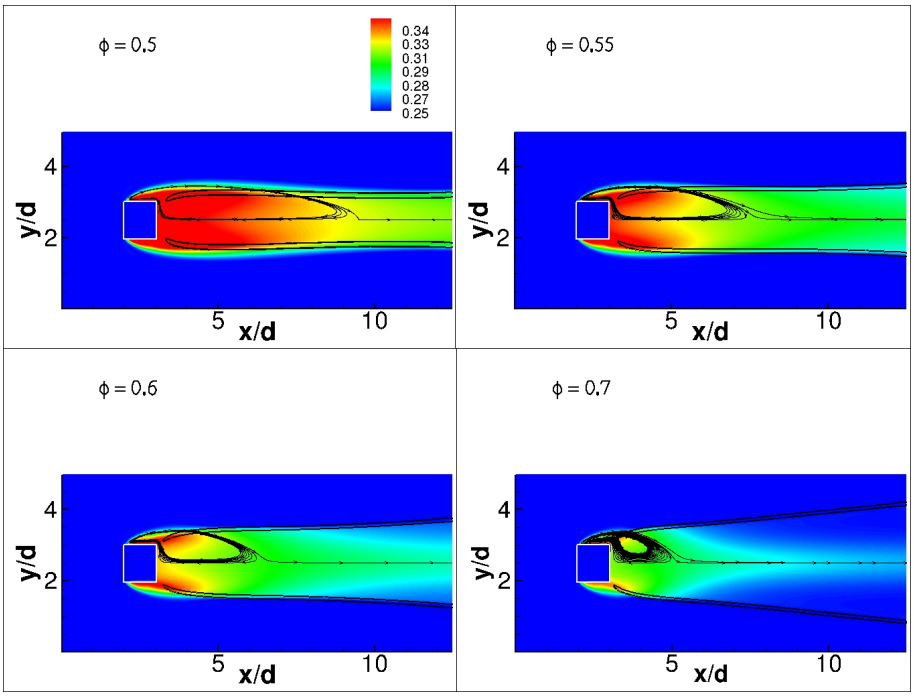

Figure 3-19: The local C/H atomic ratio contours with overlaid streamlines and 10% Y_{HCO} black contour line for various ϕ using the ceramic bluff-body marked by the white square.

Figure 3-19 shows the preferential diffusion through the C/H atomic ratio for various ϕ, indicating that the hydrogen containing major species diffuse ahead of the carbon containing major species (consistent with the observations reported in [25]), resulting in a local accumulation within the recirculation zone. The region of maximum ϕ_{local}, where the flame anchored, was also the region with the maximum C/H atomic ratio. Figure 3-20 shows the contours of the major species for the case with $\phi = 0.5$. These contours visually show that the flame-tangential gradients are strong near the upstream side of the recirculation zone, which is a manifestation of the two-dimensionality of the flow. It is thus concluded that the primary source of

preferential diffusion is the flow two-dimensionality. The far downstream location for the case with $\phi = 0.5$ is not "far" enough to forget the two-dimensionality; thereby not allowing it to recover the preferential diffusion behavior of its corresponding one-dimensional flame; unlike the case with $\phi = 0.7$.

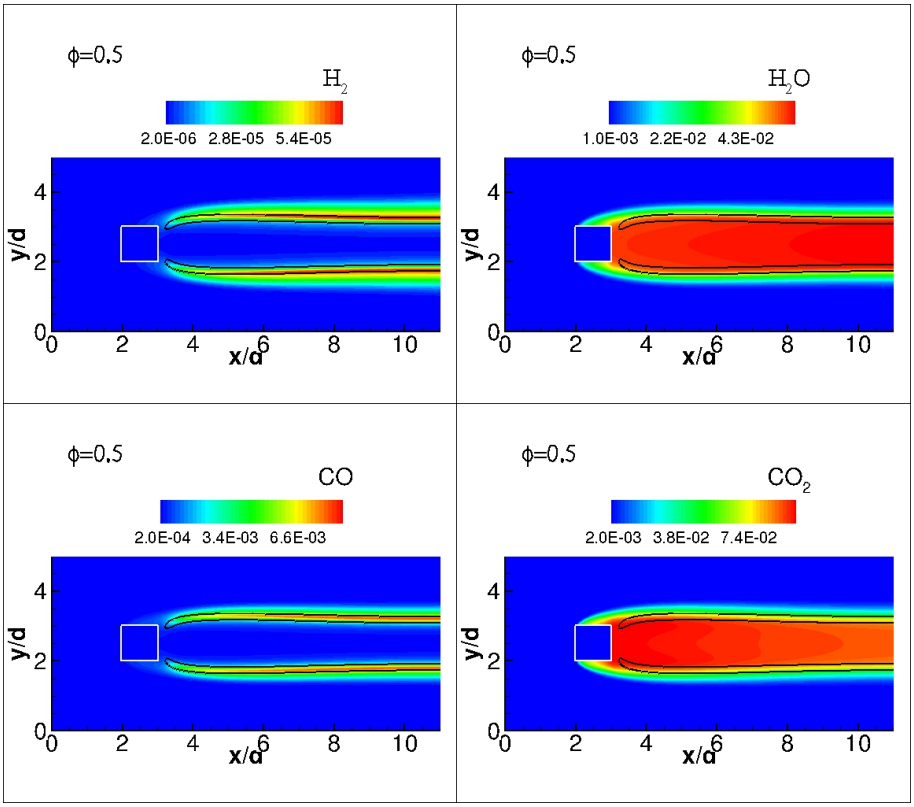

Figure 3-20: Major species : H_2, H_2O, CO and CO_2 contours with overlaid streamlines and 10% Y_{HCO} black contour line for the case with $\phi = 0.5$ using the ceramic bluff-body marked by the white square.

3.2.7 Flame anchoring mechanism

Based on the observations reported above in this paper, I propose the following mechanism for the laminar flame anchoring near a heat-conducting bluff-body. Flame anchoring relies on suitable "ignition" conditions to be established at a downstream location near the bluff-body. For any mixture to ignite a sufficiently high temperature and a suitable mixture conditions must be achieved near the flame location. The unconventional flame-structure discussed in Section 3.2.4 shows that this loca-

tion resides inside the recirculation zone (resulting in a negative flame displacement speed); thereby fresh reactants are provided to the reaction zone by diffusion across streamlines. Conjugate heat exchange discussed in Section 3.2.5 controls the location of the ignition temperature depending on the thermal properties of the bluff-body. Preferential diffusion discussed in Section 3.2.6 contributes to the formation of the favorable ignition mixture composition, providing a region of locally increased stoichiometry. A complex interplay of all these conditions establishes a suitable location for flame anchoring. To the best of my knowledge, such a detailed investigation of the flame anchoring zone has not been undertaken in the literature.

3.3 Unsteady simulations

3.3.1 Ignition to start a simulation

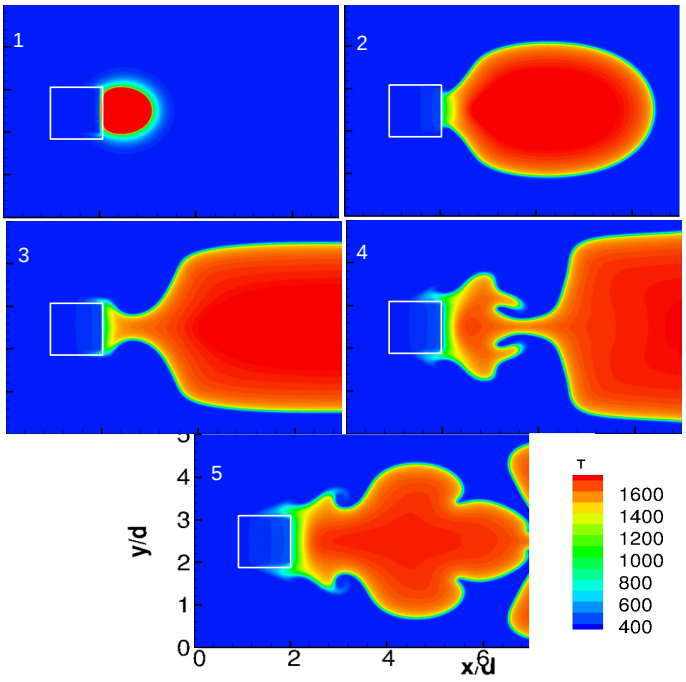

Figure 3-21: Temperature contours showing the ignition transient process (few ms timescale) from a hot-spot created immediately downstream of a ceramic bluff-body.

A good initial condition for the above discussed simulations is required for a

starting guess. The transient generated by this initial condition then gets convected out before a steady-state is reached. There are various ways to ignite a numerical slow-field. In the bluff-body simulations, I first simulated a cold-flow for some time allowing a small recirculation zone to develop behind the downstream face of the bluff-body (a visual image can be seen in the insert of the Fig. 7-2). The cold-flow solution is then restarted with a high temperature hot-spot field imposed inside the recirculation zone, flow-field marked as (1) in Fig. 3-21. The cold-flow is first simulated to trap the hot-spot inside a recirculating fluid, otherwise it will quickly convect downstream and then out of the domain. If this convection was faster than the ignition delay of the mixture or if the ignition happened far downstream from the bluff-body, no anchored flame sheet was observed. Hot-spot inside a recirculation zone avoids this problem. A sequence of events during the transient is shown in Fig. 3-21. Eventually, all the transients were convected out and the laminar steady flame discussed in the above sections was established. This transient process is often violent because of its "artificial" nature. The first-order buffer zone method presented in Section 2.3.3 was observed to be numerically more stable than the second-order method for the initial transient. The above ignition method was used only for the highest $\phi = 0.8$ investigated in this thesis. All the other simulations were started from an already established steady-state simulation; for example $\phi = 0.55$ was started using the established steady solution of $\phi = 0.6$ and changing the inflow conditions of the reactants.

3.3.2 Unsteady simulation with inlet forcing

Understanding dynamic response of flame to velocity perturbations if an important practical problem. The coupling between the acoustics and unsteady heat release rate often leads to self-excited oscillations in combustion systems, which can be dangerous (see, e.g., Lieuwen [73], Ducruix et al. [74], Candel [75] for instability related mechanisms and models). One way to carry out a numerical investigation is to force the inflow at a fixed frequency and small amplitude and investigate the response of the flame to this forcing. Figure 3-22 shows such a simulation. Here the inflow ve-

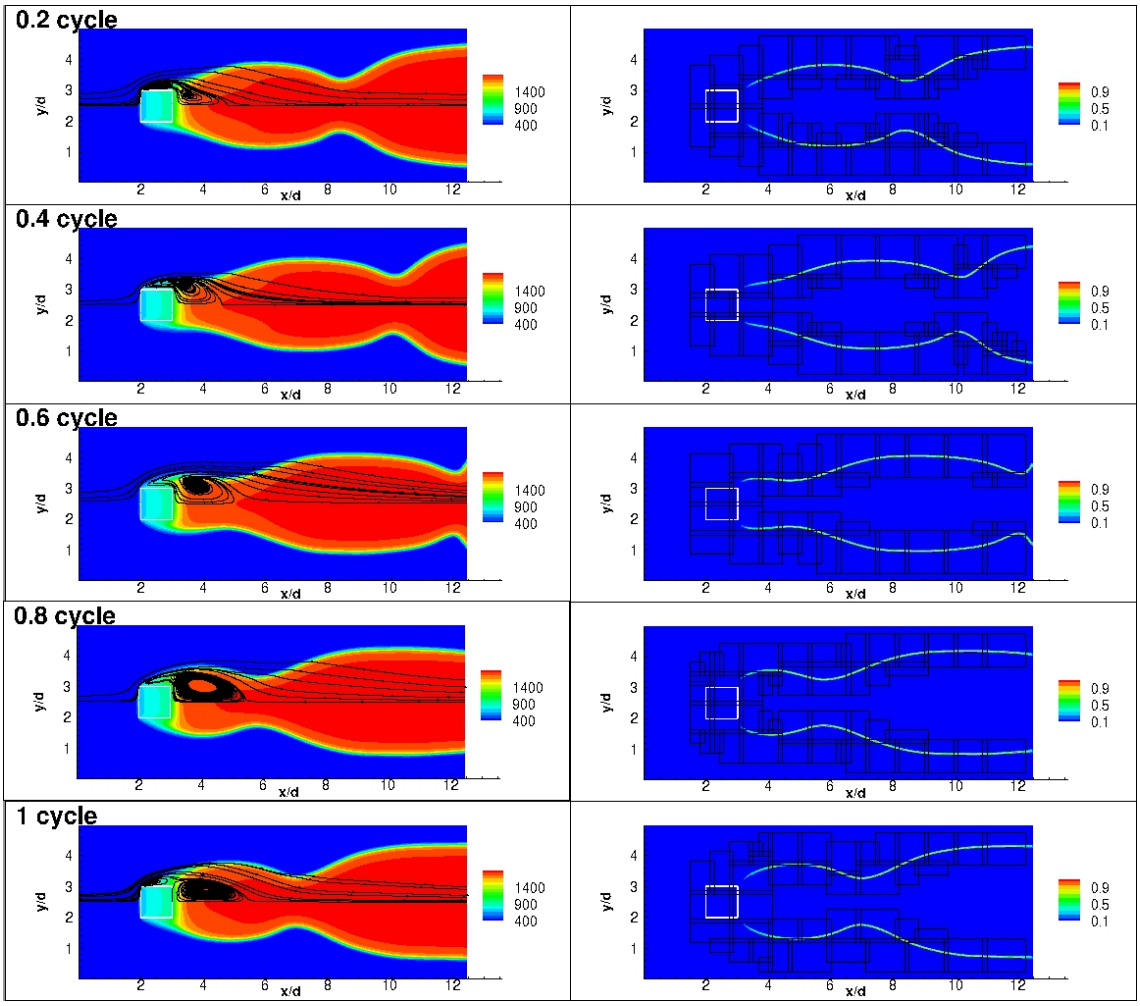

Figure 3-22: (left column) Temperature contours with overlaid streamlines (right column) normalized Y_{HCO} contours with overlaid adaptive mesh patches during an unsteady cycle with inlet velocity forcing of 100 Hz frequency and $0.1U$ amplitude.

locity was forced sinusoidally at a frequency of 100Hz and amplitude of 10% of the mean flow. One cycle of simulation is shown in the figure. Left column shows the temperature contours with overlaid streamlines and the right column shows the flame location via normalized Y_{HCO} species mass-fraction. The adaptive tracking of the flame is also visible. The flame front also oscillated at the same frequency as the inlet velocity oscillations. The recirculation zone size and shape varied during the oscillation. The flame anchoring location oscillated near the downstream corner of the bluff body, showing that the fixed flame anchoring used as a boundary condition in dynamic response models [75] is not entirely valid. I will discuss an analytical model in context of perforated-plate burners in Chapter 6 accounting for the flame anchoring location in the dynamic response modeling. Similar investigations for bluff-body flames must be undertaken in the future.

3.4 Conclusions

In this chapter, I investigated the mechanism of a confined bluff-body stabilized laminar methane/air premixed flame anchoring using the numerical method discussed in Chapter 2. I also demonstrated the capability of the numerical tool to simulate unsteady flame behavior.

Steady flame simulations showed a shear-layer stabilized flame just downstream of the heat-conducting bluff-body, with a recirculation zone formed by the products of combustion. A steel bluff-body resulted in a slightly larger recirculation zone than a ceramic bluff-body; the size of which grew as the equivalence ratio was decreased. Flame anchoring was defined as the most upstream location where the Y_{HCO} mass-fraction reaches 10% of its maximum value far downstream from the bluff-body; Y_{HCO} was shown to be an excellent surrogate for the reaction zone in the range of conditions investigated.

A significant departure from the conventional two-zone flame-structure (convection-diffusion preheat zone and a thinner reaction-diffusion zone) was observed in the anchoring region. The reaction zone was associated with a large negative convection

of energy directed from products to reactants resulting in a local negative flame-displacement speed. A significant part of the flame was observed to reside inside the recirculation zone; the extent of embedding increased as ϕ was decreased. In the anchoring region, fresh reactants reach the reaction zone by diffusion across the streamlines. The two-zone structure was fully recovered towards the end of the recirculation zone.

The role of conjugate heat exchange between the bluff-body and the reacting flow and preferential diffusion on flame anchoring was investigated. The anchoring location moved upstream as the thermal conductivity was decreased; the dependence was non-linear. It also moved upstream as ϕ was increased. The ceramic bluff-body allowed a lower heat flux at its downstream face and was at a higher temperature as compared to the steel bluff-body at the same ϕ. Strong two-dimensionality resulted in preferential diffusion effects inside the recirculation zone; an increase in local equivalence ratio and C/H atomic ratio were observed. Based on the results, I propose that the bluff-body flame anchors at downstream location near the bluff-body where favorable ignition conditions are established; a region associated with (1) a sufficiently high temperature (impacted by the conjugate heat exchange) and (2) a favorable mixture composition with an increased stoichiometry (impacted by the preferential diffusion).

The preferential diffusion effects depended strongly on the relative location within the recirculation zone and was observed to be decoupled from the flame stretch. Experimental investigations comparing the local change in equivalence ratio must account for this change and choose a fluid-dynamically similar location for comparing the cases in which the size of the recirculation zone changes.

In the next chapter, I will elucidate the mechanism of blow-off of the bluff-body flames disccussed in this chapter.

Chapter 4

Mechanism of laminar premixed flame blow-off on a bluff-body

4.1 Overview

In the previous chapter, flame anchoring was investigated. Preferential diffusion was shown to be strong in the recirculation zone and the critical role of flame-wall conjugate heat exchange on flame anchoring was highlighted. The objective of this chapter is to investigate the mechanism of blow-off of the bluff-body premixed flames discussed in the previous chapter. Blowoff is approached by decreasing the mixture equivalence ratio at a fixed Reynolds number of the incoming flow. A flame is stable (does not undergo blow-off) when (1) flame displacement speed is equal to the flow speed and (2) the gradient of the flame displacement speed normal to the flame is higher than the gradient of the flow speed along the same direction. As the equivalence ratio is reduced, the difference between the former and the latter shrinks until the dynamic stability condition (2) is violated, leading to blow-off. The blow-off initiates at the location where this is first violated along the flame. The results show that this location is far downstream from the flame anchoring zone, near the end of the recirculation zone. The blow-off starts by flame pinching separating the flame into an upstream moving (carried within the recirculation zone) and a downstream convecting (detached from the recirculation zone) flame piece. In the range of oper-

ating conditions investigated, the conjugate heat exchange with the bluff-body has no impact on the flame blow-off.

4.2 Results and discussions

Blowoff can be achieved by fixing the Reynolds number, $\mathbf{Re}_d$ and decreasing/increasing the equivalence ratio ϕ for a lean/rich premixed mixture or by fixing ϕ and increasing the $\mathbf{Re}_d$. I choose the latter for the numerical simulations discussed in this chapter. As typically done in experiments, a sweep for a large range of $\mathbf{Re}_d$ and ϕ is not possible due to the large computational expense. To investigate blow-off, cases with $\phi = 0.42$, 0.45, 0.5, 0.55, 0.6, 0.7 and 0.8 were simulated keeping all the other operating conditions the same. Like in Chapter 3, $\mathbf{Re}_d$ was fixed at 500 and no artificial flame anchoring conditions were used. The same C1 chemical kinetics (16 species, 46 reactions) model was used. The Y_{HCO} contours are again used as a surrogate for visualizing the heat-release rate contours, as discussed in Section 3.2.3

4.2.1 The blow-off process

Steady flames were observed for all the cases with $\phi \geq 0.45$. However blow-off occurred for the case with $\phi = 0.42$, thereby showing that the exact value of ϕ where the flame blow-off occurs is within the range $0.42 \leq \phi < 0.45$ for $\mathbf{Re}_d = 500$. Similar value of the blow-off ϕ was also reported for methane/air flames in [30][1]. Finding the exact blow-off value of ϕ would require a large computational expense. The blow-off value was shown to strongly depend on the shape and size of the bluff-body [30, 32] and to some extent on its thermal properties [28, 37] for high Reynolds number flows; along-with the inflow reactant velocity and the equivalence ratio. The sequence of the laminar flame blow-off is shown through the normalized Y_{HCO} contours (normalized by its maximum value far downstream from the bluff-body) in Fig. 4-1. The entire

[1]Fig. 23 in [30] showed that blow-off value of $\phi \approx 0.45$ for a cylindrical flame holder of diameter 0.125" (3.2 mm) with inflowing reactant velocity $\approx$ 60 ft/s (18.2 m/s). This experiment corresponded to $\mathbf{Re}_d \approx 3500$.

transient process was observed to be symmetric, until the flame completely disappeared and a non-reacting unsteady flow was established. A distinct flame pinch-off was observed downstream during the transient. A part of the flame was then engulfed in the recirculation zone and was carried convectively upstream. It eventually disappeared within the recirculation zone after a short anchoring period during its upstream convection. The other part of the flame convected downstream out of the domain. It remained completely detached from the recirculation zone throughout the transient and convected out faster than the upstream moving piece. The upstream part of the pinched-off flame is similar to the experimental observations reported in [30, 31], where a luminous flame existed in the recirculation zone for a long period of time before entirely disappearing. It was referred to as the "residual flame".

In the following section, I will investigate a dynamic stability criterion and propose a mechanism for the blow-off phenomenon. I will also explain physically why the blow-off initiates downstream with a pinch-off.

4.2.2 Dynamic stability criterion

For a stable flame, it is well known that the displacement speed at every point along on the flame must be equal to the flow velocity normal to the flame,

$$|S| = |v_n| \tag{4.1}$$

The displacement speed of the flame is well-defined in an asymptotic analysis where the reaction zone is very thin. In a numerical investigation, this is typically estimated at a fixed contour line. Equation 4.1 is a necessary but not a sufficient condition for flame stabilization. An additional dynamic stability criterion, originally proposed for inverted premixed flames in [46] without experimental or alternate evidence, must also be satisfied

$$|\frac{dS}{dn}| > |\frac{dv_n}{dn}| \tag{4.2}$$

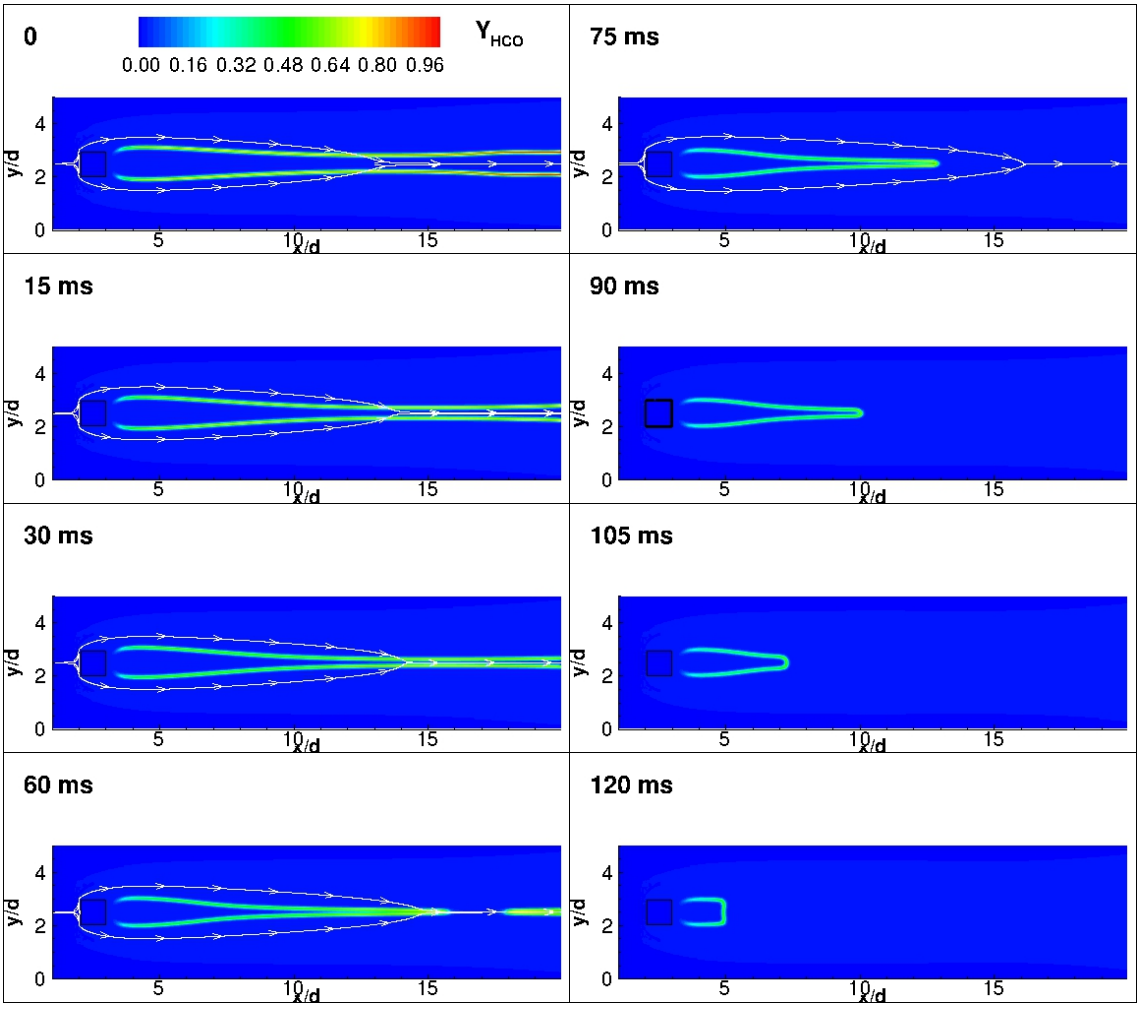

Figure 4-1: Species mass-fraction contours of normalized Y_{HCO} with overlaid streamlines at different time-instants during the blow-off for $\phi = 0.42$ around a confined bluff-body marked by the black square. Time $t = 0$ corresponds to an arbitrarily selected reference beginning time during the transient.

where n is the normal to the flame front directed towards the reactants. $|\frac{dS}{dn}|$ is a measure of the change in the flame displacement speed if it were to stabilize at a small distance normal to its current location whereas $|\frac{dv_n}{dn}|$ quantifies the rate of change of the incoming reactant velocity along the flame-normal in the non-uniform flow-field[2]. Figure 4-2 shows a schematic diagram illustrating this criterion for dynamic stability for a stable flame location n_0. At this location, the flame and flow speeds must be the same; $|S| = |v_n|$. If the flow is accelerating, $|v_n|_{n_o+dn} < |v_n|_{n_o} < |v_n|_{n_o-dn}$, then the flame can be stable to small perturbations only if $|S|_{n_o+dn} < |v_n|_{n_o+dn}$ and $|S|_{n_o-dn} > |v_n|_{n_o-dn}$. This is mathematically equivalent to the condition $|\frac{dS}{dn}| > |\frac{dv_n}{dn}|$. This physically ensures that if a small convective disturbance perturbs the flame towards/away from the reactants, then the flame displacement speed increases/decreases more than the flow speed bringing it back to the original location and a stable flame is sustained. I will demonstrate that the flame blow-off occurs when the dynamic stability criterion is violated for bluff-body stabilized laminar flames. I will also show that the blow-off initiates at the location where this criterion first fails. I will also discuss the dynamic stability criterion in the context of blow-off of perforated-plate stabilized flames in Chapter 5.

To check the validity of the dynamic stability criterion, $|\frac{dv_n}{dn}|$ was directly computed from the numerical results; the local flame-normal n was estimated by high-order polynomial curve-fitting of the reference location. However computing the gradient of the flame speed $|\frac{dS}{dn}|$ is not trivial. I estimate this indirectly by

$$|\frac{dS}{dn}| = |\frac{dS}{d\kappa} \times \frac{d\kappa}{dn}| \tag{4.3}$$

where κ is the total flame stretch. Equation 4.3 decomposes $|\frac{dS}{dn}|$ into a directly measurable flow property, $\frac{d\kappa}{dn}$, from the simulations and a physico-chemical property of the reacting mixture, $\frac{dS}{d\kappa} \sim O(1)$mm, discussed in the following section. There is no

[2]In a uniform planar flow-field, an adiabatic unstretched premixed flame normal to it will sustain itself at a fixed location as long as the reactant velocity is exactly equal to its flame speed. In this case, both $|\frac{dS}{dn}| = 0$ and $|\frac{dv_n}{dn}| = 0$ and the flame is neutrally stable. If perturbed, it will move by a distance corresponding to the disturbance and sustain at that new location when the perturbation is removed.

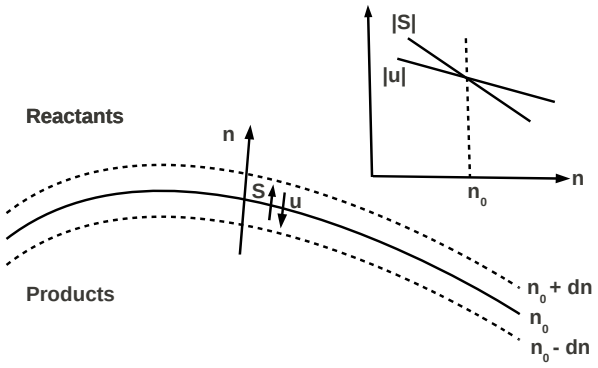

Figure 4-2: Schematic illustration of the dynamic stability criterion. A curved flame-front (solid line) is shown with it normal n marked at a location.

local external heat losses experienced by the flame, especially near the blow-off point which is far downstream from the heat conducting bluff-body. Hence the implicit assumption of $S = S(\kappa)$ in the decomposition shown in Eq. 4.3 is justified.

4.2.3 The Markstein length and flame stretch

The fame stretch κ is a combined effect of the strain of the flow-field, curvature of the flame-front and the local unsteadiness during a transient flame motion. The flame displacement speed is sensitive to κ and depends linearly on it when κ is sufficiently small. This was first proposed by Markstein [76]:

$$S = S_u^0 - \mathcal{L}\kappa \tag{4.4}$$

where S is the flame displacement speed of the stretched flame with respect to the unburnt reactants, S_u^0 is the corresponding unstretched laminar flame speed and $\mathcal{L}$ is the Markstein length, which is of the order of the flame thickness. $\mathcal{L}$ depends on the physico-chemical properties of the reacting mixture and can be positive or negative; although generally positive for most fuels [77]. For weakly stretched flames, $\frac{dS}{d\kappa}$ in Eq. 4.3 is thus the negative of the Markstein length $\mathcal{L}$.

$\mathcal{L}$ is often non-dimensionalized by the characteristic premixed flame thickness δ_T

and reported as Markstein number **Ma** in the literature. Analytical expression for **Ma** was developed in the classical work of Clavin and Williams [78] using asymptotic analysis

$$\mathbf{Ma} = \mathcal{L}/\delta_T = \frac{1}{\gamma}\ln\frac{1}{1-\gamma} + \frac{\beta(\mathbf{Le}-1)}{2}\frac{1-\gamma}{\gamma}\int_0^{\gamma/1-\gamma}\frac{\ln(1+x)}{x}dx \tag{4.5}$$

$$\delta_T = \frac{\alpha_{mix,u}}{S_u^0}, \quad \gamma = \frac{T_b - T_u}{T_b}, \quad \beta = \frac{T_a(T_b - T_u)}{T_b^2} \tag{4.6}$$

where $\alpha_{mix,u}$ is the thermal diffusivity of the unburnt mixture, T_b and T_u are the adiabatic burnt gas and the unburnt gas temperature respectively, T_a is the activation temperature, β is the Zeldovich number, **Le** is the Lewis number based on the deficient reactant (methane in this investigation). The above theoretical result is restricted to small flame surface deformations. More general expressions for large deformations associated with extensive flame wrinkling were derived in [79, 80].

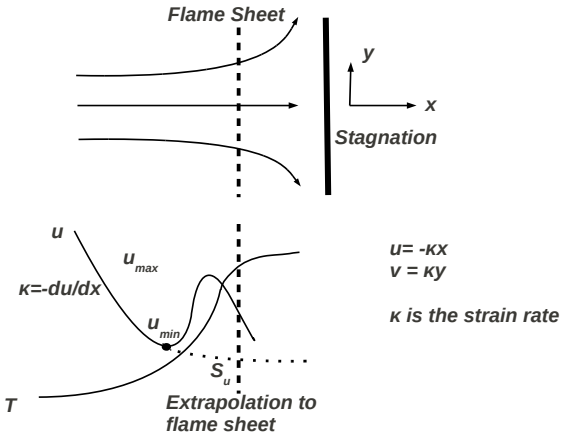

Figure 4-3: Schematic illustration of (top) a planar stagnation point premixed flame (bottom) the velocity profile, the temperature profile and the location used in literature for the stretch rate and the flame speed computation.

Many experimental and numerical investigations have also been carried out in the literature to estimate the **Ma** for different fuels and at different equivalence ratios [81–85]. In practice, determining **Ma** is non-trivial because of the non-uniformity in the flow-field associated with the heat-release driven flow divergence and the finite-

thickness flame region resulting from the detailed chemical kinetics. Determining **Ma** in an experimental or a numerical investigation requires (i) defining an "upstream reference location" where the flame stretch is computed and (ii) defining a "flame reference location" where the flame displacement is estimated based on velocity extrapolation from the "upstream reference location" [84]. In a stagnation point flow, the common choice for the "upstream reference location" in the above cited references is the location where the velocity reaches a minimum. In this configuration, the velocity far upstream decreases as it approaches the flame front; it then starts to increase as the reactants are preheated and divergence is created in the flow-field due to combustion and it again starts to decrease to become zero at the stagnation point. This is shown in the schematic illustration of a stagnation point flame in Fig. 4-3. The stretch κ is usually estimated as the maximum gradient in the upstream velocity field. **Ma** depends significantly on the "flame reference location" definition. Clavin and Joulin [86] showed that if the "flame reference location" is displaced by a distance equal to the Markstein length, then error in estimation of **Ma** is 100%. It can be positive or negative for the same flame based on the choice of this definition as demonstrated by Deshaies and Cambray [82]. Tien and Matalon [87] theoretically derive **Ma** relative to different "flame reference location" such as location at a fixed contour of 1% temperature rise at the upstream edge of the preheat zone, location of a velocity minimum in the preheat zone (used in [81]) and location of a velocity maximum at the downstream edge (used in [88]) using the counterflow premixed flame configuration. Hence great caution must be exercised during any analysis before directly using the Markstein numbers reported in the literature.

In this investigation, I used the analytical expression of Clavin and Williams [78] (shown in Eq. 4.5) for estimating **Ma**. It is reasonable to use this expression for laminar flames investigated here as it was developed assuming small flame surface deformations. Table 4.1 shows the values of $\mathcal{L}$ calculated from this expression at different ϕ investigated here. I chose $T_a = 24400$ K for methane/air flame, $T_u = 300$K. S_u^o was obtained using the PREMIX code in Chemkin.

The stretch rate of a flame surface element dA is defined in the tensor notation

ϕ	T_b[K]	β	**Le**	**Ma**	$\alpha_{mix.u}$	S_u^o[cm/s]	$\mathcal{L}$[mm]
0.45	1430	13.48	0.983	1.91	0.222	2.57	1.65
0.50	1501	13.01	0.982	1.94	0.222	4.80	0.90
0.55	1585	12.48	0.980	1.98	0.223	7.96	0.55
0.60	1669	11.99	0.978	2.02	0.223	11.57	0.39
0.70	1835	11.12	0.975	2.09	0.223	19.56	0.24
0.80	1992	10.40	0.972	2.15	0.223	27.81	0.17

Table 4.1: Markstein length using the analytical expression of Clavin and Williams [78] shown in Eq. 4.5.

as [89]

$$\kappa = \frac{1}{A}\frac{dA}{dt} = (\delta_{ij} - n_i n_j)\frac{\partial u_i}{\partial x_j} + S\frac{\partial n_i}{\partial x_i} \tag{4.7}$$

where δ_{ij} is the Kronecker delta, i, j are the directional indices in the Cartesian coordinate system (x_i, x_j), n is the unit vector normal to the flame front towards the reactants, S is the burning velocity normal to the flame surface. The first term on the right hand side is the strain rate induced by the velocity field (κ_s), while the second term represents the curvature contribution κ_c to the flame stretch ($\kappa = \kappa_s + \kappa_c$). For a stationary flame, S at each point is equal to the the flow speed at that point normal to the flame surface. For a two-dimensional Cartesian coordinate system, the stretch rate simplifies to

$$\kappa = -n_x n_y(\frac{\partial u}{\partial y} + \frac{\partial v}{\partial x}) - n_x^2\frac{\partial u}{\partial x} - n_y^2\frac{\partial v}{\partial y} - (un_x + vn_y)(\frac{dn_x}{dx} + \frac{dn_y}{dy}) \tag{4.8}$$

Computing the flame stretch at an "upstream reference location" in a stagnation point flame (configuration used in the literature for numerically computing or experimentally measuring the **Ma**) is relatively easier because of the uniformity of the flow normal to the flame. However, the flow-field in the simulations shown in this chapter is not uniform because of the channel and high flame angle to the incoming flow. I thus define an "upstream reference location" by a fixed contour, where 1% consumption of methane is completed as the location to compute the stretch. This definition ensures that the flame stretch is computed at a location just ahead of the preheat zone of the flame.

(a)

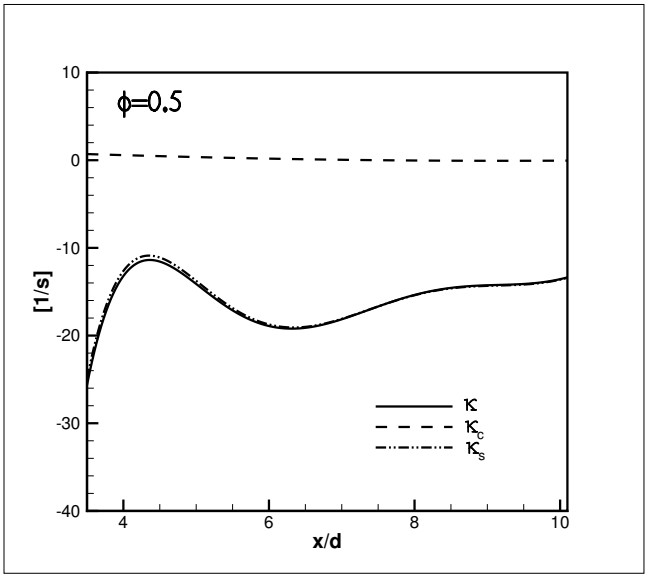

(b)

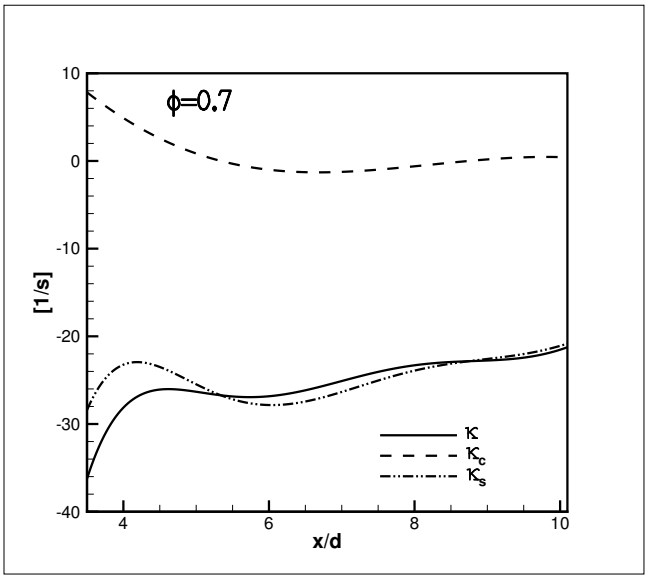

Figure 4-4: The variation of the total flame stretch, with the strain and curvature components computed at the upstream reference location, in the streamwise x-coordinate for the cases (a) $\phi = 0.5$ and (b) $\phi = 0.7$.

Figure 4-4 shows the flame stretch profile for the cases with $\phi = 0.5$ and $\phi = 0.7$. The two-dimensional flow-field of these cases was discussed in Fig. 3-5 of the previous chapter. The stretch profile was computed along the upstream reference location in the top half of the y-domain ($y/d \geq 2.5$ in Fig. 3-5) because of the observed symmetry. The flame normal was computed at each location, using high-order polynomial curve fitting, to obtain the projected flame normal unit vectors n_x and n_y for Eq. 4.8. Figure 4-4 shows that the stretch was dominated by the strain component almost along the entire flame for both cases. There is a weak positive curvature (convex towards the reactants) near the anchoring location and zero curvature further downstream; flame for the higher ϕ case was curved more as also visualized by the contours in Fig. 3-5. The stretch profiles for all the other ϕ investigated in this study also showed the same result and are not plotted here.The total flame stretch was weak ($|\kappa|$ <50s^{-1}). This is not surprising, especially at downstream locations because the flame is unconstrained / free to move and is not distorted by any unsteady flow-field feature. This also justifies the use of the Markstein theory developed for weak stretch (Eq. 4.4) for the blow-off analysis in the next section. The flame stretch was relatively higher near the anchoring zone, but not large enough to lead to extinction as seen in turbulent flames [35, 36].

The flame stretch discussed above was observed to be negative for all ϕ, demonstrating that the flame stabilized in an accelerating flow. This is unlike the decelerating conventional stagnation point flow used widely in the literature, described schematically in Fig. 4-3. Instead, this is a manifestation of the boundary conditions. The flame at $\phi = 0.50$ was observed to be almost columnar in the downstream region (see Fig. 3-5). In this region, the speed of the incoming reactants into the flame zone corresponds to the y-component of the velocity vector; v. For the confined-channel, $v = 0$ at the channel walls ($y/d = 0$, $y/d = 5$) and at the centerline ($y/d = 2.5$) due to symmetry. This enforces $|v|$ to increase and then decrease from the channel walls to the centerline. As a result, the flame experiences a locally accelerating flow, before further accelerating it by thermal expansion. Figure 4-5 shows the v-velocity profile at various downstream x/d locations for the case with $\phi = 0.5$. The flame (preheat

and the reaction zone) is seen in the region $1.2 \lessapprox y/d \lessapprox 1.7$ and $3.3 \lessapprox y/d \lessapprox 3.8$ where the thermal expansion results in a significant acceleration of the flow, before it peaks and decelerates to become zero at the centerline $y/d = 2.5$.

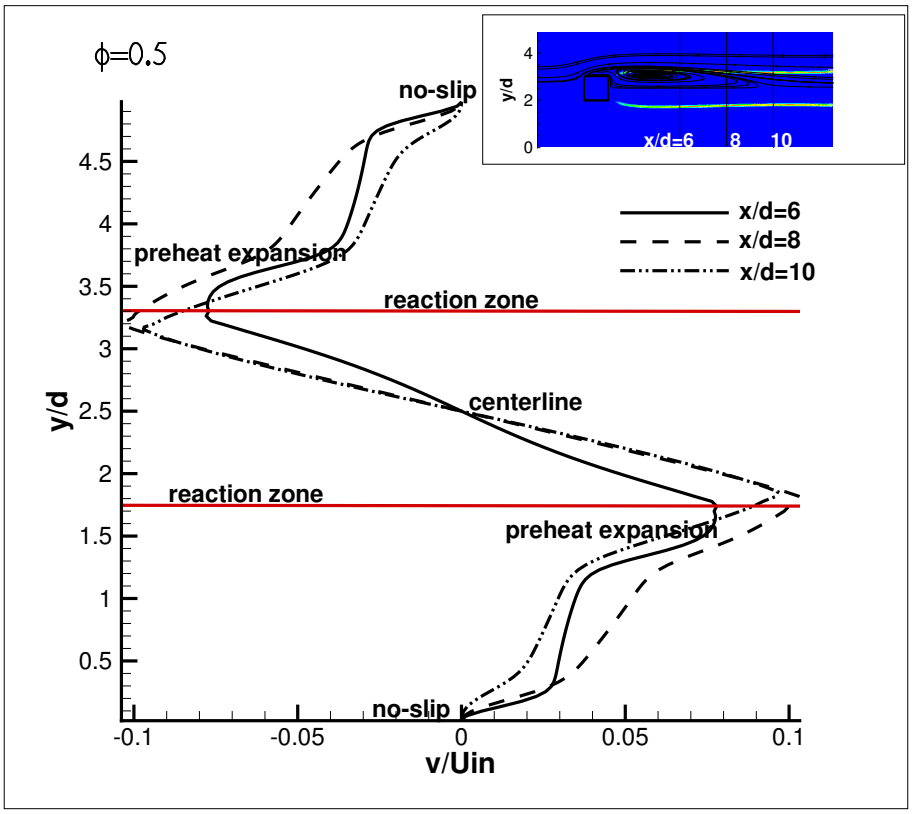

Figure 4-5: The profile of v-velocity normalized by the mean inlet velocity $U_{in} = 1.6$m/s versus the non-dimensionalized y-co-ordinate for the case with $\phi = 0.5$ at different x/d. The insert shows the flame location through the Y_{HCO} contour and overlaid streamlines.

4.2.4 The blow-off mechanism

In this section, I will show that the dynamic stability criterion, expressed in Eq. 4.2, got closer to being violated when the blow-off conditions were approached. I chose an x/d location just downstream of the end of the recirculation zone for all the cases with different ϕ and plotted the components of Eq. 4.2, $|\frac{dv_n}{dn}|$ and $|\frac{dS}{dn}|$, in Fig. 4-6. An immediate downstream location to the recirculation zone was chosen because the blow-off process was shown to initiate around this region in Fig. 4-1. The results

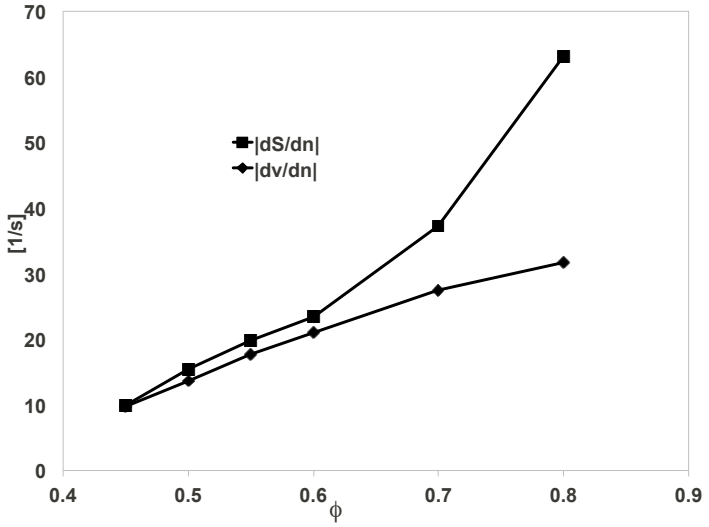

Figure 4-6: $|\frac{dv_n}{dn}|$ and $|\frac{dS}{dn}|$ components of Eq. 4.2 at the upstream reference location, just downstream of the recirculation zone for different ϕ.

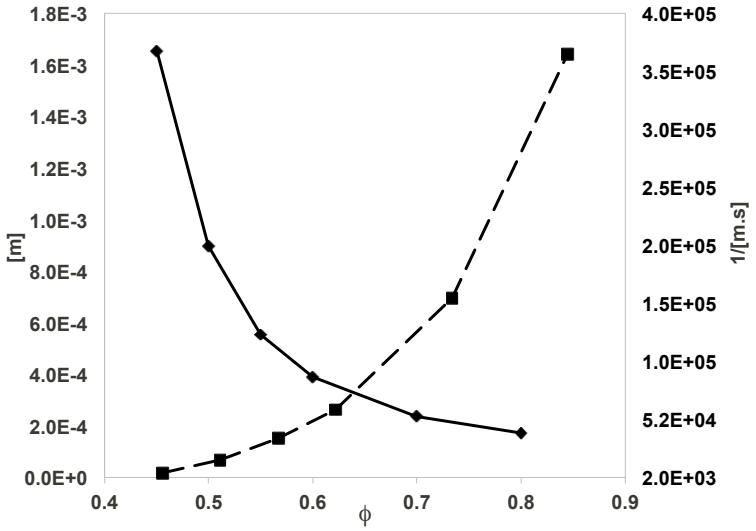

Figure 4-7: (left axis: solid line) Markstein length $\mathcal{L}$ tabulated in Table 4.1 and (right axis: dashed line) $\frac{d\kappa}{dn}$ from the simulations at various ϕ.

(a)

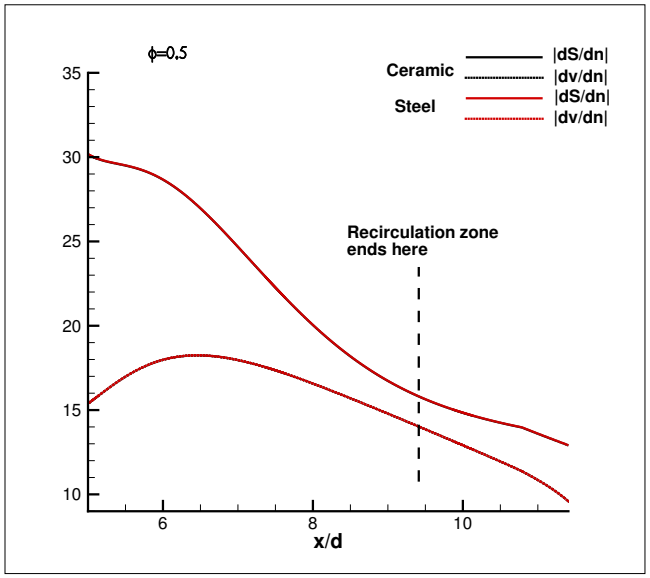

(b)

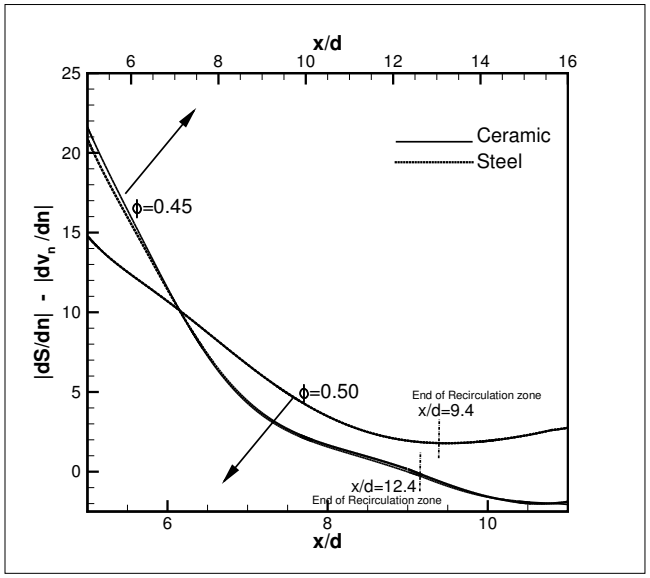

Figure 4-8: For steel and ceramic bluff-bodies, (a) $|\frac{dv_n}{dn}|$ and $|\frac{dS}{dn}|$ terms along the upstream reference location for $\phi = 0.5$ (b) the difference $|\frac{dS}{dn}| - |\frac{dv_n}{dn}|$ for the cases with $\phi = 0.45$ and $\phi = 0.5$.

for the ceramic bluff-body are reported; similar observations were also made for the the steel bluff-body. $|\frac{dS}{dn}|$ was estimated using the decomposition shown in Eq. 4.3. $\frac{dS}{d\kappa}$ is the Markstein length $\mathcal{L}$ (Table 4.1); $\frac{d\kappa}{dn}$ and $\frac{dv_n}{dn}$were directly estimated using the flow-field at the upstream reference location identified by the fixed 1% methane-consumption contour (discussed in Sec. 4.2.3). The flame stretch κ was computed using Eq. 4.8. Fig. 4-6 shows that when ϕ was reduced, $|\frac{dv_n}{dn}|$ and $|\frac{dS}{dn}|$ approached each other; thereby demonstrating that the dynamic stability criterion is the physical mechanism that governs blow-off in this configuration. The difference $(|\frac{dS}{dn}| - |\frac{dv_n}{dn}|)$ was observed to be 0.001 s^{-1} for $\phi = 0.45$. Figure 4-7 shows the following decomposed flame and flow components of the expression Eq. 4.3: (left axis) $\mathcal{L}$ and (right axis) $\frac{d\kappa}{dn}$. As ϕ was reduced; $\mathcal{L}$ increased and $\frac{d\kappa}{dn}$ decreased nonlinearly; however decreasing their product $|\frac{dS}{dn}|$. Both undergo significant variation with ϕ and thus form important pieces of the dynamic stability criterion.

I now investigate the observation of blow-off initiating at a downstream location, away from the bluff-body.Based on the dynamic stability criterion, shown above for a location just downstream of the recirculation zone, the flame blow-off is expected to occur at the location where the stability criterion is first expected to fail. Figure 4-8(a) shows $|\frac{dv_n}{dn}|$ and $|\frac{dS}{dn}|$ along the entire flame for the case with $\phi = 0.50$. The location where $|\frac{dv_n}{dn}|$ and $|\frac{dS}{dn}|$ were closest to each other was near the end of the recirculation zone. I plotted the difference $|\frac{dS}{dn}| - |\frac{dv_n}{dn}|$ in Fig. 4-8(b)[3] for $\phi = 0.45$ and $\phi = 0.50$. This plot also confirms that the dynamic stability criterion is closer to failure near the downstream region where the recirculation ends; showing that blow-off is expected to initiate at a downstream location with flame pinch-off. The part of the flame near the upstream anchoring zone strongly satisfied the dynamic stability criterion ($|\frac{dS}{dn}| - |\frac{dv_n}{dn}| > 0$); explaining the experimentally reported and numerically observed residual flame in Fig. 4-1 for a long period (few hundred ms) after blow-off. Figure 4-8 shows these results for the ceramic and metal bluff-bodies and will be discussed in detail in Section 4.2.5.

[3]The simulation domain downstream of the bluff-body was chosen to be much larger for $\phi = 0.45$ case because of the very long recirculation zone; thus separate x-axes were chosen for clarity

The case with $\phi = 0.45$ in Figure 4-8(b) shows that the dynamic stability criterion was violated for a part of the downstream region; the difference $((|\frac{dS}{dn}| - |\frac{dv_n}{dn}| < 0)$ was observed to be small. However, the numerical simulations did not show blow-off for this case. This can be attributed to the theoretical simplifications associated with the analytical expression used to compute $\mathcal{L}$ accurately. Despite that, Markstein's theory shows remarkable success in understanding the blow-off mechanism.

Figure 4-9 shows v_n, the flow speed normal to the upstream reference location, in the top half of the y-domain for the cases with $\phi = 0.45$ and (b) $\phi = 0.5$. For a stable flame, this is equal to the flame displacement speed S at that location. Its magnitude was observed to be higher at upstream locations for both cases because of the large negative stretch there (Fig. 4-4), consistent with Markstein's expression shown in Eq. 4.4. The flame speed decreased at downstream locations as the flame stretch weakened. These values also indicate that although the flame stretch is weak, it is significant enough to change the flame speed if it moves a small distance normal to itself, thereby playing a critical role in the dynamic stability criterion via the $|\frac{dS}{dn}|$ term.

On the basis of the results discussed above, we propose the following physical portrait of the blow-off mechanism, illustrated in Fig. 4-10. The flame downstream of the bluff-body moves to a location where its flame speed is equal to the normal flow speed (along the entire sheet). The dynamic stability criterion discussed above must be additionally satisfied along the entire flame. If this is the case, flame is stable. Otherwise, the flame will move to a different location; thereby changing the flame-normal flow speed and the associated stretch rate. Concomitantly, the flame speed will change. For the flame to be stable at this new location, again both criteria discussed above must be satisfied. This "adjustment" process will continue until the flame finds a stable location; otherwise it will blow-off. I showed the downstream section of the flame, near the downstream end of the recirculation zone, violates the criteria first resulting in pinch-off. The resulting upstream piece was relatively stable and persisted in the form of a residual flame for a long time before complete blowout.

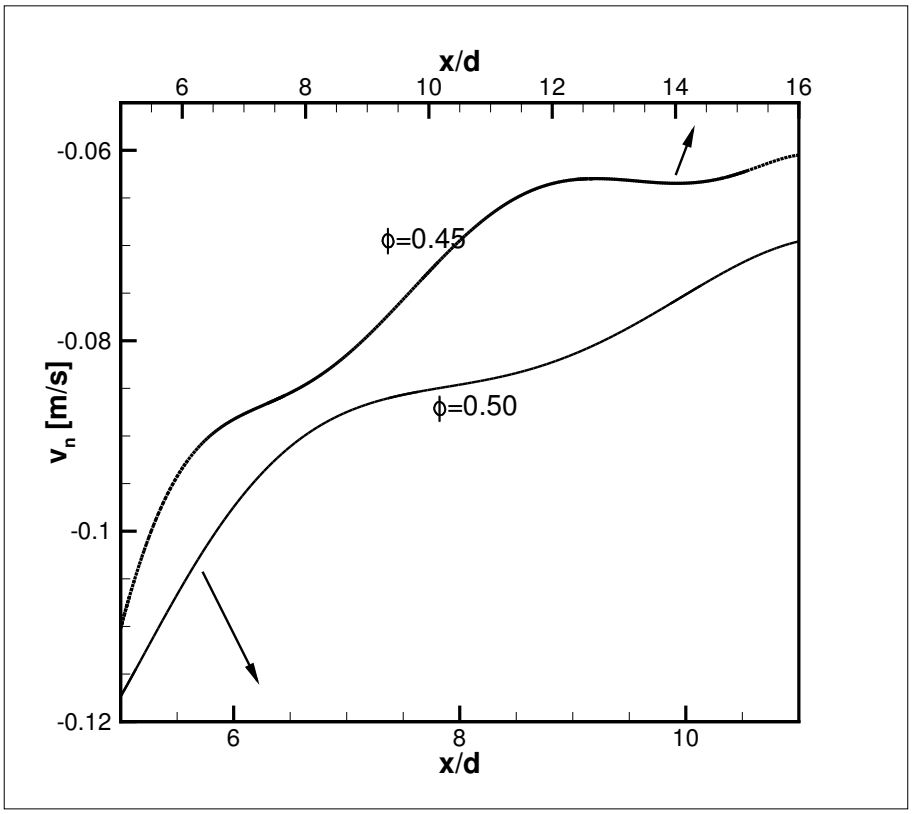

Figure 4-9: The variation of the flow speed, normal to the upstream reference location, along its non-dimensional streamwise x-co-ordinate for the cases (a) $\phi = 0.45$ and (b) $\phi = 0.5$.

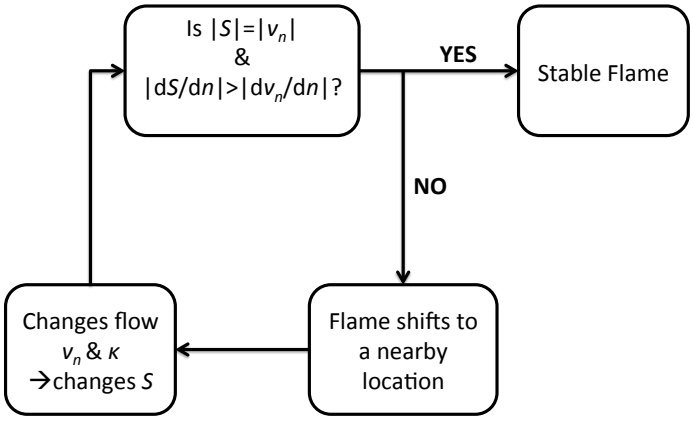

Figure 4-10: Proposed physical portrait of the blow-off mechanism.

4.2.5 The role of conjugate heat exchange on blow-off

Conjugate heat exchange between the reacting flow and the heat-conducting bluff-body is critical in determining the stable location or the anchoring point of the flame as shown in Chapter 3. However, its role in blow-off is still unclear and not explored in the literature. I checked the blow-off mechanism in the context of conjugate heat exchange with the bluff-body to investigate its impact on blow-off by simulating the steady laminar flame, close to the blow-off ϕ, for two different thermal properties of the bluff-body (i) corresponding to a ceramic material (used until now in this chapter) with $\rho_{fh} = 673$ kg/m^3, $c_{fh} = 840$ J/kgK and $\lambda_{fh} = 1.5$ W/mK ; and (ii) corresponding to a steel material with $\rho_{fh} = 8000$ kg/m^3, $c_{fh} = 503$ J/kgK and $\lambda_{fh} = 12.0$ W/mK. The flow-field was discussed in Figs. 3-8 and 3-9 in Chapter 3. The flame anchored at a relatively closer distance to the bluff-body for the ceramic case compared to the steel case. The average bluff-body temperature of the downstream face was approximately 20% higher for the ceramic case (789 K for the ceramic bluff-body and 662 K for the steel bluff-body). Its recirculation zone was observed to be slightly smaller than the steel case; downstream stagnation point was located at $x/d = 9.4$ for the former while at $x/d = 9.9$ for the latter.

Fig. 4-8 shows $|\frac{dv_n}{dn}|$ and $|\frac{dS}{dn}|$ along the flame for the two cases discussed above. The impact of the conjugate heat exchange on the dynamic stability balance is observed to be negligible. I observed flame blow-off at $\phi = 0.42$ and a steady-state flame at $\phi = 0.45$ for both the cases. Russi et al. [37] also showed that for relatively low inlet velocities (moderate $\mathbf{Re}_d$ flows), blow-off was independent of the flame holder temperature, but was dependent on it for very high $\mathbf{Re}_d$ flows. Their conjecture was that the heat flux to the flame holder may be small at these $\mathbf{Re}_d$ and thus did not impact blow-off. However, the heat flux was not small, as was quantitatively shown in Section 3.2.5. The downstream stretch field and thus the dynamic stability criterion along the flame is unchanged for the two thermal conductivities at the $\mathbf{Re}_d$ investigated in this chapter, thereby not changing the blow-off value.

4.2.6 Relationship to the Damköhler number correlation

Shanbhogue et al. [34] comprehensively reviewed the blow-off dynamics of the bluff-body stabilized flames at various Reynolds numbers. They compiled large experimental datasets on bluff-body blow-off from the literature and hypothesized that the Damköhler number correlations encapsulates the essential physical mechanism responsible for blow-off. The Damköhler number ($\mathbf{Da} = \tau_{flow}/\tau_{chem}$) is the ratio of the flow time-scale (τ_{flow}) to the chemical time scale (τ_{chem}). τ_{flow} was estimated by choosing a characteristic length scale: typically the bluff-body diameter [34] or the length of the recirculation zone [32] and characteristic velocity scale: typically the mean inlet velocity. To estimate τ_{chem}, three different time-scales were considered in [34]; the inverse of the extinction strain rate, blow-off residence time of a perfectly stirred reactor and unstretched laminar premixed time scale $\frac{\delta_T}{S_u^0}$ (ratio of flame thickness to the flame speed). Damköhler number based on each of these time scales definition correlated well with blow-off; with $\mathbf{Da} \sim O(1)$. The dynamic stability criterion discussed in Section 4.2.2 can be expressed as a balance between an inverse flow timescale: $|\frac{dv_n}{dn}|$ manifested in the form of inverse of the stretch and an inverse premixed flame timescale $|\frac{dS}{dn}|$. The results show that blow-off occurs when this time-scale ratio become $O(1)$, thereby demonstrating the physical basis of this widely reported correlation.

4.3 Conclusions

In this chapter, I investigated the blow-off mechanism of a confined bluff-body stabilized laminar methane/air premixed flame using the numerical method discussed in Chapter 2. Flame blow-off was simulated by fixing the incoming Reynolds number of the flow at 500 (based on the bluff-body diameter) and decreasing the mixture equivalence ratio. The stretch rate along the flame was strain dominated; the contribution of curvature was shown to be negligible. The flame was shown to be stable (does not undergo blow-off) when (1) the local flame displacement speed was equal to the flow speed, $|S| = |v_n|$ (static stability) and (2) the gradient of the flame displacement

speed normal to its surface was higher than the gradient of the flow speed along the same direction $|\frac{dS}{dn}| > |\frac{dv_n}{dn}|$ (dynamic stability). The difference between the former and the latter decreased as ϕ was reduced. $|\frac{dS}{dn}|$ was computed by decomposing it into a physico-chemical property $|\frac{dS}{d\kappa}|$ or the Markstein length and a flow property $|\frac{d\kappa}{dn}|$.

The flame blow-off started at a section of the flame where the dynamic stability criterion was first violated. This was shown to occur far downstream from the flame anchoring zone, near the end of the recirculation zone. The blow-off initiated by flame pinching at this location; separating it into an upstream moving section carried within the recirculation zone and a faster downstream convecting piece, detached from the recirculation zone. The experimentally reported "residual flame" was observed before the complete blow-off because the upstream section of the flame strongly satisfied the stability criterion, even though it was violated downstream. The mechanism based on this criterion explains the widely reported Damköhler number correlation for blow-off. Within the range of operating conditions investigated, the conjugate heat exchange had no impact on blow-off. However, I will show in Chapter 5 that it plays a critical role in the blow-off of perforated-plate stabilized premixed flame. In that chapter, I will also show that although the flame configuration is different than bluff-body flames, the dynamic stability criterion still governs the blow-off mechanism of those flames.

Chapter 5

Mechanism of laminar premixed flame stabilization and blow-off on a perforated-plate

5.1 Overview

The objective of this chapter is to investigate the flame stabilization mechanism and the conditions leading to the blow-off of a laminar premixed flame anchored downstream of a heat-conducting perforated-plate/multi-hole burner, with overall nearly adiabatic conditions. Results show a bell-shaped flame stabilizing above the burner plate hole, with a U-shaped section anchored between neighboring holes. The anchoring location is based on a combined impact of flame curvature and conjugate heat exchange with the perforated-plate. I simulate blowoff by maintaining a constant equivalence ratio and slowly increasing the incoming flow velocity of the premixed reactants. The dynamic stability criterion discussed for bluff-body flame blowoff shown in Chapter 4 is found to be the underlying mechanism for blowoff on perforated-plates also. As discussed in Chapter 4, for a stable flame, the gradient of the flame base displacement speed normal to the flame is higher than the gradient of the flow speed along the same direction, leading to dynamic stability. However, in this chapter, I will

show that unlike bluff-body flames, the blowoff is critically impacted by the conjugate heat exchange with the perforated-plate because blowoff initiates close to it.

5.2 Nomenclature

Roman

d	Thickness of the burner plate
D	Diameter of the inlet hole
K_B	Total stretch at the flame base
L_f	Total length of the typical bell-shaped flame
m_B	Mass burning flux at the flame base $= \rho_B S_B$
q_p	Heat flux at the burner plate at $z/D = 0$ and $r/D = 1$
r	Radial coordinate
S_B	Flame base displacement speed
S_c	Flame consumption speed
S_T	Flame tip displacement speed
t	Time
T_{ad}	Adiabatic flame temperature
$0.8 \times T_{ad}$	Temperature contour used to define the flame location
T_B	Flame base temperature
T_p	Temperature of the burner plate at $z/D = 0$ and $r/D = 1$
u	Streamwise velocity
U	Mean inlet velocity of the reactants far upstream
v	Radial velocity
$v_{r,B}$	Strain at the flame base; $\frac{1}{r}\frac{\partial(rv)}{\partial r}$
z	Streamwise coordinate

Greek

γ_B	Radius of curvature of the flame base

ρ_B	Density at the flame base
ψ_B	Flame stand-off distance above the burner plate
ψ_T	Location of the flame tip above the burner plate
ω	Volumetric heat release rate
ζ	Location of the stagnation point above the burner plate

5.3 Numerical Methodology

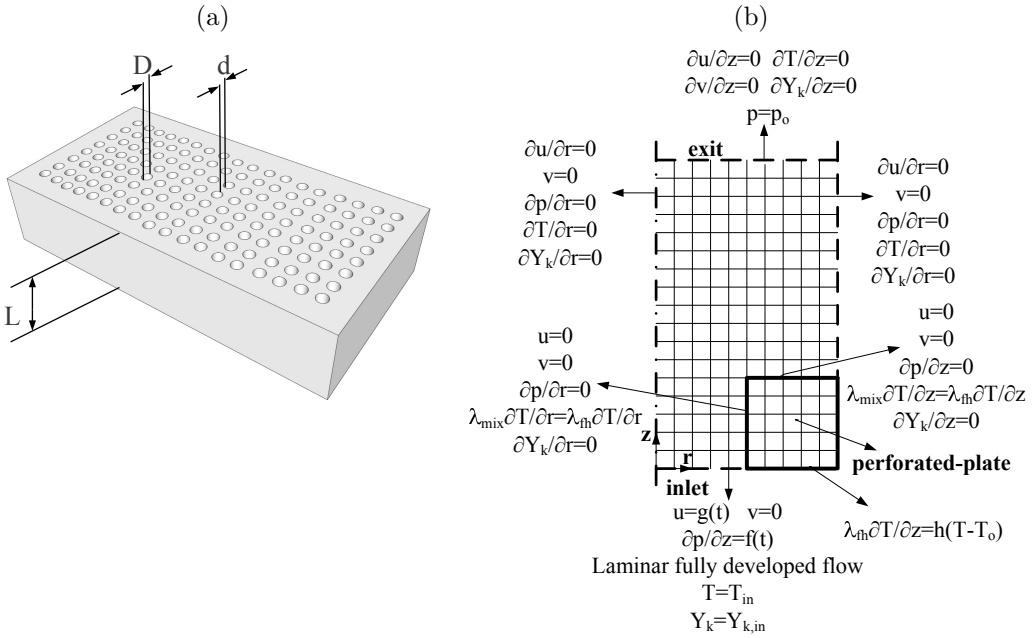

Figure 5-1: (a) Schematic diagram of a perforated-plate burner; and (b) Boundary conditions used for the two-dimensional computational domain..

I previously worked on the development of an axi-symmetric, time accurate, two-dimensional numerical simulation tool to study perforated-plate stabilized flames, incorporating detailed chemical kinetics and species transport mechanisms. This tool was discussed in my previous thesis [90]. In that, I also presented numerical investigations of the dynamic response of perforated-plate stabilized flames to inlet velocity perturbations . The semi-implicit operator-split projection method was used, similar to the numerical method discussed in Chapter 2. However, no adaptive mesh

refinement was employed; the code employs uniform structured grid with a staggered arrangement. SAMR was not required for these simulations (unlike the Bluff-body flames discussed in previous chapters) since the perforated-plate thickness is comparable to the flame thickness, keeping the domain size small enough to be fully resolved on a uniform grid. The low Mach number formulation of the reactive flow was used in radial coordinates, shown in [90]. The assumptions remain the same as in Chapter 2. Instead of using an immersed boundary formulation, the solid and the fluid domain were solved separately and the solutions were updated at each time-step in the form of boundary conditions. A detailed chemical kinetics mechanism with 20 species and 79 reactions for a methane-air mixture, described and validated in [91], is used. The calculation of the production rates of each species and the evaluation of the thermodynamic and transport properties are performed using Cantera [92]. Code validation, grid independence and time-step independence studies of the code are shown in [90]. The results presented in this chapter are obtained using this numerical tool developed in [90].

Figure 5-1b shows a schematic diagram of the computational domain at an arbitrary angular slice, illustrating the boundary conditions specified at each surface. Conduction heat exchange between the perforated-plate and the gas mixture is considered. Convective heat transfer is modeled at the bottom surface of the perforated-plate using a constant specified convective heat transfer coefficient, h; the impact of which can be ignored for small h and relatively long plates as noted in [91]. The gas temperature at the inlet is assumed to be uniform and at the free stream value ($T_o = T_{in} = 300\text{K}$). Symmetry boundary conditions are imposed at the centerline, $r = 0$. Adiabatic, impermeable, slip-wall boundary conditions are used at the right boundary in order to model the interaction between adjacent flames. At the exit, typical out-flow boundary conditions are used. The thermodynamic pressure, $p_o = 1\text{atm}$, is kept constant. The mean inlet velocity, U, is kept constant to simulate steady flames. The mixture composition at the inlet is steady and uniform and calculated based on the specified equivalence ratio of the reactant mixture. The pressure gradient, and the velocity profile at the inlet are calculated based on the the laminar, fully

developed flow assumption. They can be imposed as functions of time, t; however they are temporally independent in this investigation.

5.4 Results and Discussions

The following parameters are kept constant throughout the numerical simulations: the thickness of the plate or the distance between neighboring holes (see Fig. 5-1a), $d = 1$ mm; the diameter of the hole (see Fig. 5-1a), $D = 1$ mm; the distance between the top surface of the plate and the bottom surface/inlet section or the height of the plate, L =13.2 mm (see Fig. 5-1a); the distance between the top surface of the plate and the exit of the domain, L_d=15 mm; the inlet temperature, T_{in}= 300 K; the inlet Prandtl number of the mixture, Pr = 0.71; the equivalence ratio of the reactants at the inlet, $\phi = 0.75$; the burner plate density $\rho_{fh} = 2400$ kg/m^3; the burner plate specific heat $c_{fh} = 1070$ J/kgK; the thermal conductivity of the perforated-plate, $\lambda_{fh} = 1.5$ W/mK. The cell size in the flow direction is $\Delta z = 0.04$ mm, in the radial direction is $\Delta r = 0.02$ mm and the time step is $\Delta t = 0.9$ μs. The Lewis number based on the deficient reactant (methane for a lean methane-air mixture) is Le$\approx$ 1. Hence in my analysis, the preferential diffusion effects are not significant [93].

In my previous thesis work [90], I investigated the impact of the operating conditions and the perforated-plate design on the steady-state characteristics of lean premixed flames. I varied the equivalence ratio, the mean inlet velocity, the distance between the perforated-plate holes and the plate thermal conductivity. I observed that when the plate is modeled as adiabatic, i.e. when no heat exchange between the flame and the plate is allowed, a conical flame is anchored near the corner of the plate. However, when heat exchange between the burner plate and the flame is finite, a bell-shaped flame stabilizes at a stand-off distance above the burner plate. The flame stabilizes further downstream as the mean inlet velocity increases and/or the equivalence ratio decreases.

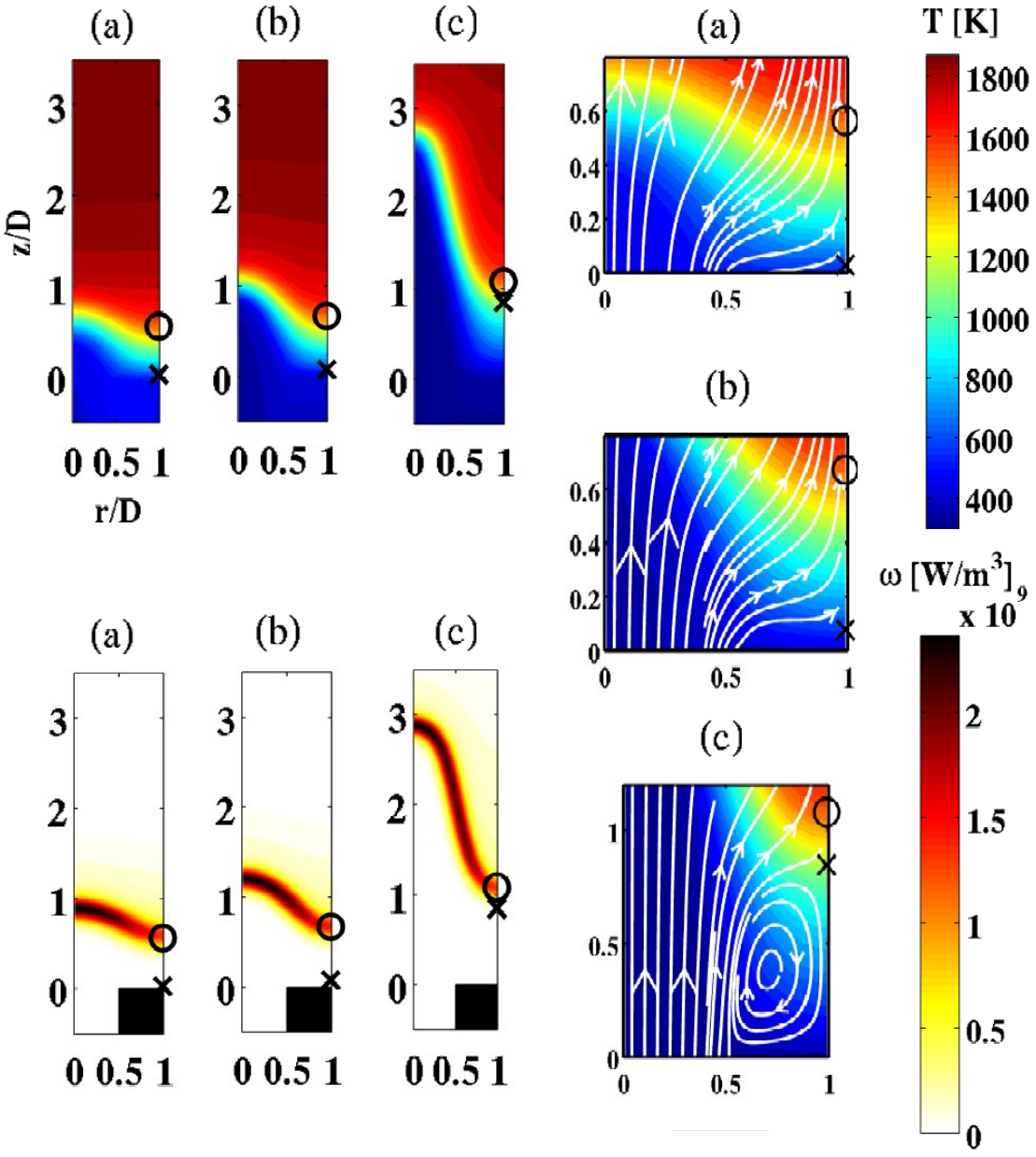

Figure 5-2: Contours of ω and T and the streamlines superimposed on T contours in the region close to the burner plate at (a) $U = 0.5$ m/s; (b) $U = 0.8$ m/s; and (c) $U = 2.0$ m/s. The corresponding locations of ζ and ψ_B are marked by $\times$ and o respectively.

5.4.1 The Stagnation Zone

Figure 5-2 shows contours of heat release rate, ω and temperature, T across the domain where finite values of the former are detected, and the streamlines superimposed on the T contours in the region close to the burner plate, for stable laminar flames at $U = 0.5$, 0.8 and 2.0 m/s. The corresponding locations of the stagnation point, ζ and the flame stand-off distance, ψ_B are marked by $\times$ and o, respectively. Only part of the computational domain is shown in these plots. The typical bell-shaped flame above the hole is observed with a negatively curved flame tip, positively curved flame base above the plate and weakly curved flame wing in between. The flame stabilizes just above the recirculation zone in a low velocity region, where the flow velocity recovers to small positive values downstream of the stagnation point. Because of the presence of the stagnation zone, the flame base is located at a finite stand-off distance, ψ_B, above the burner plate. As U increases, the recirculation zone grows and stagnation point moves downstream forcing the flame stabilization point to move downstream or ψ_B to increase. Meanwhile, as shown in the figure, the flame base moves closer to the stagnation point. The stagnation point lies inside the flame thickness at the higher velocity values. The flame moves away from the plate as U increases, lowering heat loss to the burner plate. Heat lost to the plate top-side is significant, and it is recirculated back to the reactants from the burner side along the hole in the perforated plate in this almost adiabatic system (the overall problem is nearly adiabatic because of a high L/D plate used here and the heat loss from the lower side is found to be negligible).

The top of the burner plate is located at $z/D = 0$ and $0.5 < r/D < 1$. In the following discussions, I focus on the results along the symmetry axis above the burner plate $z/D \geq 0; r/D = 1$, unless otherwise noted. This is because my primary interest is to examine the stabilization of the flame base downstream of the plate. Along this streamwise direction, the flame is always normal to the flow because a symmetry boundary condition is enforced. I examine the change in the flame location and structure along this line as the inlet velocity changes.

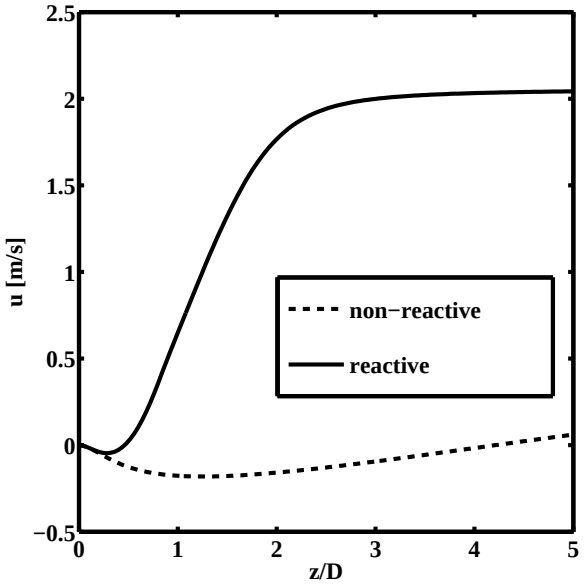

Figure 5-3: Streamwise velocity at $r/D = 1$ along z/D for reactive flow and non-reactive flow at $U = 1.3$ m/s.

It is widely established experimentally and numerically that the presence of a flame significantly reduces the size of the recirculation region as compared to a non-reacting flow [40, 46, 47, 91]. Figure 5-3 shows that my results capture this trend. Under non-reactive conditions, the recirculation zone covers the range $0 < z/D < 4.3$. For identical inlet flow conditions, but in the presence of exothermic chemical reactions, the extent of the recirculation zone is significantly reduced to $0 < z/D < 0.5$. The slow recovery of the velocity beyond the stagnation point in the cold flow case as compared to the case of the reactive flow where significant acceleration is observed must be noted. Downstream of the flame zone, velocities are different because of the thermal expansion in the reactive flow case.

Flame front definition

Within the reaction-diffusion zone of the flame, there is a significant change in the streamwise velocity because of the flow recovery after the stagnation point, besides the usual change in the density across the flame (thermal expansion). Because of

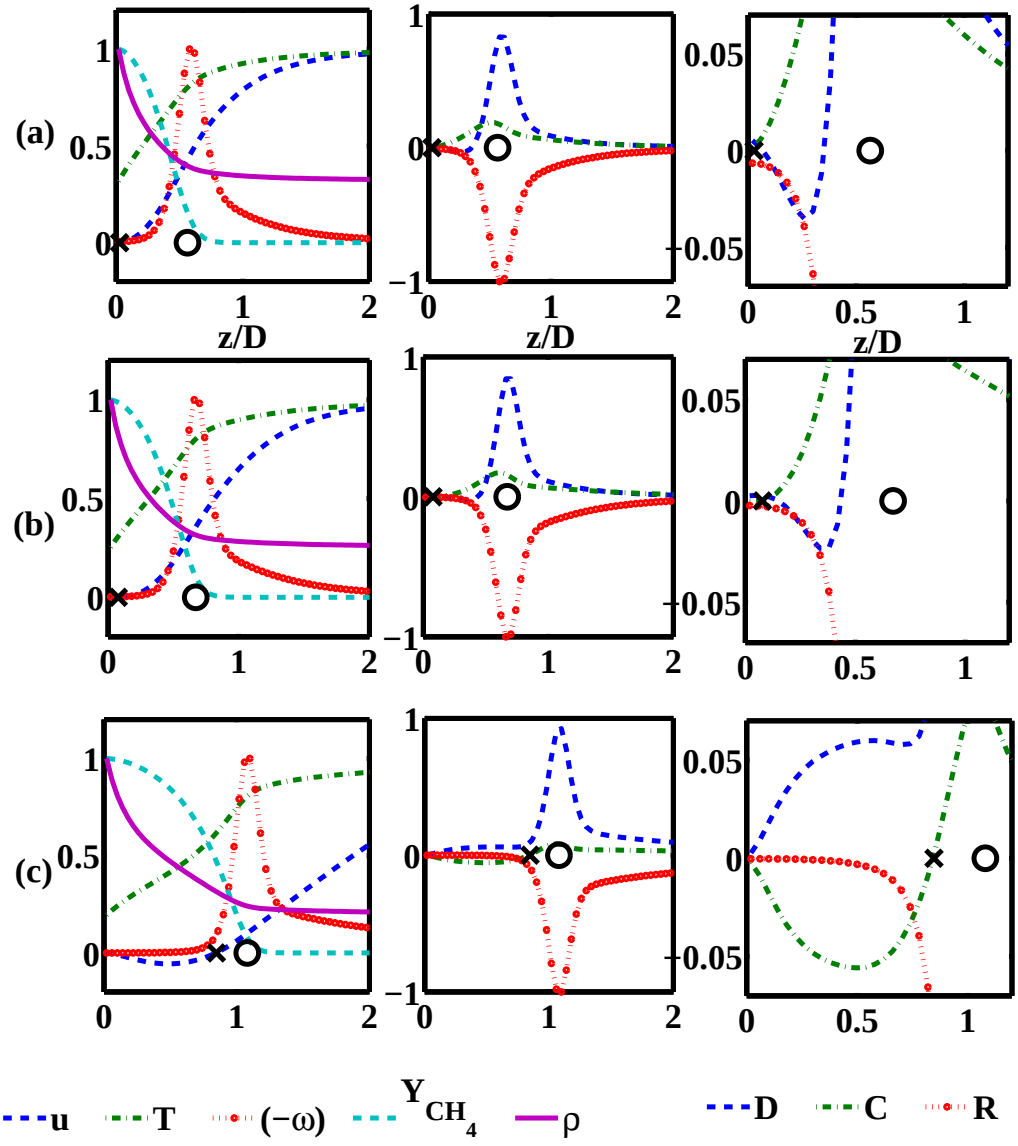

Figure 5-4: Column 1 and Column 3: The net convection, net diffusion and reaction rates from the energy equation normalized with respect to ω_{max}; Column 2: the streamwise velocity profile and the different scalar profiles normalized with respect to their respective maximum for (a) $U = 0.5$ m/s; (b) $U = 0.8$ m/s; and (c) $U = 2.0$ m/s.The corresponding locations of ζ and ψ_B are marked by $\times$ and o respectively; $r/D = 1$; D =Diffusion, C=Convection, R=Reaction.

that, definitions of a flame location and a single flame displacement speed are not obvious. There are multiple ways to define them (see Poinsot and Veynante [94]). I define the location where $T \approx 0.8 \times T_{ad}$ as the flame base location and the flow speed at this location as the flame displacement speed, S_B. The T plots in Fig. 5-4 show that this is a reasonable location near which maximum burning occurs or ω peaks, for all the different values of U. Other definitions used in literature, such as the location where 95% of methane is consumed, correspond very closely to this location, as can be seen in Fig. 5-4.

Fame base structure

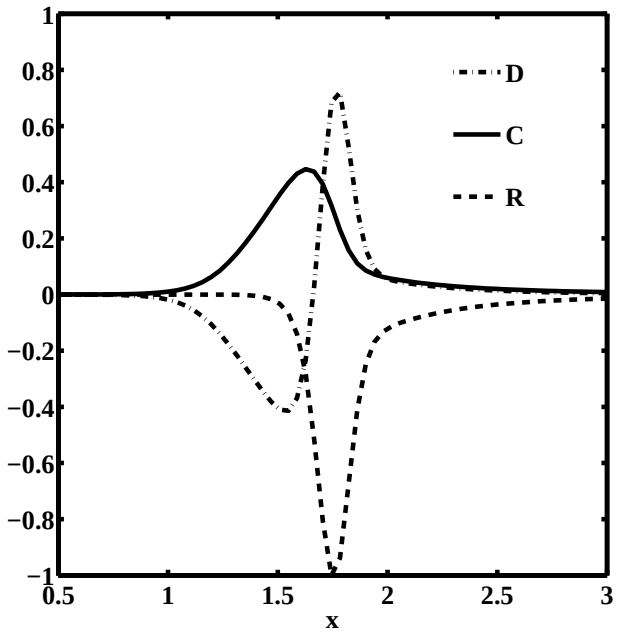

Figure 5-5: The net convection, net diffusion and reaction rates from the energy equation normalized with respect to ω_{max} for an unstrained one-dimensional flame; D =Diffusion, C=Convection, R=Reaction.

The net convection, net diffusion and local reaction rates, estimated by evaluating the corresponding terms in the energy equation, the streamwise velocity profile and some scalar profiles are shown in Fig. 5-4 for three inlet velocities. The net convection

and diffusion rates are normalized with respect to the maximum volumetric heat release rate (ω_{max}) along the symmetry axis. The velocity profile and the different scalar profiles are normalized with respect to their respective maximum values on the symmetry axis. The corresponding locations of ζ and ψ_B are marked by $\times$ and o respectively. The recirculation zone is almost absent for $U = 0.5$ m/s and is very small for $U = 0.8$ m/s case, but is significant in the case of $U = 2$ m/s. Moreover, while the stagnation point is outside the flame-temperature thickness at low velocity, it is located well within this thickness at higher velocity. On the other hand, the stagnation point is essentially outside the reaction zone in all cases. The figures also show that the flame stand-off distance, defined as the point where $T \approx 0.8 \times T_{ad}$ (where T_{ad} is the adiabatic flame temperature) also coincides with the point of maximum reaction rate, showing that this is a reasonable surrogate for the flame.

There is a diffusion-reaction-convection balance near the stagnation point. On the other hand, near the flame location, there is a strong reaction-diffusion balance, as seen in conventional flames. At $U = 2.0$ m/s case, the size of the recirculation region is significant. Moreover, a convection-diffusion balance is established in this recirculation region with negative streamwise velocities and an overall positive diffusion rate due to the positive diffusion of energy by the diffusing species in the recirculation region, although there is a negative diffusion associated with upstream conduction. The flame region is again characterized by a reaction-diffusion balance. In all cases, there is a significant change in the flow velocity within the reaction-diffusion region. For comparison, a similar plot of the net convection, net diffusion and reaction rates normalized with respect to the maximum volumetric heat release rate or reaction rate (ω_{max}) in the one-dimensional unstrained planar flame ($\phi = 0.75$) is shown in Fig. 5-5. Such flames are characterized by a distinct convection-diffusion preheat zone and a reaction-diffusion flame zone downstream. It is interesting to note that Fig. 5-4c and Fig. 5-5 are different with respect to the opposite signs and lower magnitudes of convection and diffusion in the upstream zone. Results in Fig. 5-4 also emphasize my conclusion that, while stabilizing in an accelerating flow, the flame moves closer to the stagnation point at higher velocity, where the flow velocity is significantly lower.

5.4.2 The non-monotonic flame displacement speed

The flame base has the lowest displacement speed along the bell-shaped flame stabilized on perforated-plate burners; this can easily be deduced from Fig. 5-2. The ability of the positively curved flame base to sustain steady combustion determines where the flame is anchored and whether a stable equilibrium can be established, that is the overall stability of the flame. It must be noted that the flame base characteristics depend on the overall shape of the flame. For a systematic analysis of flame stabilization and to understand the sequence of events leading to eventual blow-off downstream of the perforated plate, I start with a steady-state numerical solution at a low mean inlet velocity. The equivalence ratio is fixed at $\phi = 0.75$, as well as all the other conditions except for the inlet velocity. I then incrementally increase U to obtain the next steady-state solution, until the flame is no longer able to stabilize on the burner and blows out. The flame shapes obtained using this procedure are shown in Fig. 5-6a, for different values of U, shown on their corresponding flame shape. Overall, the flame shape maintains the same structure of a base-wing-tip.

Figure 5-6b shows the variation of the mass burning flux at the flame base (or the density weighted displacement speed), $m_B = \rho_B S_B$ with U until blow-off occurs, where ρ_B is the density at the flame base just ahead of the point of $0.8 \times T_{ad}$ and S_B is the flame displacement speed at the same point. Fig. 5-6b shows that the value of ρ_B decreases slightly, but the trends of m_B and S_B are the same. Both undergo a maximum as U increases and then decrease, with the former starting out at ≈ 0.075, growing rapidly to ≈ 0.1; then decreasing gradually back to ≈ 0.07 at higher velocities. The three cases of U chosen in Figs. 5-2 and 5-4 correspond to: (a) the smallest value of U I used in the simulations, 0.5 m/s; (b) the value of U where m_B (and correspondingly S_B) peaks, 0.8 m/s; and (c) the maximum value of U before blowoff occurs, 2.0 m/s. The corresponding unstretched adiabatic values of the laminar flame speed $S^o = 0.21$ m/s and the mass burning flux $m^o = 0.045$ kg/m^{2}s for a one-dimensional methane-air premixed flame at $\phi = 0.75$. Note that the value of S^o is less than the values of S_B because of the definition of the flame front in the

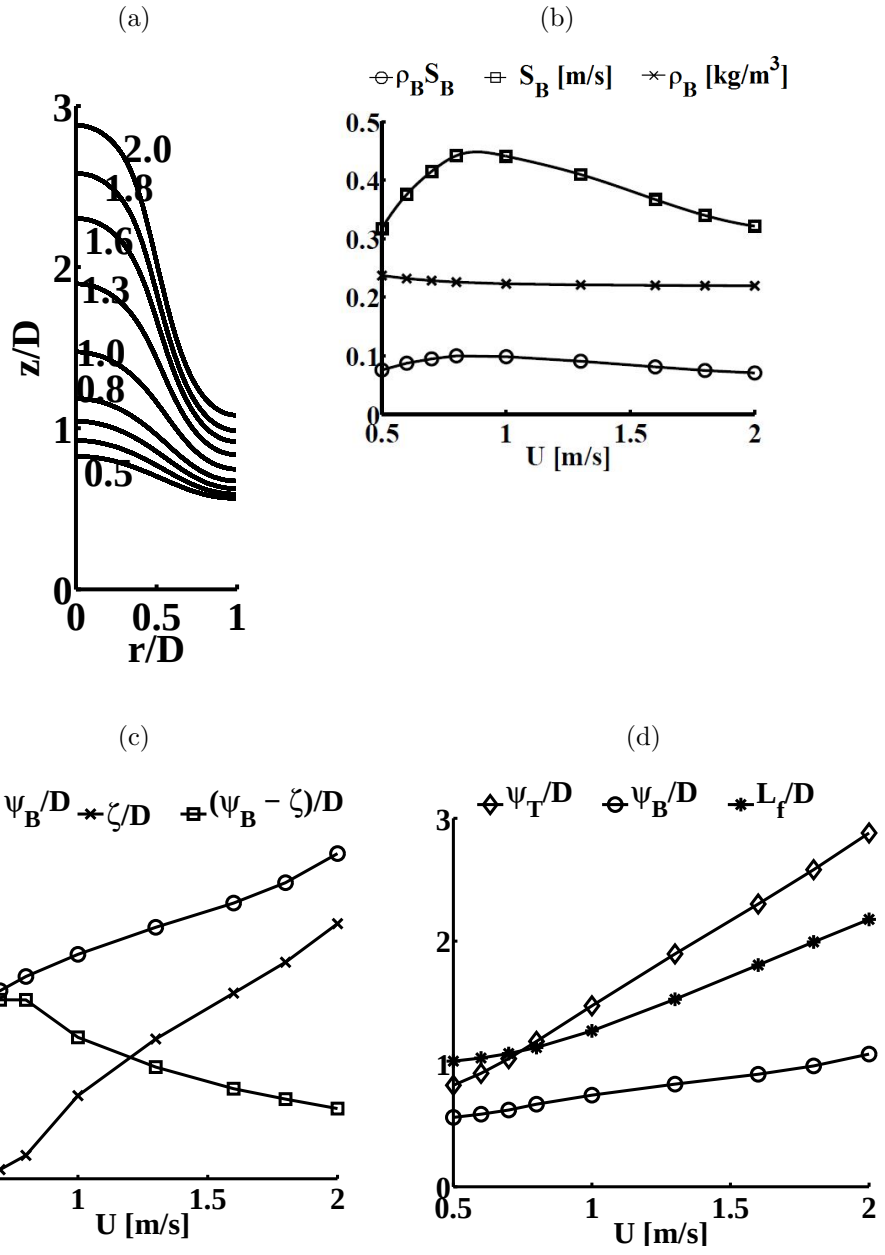

Figure 5-6: (a) The steady-state flame shape for $U = 0.5 - 2.0$ m/s (b) Density, flame displacement speed and density weighted flame displacement speed at the flame base (c) Normalized flame base stand-off distance, the distance of the stagnation point and relative location of the flame base from the stagnation point (d) Normalized flame base stand-off distance, distance of the flame tip and the length of the bell-shaped flame L_f.

stagnation zone used in this chapter, as described in Section 5.4.1.

Figure 5-6c shows that both ψ_B and ζ increase with U. The recirculation zone size (ζ) is a 'flow effect ', that is, its size is determined by the reactive flow dynamics. Although its absolute size is reduced in the presence of a flame as compared to a non-reactive flow, it monotonically increases with increasing U. For low values of U, the figure shows that the recirculation zone almost vanishes. The stand-off distance results from a combined effect of the flow (recirculation zone size) and combustion (flame structure and associated displacement speed). It increases monotonically with U, as ζ increases and the combustion characteristics change. However, the relative location of the flame base with respect to the stagnation point is not a monotonic function of U. Initially, at low inlet velocity and when the recirculation zone length is almost zero, the stand-off distance and the relative location of the flame base with respect to the stagnation point increase with U. However, as the recirculation zone starts to grow, the flame moves closer to the stagnation point. I will show that while the growth of the recirculation zone reduces the heat loss, the flame base radius of curvature decreases and hence the flame displacement speed is reduced. The reduction of the displacement speed explains the non-monotonic behavior of m_B. A field visualization of these distances can be seen in Fig. 5-2 where $\times$ and o are used to mark ζ and ψ_B respectively.

Figure 5-6d shows that similar to ψ_B, ψ_T monotonically increases with U (ψ_T is the distance of the flame tip). Moreover, the total length of the flame from the flame base to the flame tip, L_f, grows with U to accommodate the extra mass flow of reactants. However, L_f does not grow linearly with U because the flame displacement speed changes along the length of the flame due to stretch. Hence the slopes of L_f, ψ_B and ψ_T curves are different.

The non-monotonic behavior of the flame displacement speed, as I will show, is a result of competing impacts of the flame base curvature and the heat loss to the burner.

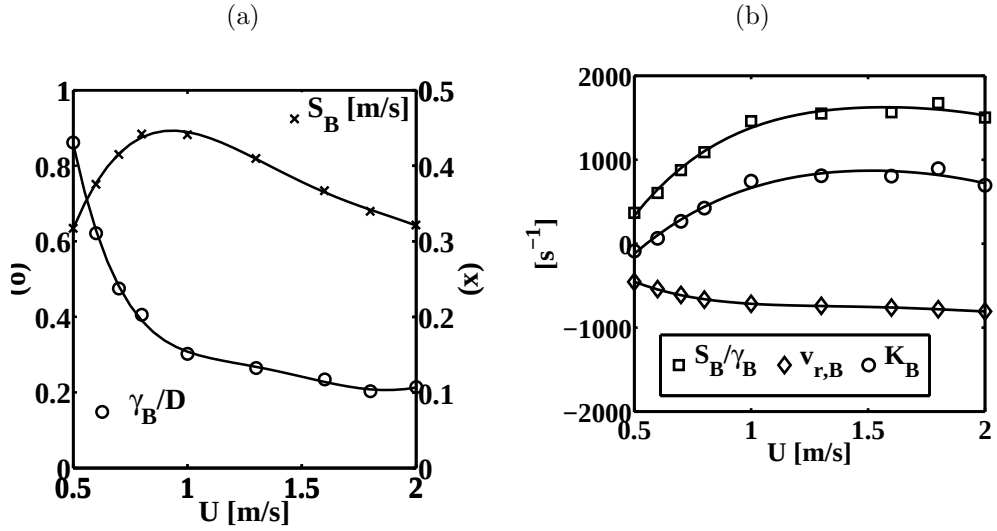

Figure 5-7: (a) Normalized radius of curvature of the flame base and flame base displacement speed (b) Curvature induced stretch (S_B/γ_B), strain induced stretch ($v_{r,B}$) and the total stretch ($K_B = S_B/\gamma_B - v_{r,B}$) at the flame base.

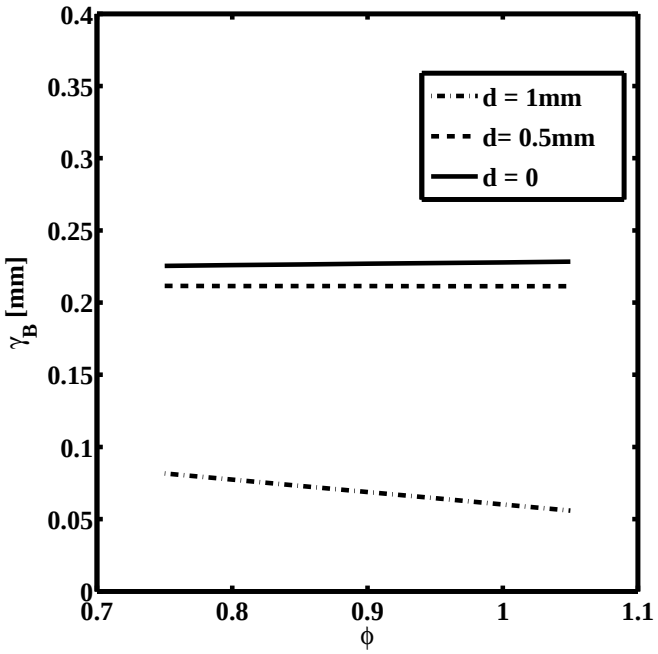

Figure 5-8: Experimentally determined critical flame base radius of curvature just before blow-off for inverted methane/air flames at different stabilization plate thicknesses (see Fig. 1-2b) and equivalence ratios. Data from Ref. [39]. $d = 0$ corresponds to a very sharp edge.

The role of flame base curvature

Figure 5-7a shows that the normalized flame base radius of curvature, γ_B/D, decreases as U increases (also seen qualitatively in Fig. 5-6a). Note that γ_B decreases because the flame length L_f grows to accommodate a higher reactant mass flow rate and hence it can be considered as a kinematic effect. Choi and Puri [95] studied the response of the flame to strain and curvature induced stretch using inverted methane-air and propane-air flames stabilized on thin ceramic rods, and concluded that positive/negative curvature decreases/increases the flame displacement speed. This trend is also well established in the literature [46, 47, 96] for curved flames in various configurations. At higher U, smaller positive radius of curvature of concave (towards products) flames lowers the flame displacement speed as shown in Fig. 5-7a. As the displacement speed decreases, the flame moves closer to the stagnation point until it finds an equilibrium position where the flow speed equals the flame displacement speed.

The geometry of the problem establishes conditions in which γ_B is comparable to the thickness of the flame at its base, this is especially true at large U. In this range, γ_B approaches a critical value, which is constant near blow-off. I discuss flame blowoff in detail in Section 5.4.3. It is for this reason that Kawamura et al. [39, 46] experimentally observed a strong relation between blowoff and the flame curvature. For methane/air flames at $0.7 < \phi < 1.1$, Kawamura et al. reported a blowoff radius of curvature of $0.1 < \gamma_B < 0.2$ mm, see Fig. 5-8. The numerical value of the critical radius of curvature is in the same range. Mikolaitis [97] showed analytically that there exists a minimum radius of curvature for strongly curved concave (towards products) premixed flames; below which a flame can not survive. Similar remarks on a limiting flame curvature were also made by Echekki and Mungal [98] and Poinsot et al. [99] in the context of flame displacement speed measurements at the negatively curved flame tip on a cylindrical slot burner. They interpret the existence of a critical radius of curvature on the grounds that the flame thickness cannot exceed the value of a radius of curvature. The limiting radius of curvature for their flame tip was 0.36 mm, which is in the same range as our numerical value. For the perforated-plate burner, this value

depends strongly on the equivalence ratio, geometry of the burner as determined by its height and the distance between neighboring holes, and its thermal conductivity.

Flame curvature, flow non-uniformity (strain) and unsteady flame motion together determine the stretch imposed on a flame. Under steady conditions analyzed here, the total stretch at the flame base is characterized by $K_B = S_B/\gamma_B - v_{r,B}$, (see [47]) where S_B/γ_B is the contribution of the flame base curvature and $v_{r,B} = \frac{1}{r}\frac{\partial(rv)}{\partial r}$ is the contribution of the strain at the flame base. Figure 5-7b shows the two individual contributions at the flame base for different values of U. The curvature and strain make opposite contributions to the flame stretch for this concave premixed flame established in an accelerating flow downstream of the stagnation point. The contribution of the strain is relatively small compared to that of the curvature at large U and hence near blow-off. Also note that at lower values of U, K_B is small and thus flame stretch does not significantly impact the flame displacement speed, although the impact of heat transfer is significant.

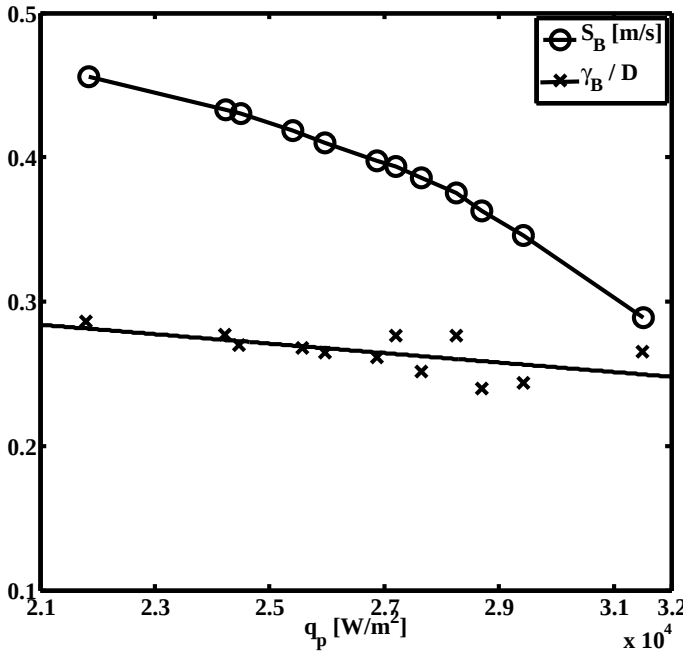

Figure 5-9: Impact of the upstream heat loss to the burner plate, q_p, on the laminar flame displacement speed, S_B at an almost constant flame base curvature. U = 1.3m/s and the thermal conductivity of the burner plate is varied between 0.1W/mK - 50W/mK to vary q_p.

The role of heat loss to the burner plate

Individual impact of the heat loss to the burner plate on the flame displacement speed is demonstrated in Fig. 5-9. It shows that, at an almost fixed value of curvature, heat loss to the burner plate reduces the flame displacement speed. To maintain the curvature constant, the mean inlet velocity was fixed at $U = 1.3$m/s. The thermal conductivity of the burner plate was varied resulting in different standoff distances and hence different heat loss to the plate. The increasing slope of the curve as q_p is raised shows that the impact of heat loss on the flame displacement speed increases as q_p grows. This result, as will shown in Section 5.4.3, is crucial in understanding the dynamic stability mechanism for blowoff, contrary to many of the observations in the literature. It must me noted that approximately 50% increase in q_p reduces S_B by 38% whereas the variation in the curvature was less than 8%. While the curvature exhibits weak dependence on q_p, the impact of heat loss to the plate on S_B is much stronger.

Figure 5-10a shows that as U is raised, the flame stabilizes further away from the burner plate decreasing its temperature and reducing the heat loss to the burner plate. Furthermore, as the flame moves downstream, Fig. 5-10b shows that the flame temperature at the base, T_B, and the maximum volumetric heat release rate, ω_{max} grow as the heat loss is lowered. Thus, at lower U, when the impact of weak flame stretch is not significant, higher heat loss to the burner plate lowers the flame displacement speed. This is contrary to the cases at higher U, where the impact of flame stretch is stronger. This explains the non-monotonic behavior of S_B.

Flame base consumption speed and the displacement speed

The consumption speed of a flame is related to the integral of the volumetric heat release rate. Figure 5-10c shows that the flame base consumption speed, S_c, increases when U is raised, unlike the non-monotonic trend observed for the displacement speed, S_B. I use the following definition of the flame consumption speed at the flame base, S_c, which is obtained by integrating the energy equation across the flame, above the

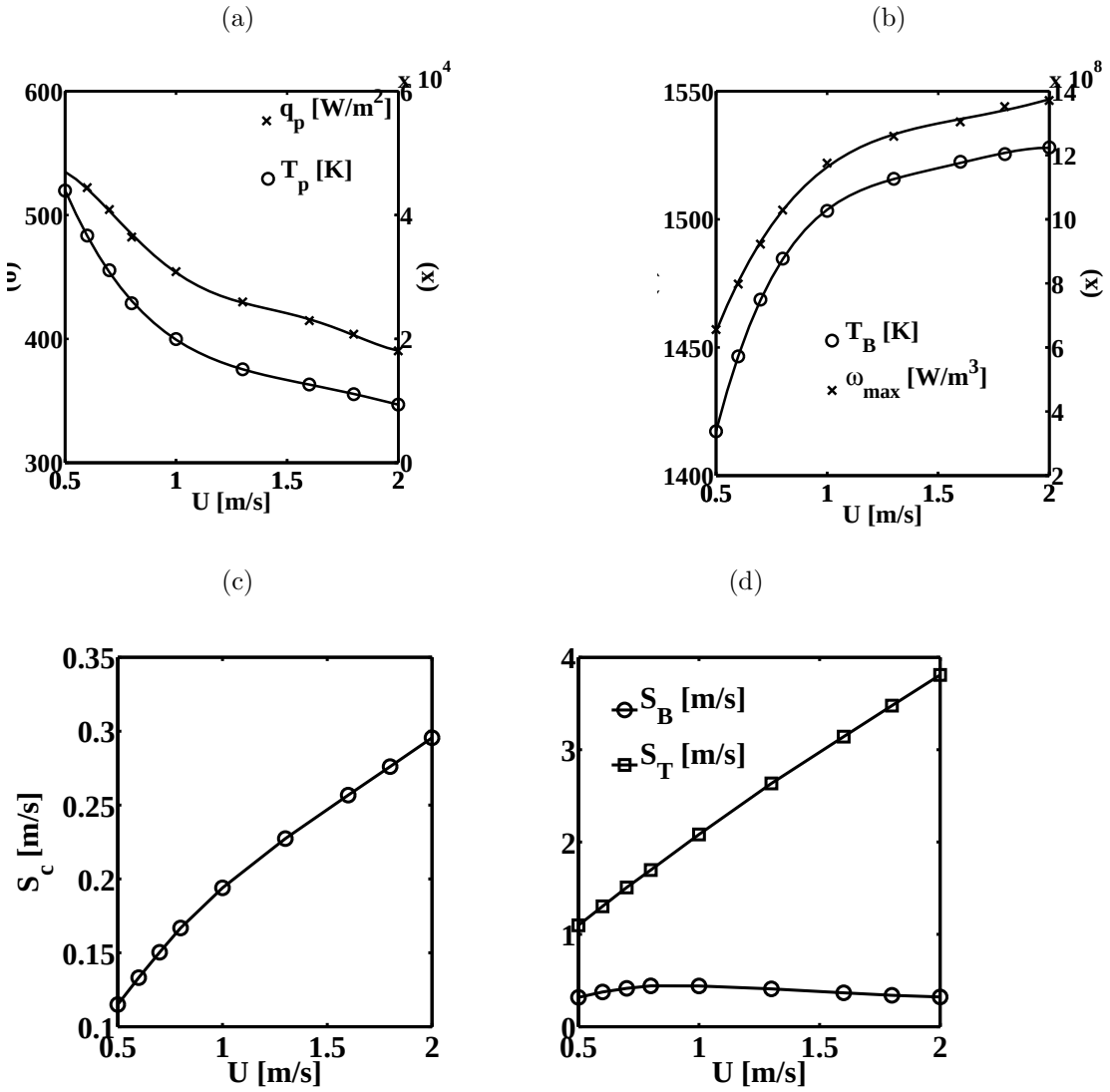

Figure 5-10: (a) Temperature and the heat flux at the burner plate at $z/D = 0$ and $r/D = 1$; (b) Temperature at the flame base and the maximum volumetric heat release rate along $z/D = 1$; (c) Consumption speed of the flame base; (d) Displacement speed of the flame base and the flame tip for $U = 0.5 - 2.0$ m/s.

burner plate, along $r/D = 1$

$$S_c = \frac{\int_0^\infty \omega/c_p \; dz}{\rho_u \left(T_b - T_u\right)} \tag{5.1}$$

where ρ_u is the unburned mixture density, T_u and T_b are the unburned and burned temperature, respectively. For reference, the corresponding unstretched adiabatic flame consumption speed of a one-dimensional methane-air premixed flame at $\phi = 0.75$ is $S_c^o = 0.29$m/s. Note that the adiabatic flame displacement speed and the adiabatic flame consumption speed of an unstretched one-dimensional premixed flame are equal. Poinsot et al. [99] noted that for near-unity Lewis numbers, only chemical mechanisms (related to the reaction zone structure) modify the flame consumption speed, while combined chemical, hydrodynamic and diffusive mechanisms (related to the aerodynamics of the flow) modify the flame displacement speed. With increasing U, as the flame moves away from the burner, lower heat loss to the burner plate raises the flame temperature and the reaction rate (chemical mechanism). This enhances both the flame displacement speed and the consumption speed. However, since curvature does not impact the flame consumption speed, S_c continues to grow monotonically, whereas curvature dominates S_B decreasing its value. Thus, within the range of conditions investigated here, the chemical mechanism does not play a significant role in the modification of the displacement speed as compared to the hydrodynamic and diffusive mechanisms.

Figure 5-10d shows the changes in the displacement speed of the flame tip and the flame base as U is increased. The shape of the flame base depends on the response of the overall flame to the flow-field on the reactants side. But at higher U, S_T increases whereas S_B decreases with increasing U. Because of that, the tendency of the flame tip to move upstream whereas the tendency of the base to move downstream or to blow-off increases with growing U. Thus it is concluded that the stabilization and blowoff are more critically dependent on the local events at the flame base rather than the flame tip, even though the flame base structure depends on the overall flame shape to a certain extent.

Mallens et al. [47] reported constant values of m_B for all inlet velocities until

blow-off occurs. Based on this observation, they concluded that despite of its presence, flame curvature plays no role in flame blowoff, contrary to the conclusions of Kawamura et al. [39, 46]. Mallens et al. postulated that the streamtube contraction (fluid dynamic effect) of the strain influences the stabilization mechanism and not the change in flame displacement speed due to net stretch. Results reported by Mallens et al. could not be explained using the theory of stretched flames in which the flame displacement speed undergoes significant changes in the presence of curvature induced stretch [93, 95, 100, 101]. My results, which are based on a model that incorporates detailed chemical kinetics and heat exchange between the flame and the plate, show that m_B varies with U, following the changes in S_B although the percentage change is not as high. Moreover, I show that the flame base curvature contributes significantly to its stretch and hence to S_B.

To summarize, I propose the following scenario for flame stabilization on a perforated plate. In the lower range of U, as U increases, ζ grows slowly while remaining very small, q_p and T_p decrease, resulting in stronger flame, higher T_B and higher values of S_B, and the flame finds an equilibrium position further downstream of the stagnation point where the flow velocity is relatively high. On the other hand, in the higher range of U, as U increases, ζ increases more readily and hence decreasing the heat loss to the plate, γ_B decreases to accommodate the growing flame length and decreasing S_B, hence moving the flame closer to the stagnation point. These two competing effects at low and high values of U result in the observed non-monotonic behavior of S_B. A stronger/weaker flame with higher/lower S_B stabilizes away from/closer to the stagnation point.

5.4.3 Blowoff

As U increases, the reduction of the displacement speed associated with the increasing curvature does not continue forever. Instead, at a critical radius of curvature, the flame moves downstream continuously, i.e. blow-off occurs. Blowoff is a critical phenomenon, like flashback and quenching, that occur when a certain condition is satisfied. I illustrate this condition in the next section.

Dynamic stability mechanism

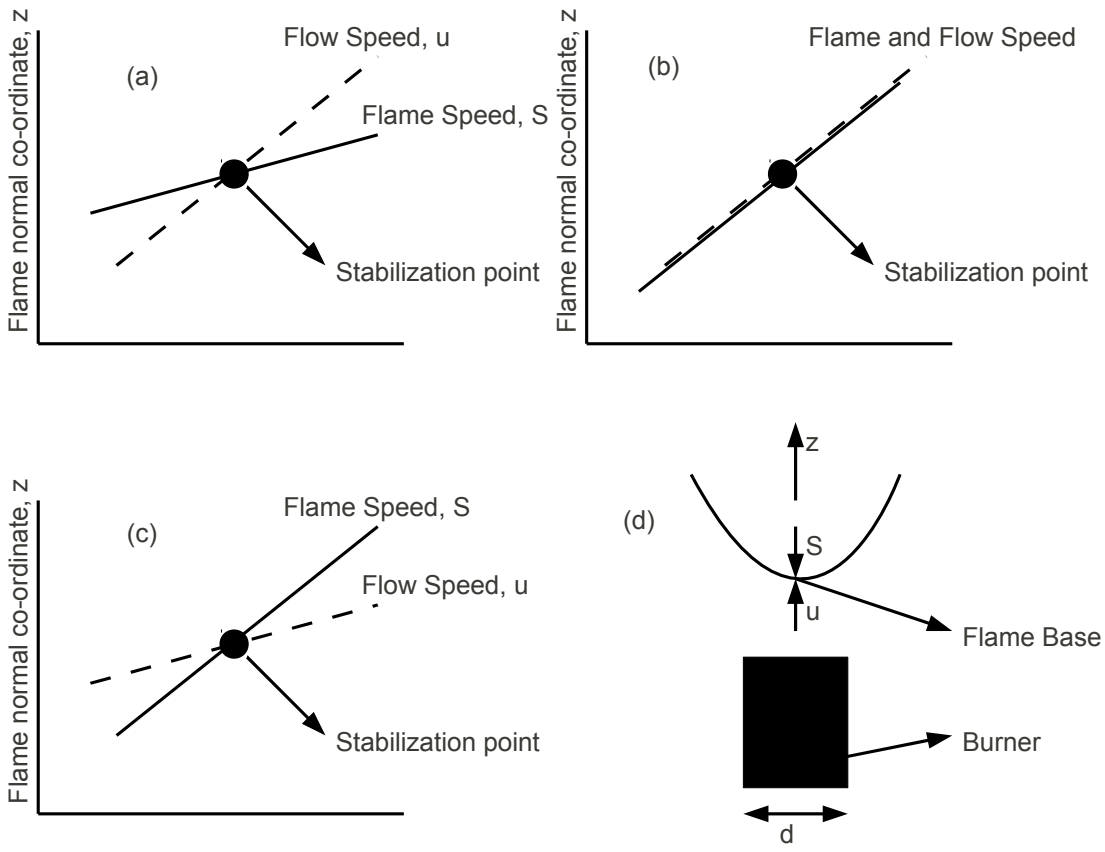

Figure 5-11: Mechanism for dynamic stability at the flame base. (a) Stable case, $S_B = u_B$ and $\frac{dS_B}{dz} > (\frac{du}{dz})_B$; (b) Critical case for blow-off, $S_B = u_B$ and $\frac{dS_B}{dz} = (\frac{du}{dz})_B$; (c) Unstable case, $S_B = u_B$ and $\frac{dS_B}{dz} < (\frac{du}{dz})_B$; and (d) Schematic diagram of a U-shaped flame base downstream of the plate of thickness d.

For a stable flame, its displacement speed at every point must be equal to the flow velocity normal to the flame. At the flame base $S_B = u_B$. However, this is a necessary but not a sufficient condition for flame stabilization. For dynamic stability, an additional condition that $\frac{dS_B}{dz} > (\frac{du}{dz})_B$ must also be satisfied. This was discussed in the context of bluff-body flames in Chapter 4. Note that the z co-ordinate is normal to the flame base. This hypothesis was proposed in [46] but no experimental or alternate evidence was provided. Further, although the role of curvature was highlighted in [46], the simultaneous role of heat loss was ignored. Figure 5-11 shows a schematic diagram illustrating this condition for dynamic stability at the flame base. For all the three

cases in the figure, $S_B = u_B$ but the relative magnitude of the velocity gradient and the displacement speed gradient change. At a fixed U, $\frac{dS_B}{dz} > 0$ is always true for a stable flame because of the impact of heat loss to the burner plate on S_B (higher/lower heat loss decreases/increases the flame displacement speed). This was shown in Fig. 5-9 where the impact of q_p on the flame displacement speed at an almost constant curvature or equivalently constant U was discussed. Further the value of $\frac{dS_B}{dz}$ changes with U as the flame standoff distance changes. I also note that $(\frac{du}{dz})_B > 0$ is also always true because the flame stabilizes in an accelerating flow on the top of the burner plate. In Fig. 5-11a, $\frac{dS_B}{dz} > (\frac{du}{dz})_B$. If a small convective disturbance moves the flame downstream/upstream, the flame displacement speed increases/decreases more than the flow velocity bringing it back to the original location and a stable flame is sustained. This is contrary to the case shown in Fig. 5-11c. Note that Fig. 5-11b shows the critical case when $\frac{dS_B}{dz} = (\frac{du}{dz})_B$, at the onset of blowoff. Figure 5-11 is true not just for a 1D planar flame but also for a flame with finite curvature.

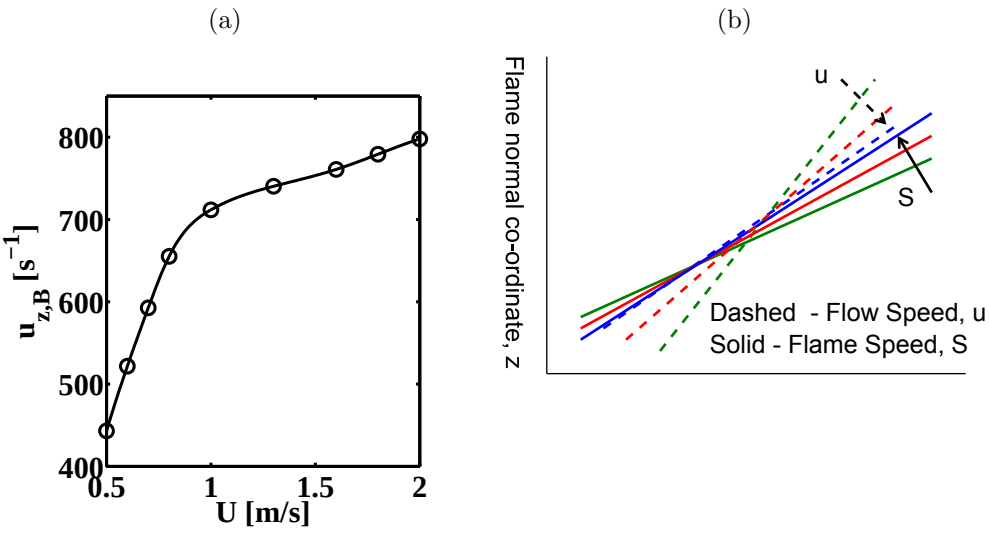

Figure 5-12: Streamwise velocity gradient, $u_{z,B}$ or $(\frac{du}{dz})_B$ at the flame base for $U = 0.5 - 2.0$ m/s; (b) Blowoff mechanism as $\frac{dS_B}{dz}$ approaches $(\frac{du}{dz})_B$

I indirectly validate the hypothesis, illustrated in Fig. 5-11, using my numerical results. Figure 5-12a shows from my simulations that the flow velocity gradient $(\frac{du}{dz})_B > 0$ grows with increasing mean inlet velocity U. At a fixed U, if I convectively

disturb the flame to move slightly away from/towards the plate, the heat loss to the burner plate decreases/increases. The curvature remains fixed as the incoming mass flow accommodated by the flame is constant. This can be alternatively visualized as the flame convectively moving up or down as a whole entity in the vicinity of its stabilization point in the process of locating it before the stable solution is achieved. The corresponding change in the displacement speed will be higher/lower when q_p is large/small. This was shown in Fig. 5-9 which illustrated that the gradient in S_B is smaller for lower q_p, when the latter was varied at a constant curvature. Equivalently, the impact of heat loss on lowering the flame displacement speed becomes weaker when U increases (or heat loss decreases). As a result, the magnitude of $\frac{dS_B}{dz}$ is expected to decrease with growing U, even for curved flames. Thus as U increases $(\frac{du}{dz})_B$ grows and $\frac{dS_B}{dz}$ diminishes gradually, taking the situation from being dynamically stable as shown in Fig. 5-11a to being dynamically unstable as shown in Fig. 5-11b, eventually leading to blow-off (see Fig. 5-12b for a schematic illustration). It must be noted that the quantity $\frac{dS_B}{dz}$ makes physical sense only at a given U and is hence difficult to numerically measure unless transient simulations are performed near the stabilization point. There exists a unique $\frac{dS_B}{dz}$ for every U. I assumed that the flame blowoff is a convective phenomena in this analysis (curvature remains fixed as the flame is locating the stabilization point at a given U), which is valid as will be shown in Section 5.4.3. Furthermore, at higher U, the results also show that the radius of curvature is almost constant or a critical value as discussed before.

Figure 5-13 shows additional support for the hypothesis illustrated in Figs. 5-11 and 5-12, where the flame base displacement speed as a function of the flame base location is shown during an unsteady simulation (commonly referred to as phase-portrait). To obtain (a), (b) and (c), steady solutions corresponding to $U = 0.8$ m/s, $U = 1.0$ m/s and $U = 1.3$ m/s respectively are instantaneously perturbed by a sudden increase in the inlet velocity by 10%. This perturbs the flame convectively and the flame executes an oscillation before finding a new stable location. Since the flame is in motion, S_B is computed by tracking the base of the flame contour at successive times in the unsteady simulation and adding to it the flow velocity at the base of the

contour, u_B. For a stationary flame, $S_B = u_B$, because the contour velocity is zero. A dynamically stable physical system executes a converging spiral phase-portrait in the phase-plane. Thus, the converging spirals in Fig. 5-13 indicate that the stability mechanism illustrated in Fig. 5-11 is valid. Figure 5-13d shows the phase-portrait of the unstable case, where both S_B and ψ_B increase as blow-off progresses. Additional details of the blowoff process are discussed in the next section.

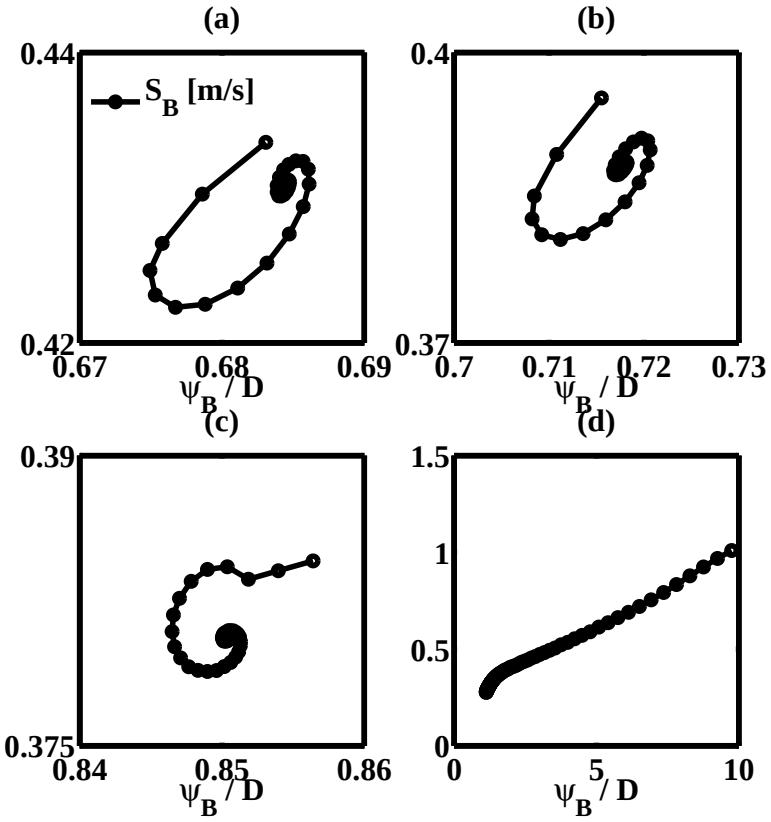

Figure 5-13: Flame base displacement speed versus the flame base location after a small convective perturbation is added to the inlet velocity. (a) $U = 0.88$ m/s, (b) $U = 1.1$ m/s and (c) $U = 1.43$ m/s correspond to statically stable flame; (d) $U = 2.3$ m/s corresponds to flame blow-off

During blow-off

Figure 5-14 shows a visualization of the streamlines and the volumetric heat release rate contours during the process of flame blowoff which, for the case analyzed, occurs

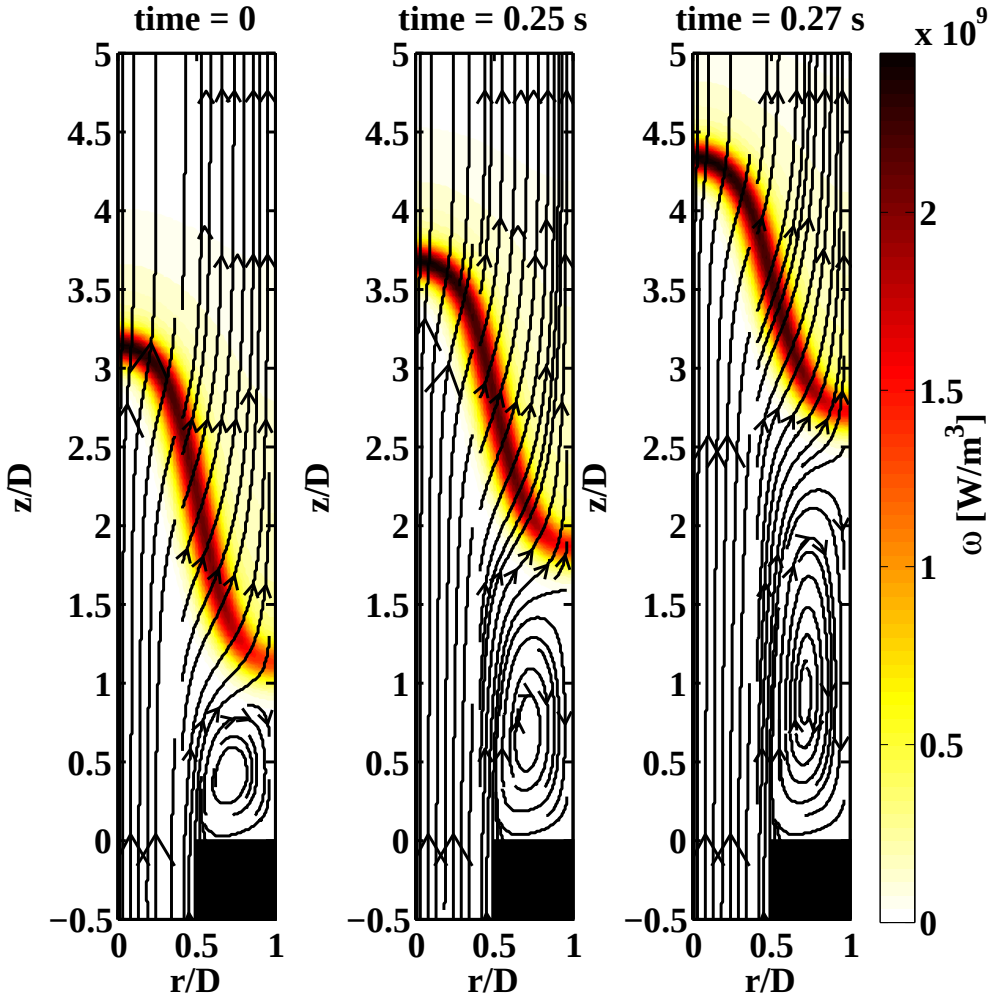

Figure 5-14: Volumetric heat release rate contours and superimposed streamlines at successive time instants during blow-off for $U = 2.2$m/s. $time = 0$ corresponds to the time when steady-state solution for $U = 2.0$ m/s was used as the initial solution in the simulation.

at $U = 2.2$ m/s. During blowoff, the results show that the recirculation region grows with time while the inlet flow velocity is fixed. Furthermore, as the flame moves away from the plate, the plate temperature decreases, and the flame length gradually decreases. The time history of different relevant physical quantities is shown in Fig. 5-15. The flame stand-off distance, recirculation zone size and the relative location of the flame with respect to the stagnation point all increase during this period. It is interesting to see that initially they change only gradually. The impact on the radius of curvature is especially minimal when compared to the impact on the heat loss, confirming that the blowoff process initiates in a convective manner as discussed in the dynamic stability mechanism. However as the burner plate cools down (T_p and q_p curves), the blowoff process, as manifested by the increase in stand-off distance, accelerates. During blowoff, the flame base displacement speed, S_B, is less than the flow speed, u_B. This confirms the blowoff hypothesis illustrated in Fig. 5-11, that the flame is unable to find a stable location because at every location $S_B < u_B$. Since the flame is in motion, S_B is computed by tracking the base of the flame contour at successive times in the unsteady simulation and adding to it the flow velocity at the base of the contour, u_B. The difference in S_B and u_B is very small in the initial stages of blowoff and keeps increasing as the blowoff process continues, showing flame acceleration. During blowoff, as heat loss decreases and S_B increases, the radius of curvature increases slightly, further contributing to raising S_B. The flame displacement speed increases as the effect of curvature decreases rapidly, thus moving the flame away from the stagnation point. It is interesting to note that the acceleration of the growth of the stand-off distance coincides with the rise in γ_B, further supporting the contribution of the flame base curvature to the flame dynamics mechanism. The recirculation zone continues to grow until it reaches values close to those corresponding to what is observed under non-reactive flow conditions. Thus, an interesting feedback mechanism between the growing size of the recirculation zone and the cooling of the burner plate is seen, which determines the flame speed during blowoff.

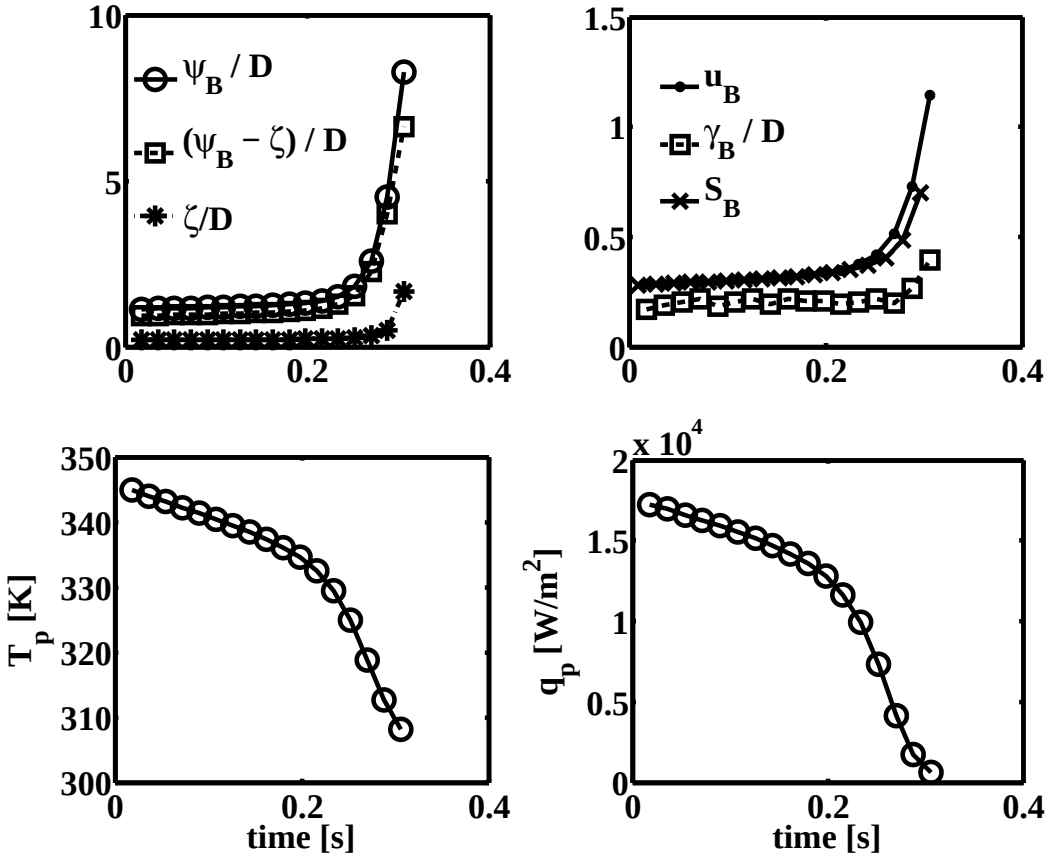

Figure 5-15: Time history of the (a) Normalized flame base stand-off distance, stagnation point location and relative distance of the flame base from the stagnation point; (b) Flame base displacement speed and the normalized flame base radius of curvature; (c) Temperature at the burner plate surface; and (d) Heat flux at the burner plate surface; during flame blow-off data for $U = 2.2$m/s. $time = 0$ corresponds to the time when steady-state solution for $U = 2.0$ m/s was used as the initial solution in the simulation.

5.5 Conclusions

In this chapter, I investigate the stabilization and blow-off mechanisms of a periodic array of lean premixed flames downstream of a heat conducting perforated plate using two-dimensional numerical simulations. I use a detailed chemical kinetics mechanism for a methane-air mixture for the analysis. The results show that the flame stabilizes with its base located close to the stagnation point in the accelerating flow above the burner plate. Significant thermal and aerodynamic interaction between the flame and its environment are observed, manifested in the heat exchange with the burner plate, with the associated rise of the plate temperature and drop in the flame temperature, and the flow non-uniformity. Lower heat loss (increases flame displacement speed) and smaller radius of curvature (decreases flame displacement speed) have opposing impact on the flame displacement speed when imposed independently on the flame. These effects are coupled in the configuration under investigation.

The flame displacement speed at its base varies non-monotonically with the mean inlet velocity of the reactants. In the lower range, as the mean inlet velocity of the reactants increases, the recirculation zone is virtually non existent. The flame stand-off distance increases and the heat transfer to the burner plate decreases strengthening the flame and increasing its displacement speed. This causes the flame to move away from the stagnation point. As the mean velocity increases further, the recirculation zone grows and the stagnation point moves downstream. The radius of curvature of the flame base decreases to accommodate growing but confined flame length. This weakens the flame, lowering the displacement speed at the base and bringing it closer to the stagnation point.

At higher mean inlet velocity, the radius of curvature of the flame base approaches a critical value limited by a physical minimum radius which is comparable to the flame thickness. This curvature remains almost constant until the flame blows off. The total flame stretch is dominated by the curvature of the flame base near blow-off. Thus, my results ascertain that the 'critical velocity gradient theory' [40], which ignores the presence of strong positive curvature, cannot explain blowoff in this configuration.

I show that heat loss to the burner plate is critical in providing a mechanism for dynamic stability of the flame, under the conditions explored in this chapter. This was not the case for bluff-body stabilized flames (Chapter 4) which also undergoes blowoff when the dynamic stability criterion fails. At its stabilization point, the flame displacement speed is equal to the flow speed; and the gradient normal to the flame base of the former is greater than the corresponding gradient of the latter. Near blowoff, as U is increased, the flame displacement speed gradient is reduced and the flow speed gradient grows. The flame blows off when the two values are equal. During blowoff, the recirculation zone size, flame stand-off distance, and the flame displacement speed increases and the burner plate cools down. The change in the radius of curvature of the flame base is negligible during the initial phase when the blowoff starts, showing that the flame blows off convectively. As the rate of the burner plate cooling increases, the blowoff process accelerates. There is a strong feedback between the growing recirculation zone and the cooling burner plate, which determines the flame speed during blowoff.

Chapter 6

Modeling dynamic response of a premixed flame stabilized on a perforated-plate

6.1 Overview

The dynamic response of a premixed flame stabilized on a heat-conducting perforated plate depends critically on their coupled thermal interaction, which was discussed in Chapter 5. The objective of this chapter is to develop an analytical model to capture this coupling. A critical step in the development is the hypothesis presented in Section 6.2.2 for model closure. This hypothesis is based on the observations of flame stabilization using the numerical simulations discussed in Chapter 5, showing the powerful applications of high-fidelity numerical simulations.

The model developed in this chapter predicts the mean flame base standoff distance; the flame base area, curvature and speed; and the burner plate temperature given the operating conditions; the mean velocity, temperature and equivalence ratio of the reactants; thermal conductivity and the perforation ratio of the burner. The dynamic response is typically characterized by the flame transfer function (FTF). A linear FTF is defined as $\mathrm{TF}(f) = \frac{Q'_f/Q_f}{U'/U}$, where f is the frequency of the velocity per-

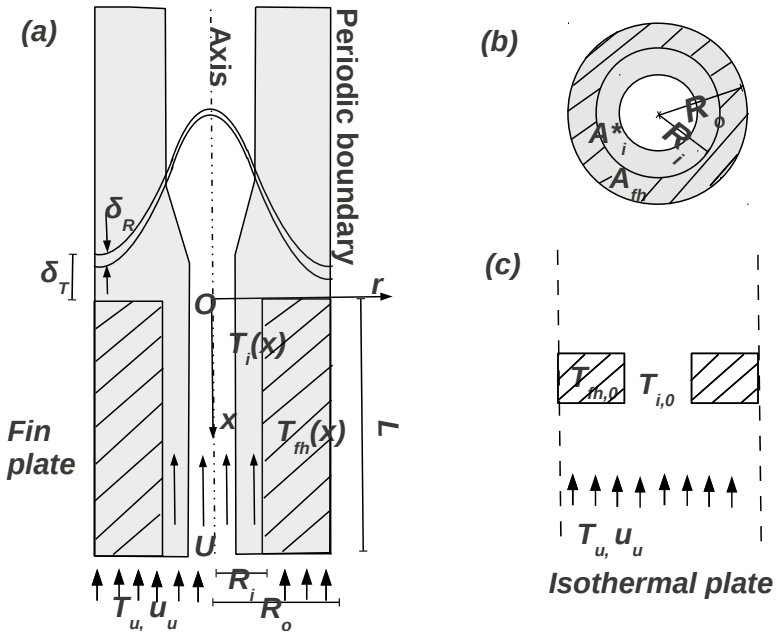

Figure 6-1: (a) Schematic illustration of the analytical domain with a thick flame holder to use fin approximation ; (b) Top view of the burner shown in part (a) ; (c) Isothermal plate illustration to model a thin flame holder, to compare the flame transfer function model with the experimental results in [102]

.

turbations (U') and Q_f is the net heat release rate. My model is combined with the flame transfer function (FTF) model described in [52] to predict the dynamic response of the flame to velocity perturbations. I show that modeling the thermal coupling between the flame and the burner, while accounting for the two-dimensionality of the former, is critical to predicting the dynamic response characteristics such as the overshoot in the gain curve (resonant condition) and the phase delay. Good agreement with the numerical and experimental results is demonstrated over a range of conditions.

6.2 Governing Equations

Figure 6-1a schematically illustrates a two-dimensional slice of an axis-symmetric bell-shaped premixed flame stabilized on a heat conducting plate. Figure 6-1b shows a top-view of the perforated-plate burner. A co-ordinate system $r - x$ is used. The control volume under consideration is shaded in Fig. 6-1a. It includes the solid burner

region, additionally marked by hashed lines. The part of the flame above the burner plate and within the shaded region in Fig. 6-1a is referred to here as the flame base. In this section, I develop the governing equations to predict the steady-state physical quantities given the mean inlet velocity, U, through inner hole of perforated-plate; equivalence ratio ϕ; thermal conductivity of the plate (or flame-holder) λ_{fh} and the perforation ratio $\kappa = R_o/R_i$. R_o is the outer radius of the domain and R_i is the inner hole radius. U is assumed to be constant across $0 < r < R_i$. T_u, ρ_u are the temperature and the density of the unburnt reactants.

δ_T is the flame base standoff distance. I assume that the temperature at the flame base (where the reaction rate is zero) is the burnt gas temperature, T_b. This assumption over-estimates the flame base temperature. The actual value at that location is lower due to factors such as incomplete oxidation of CO and heat losses to the surroundings. There is typically a small recirculation zone region within δ_T that plays an important role in the overall stability of the flame as discussed in detail in Chapter 5. δ_R is the reaction zone thickness where the reaction rate is finite and high, which lies immediately above the recirculation zone. For modeling simplicity, I assume that δ_T and δ_R are the mean characteristic distances of the entire flame base. This is an approximation because the flame base is often highly curved, with its curved area, A_F, greater than the flame holder area, $A_{fh} = \pi(R_o^2 - R_i^2)$. The thickness of the plate is denoted by L. The specific heat, $c_{p,u}$, and the thermal conductivity, λ_u, of the mixture are assumed constant throughout the domain at their unburnt values.

The outer (due to periodicity) and the inner streamwise edges of the shaded domain in Fig. 6-1a are modeled as adiabatic slip walls. This is chosen to separate the flame base region from the flame tip region, such that $A_i^*/\pi R_i^2 = A_{fh}/\pi R_o^2$. A_i^* is the cross-sectional area of the shaded region of the inner hole (see Fig. 6-1b). This relation suggests that at each streamwise location of the control volume, the fraction of the total cross-sectional area occupied by the streamtube under consideration is the same. The flame base speed is denoted by S_F. Mass conservation in the shaded control volume is

$$\rho_u U A_i^* = \rho_u S_F A_F \tag{6.1}$$

I assume that the density at the unburnt side of the reaction front (where the flame speed S_F is to be estimated) is ρ_u for simplicity. The actual value is slightly lower due to the preheating via heat recuperation from the burner, as discussed later. Similar to δ_T and δ_R, S_F is also an average over the curved flame base. The energy conservation, assuming an overall adiabatic system, is

$$\rho_u U A_i^* c_{p,u}(T_b - T_u) = \bar{w_f} \Delta H_{R,f} \delta_R A_F \tag{6.2}$$

where $\bar{w_f}$ is the average volumetric fuel consumption rate and $\Delta H_{R,f}$ is the heat of reaction of the fuel (methane). The overall adiabatic assumption is consistent the numerical simulations in Chapter 5. However, the burner plate may be externally cooled as discussed in [51, 102]. Including this non-adiabaticity is a natural extension of my model; however the focus of this chapter is to see the critical impact of the internal parameters of the system alone on the physical quantities of interest. $\bar{w_f} \Delta H_{R,f}$ is estimated using our one-dimensional simulations in [91]. The consumption speed of a flame, S_c, defined on the basis of the rate of energy consumption, is used because it does not depend significantly on the flame curvature [99]. For a given ϕ and T_u; the 1D flame thickness δ_R^o, T_b and the adiabatic laminar flame speed S_L^o (equal to its consumption speed for one-dimensional adiabatic unstretched flames),

$$\bar{w_f} \Delta H_{R,f} = \frac{\rho_u S_L^o c_{p,u}(T_b - T_u)}{\delta_R^o} \tag{6.3}$$

I assume that the temperature increases linearly from $T_{fh,0}$ to T_b in the region above the flame-holder, where $T_{fh,0}$ is the plate surface temperature. Hence the average heat flux on the top of the flame-holder

$$\dot{q}''_{fh} = \frac{\lambda_u (T_b - T_{fh,0})}{\delta_T} \tag{6.4}$$

The heat transfer to the burner plate's top surface re-enters into the reactants from

the inner-hole wall. The balance of this recirculated heat is

$$\dot{q}''_{fh} A_{fh} = \rho_u U A_i^* c_{p,u} (T_{i,0} - T_u) \tag{6.5}$$

where $T_{i,0}$ is the mean temperature of the reactants exiting the inner hole. The flame base geometry is assumed to be parabolic with its axis as the periodic outer edge of the domain and curvature $\gamma = \frac{d^2 x_F}{dr'^2}$ at the tip of the parabola (where $r' = R_o - r$). The area of the flame base is larger than A_{fh} for positively curved (concave towards products side) flame base. I assume a circular burner surface area for simplicity. The flame base above the burner plate can then be represented as $\frac{dx_F}{dr'} = -\gamma r'$ and its base area is approximately

$$A_F = \int_{R_i}^{R_o} 2\pi (R_o - r) \sqrt{1 + \gamma^2 (R_o - r)^2} dr \tag{6.6}$$

Due to double-periodicity, the perforations and the flames form an artificial ring-like pattern. The integration in Eq. 6.6 to estimate the curved flame area, can also be performed along a circle with an origin at inner axis rather than at the outer periodic edge. I found that the results do not change with this modification. High activation energy asymptotics [103] is used to approximate the relative size of the reaction zone thickness to the flame standoff distance, which is equivalent to a thermal thickness of the flame base. For chemical reaction with overall reaction order n, Zeldovich number $Z = \frac{T_a}{T_b^2}(T_b - T_u)$ (T_a is the activation temperature of the fuel) and the ignition temperature T_{ig},

$$\frac{T_b - T_{ig}}{T_b - T_u} = \frac{n}{Z} \tag{6.7}$$

Ignition corresponds to the start of the reaction zone. Hence geometrical constraint results in

$$\frac{T_b - T_{ig}}{T_b - T_{fh,0}} = \frac{\delta_R}{\delta_T} \tag{6.8}$$

6.2.1 Estimating $T_{i,0}$ and $T_{fh,0}$

The governing equations that determine the thermal coupling between the plate and the fluid depend on the burner geometry and the natural thermal boundary conditions. There is a temperature gradient within the plate if the Biot number, based on the plate thickness, $h_c L/\lambda_{fh} > 0.2$, where h_c is a convective heat transfer coefficient. The resulting temperature profile within the burner plate and the bulk temperature of the fluid in the inner hole is denoted by $T_{fh,x}$ and $T_{i,x}$ respectively. The subscripts fh and i denotes the flame-holder (burner plate) and the inner hole respectively; and x denotes their variation in that direction. The corresponding burner surface temperature and the exit hole temperature are given by $T_{fh,0}$ and $T_{i,0}$, discussed in Case A. Alternatively a thin plate, with a small Biot number (illustrated in Fig. 6-1c) used in the experiments in [51, 102], can be modeled as being isothermal as discussed in Case B. In both the cases, the Biot number based on the characteristic radial dimension, $h_c(R_o - R_i)/\lambda_u < 0.2$, for the typical burner geometries used in this chapter and hence I neglect any radial variation in T_i and T_{fh}.

Case A: Fin approximation for a thick plate

There is a laminar flow through the inner hole of the perforated plate. An average Nusselt number for the convective heat transfer ≈ 4 [104], resulting in $h_c = \frac{2\lambda_u}{R_i}$. Similar to fin analysis [104], the governing equation within the flame-holder is

$$\lambda_{fh}\frac{d^2T_{fh}(x)}{dx^2} = 2\pi R_i h_c(T_{fh}(x) - T_i(x)) \tag{6.9}$$

with the boundary conditions as $T_{fh}(x = 0) = T_{fh,0}$ and $\frac{dT_{fh}(x)}{dx}(x = L) = 0$. Similarly, the governing equation for the bulk motion of the fluid within the hole is

$$\rho_u U A_i^* c_{p,u}\frac{dT_i(x)}{dx} = -2\pi R_i h_c(T_{fh}(x) - T_i(x)) \tag{6.10}$$

with the boundary condition at the inlet of the hole as $T_i(x = L) = T_u$. The ordinary differential Eqs. 6.9 and 6.10 are simultaneously solved numerically to obtain $T_{fh}(x)$

and $T_i(x)$. Using the solution, I obtain the exit hole bulk temperature of the fluid

$$T_{i,0} = T_i(x = 0) \tag{6.11}$$

Case B: Isothermal thin plate

In this case, the natural boundary condition corresponds to the heat being convected upstream from the thin perforated plate, illustrated in Fig. 6-1c. The average convective heat transfer coefficient, h_{pp} can be estimated using the Nusselt number correlation for convective heat transfer from an isothermal perforated plate to upstream impinging reactants [105],

$$h_{pp} = 0.881 \frac{\lambda_u}{L*} (\frac{2R_i U}{\nu_u})^{0.476} \mathrm{Pr}^{\frac{1}{3}} \tag{6.12}$$

where $L* = A_{fh}/(2R_o)$. I take $\mathrm{Pr} = 0.69$ and $\nu_u = 1.5 \times 10^{-6} \mathrm{m}^2/\mathrm{s}$. The heat transferred upstream from the isothermal perforated-plate increases the sensible enthalpy of the incoming reactants such that

$$\rho_u U A_i^* c_{p,u} (T_{i,0} - T_u) = h_{pp} A_{fh} (T_{fh,0} - T_u) \tag{6.13}$$

In both the cases, it is assumed that the heat lost to the environment is negligible. This may not be the case for externally cooled plate, as in the experiments in [51, 102].

6.2.2 Hypothesis for model closure

In the governing equations, S_F is an average flame base speed. The local flame structure above the flame holder, at the curved base, was discussed in detail in Chapter 5. I showed that the unburnt side of the reaction front is immediately above the stagnation point of the recirculation zone over the burner plate. Hence, I assume here that the edge of the parabolic flame base has a zero local flame displacement speed. The structure of the flame wing resembles that of a one-dimensional flame as the influence of the burner wall is reduced. Thus I assume a linear decrease of the

flame speed from S_L^o at the inner edge to zero at the outer periodic edge of the shaded region in Fig. 6-1a. The area averaged flame speed is then

$$S_F = \frac{1}{A_F} \int_{R_i}^{R_o} \frac{S_L^o (R_o - r)}{R_o - R_i} 2\pi r \sqrt{1 + \gamma^2 (R_o - r)^2} dr \tag{6.14}$$

Depending on the boundary conditions, Eqs. 6.1-6.11 and 6.14 or Eqs. 6.1-6.8 and 6.12-6.14 form a complete set of nonlinear equations. These are solved simultaneously to obtain the physical quantities of interest δ_T, δ_R, $T_{fh,0}$, $T_{i,0}$, γ, S_F, A_F and $\dot{q}''_{fh}$, given the operating parameters ϕ, U, κ, λ_{fh}, T_u.

6.2.3 Linear flame transfer function model

Altay et al. [52] developed an analytical model to predict FTFs by assuming a series of plane and conical flame fronts above the perforated-plate to account for two-dimensionality. The kinematics of 2D flame surfaces were modeled, extending the assumptions of Fleifil et al.[106] to couple the flame surface kinematics equation with the heat loss to the burner plate. I improved this model by coupling the above developed steady-state model. The major changes are highlighted below[1].

The flame speed above the burner plate ($\bar{S}_u$ in [52]), which was assumed to be S_L^o, is modified to S_F. The burnt gas temperature ($\bar{T}_b$ in [52]) was assumed to be a free parameter to account for non-adiabaticity. This is changed to the adiabatic value since I have developed an overall adiabatic model. $T_{fh,0}$ was accounted for in the form of the density weighted flame stand off distance, $\bar{\psi}_{fp}$, which was estimated using Rook's logarithmic model in [16]. This is replaced here by the average temperature weighted flame standoff distance, $\frac{\bar{\psi}_{fp}}{\delta} = 1.5 \frac{\delta_T}{\delta} \frac{T_u}{T_b}$. $\delta = \frac{\lambda_u}{rho_u c_{p,u} S_L^0}$ is a reference thermal thickness of the flame. The factor of 1.5 is used because it provided a reasonable agreement with the FTFs from my previous numerical simulations, discussed in Sec. 6.3.

[1]Nomenclature in [52]: $T_s = T_{fh,0}$, $A_{open} = \pi R_i^2$, $A_u = \pi R_o^2$ and $A_p = A_{fh}$

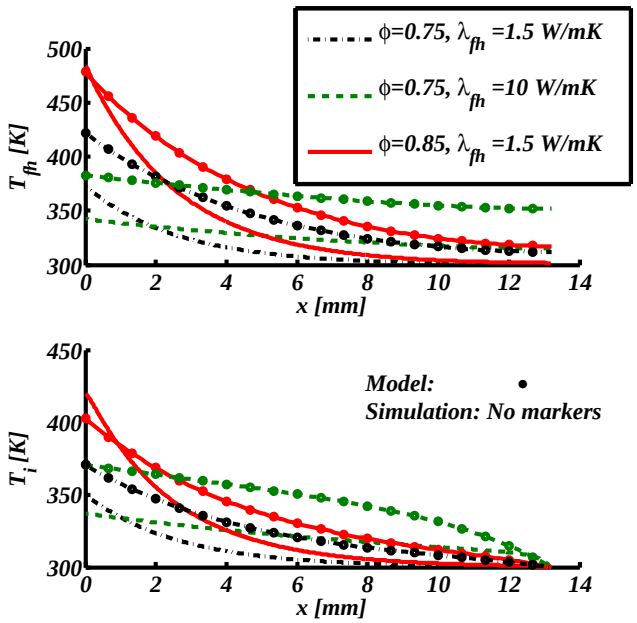

Figure 6-2: Mean temperature profiles, $T_{fh}(x)$ and $T_i(x)$, validation of the model using the two-dimensional steady-state simulations described in [90] for the case: $\kappa = 1$, $U = 1.3$ m/s

6.3 Results and Discussions

The discussions in this section are divided into three parts. First, the steady-state model described in this chapter is validated using my numerical simulations from [90] and Chapter 5. The results of the steady-state model coupled with the FTF model described in Section 6.2.3 are then compared to the numerical simulations in [53] at the same operating conditions. Lastly, I compare my model results to the experimentally obtained FTFs from [102]. The parameters that are kept constant throughout the analysis are, $R_i = 0.5$ mm; the plate thickness, L =13.2 mm (except in Section 6.3.3 where the plate is very thin), T_u= 300 K, $\rho_u = 1.15$ kg/m^3, $c_{p,u} = 1059.4$ J/kgK, $\lambda_u = 0.0275$ W/mK, lower heating value of methane $LHV = 50.1$ MJ/kg, $T_a =$ 24400 K and order of reaction $n = 1.9$. S_L^o, δ_R^o and T_b depend on ϕ and T_u and the values are determined using our 1D simulations in [91]

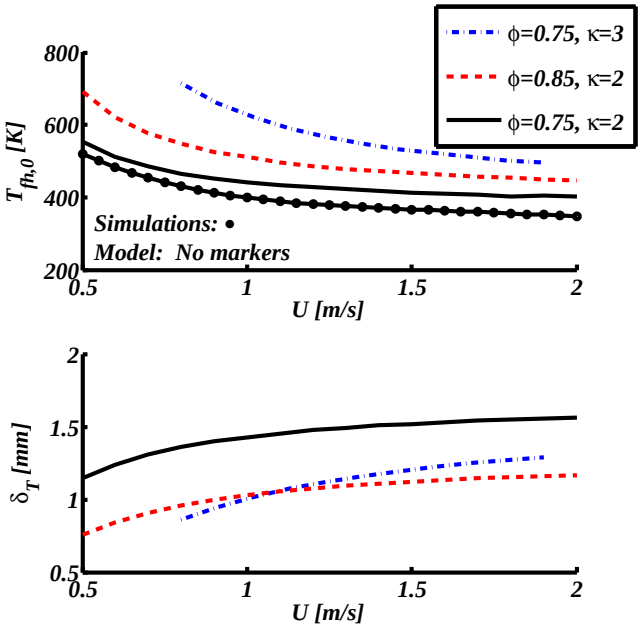

Figure 6-3: Plate temperature and the flame standoff distance predicted using the model for burner with $\lambda_{fh} = 1.5$ W/mK as function of the mean inlet velocity at different equivalence ratio and perforation ratio. The average plate temperature computed from simulations in [53] is also shown for the case with $\phi = 0.75$, $\lambda_{fh} = 1.5$ W/mK and $\kappa = 2$

6.3.1 Steady-state Model Validation and Verification

Fig. 6-2 shows good agreements for $T_{i,x}$ and $T_{fh,x}$ obtained using the model and simulations at different operating conditions. The natural boundary conditions discussed in Sec. 6.2.1 Case A are used in the model. The temperature field from the simulations was averaged in the radial direction to obtain a variation with x. The plate temperature increases as ϕ and κ grow. Moreover, the standoff distance predicted by the model is of the same order of magnitude as seen in the simulations. The standoff distance depends on the definition of the flame front. For example, for the case with $U = 1.3$ m/s, $\phi = 0.75$ and $\kappa = R_o/R_i = 2$, the model predicts δ_T =1.49 mm and δ_R =0.29 mm. This is in close agreement with the values obtained from the simulations for $T = 0.9 \times T_b$ contour discussed in Chapter 5; δ_T =1.3 mm and δ_R =0.4 mm, computed at the periodic edge of the domain where there flame is the closest to the burner plate.

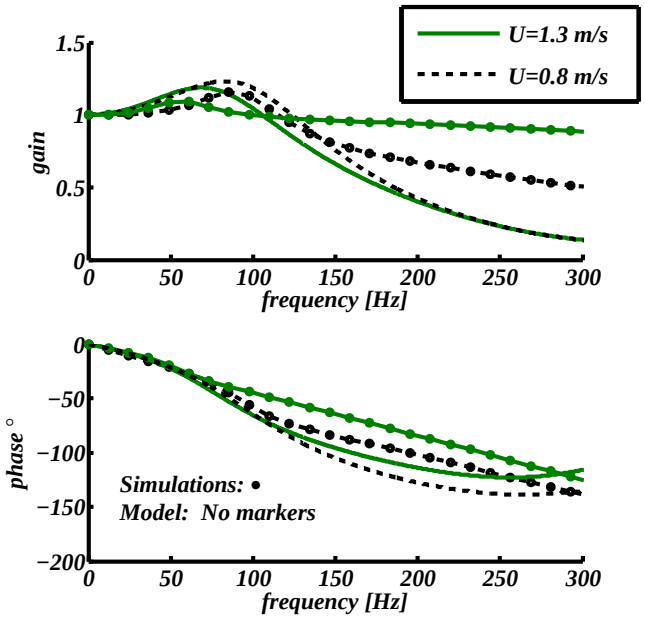

Figure 6-4: FTF comparison with simulations in [53] for the cases with $\phi = 0.75$, $\kappa = 2$ and $\lambda_{fh} = 1.5$ W/mK

I numerically demonstrated the increase in the flame standoff distance, and decrease in the burner temperature as U grows Figs. 5-6 and 5-10 of Chapter 5. In [90] I showed that δ_T decreases and $T_{fh,0}$ increases as ϕ or κ were increased at a constant U. Figure 6-3 shows that all these trends are well captured in the model with the changing operating (ϕ, κ, U). It also shows a good agreement in $T_{fh,0}$ between the model and the simulation results for $\phi = 0.75$ and $\kappa = 2$ for a wide range of U.

6.3.2 FTF comparison with numerical simulations

In this section, I discuss the impact of the operating conditions on the FTFs obtained using the model and compare them with the simulations in [53]. Figures 6-4 and 6-5 show the gain and the phase of the response at different operating conditions.

The overall shape of the FTF of such heat conducting perforated-plate burner are discussed in detail in [51–53]. The model predicts rather well the FTFs in all the conditions of interest. At low frequencies, as the flame moves away / towards the burner, its burning velocity increases / decreases, amplifying the flame motion

at certain frequencies, the gain overshoots unity and exhibits a resonance behavior. The flame responds weakly to high frequency oscillations (diminishing gain in FTF), due to quick dissipation of small scale-structures in the flame. There is a time delay associated with the convection time needed for the reactants to reach the flame base, $\tau \sim \delta_T/S_F$ [53]. Depending on the frequency of the imposed velocity oscillations, f, the convective time delay results in a phase difference of $2\pi\tau f$, growing linearly with frequency as I observe in Fig. 6-4 and 6-5. The resonant frequency is likely to depend on this time lag, $f_{res} \sim 1/\tau \sim S_F/\delta_T$. For $U = 1.3$ m/s, $\phi = 0.75$ and $\kappa = 2$, my model predicts $S_F/\delta_T \approx 80$ Hz, which is very close to the f_{res} seen in Fig. 6-4. S_F/δ_T predicts f_{res} reasonably well for all the other cases also. Similar dependency is noted in [52, 102]. I demonstrated in [53] that the flame-wall interaction is a critical mechanism which results in the observed resonance, which is completely missed if a perfectly adiabatic burner plate is assumed. The slope of the phase curve changes near the resonant frequency, showing that the large amplitude oscillations near the resonant condition alters the time lag, also observed by Durox et al. [50]. The physical mechanism of the system's affinity to certain low frequencies for an under-damped response is still unclear.

Figures 6-4 and 6-5 show that the low frequency response of the FTF (both in gain and phase) is captured reasonably well by the model. The resonance frequency shifts to the right and the phase delay decreases as the plate temperature increases or the standoff distance decreases, as seen when U changes from 1.3 m/s to 0.8 m/s in Fig. 6-4, and when ϕ increases from 0.75 to 0.85 in Fig. 6-5. This is also consistent with the hypothesis that $f_{res} \sim 1/\tau \sim S_F/\delta_T$. Similar trends are observed when κ increases from 2 to 3. Thus, the plate temperature and the standoff distance must be accurately predicted to capture the correct dynamics. In the experimental results in [102], the resonant frequency increases with U contrary to the results shown here, because of the additional influence of the external cooling on δ_T when U (or equivalently S_F) changes. Since $f_{res} \sim S_F/\delta_T$, the shift in resonant frequency will depend on this modified thermal boundary condition.

It was shown in [52] that at low frequencies with respect to f_{res}, the contribution

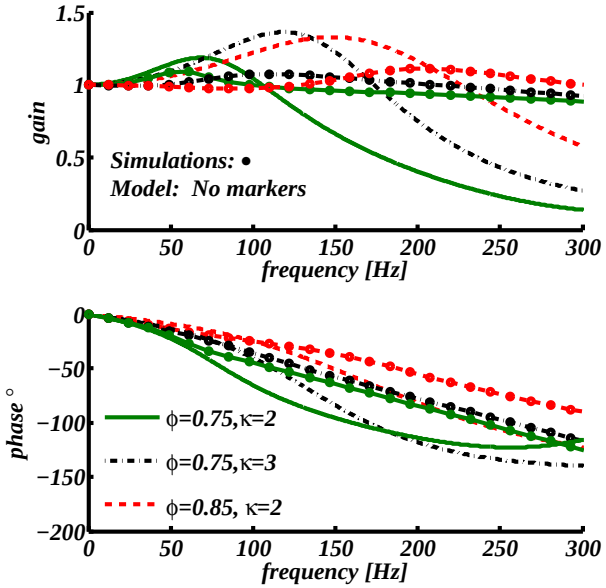

Figure 6-5: FTF comparison with simulations in [53] for the cases with $U = 1.3$ m/s, $\lambda_{fh} = 1.5$ W/mK

of flame area oscillations to the net heat release rate is weak compared to that of the burner heat loss oscillations, resulting in the rapid increase in the phase lag. For $f > f_{res}$, only flame area oscillations contribute to the net heat release rate fluctuations, which arise as a result of the inlet velocity fluctuations, saturating the phase behavior. The model predictions are poor compared to the simulations near the frequency where the phase saturates; this is the cut-off frequency of my model f^*. In all the FTF phase curves obtained using my model, $f^* \approx 1.5 \times f_{res} \sim 1.5 \times S_F/\delta_T$. $f^* \approx 140$ Hz for the cases shown in Fig. 6-4. f^* is a result of the assumptions of my analytical model and is not a physical quantity.

Several factors account for the quantitative differences between the predictions in Figs. 6-4 and 6-5 using the model and in simulations. The dynamic response model used from [52] does not account for increased flame base area due to curvature. I also assumed complete adiabaticity, whereas there may be some heat loss to the inner streamtube which was thermally detached in my assumptions. Lastly, the application of Rook's model to the plane front of the flame over the burner in [52] to predict

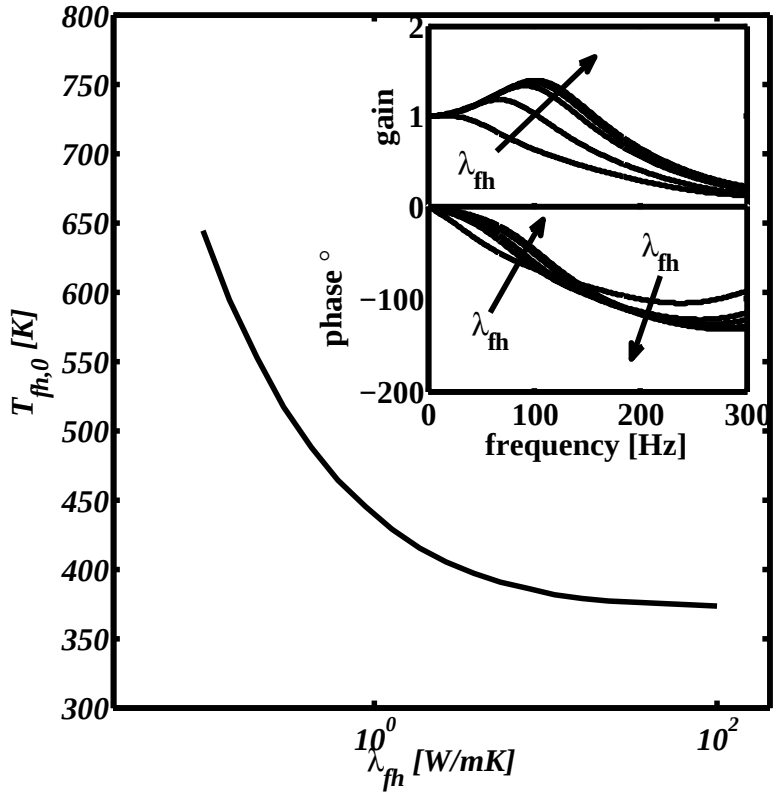

Figure 6-6: Variation of the plate temperature predicted using the model for fixed $\phi = 0.75$, $\kappa = 2$ and $U = 1.3$ m/s at different thermal conductivities of the burner. The inserted figure shows gain and phase of FTF as λ_{fh} is increased

its burning velocity oscillations is incorrect in strictest sense because it was mainly developed for one-dimensional flat flames over non-adiabatic porous burners.

Impact of thermal conductivity

Figure 6-6 shows the impact of the plate thermal conductivity on its surface temperature; the gain and phase of the FTFs. The impact quickly saturates with increasing thermal conductivity as one moves away from a ceramic and other low conductivity material. The "resonance" behavior of such burners can thus be controlled if the burner plate is made of low thermal conductivity material. The dependency of the system dynamics on λ_{fh}, including the saturation for high λ_{fh}, was also shown by McIntosh and Clarke in [72] for flat flames stabilized over cooled porous-plug type

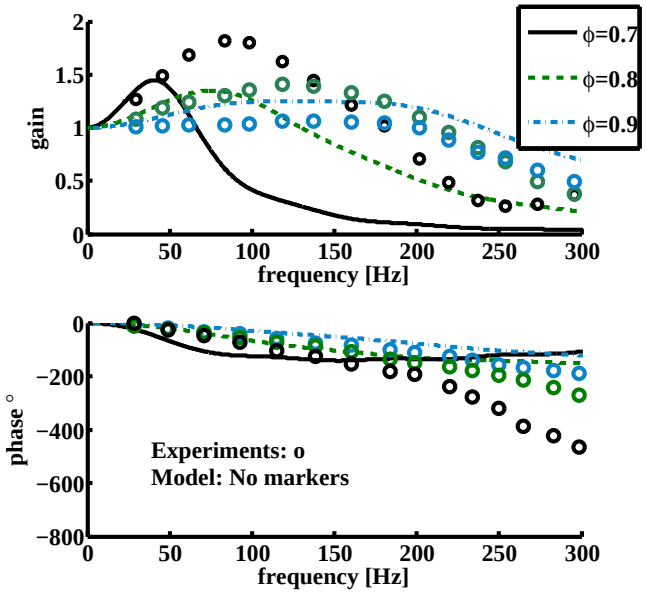

Figure 6-7: FTF comparison with experiments in [102] at different equivalence ratios for the cases with $U = 1.25$ m/s and $\kappa = 1.5$.

of flame-holders, where they reviewed models determining the flame stand-off distance and its temperature. The thermal conductivity plays a role in determining $T_{fh,0}$ through Eqs. 6.9 and 6.11 developed for thick plates. This is not the case for isothermal thin plates as can be seen through Eqs. 6.12-6.13.

6.3.3 FTF comparison with experiments

In this section I show that my model qualitatively predicts the FTFs in [102]. I use an isothermal plate, which is the natural boundary condition for thin plates (discussed in Sec. 6.2.1, Case B), since the Biot numbers, $h_c L/\lambda_{fh} < 0.2$ and $h_c(R_o - R_i)/\lambda_{fh} < 0.2$ for thin plates (see schematic illustration in Fig. 6-1c). Figure 6-7 shows a comparison between the predicted FTF assuming overall adiabaticity and the experimental FTFs in [102] determined in the presence of external cooling of the plate. I qualitatively capture the trends of the experiment showing that the non-adiabaticity must be introduced in the model. Moreover, the amount of external cooling in [102] is likely to depend on ϕ, because at high ϕ the flame is closer to the plate, increasing the plate

temperature, which will likely increase its non-adiabaticity.

The FTFs depends on the accurate estimation of $T_{fh,0}$ and δ_T. These quantities are coupled and their relationship will be strongly influenced when there is an additional external control over the thermal boundary conditions of the system, such as external cooling of the burner plate. This is a major reason that some trends of the FTFs in [102] were reported to be different from those predicted in [53]. The secondary peak, seen at high frequencies (around 500 Hz) in the experimental results in [102], are not reproduced. This secondary peak is also missing in my numerical simulations [53], although a finite gain at high frequencies is predicted due to the detailed length scale resolution of the flame structure. This should be investigated in the future work in this area.

6.4 Conclusions

A coupled analytical model for perforated-plate stabilized flames has been developed to predict the burner surface temperature, flame standoff distance, flame base speed, area and curvature given the operating conditions. I validated the model using my detailed numerical simulations data from Chapter 5 and my previous research thesis [90]. The mean flame standoff distance and the flame base speed are used as inputs to the linear flame transfer function model described in [52]. The two models are coupled and used to predict the linearized dynamic response of the flame to velocity perturbations. Under-damped oscillations resulting in gain overshooting unity (resonance) and the phase lag behavior are recovered. The resonant frequency, $f_{res} \sim S_F/\delta_T$, depends on the thermal coupling between the flame and the heat loss to the burner surface. This coupling manifests itself in the burner surface temperature and the flame standoff distance. Thus models used to predict such flame dynamics must capture their dependency. The FTF model used in this chapter resolves only the large length-scales of the system; as a result high frequency response, beyond the model cut-off frequency f^*, is not accurately predicted. For $f < f^*$, the FTFs are in good agreement with my numerical simulations presented in [53], with all the trends predicted correctly. By

changing the thermal boundary conditions to match the experiments in [102], good qualitative predictions are also achieved showing that non-adiabaticity, to account for heat losses to the environment, needs to be incorporated in the model. The flames are modeled as a series of conical flame front over the holes and plane flame fronts above the burner in the FTF model in [52]. The dynamic response of the plane flame-front was predicted using the Rook's model developed for 1D flat flames above a porous burner in [15]. This mismatch is a limitation in my FTF model, which needs to be addressed. A mechanistic understanding of the resonance behavior is still unclear and must be investigated in more detail in future research.

THIS PAGE INTENTIONALLY LEFT BLANK

Chapter 7

Advanced numerical developments

7.1 Overview

I presented a second-order buffer zone immersed boundary method for rectangular solid objects in Chapter 2 and demonstrated its application to flame-stabilization and blow-off mechanisms in Chapters 3-5. The immersed solid object in that second-order development was restricted to grid conforming rectangular or block-rectangular (T-shaped, L-shaped) geometries . An advanced development must capture the effects of complex geometries, with smooth boundaries cutting across grid-cells. However, this is a very challenging task especially in reacting flows. The current state-of-the-art immersed boundary methods capable of this are restricted to non-reacting flows. In this chapter, as an intermediate step, I discuss the development of a first-order method incorporating grid-conforming stair-stepped geometry and the surrounding reacting flow. I will also show the three-dimensional code development for "fluid-only" domain coupling the SAMR framework with the semi-implicit projection method.

7.2 Arbitrary shaped stair-stepped immersed solid

The buffer zone immersed boundary method discussed in Section 2.3.3 is simplified for a stair-stepped solid object illustrated in Fig. 7-1(a). Stair-step treatment is a trade-off between the order of accuracy and the range of applicability in terms

of flame-holder geometry. For several practical problems at small scales, such as combustion and gasification of coal particles, micro-scale liquid fuel droplet burning, micro-fluidic particle transport, the local Reynolds number is sufficiently low to allow direct numerical simulation (DNS) in the laminar regime. If the boundary layers are fully resolved, a first order-accurate method can give adequate accuracy, while providing substantial ease of implementation.

7.2.1 Numerical method

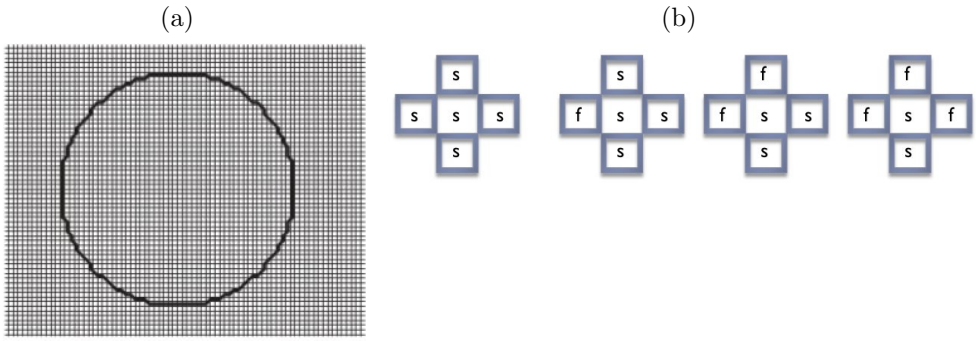

Figure 7-1: (a) Typical stair-stepped circle on a Cartesian mesh (b) Schematic illustration of 4 cases: (left to right) a solid domain cell (marked by center box s) surrounded by all solid cells, by 1 fluid cell (marked as f) , by 2 fluid cells and by 3 fluid cells.

For an overall first-order accurate solution, one layer of buffer zone for the species mass fractions is constructed using a finite-volume approach, unlike the three-celled layer as discussed in Section 2.3.3 which was based on a finite difference approach. The no-penetration of species is imposed by enforcing a zero-net flux through the solid cell immediately next to the solid-fluid boundary. Each solid domain cell is tagged based on the number of fluid and solid neighbors around it, see Fig. 7-1(b) for a schematic. If all its neighbors belong to the solid object, then that cell is tagged as an embedded cell (completely within the solid) and is not included in the single-cell wide buffer layer. All the other solid cells are included in the buffer zone. This single-celled buffer layer inside the solid is then filled cell-by-cell by enforcing a net zero flux through it. For two-dimensions,

$$\sum_{k=1}^{4} \frac{\partial Y_i}{\partial n_k} \delta_{sf,k} = 0 \tag{7.1}$$

where k represents the four faces of each solid cell with the normal direction n_k pointing in the positive x or y co-ordinate directions, $\delta_{sf,k}$ is the Kroneckor delta which is 1 if the face k is a solid-fluid boundary and 0 otherwise. The derivative (face-centered because of the staggered arrangement) is then computed using the second-order stencil on the cell-centered mass-fractions such that

$$\frac{\partial Y_i}{\partial x} = \frac{Y_{i,f} - Y_{-1}}{x_{i,f} - x_{-1}} \tag{7.2}$$

$$\frac{\partial Y_i}{\partial y} = \frac{Y_{i,f} - Y_{-1}}{y_{i,f} - y_{-1}} \tag{7.3}$$

where $Y_{i,f}$ is the species-mass fraction in the fluid cell, Y_{-1} is the value of the buffer cell. Using the above equations, the single-celled buffer layer is created inside the solid zone that imposes the no-penetration boundary conditions for the species at the immersed boundaries. This is constructed for each species at all the levels of the SAMR grid and at every substep of the multistage RKC integration of the scalar field. Dual buffer zones for temperature matching conditions as discussed in Section 2.3.3 are not required since high order derivative stencils are typically first-order accurate already when the thermal conductivity jumps sharply across a grid cell. The thermal conductivity jump is accounted using the binary marker function.

7.2.2 Verification of the first order construction

In this section, I show the verification of the methodology discussed above. The confined rectangular bluff-body, discussed in Chapters 3 and 4, is revisited. I simulated an unsteady non-reacting isothermal flow using both the second order method discussed in Chapter 2 and the stair-stepped approach presented above. The Reynolds number $\mathbf{Re}_d = 100$ was chosen and the rectangular bluff-body was inserted instantaneously in a channel flow. A steady recirculation zone develops before unsteady vortex shedding

begins. The rate of growth of the recirculation zone length (non-dimensionalized by the width of the rectangular cylinder d) during the steady-transient shown in Figure 7-2 using both the methods. The stair-stepped method discussed here accurately predicts this growth, verifying the numerical construction and its implementation in the code. The time is non-dimensionalized by $t* = tU/d$, where U is the mean inlet velocity.

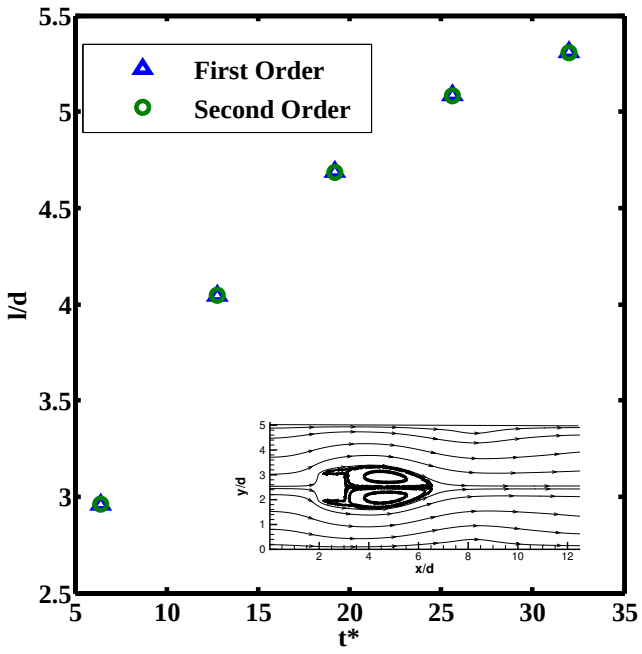

Figure 7-2: Comparison of the recirculation zone growth with time for an impulsively started channel-confined cold flow around a rectangular cylinder at $\mathrm{Re_d} = 100$, for a blockage ratio $d/H = 0.2$ using the second order numerical method developed in Chapter 2 and the first order stair-stepped method developed in this chapter.

7.2.3 Code validation using a confined circular cylinder in a non-reacting flow

I used a two-dimensional stair-stepped solid circular cylinder and obtained steady-state using the above described methodology. The flow does not shed vortices at the Reynolds numbers investigated. Comparison of the recirculation zone length (non-

dimensionalized by the diameter of the circular cylinder d) in a steady non-reacting flow across a confined circular cylinder with results of Chen et al. [107] is shown in Figure 7-3. The Reynolds number was based on the channel height for consistency with [107]. A good agreement is seen validating the solution obtained using the stair-stepped code.

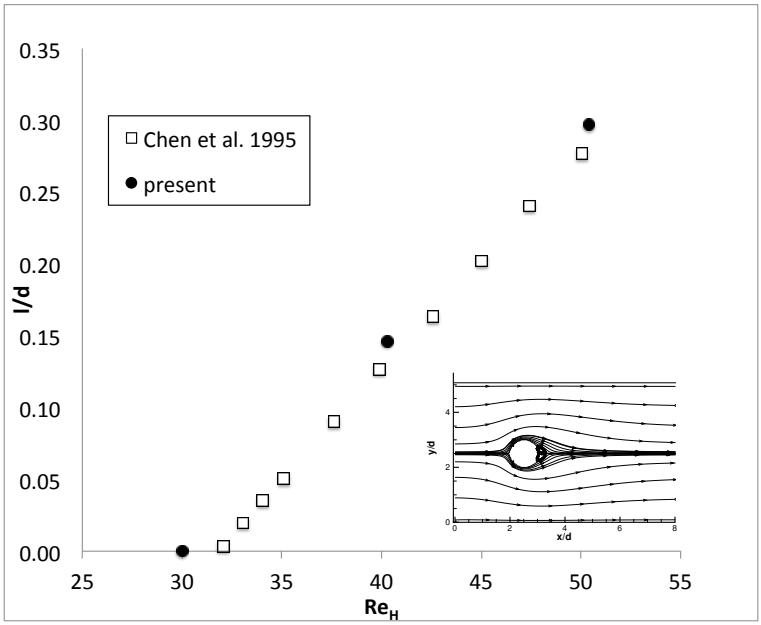

Figure 7-3: Comparison of the steady-state recirculation zone size for a channel-confined cold flow around a circular cylinder at different $\mathrm{Re_H}$, for a blockage ratio $d/H = 0.2$ using results of Chen et al. [107].

7.2.4 Premixed flame stabilized on a confined circular bluff-body

A reacting flow simulation for a flow around the confined circular cylinder is shown in Figure 7-4 at $\mathrm{Re_d} = 1000$ for a blockage ratio $d/H = 0.2$. The domain sizes is the same as discussed in Chapters 3 and 4, except the bluff-body shape is a stair-stepped circle. The single-step chemical kinetics mechanism described in Section 2.5.5 was used for this simulation[1]. Equivalence ratio of the methane-air reactants at in-flow was chosen to be $\phi = 0.8$. The black rectangles on the temperature contours

[1]The tool is flexible to use a detail chemical kinetics model as well

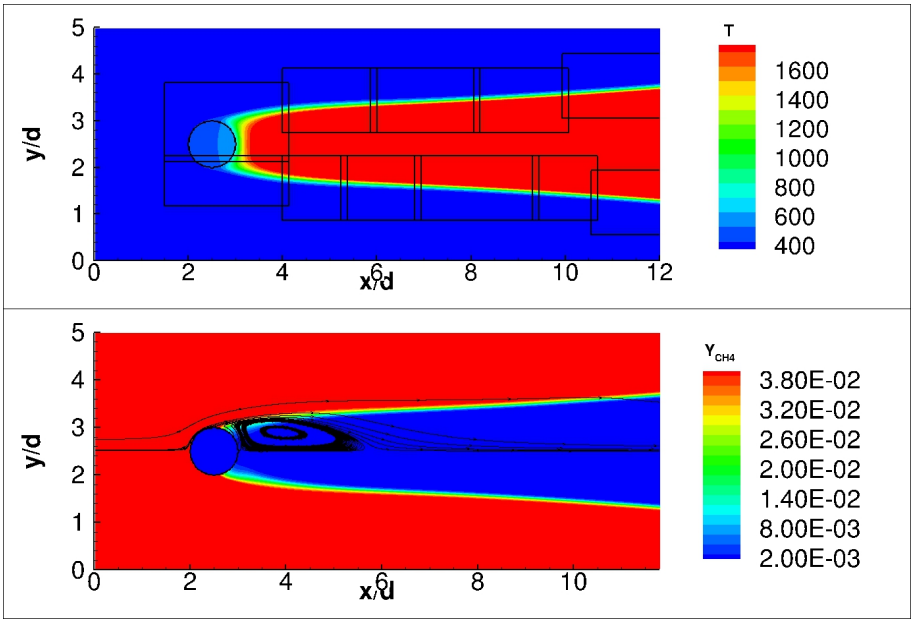

Figure 7-4: (top) Temperature contours with overlaid fine adaptive patches and (bottom) the fuel contours with overlaid streamlines for a reacting flow at equivalence ratio $\phi = 0.8$ around a confined circular cylinder at a flow $\mathrm{Re_d} = 1000$ for a blockage ratio $d/H = 0.2$.

mark the fine adaptive mesh patches. The streamlines are overlaid on the fuel contours. The flow separates at some downstream location on the circular cylinder. The temperature contours show the conjugate heat exchange between the solid circular body and the flow. The flame was allowed to naturally anchor near the wall and no forced anchoring condition was enforced as discussed before. The corresponding non-reacting isothermal flow sheds vortices in the von Karman regime, like the rectangular cylinder counterpart. This vortex shedding is shown by the non-dimensional vorticity contours in Fig. 7-5. The combustion heat-release made the unsteady flow symmetric and steady as discussed in Section 3.2.1.

Figure 7-6 shows a comparison between the reacting flow simulations using a circular and a rectangular bluff-body burner, both using single-step chemical kinetics. The temperature contours with overlaid streamlines are plotted. The diameter of the circular cylinder and the width of the rectangular cylinder were kept the same in this simulation, thereby keeping the Reynolds number based on d the same for both the cases. The circular cylinder was observed to have a smaller recirculation zone

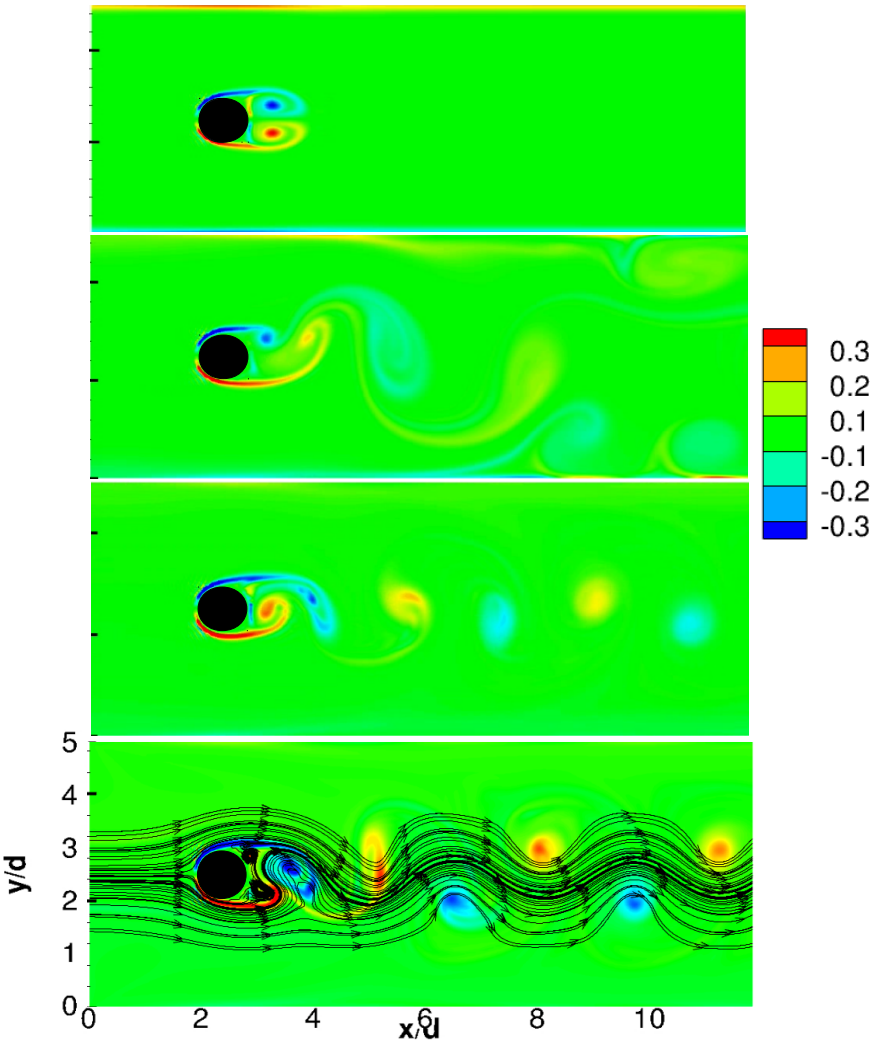

Figure 7-5: Non-dimensional vorticity contours (by its maximum value in the domain) for a non-reacting cold flow around a confined circular cylinder at a flow $\mathrm{Re_d} = 1000$ for a blockage ratio $d/H = 0.2$

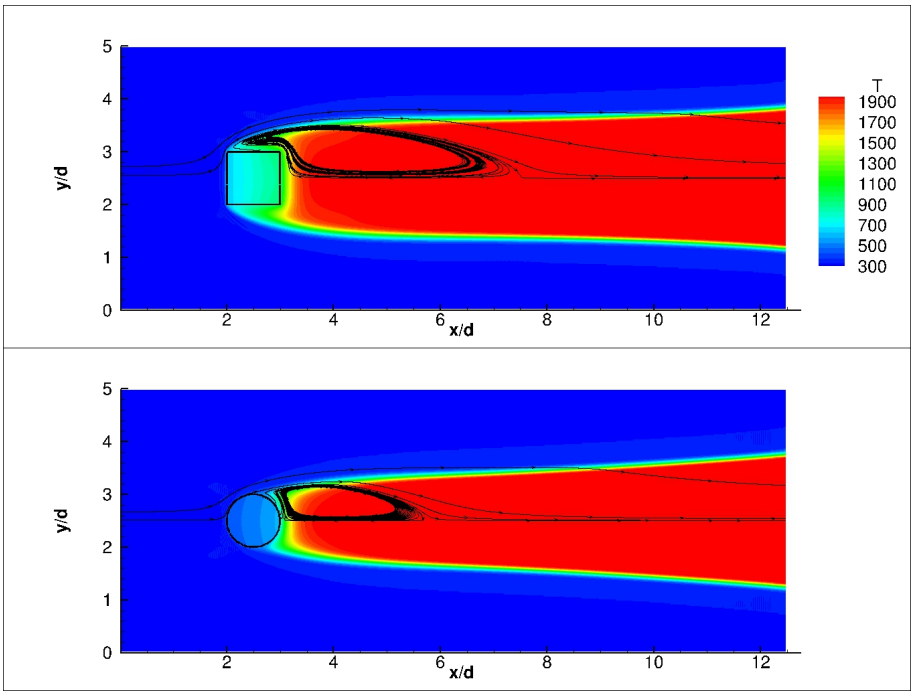

Figure 7-6: Temperature contours with overlaid streamlines for a reacting flow at equivalence ratio $\phi = 0.8$ around a confined (top) circular and (bottom) rectangular cylinder at a flow $\mathrm{Re_d} = 1000$ for a blockage ratio $d/H = 0.2$.

length of products, because of the relatively downstream separation point. The flow around the rectangular bluff-body separated at the leading edge. The circular flame-holder was much cooler than the rectangular counterpart because of relatively smaller boundary is in a direct contact with the hot products for the former. This simulation shows the significant impact that the geometry of the flame-holder can have on the reacting-flow around it.

7.2.5 Error in the stair-step approximation

A stair-step approximation will result in the surface area of the solid body to be different than its actual surface area. Figure 7-7 shows the relative error of volume depending on the number of control volumes inside a stair-stepped circular cylinder along the diameter. This is adapted from Fig. 4.12 in the book by Nikrityuk [108]. It shows that as the grid size becomes finer, the error in the surface area as a percentage of the actual area decreases. In the confined circular bluff-body simulations discussed

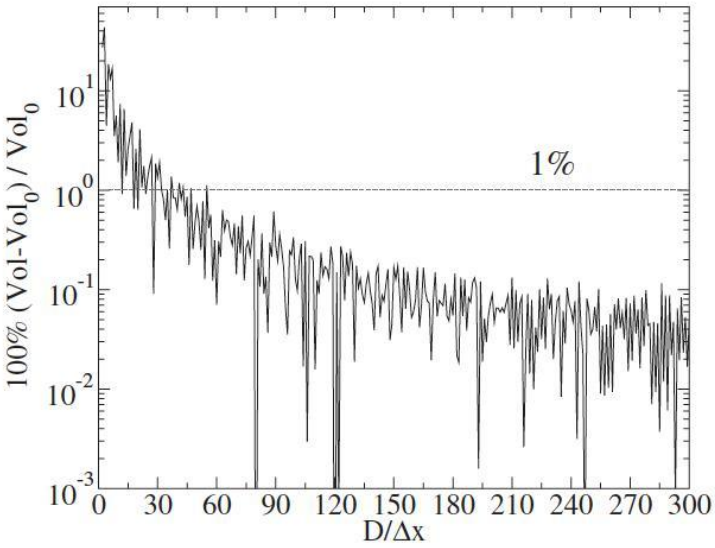

Figure 7-7: Relative error of volume depending on the number of control volumes inside a stair-stepped circular cylinder along the diameter. Adapted from Fig. 4.12 in the book by Nikrityuk [108]

above, the diameter was chosen to be 5 mm. The actual curve length of this exact circle is 15.7 mm. There were around 26×26 cells inside the circular cylinder. The approximate circular length of the boundary was estimated to be 14.7 mm using the stair-step approximation. This gives an error of 6.5% relative to the exact curve length. The local roughness introduced due to the stair-step approximation may also presumably change the location of the separation point, a detailed investigation of which should be performed in the future work.

All the simulations shown here considered a stair-stepped circle. However, the numerical method developed here is general to account for any arbitrarily complex geometry discretized in a stair-stepped manner, such as an airfoil, ellipse, v-shaped gutters.

7.3 Three dimensional code development

Another major developmental effort undertaken was to complete the three-dimensional implementation of the fluid-only code. Second-order finite difference pressure solver discussed in Section 2.3.2 was used in three-dimensions. The results of a three-

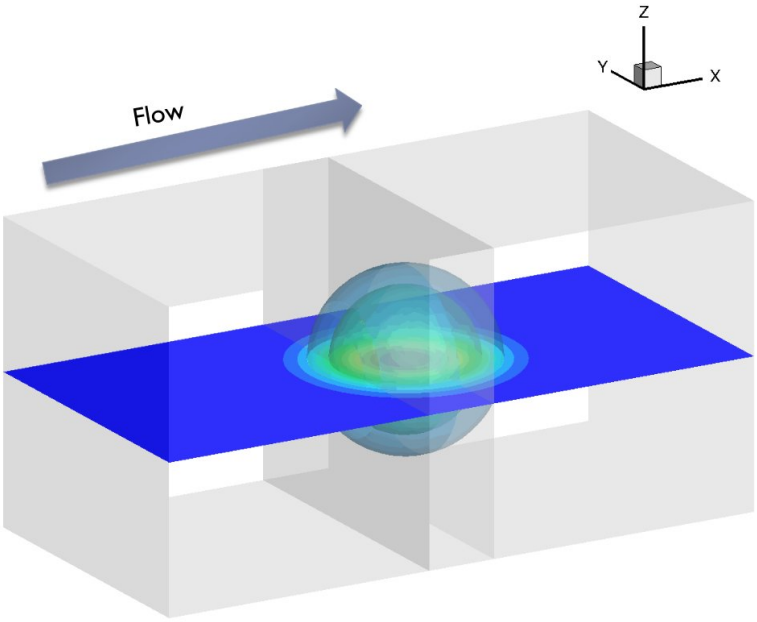

Figure 7-8: Gaussian temperature blob as the initial condition in the 3D domain. Colored temperature contours and iso-surfaces are shown.

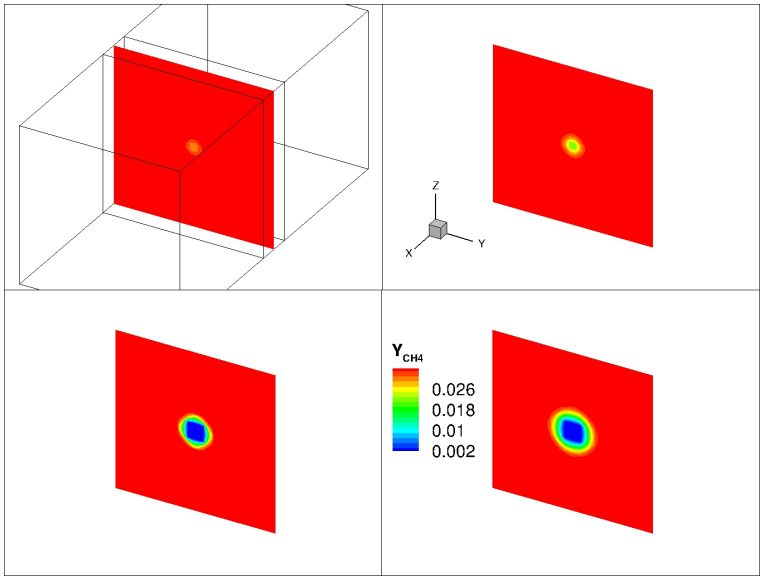

Figure 7-9: Fuel contours showing the ignition process from a hot-spot on the center x-normal slice.

dimensional channel flow with adaptive mesh refinement are shown below. A high temperature hot spot was introduced in the center of the channel in the form of a three-dimensional Gaussian blob for igniting a premixed mixture. A detailed C1 chemical kinetic mechanism, discussed in Chapter 3 was used. The mixture equivalence ratio was fixed at $\phi = 0.6$. A domain size (in mm) of $30 \times 15 \times 15$ and corresponding grid size of $64 \times 32 \times 32$ was simulated with one level of grid refinement. The mixture starts to burn because of the high temperature hot-spot introduced as the initial condition. Snapshots of this simulation are shown in the Figs. 7-8-7-10. Adaptive meshes are also shown in Fig. 7-10. The flow is along the positive x direction. As combustion proceeds, products are formed after ignition in the hot-spot. CO2 contours are shown in Fig. 7-10.

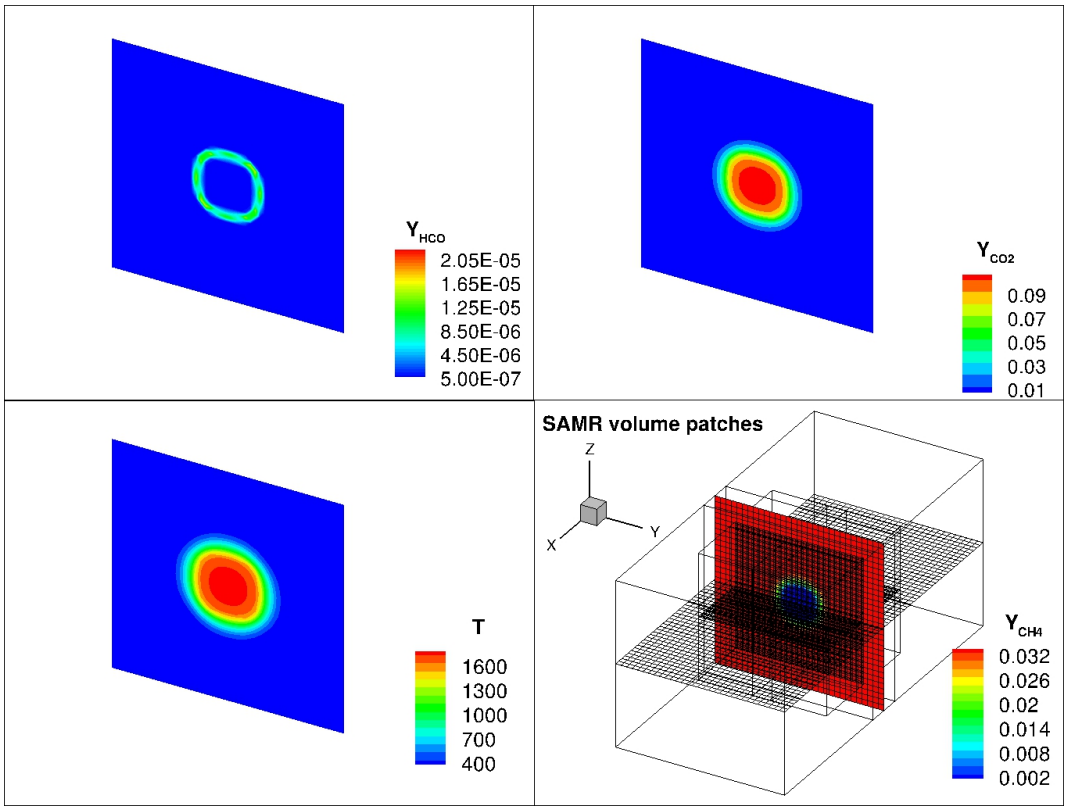

Figure 7-10: Three-dimensional adaptive mesh patches overlaid on HCO, CO_2, T and CH_4 contours on a x-normal center slice. Volume mesh patches are overlaid on the CH_4 contours.

Figure 7-12 shows a flame-structure comparison (via temperature, major and minor species profile) of the spherically outward propagating flame with a one-dimensional

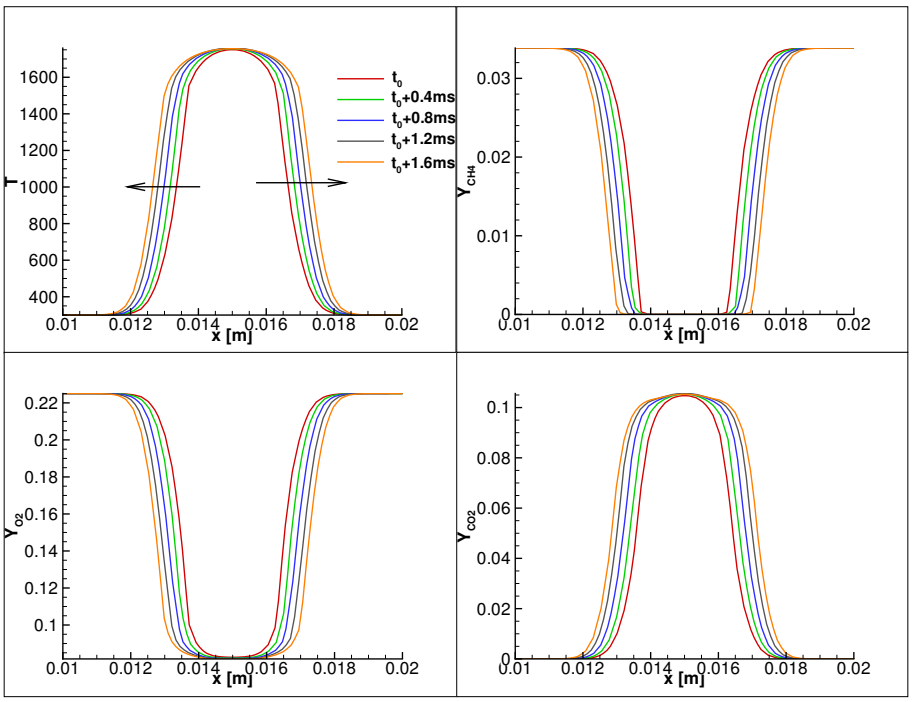

Figure 7-11: Temperature and major species profile during the unsteady spherical flame expansion.

adiabatic unstrained flame (obtained using Chemkin at the same ϕ). This was done after few iterations, once the flame propagation "reasonably" forgot the ignition conditions. The x-axis is in mm units and corresponds to the flame co-ordinate. They have been shifted to keep the peak Y_{HCO} or equivalently the peak heat release-rate location at 0. The 3D profile was taken at a line normal to the spherical flame shown in Fig. 7-10. Spherically expanding flame is an unsteady process (see Fig. 7-11) and the flame-structure is expected to change during this expansion. This comparison was carried out when the flame radius of curvature was 1.5 mm defined on the basis of peak heat-release rate location (snapshot corresponding to Fig. 7-10). A good overall agreement can be seen in the flame structure. Due to curvature effects, an exact match is not expected. Based on the Lagrangian definition 4.7, for a spherical propagating flame in a quiescent medium, the unsteady stretch simplifies to

$$\kappa = \frac{2}{r}\frac{dr}{dt} \tag{7.4}$$

where r is the instantaneous radius of curvature of the flame-front. The stretch is positive for an expanding flame and was computed to be 810 s^{-1} at the time-instant investigated here. After a long time, when the radius of curvature becomes very large compared to the flame thickness, the flame structure becomes same as that of a unstrained one-dimensional flame. Until then, the flame characteristics such as the flame speed the burnt gas temperature will be different from its one-dimensional counterpart. As discussed in Section 4.2.3, flame speed is expected to decrease from its adiabatic value for a positive flame stretch [2] for lean methane-air flames (**Le** < 1 Table 4.1). It can be estimated by

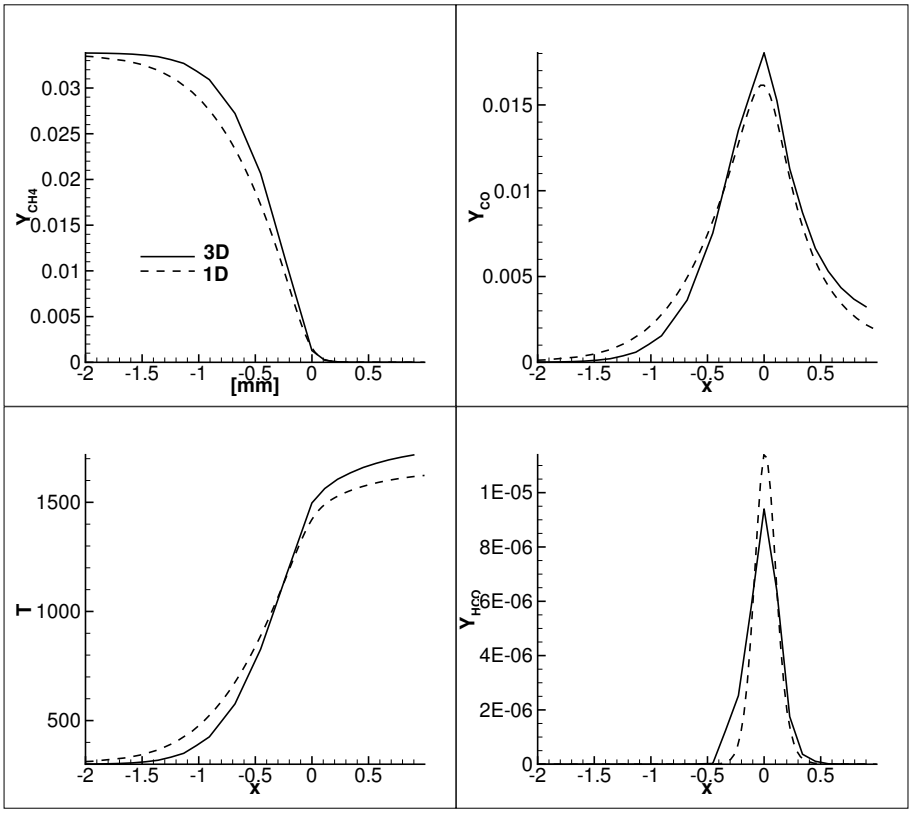

Figure 7-12: Comparison of the spherically propagating flame structure with a one-dimensional unstrained flame.

$$S_b = \frac{dr}{dt} \tag{7.5}$$

[2] Although the linear Markstein relationship discussed in Section 4.2.3 is not valid for the strong stretch computed at the time-instant considered here.

$$S_u = S_b \frac{\rho_b}{\rho_u} \tag{7.6}$$

The instantaneous flame speed computed was 10.42 cm/s (adiabatic value is 11.87 from Table 4.1). The peak burnt gas temperature was observed to be 1756 K, slightly higher than the adiabatic flame temperature of 1669 K (from Table 4.1). Matalon [109] showed that for the cases when the flame speed decreases from its adiabatic value when positively stretched, there need not be a direct correlation between the flame speed and the flame temperature. It was analytically shown that for such cases, the flame temperature increases although the flame speed decreases relative to their corresponding adiabatic unstretched values. This explains the higher temperature predicted for the spherical flame in Fig 7-12.

The SAMR framework allowed a very coarse base 3D grid, while maintaining the flame resolution by the adaptive fine patches in the above simulation.

7.4 Conclusions

In this chapter, I presented the advanced numerical developments undertaken. I discussed a first-order methodology to tackle any arbitrary shaped stair-stepped immersed solid. A simulation of a flame stabilized on a circular-cylinder was shown and the impact of flame-holder geometry on the flow was discussed. Extension of the code to three-dimensional domain was undertaken and a spherically expanding flame simulation was tested. Its structure was compared to a one-dimensional unstrained flame simulation. The 3D development was limited to "fluid-only" domains. A 3D buffer zone immersed boundary method formulation, analogous to the development in this thesis must be undertaken in the future. These developments, along-with the novel method discussed in Chapter 2 make the current simulation tool a valuable resource for future multi-physics numerical investigations.

Chapter 8

Conclusions

8.1 Summary

The major contributions of this thesis are (i) development of a state-of-the-art numerical approach to capture the wide spectra of spatio-temporal scales associated with reacting flows around immersed boundaries, (ii) elucidating the underlying mechanisms of laminar flame stabilization and blow-off in bluff-body and perforated-plate burners, and (iii) formulating an analytical model for the dynamic response of perforated-plate stabilized flames to acoustic perturbations.

A second-order immersed boundary method for reacting flow simulations near heat-conducting, grid conforming, solid object was presented in Chapter 2. The method was coupled with a block-structured adaptive mesh refinement (SAMR) framework (for the multi-length-scales) and a semi-implicit operator-split projection algorithm (for the multi-time-scales) developed by Safta et al. [11]. The immersed boundary approach captures the flame-wall interactions. A novel "buffer zone" methodology was introduced to impose the solid-fluid boundary conditions such that symmetric derivatives and interpolation stencils can be used throughout the interior of the domain comprised of fluid and solid cells, thereby maintaining the order of accuracy of the method. A binary marker function was used to track the solid cells, allowing prescribing multiple solid objects (rectangular or block rectangular like T-shaped) in the simulations. Near an immersed solid boundary, single-sided buffer

zones (inside the solid) were used to resolve the species discontinuities, and dual buffer zones (inside and outside the solid) were used to capture the temperature gradient discontinuities. The buffer zones were constructed at all the levels of the SAMR grid and before each stage of the multistage RKC integration of the scalar transport. This eliminated the need to impose artificial flame anchoring boundary conditions used in the existing stat-of-the-art numerical methods. As a result, this relaxes the current restriction of the simulations being accurate only in the far-field away from the anchoring region. The overall second-order convergence of the numerical method was demonstrated. A low-order approach was also developed to resolve the flow around complex immersed solids using a coordinate conforming representation (discussed in Chapter 7). The numerical tool developed in this thesis is valuable for future research investigating a variety of multi-physics reacting flows while incorporating flame-wall interactions.

As such, using this approach it is possible for the first time to analyze the complex and subtle processes near-walls that govern flame stabilization. Limits on flame stabilization in two canonical configurations: bluff-body and perforated-plate, were investigated and the underlying physical mechanisms were elucidated in Chapters 3-5. Detailed chemical kinetics model for methane-air combustion was used. Bluff-body simulations showed a shear-layer stabilized flame within a recirculation zone dominated by products of combustion. Perforated-plate simulations showed a bell-shaped flame stabilized on a preheated recirculation zone of reactants. A significant departure from the conventional two-zone premixed flame-structure was observed in the anchoring region for both configurations. The total flame stretch in the two configurations was strain and curvature dominated respectively. In the bluff-body wake, the location where the flame is initiated, preferential diffusion and conjugate heat exchange furnish conditions for ignition and enable streamwise flame continuation. In the perforated-plate, on the other hand, a combination of conjugate heat exchange and flame curvature is responsible for local anchoring. For both configurations, it was found that a flame was stable when (1) the local flame displacement speed was equal to the flow speed (static stability), and (2) the gradient of the flame displacement

speed normal to its surface was higher than the gradient of the flow speed along the same direction (dynamic stability). As the blow-off conditions were approached, the difference between the former and the latter decreased until the dynamic stability condition (2) was violated. The blow-off of flames stabilized in a bluff-body wake start downstream, near the end of the recirculation zone, by flame pinching into an upstream and a downstream propagating sections. The blow-off of flames stabilized in a perforated-plate wake start in the anchoring region with the entire flame front convecting downstream. Within the examined range of operating conditions, conjugate heat exchange was shown to play negligible role in the former configuration, whereas its role was critical in the latter. A "Residual flame" was observed in the bluff-body configuration before complete blow-off because the flame near the anchoring region strongly satisfied the dynamic stability criterion even though it is violated at a downstream location. The mechanism based on that criterion satisfies the widely reported Damköhler number correlation for blow-off. These investigations elucidated the thus far unknown physics of the underlying flame stabilization and blow-off mechanisms, understanding which is crucial for designing flame-holders for combustors that support continuous burning. Such an investigation is not possible without the advanced numerical tool developed in this work.

Based on the insight gained from the simulations, an analytical model was formulated in Chapter 6 to describe the dynamic response of perforated-plate stabilized flames to flow perturbations in an acoustically coupled environment. These models are instrumental in optimizing combustor designs and applying active control to guarantee dynamic stability if necessary.

8.2 Suggested future work

8.2.1 Numerical development

Although currently restricted to Cartesian geometries (second order accurate) and stair-stepped geometries (first order accurate) only, the method is a progressive step

towards developing more complex immersed boundary formulation (solid walls not aligned with the grid) for reacting flows. Current state-of-the art codes that tackle complex immersed boundaries are restricted to non-reacting flows. This is an immensely challenging task for reacting flows, specially for high-order accuracy and coupling with the SAMR framework, which must be undertaken in the future. The modularity of the code, developed using the Common Component Architecture (CCA) framework [12], will allow the numerical machinery to be directly connected to the complex immersed boundary formulation, once developed.

Investigating catalytic and plasma interactions in the presence of burner walls will be feasible, once the numerical development governing their physics is incorporated in this method. The binary marker function approach also provides an important advantage to deal with moving bodies in the future, e.g. coal or biomass particles in combustors in the future. In such cases tracking the moving boundary is not only expensive, but also complicated in terms of data structure implementation due to the search operations involved. Currently, to the best of our knowledge, second-order fully resolved numerical simulations with flow, thermal and chemical effects using a coupled SAMR-IBM is unavailable for moving bodies and research in this direction will be a significant contribution to this field.

Other major developmental task would be to incorporate flame-wall interaction in three-dimensions, which is expected to be relatively easier extension of the numerical method discussed in this thesis. This can then be potentially coupled with LES models for investigating turbulent combustion.

8.2.2 Turbulent bluff-body flame blow-off

Most experimental studies in the literature were focused on analyzing and correlating turbulent flame blow-off. Turbulence adds additional complexities to the flow-field in the form of vortex shedding, flow unsteadiness and potentially extreme stretch rates resulting in local extinction of the flame sheet. The extension of the physical mechanism for laminar flame blow-off demonstrated in this thesis to turbulent flows is unclear at this point. However, it is a good starting point for similar investigations of

weakly turbulent flames. This involves investigating flame blow-off at higher Reynolds number (transition to turbulence regime).

8.2.3 Unsteady flame dynamics

Recent experimental investigations in the Reacting Gas Dynamics Laboratory [38] showed that the conjugate heat-exchange with a backward-facing step in a combustor can significantly modify or sometimes even suppress the onset of the combustion instability. These experiments were performed in the compressible turbulent flow regime. The impact of the conjugate heat exchange on the unsteady response of the premixed flames to acoustic perturbations is a multiphysics challenging problem and its mechanism is still unclear. Investigating this is critical to understand how the acoustic oscillations couple with the combustion heat release; potentially leading to combustion instability. I demonstrated that conjugate heat exchange is the driving factor for a resonant behavior of the dynamic response of premixed flame stabilized on perforated-plate burners analytically in Chapter 6. Similar investigation in the context of bluff-bodies using the numerical tool discussed in this thesis must be undertaken. A preliminary simulation to that effect - an unsteady bluff-body flame responding to inlet velocity forcing was shown in this thesis in Section 3.3.2.

Another interesting application to the developed tool would be to study the unsteady ignition process near spark-plugs or walls. A detailed understanding of such a process will be very critical for efficient ignition equipment design in combustors.

8.2.4 Lewis number effects

Markstein length, which depends on the Lewis number, was shown to play an important role in the dynamic stability criterion in Chapter 4. This is a physico-chemical property of the mixture that will impact the flame blow-off characteristics of a fixed bluff-body operating with different fuels. The methane-air flames investigated in this thesis have Lewis number based on the deficient reactant (CH_4) close to unity. Investigating the applicability of the stability criterion to combustors with fuels having

extreme non-unity Lewis numbers such as Hydrogen ($\mathbf{Le} < 1$) and gasoline ($\mathbf{Le} > 1$) is thus a natural extension of this work.

8.2.5 Radiation

The numerical model discussed in this thesis neglected radiative heat transfer. The radiative heat flux can be estimated as $q_r \approx \epsilon\sigma T_f^4$ where q_r is the radiative heat flux, ϵ is the total gas emittance, σ is the Stefan-Boltzmann constant, and T_f is the flame temperature. ϵ is less than 0.01 for the dominant emitters H_2O and CO_2 at 1 atm [110]; while $T_f \approx 1900$ K. Thus $q_r \approx 7 \times 10^3$ W/m^2. For perforated-plate stabilized flames discussed in Chapter 5, the average conductive heat exchange with the burner plate for $\phi = 0.75$, $U = 1.3$ m/s can be estimated as $q_p \approx 3 \times 10^4$ W/m^2, which is almost an order of magnitude higher than the radiative flux. In cases where radiation contributes equally, the overall physics of flame stabilization and blow-off is not expected to change significantly. Radiation will provide an additional pathway for heat loss to the burner plate and surroundings. Quantifying radiative heat exchange and its impact on flame stabilization and blow-off is a challenging numerical task that must be undertaken in the future.

Bibliography

[1] A. Gruber, R. Sankaran, ER Hawkes, and JH Chen. Turbulent flame-wall interaction: A direct numerical simulation study. *Journal of Fluid Mechanics*, 658:5–32, 2010.

[2] F. Duchaine, F. Boudy, D. Durox, and T. Poinsot. Sensitivity analysis of transfer functions of laminar flames. *Combustion and Flame*, 158:2384–2394, 2011.

[3] J. Bell, M. Day, J. Grcar, M. Lijewski, J. Driscoll, and S. Filatyev. Numerical simulation of a laboratory-scale turbulent slot flame. *Proceedings of the Combustion Institute*, 31:1299–1307, 2007.

[4] Evatt R Hawkes and Jacqueline H Chen. Direct numerical simulation of hydrogen-enriched lean premixed methane–air flames. *Combustion and Flame*, 138(3):242–258, 2004.

[5] HN Najm and OM Knio. Modeling low mach number reacting flow with detailed chemistry and transport. *Journal of Scientific Computing*, 25(1):263–287, 2005.

[6] M. Day and J. Bell. Numerical simulation of laminar reacting flows with complex chemistry. *Combustion Theory and Modelling*, 4:535–556, 2000.

[7] Marsha J Berger and Joseph Oliger. Adaptive mesh refinement for hyperbolic partial differential equations. *Journal of computational Physics*, 53(3):484–512, 1984.

[8] M.J. Berger and P. Colella. Local adaptive mesh refinement for shock hydrodynamics. *Journal of computational Physics*, 82(1):64–84, 1989.

[9] JB Bell, MS Day, and MJ Lijewski. Simulation of nitrogen emissions in a premixed hydrogen flame stabilized on a low swirl burner. *Proceedings of the Combustion Institute*, 34:1173–1182, 2012.

[10] Fabrice Schlegel. *Hybrid Lagrangian/Eulerian 3D methods for high Reynolds number reactive flows*. PhD thesis, Massachusetts Institute of Technology, Cambridge, USA, 2011.

[11] C. Safta, J. Ray, and H. N. Najm. A high-order low-mach number amr construction for chemically reacting flows. *Journal of Computational Physics*, 229: 9299–9322, 2010.

[12] Jaideep Ray, R Armstrong, Cosmin Safta, BJ Debusschere, Benjamin A Allan, and HN Najm. Computational frameworks for advanced combustion simulations. In *Turbulent Combustion Modeling*, pages 409–437. Springer, 2011.

[13] C. K. Westbrook and F. L. Dryer. Simplified reaction mechanisms for the oxidation of hydrocarbon fuels in flames. *Combustion Science and Technology*, 27:31–43, 1981.

[14] A. C. McIntosh. On the cellular instability of flames near porous-plug burners. *Journal of Fluid Mechanics*, 161:43–75, 1985.

[15] R. Rook, L. P. H. de Goey, L. M. T. Somers, K. R. A. M. Schreel, and R. Parchen. Response of burner-stabilized flat flames to acoustic perturbation. *Combustion Theory and Modeling*, 6:223–242, 2002.

[16] R. Rook. *Acoustics in Burner Stabilized Flames*. PhD thesis, Eindhoven University of Technology, Eindhoven, The Netherlands, http://www.tue.nl/bib/, 2001.

[17] C. S. Peskin. Numerical analysis of blood flow in the heart. *Journal of Computational Physics*, 25:220–252, 1977.

[18] R. Mittal and G. Iaccarino. Immersed boundary methods. *Annual Review of Fluid Mechanics*, 37:239–261, 2005.

[19] E. A. Fadlun, R. Verzicco, P. Orlandi, and J. Mohd-Yusof. Combined immersed-boundary finite-difference methods for three-dimensional complex flow simulations. *Journal of Computational Physics*, 161:35–60, 2000.

[20] W. P. Breugem and B. J. Boersma. Direct numerical simulations of turbulent flow over a permeable wall using a direct and a continuum approach. *Physics of Fluids*, 17(2):025103, 2005. doi: 10.1063/1.1835771. URL `http://link.aip.org/link/?PHF/17/025103/1`.

[21] G. Iaccarino and S. Moreau. Natural and forced conjugate heat transfer in complex geometries on cartesian adapted grids. *Transactions of the ASME*, 128:838–846, 2006.

[22] S. Kang, G. Iaccarino, and F. Ham. Dns of buoyancy-dominated turbulent flows on a bluff body using the immersed boundary method. *Journal of Computational Physics*, 228:3189–3208, 2009.

[23] F. Paravento, M. J. Pourquie, and B. J. Boersma. An immersed boundary method for complex flow and heat transfer. *Flow, Turb. Combust.*, 80:187–206, 2008.

[24] Robert S Barlow, Matthew J Dunn, Mark S Sweeney, and Simone Hochgreb. Effects of preferential transport in turbulent bluff-body-stabilized lean premixed CH4/air flames. *Combustion and Flame*, 159(8):2563–2575, 2012.

[25] Matthew J Dunn and Robert S Barlow. Effects of preferential transport and strain in bluff body stabilized lean and rich premixed CH4/air flames. *Proceedings of the Combustion Institute*, 34(1):1411–1419, 2013.

[26] Prashant G Mehta and Marios C Soteriou. Combustion heat release effects on the dynamics of bluff body stabilized premixed reacting flows. In *41st Aerospace Sciences Meeting and Exhibit*, pages 2003–835, 2003.

[27] RR Erickson and MC Soteriou. The influence of reactant temperature on the dynamics of bluff body stabilized premixed flames. *Combustion and Flame*, 158 (12):2441–2457, 2011.

[28] GC Williams, HC Hottel, and AC Scurlock. Flame stabilization and propagation in high velocity gas streams. In *Symposium on Combustion and Flame, and Explosion Phenomena*, volume 3, pages 21–40. Elsevier, 1949.

[29] John P Longwell, Edward E Frost, and Malcolm A Weiss. Flame stability in bluff body recirculation zones. *Industrial & Engineering Chemistry*, 45(8): 1629–1633, 1953.

[30] Edward Edom Zukoski. *Flame stabilization on bluff bodies at low and intermediate Reynolds numbers*. PhD thesis, California Institute of Technology, 1954.

[31] FH Wright. Bluff-body flame stabilization: blockage effects. *Combustion and Flame*, 3:319–337, 1959.

[32] Edward E Zukoski and Frank E Marble. Experiments concerning the mechanism of flame blowoff from bluff bodies. 1983.

[33] KM Kundu, D Banerjee, and D Bhaduri. Theoretical analysis on flame stabilization by a bluff-body. *Combustion Science and Technology*, 17(3-4):153–162, 1977.

[34] S. J. Shanbhogue, S. Husain, and T. Lieuwen. Lean blowoff of bluff body stabilized flames: Scaling and dynamics. *Progress in Energy and Combustion Science*, 35:98–120, 2009.

[35] Swetaprovo Chaudhuri, Stanislav Kostka, Michael W Renfro, and Baki M Cetegen. Blowoff dynamics of bluff body stabilized turbulent premixed flames. *Combustion and Flame*, 157(4):790–802, 2010.

[36] James Kariuki, James R Dawson, and Epaminondas Mastorakos. Measurements in turbulent premixed bluff body flames close to blow-off. *Combustion and Flame*, 159(8):2589–2607, 2012.

[37] MJ Russi, I Cornet, and R Cornog. The influence of flame holder temperature on flame stabilization. In *Symposium (International) on Combustion*, volume 4, pages 743–748. Elsevier, 1953.

[38] Seunghyuck Hong, Santosh Shanbhogue, Kushal S. Kedia, and Ahmed F. Ghoniem. Impact of the flame-holder heat transfer characteristics on the onset of combustion instability. *Combustion Science and Technology*, 2013. doi: 10.1080/00102202.2013.816575. in press.

[39] T. Kawamura, K. Asato, T. Mazaki, T. Hamaguchi, and H. Kayahara. Explanation of the blowoff of inverted flames by the area-increase concept. *Combustion and Flame*, 35:109–116, 1979.

[40] B. Lewis and von Elbe. Stability and structure of burner flames. *Journal of Chemical Physics*, 11:75–97, 1943.

[41] Bernard Lewis and Guenther Von Elbe. *Combustion, flames and explosions of gases*. Academic Press, 1987.

[42] B. Karlovitz, D. K. Denniston, D. H. Knappschafer, and F.E. Wells. Studies on turbulent flames, a. flame propogation across velocity gradients, b. turbulence measurement in flames. *Fourth Symposium (International) on Combustion*, pages 819–826, 1953.

[43] Stuart B Reed. Flame stretchâa connecting principle for blow-off data. *Combustion and Flame*, 11(3):177–189, 1967.

[44] H. Edmondson and M. P. Heap. Blowoff of inverted flames. *Combustion and Flame*, 14:191–194, 1970.

[45] A. Melvin and J. B. Moss. Evidence for the failure of the flame stretch concept for premixed flames. *Combustion Science and Technology*, 7:189–196, 1973.

[46] T. Kawamura, K. Asato, and T. Mazaki. Reexamination of the blowoff mechanism of premixed flames - inverted flames. *Combustion and Flame*, 45:225–233, 1982.

[47] R. M. M. Mallens, L. P. H. de Goey, and C. K. Law. A numerical study of the stabilisation of a lean premixed v-shaped flame. *Combustion Science and Technology*, 159:373–389, 2000.

[48] C. Trevino, S. Donnerhack, and N. Peters. Lda measurements in the premixed v flame stabilized in the wake of a flat plate boundary layer. *Combustion and Flame*, 85:505–510, 1991.

[49] C. J. Sung, C. K. Law, and A. Umemura. On adiabatic stabilization of inverted flames. *Twenty-Fourth Symposium (International) on Combustion*, pages 205–212, 1992.

[50] D. Durox, T. Schuller, N. Noiray, and S. Candel. Experimental analysis of nonlinear flame transfer functions for different flame geometries. *Proc. Combust. Inst.*, 32:1391–1398, 2009.

[51] V.N. Kornilov, R. Rook, J.H.M. ten Thije Boonkkamp, and L.P.H. de Goey. Experimental and numerical investigation of the acoustic response of multi-slit bunsen burners. *Combustion and Flame*, 156:1957–1970, 2009.

[52] H. M. Altay, S. Park, D. Wu, D. Wee, A. M. Annaswamy, and A. F. Ghoniem. Modeling the dynamic response of a laminar perforated-plate stabilized flame. *Proc. Combust. Inst.*, 32:1359–1366, 2009.

[53] K. S. Kedia, H. M. Altay, and A. F. Ghoniem. Impact of flame-wall interaction on flame dynamics and transfer function characteristics. *Proceedings of the Combustion Institute*, 33:1113–1120, 2011.

[54] P. N. Brown, G. D. Byrne, and A. C. Hindmarsh. Vode: a variable-coefficient ode solver. *SIAM Journal of Scientific Computing*, 10(5):1039–1051, 1989.

[55] Jaideep Ray, Christopher A Kennedy, Sophia Lefantzi, and Habib N Najm. Using high-order methods on adaptively refined block-structured meshes: derivatives, interpolations, and filters. *SIAM Journal on Scientific Computing*, 29(1): 139–181, 2007.

[56] Patrick J Roache. Verification of codes and calculations. *AIAA journal*, 36(5): 696–702, 1998.

[57] Y. C. Zhou, S. Zhao, M. Feig, and G. W. Wei. High order matched interface and boundary method for elliptic equations with discontinuous coefficients and singular sources. *Journal of Computational Physics*, 213:1–30, 2006.

[58] O. M. Knio, H. N. Najm, and P. S. Wyckoff. A semi-implicit numerical scheme for reacting flow, II. stiff, operator-split formulation. *Journal of Computational Physics*, 154:428–467, 1999.

[59] S. Taneda and H. Honji. Unsteady flow past a flat plate normal to the direction of motion. *Journal of Physical Society of Japan*, 30(1):262, 1971.

[60] SCR Dennis, W. Qiang, M. Coutanceau, and JL Launay. Viscous flow normal to a flat plate at moderate Reynolds numbers. *Journal of Fluid Mechanics*, 248: 605–605, 1993.

[61] Y. Yoshida and T. Nomura. A transient solution method for the finite element incompressible Navier-Stokes equations. *International Journal for Numerical Methods in Fluids*, 5(10):873–890, 1985.

[62] H. Laval and L. Quartapelle. A fractional-step Taylor–Galerkin method for unsteady incompressible flows. *International Journal for Numerical Methods in Fluids*, 11(5):501–513, 1990.

[63] HR Tamaddon-Jahromi, P. Townsend, and MF Webster. Unsteady viscous flow past a flat plate orthogonal to the flow. *Computers and fluids*, 23(2):433–446, 1994.

[64] P. Koumoutsakos and D. Shiels. Simulations of the viscous flow normal to an impulsively started and uniformly accelerated flat plate. *Journal of Fluid Mechanics*, 328(10):177–227, 1996.

[65] John Kim and Parviz Moin. Application of a fractional-step method to incompressible Navier-Stokes equations. *Journal of computational physics*, 59(2): 308–323, 1985.

[66] E Weinan and Jian-Guo Liu. Projection method. I: Convergence and numerical boundary layers. *SIAM journal on numerical analysis*, 32(4):1017–1057, 1995.

[67] H. Suzuki, Y. Inoue, T. Nishimura, K. Fukutani, and K. Suzuki. Unsteady flow in a channel obstructed by a square rod (crisscross motion of vortex). *International journal of heat and fluid flow*, 14(1):2–9, 1993.

[68] F.W. Davis, F. Moore, and P. Purtell. A numerical-experimental study of confined flow around rectangular cylinders. *Physics of Fluids*, 27:1, 1984.

[69] MD Smooke, IK Puri, and K Seshadri. A comparison between numerical calculations and experimental measurements of the structure of a counterflow diffusion flame burning diluted methane in diluted air. In *Symposium (International) on Combustion*, volume 21, pages 1783–1792. Elsevier, 1988.

[70] Habib N Najm, Phillip H Paul, Charles J Mueller, and Peter S Wyckoff. On the adequacy of certain experimental observables as measurements of flame burning rate. *Combustion and Flame*, 113(3):312–332, 1998.

[71] Inge R Gran, Tarek Echekki, and Jacqueline H Chen. Negative flame speed in an unsteady 2-d premixed flame: A computational study. In *Symposium (International) on Combustion*, volume 26, pages 323–329. Elsevier, 1996.

[72] A. C. McIntosh and J. F. Clarke. A review of theories currently being used to model steady plane flameson flame-holders. *Combustion Science and Technology*, 37(3-4):201–219, 1984.

[73] T. Lieuwen. Modeling premixed combustion-acoustic wave interactions: A review. *Journal of Propulsion and Power*, 19(5):765–781, 2003.

[74] S. Ducruix, T. Schuller, D. Durox, and S. Candel. Combustion dynamics and instabilities: Elementary coupling and driving mechanisms. *Journal of Propulsion and Power*, 19(5):722–733, 2003.

[75] S. Candel. Combustion dynamics and control: Progess and challenges. *Proc. Combust. Inst.*, 29:1–28, 2002.

[76] George H Markstein. Experimental and theoretical studies of flame front stability. *Journal of Aerospace Sciences*, 18:199–209, 1951.

[77] P. Clavin. Dynamic behavior of premixed flame fronts in laminar and turbulent flows. *Progress in Energy and Combustion Science*, 11:1–59, 1985.

[78] P Clavin and FA Williams. Effects of molecular diffusion and of thermal expansion on the structure and dynamics of premixed flames in turbulent flows of large scale and low intensity. *Journal of fluid mechanics*, 116(1):251–282, 1982.

[79] M Matalon and BJ Matkowsky. Flames as gasdynamic discontinuities. *Journal of Fluid Mechanics*, 124(1):239–259, 1982.

[80] P Clavin and G Joulin. Premixed flames in large scale and high intensity turbulent flow. *Journal de Physique Lettres*, 44(1):1–12, 1983.

[81] CK Law, DL Zhu, and G Yu. Propagation and extinction of stretched premixed flames. In *Symposium (International) on Combustion*, volume 21, pages 1419–1426. Elsevier, 1988.

[82] B Deshaies and P Cambray. The velocity of a premixed flame as a function of the flame stretch: an experimental study. *Combustion and Flame*, 82(3): 361–375, 1990.

[83] UC Müller, M Bollig, and N Peters. Approximations for burning velocities and markstein numbers for lean hydrocarbon and methanol flames. *Combustion and Flame*, 108(3):349–356, 1997.

[84] G Searby and J Quinard. Direct and indirect measurements of markstein numbers of premixed flames. *Combustion and Flame*, 82(3):298–311, 1990.

[85] SG Davis, Joël Quinard, and Geoffrey Searby. Markstein numbers in counterflow, methane-and propane-air flames: a computational study. *Combustion and flame*, 130(1):123–136, 2002.

[86] Paul Clavin and Guy Joulin. Flamelet library for turbulent wrinkled flames. In *Turbulent Reactive Flows*, pages 213–240. Springer, 1989.

[87] JH Tien and M Matalon. On the burning velocity of stretched flames. *Combustion and Flame*, 84(3):238–248, 1991.

[88] J. M. C. Mendes-Lopes and H. Daneshyar. Influence of strain fields on flame propagation. *Combustion and Flame*, 60(1):29–48, 1985. URL `www.scopus.com`.

[89] Sebastien M Candel and Thierry J Poinsot. Flame stretch and the balance equation for the flame area. *Combustion Science and Technology*, 70(1-3):1–15, 1990.

[90] K. S. Kedia. Numerical simulations of perforated plate stabilized premixed flames with detailed chemistry. Master's thesis, Massachusetts Institute of Technology, Cambridge, USA, http://dspace.mit.edu/handle/1721.1/61793, 2010.

[91] H. M. Altay, K. S. Kedia, R. L. Speth, and A. F. Ghoniem. Two-dimensional simulations of steady perforated-plate stabilized premixed flames. *Combustion Theory and Modelling*, 14:135–154, 2010.

[92] D. G. Goodwin. An open-source, extensible software suite for cvd process simulation. pages 155–162, 2003. Chemical Vapor Deposition XVI and EUROCVD 14, ECS Proceedings Volume 2003-08, M. Allendorf, F. Maury, and F. Teyssandier, editors, The Electrochemical Society.

[93] C. K. Law. Dynamics of stretched flames. *Twenty-Second Symposium (International) on Combustion*, pages 1381–1402, 1989.

[94] T. Poinsot and D. Veynante. *Theoretical and Numerical Combustion (2nd ed.)*. R.T. Edwards, 2005.

[95] C. W. Choi and I. K. Puri. Response of flame speed to positively and negatively curved premixed flames. *Combustion Theory and Modelling*, 7:205–220, 2003.

[96] A. Palm-Leis and R.A. Strehlow. On the propagation of turbulent flames. *Combustion and Flame*, 13:111–129, 1969.

[97] D. W. Mikolaitis. The interaction of flame curvature and stretch, part 1: The concave premixed flame. *Combustion and Flame*, 57:25–31, 1984.

[98] T. Echekki and M. G. Mungal. Flame speed measurements at the tip of a slot burner: Effects of flame curvature and hydrodynamic stretch. *Twenty-Third Symposium (International) on Combustion*, pages 455–461, 1990.

[99] T. Poinsot, T. Echekki, and M. G. Mungal. A study of the laminar flame tip and implications for premixed turbulent combustion. *Combustion Science and Technology*, 81:45–73, 1992.

[100] C. W. Choi and I. K. Puri. Response of flame speed to positively and negatively curved premixed flames. *Combustion and Flame*, 126:1640–1654, 2001.

[101] J. H. Chen and H. G. Im. Correlation of flame speed with stretch in turbulent premixed methane/air flames. *Twenty-Seventh Symposium (International) on Combustion*, pages 1967–1974, 1998.

[102] M. Manohar. *Thermo-Acoustics of Bunsen type premixed flames*. PhD thesis, Eindhoven University of Technology, Eindhoven, The Netherlands, 2011.

[103] Irvin Glassman. *Combustion*. Academic press, 1997.

[104] A. F. Mills. *Heat Transfer*. Prentice Hall, Inc., 1999.

[105] E. M. Sparrow and M. Carranco Ortiz. Heat transfer coefficients for the upstream face of a perforated plate positioned normal to an oncoming flow. *International Journal of Heat and Mass Transfer*, 25:127–135, 1982.

[106] M. Fleifil, A. M. Annaswamy, Z. A. Ghoneim, and A. F. Ghoniem. Response of a laminar premixed flame to flow oscillations: A kinematic model and thermoacoustic instability results. *Combustion and Flame*, 106(4):487–510, 1996.

[107] JH Chen, WG Pritchard, and SJ Tavener. Bifurcation for flow past a cylinder between parallel planes. *Journal of Fluid Mechanics*, 284(5):23–41, 1995.

[108] Petr A Nikrityuk. *Computational thermo-fluid dynamics: in materials science and engineering*. John Wiley & Sons, 2011.

[109] Moshe Matalon. On flame stretch. *Combustion Science and Technology*, 31 (3-4):169–181, 1983.

[110] R. Siegel and J.R. Howell. *Thermal radiation heat transfer*. Number v. 1. Taylor & Francis, 2002. ISBN 9781560328391. URL `http://books.google.com/books?id=0389yQ0-fecC`.

THIS PAGE INTENTIONALLY LEFT BLANK

List of Publications Based on this Thesis

1. Kushal S. Kedia and Ahmed F. Ghoniem, Mechanism of stabilization and blowoff of a premixed flame downstream of a heat-conducting perforated plate. *Combustion and Flame*, Volume 159 (1), pp. 1055 - 1069, 2012.

2. Kushal S. Kedia and Ahmed F. Ghoniem, An analytical model for the prediction of the dynamic response of premixed flames stabilized on a heat-conducting perforated plate. *Proceedings of the Combustion Institute*, Volume 34 (1), pp. 921-928, 2013.

3. Kushal S. Kedia, Cosmin Safta, Jaideep Ray, Habib N. Najm and Ahmed F. Ghoniem, A second-order coupled immersed boundary-SAMR construction for chemically reacting flow over heat-conducting Cartesian grid-conforming solid. *Journal of Computational Physics*, under review.

4. Kushal S. Kedia and Ahmed F. Ghoniem, On the anchoring mechanism of a laminar premixed flame stabilized on a bluff-body. *Combustion and Flame*, under review.

5. Kushal S. Kedia and Ahmed F. Ghoniem, On the blow-off mechanism of a laminar premixed flame stabilized on a bluff-body. *Combustion and Flame*, under review.